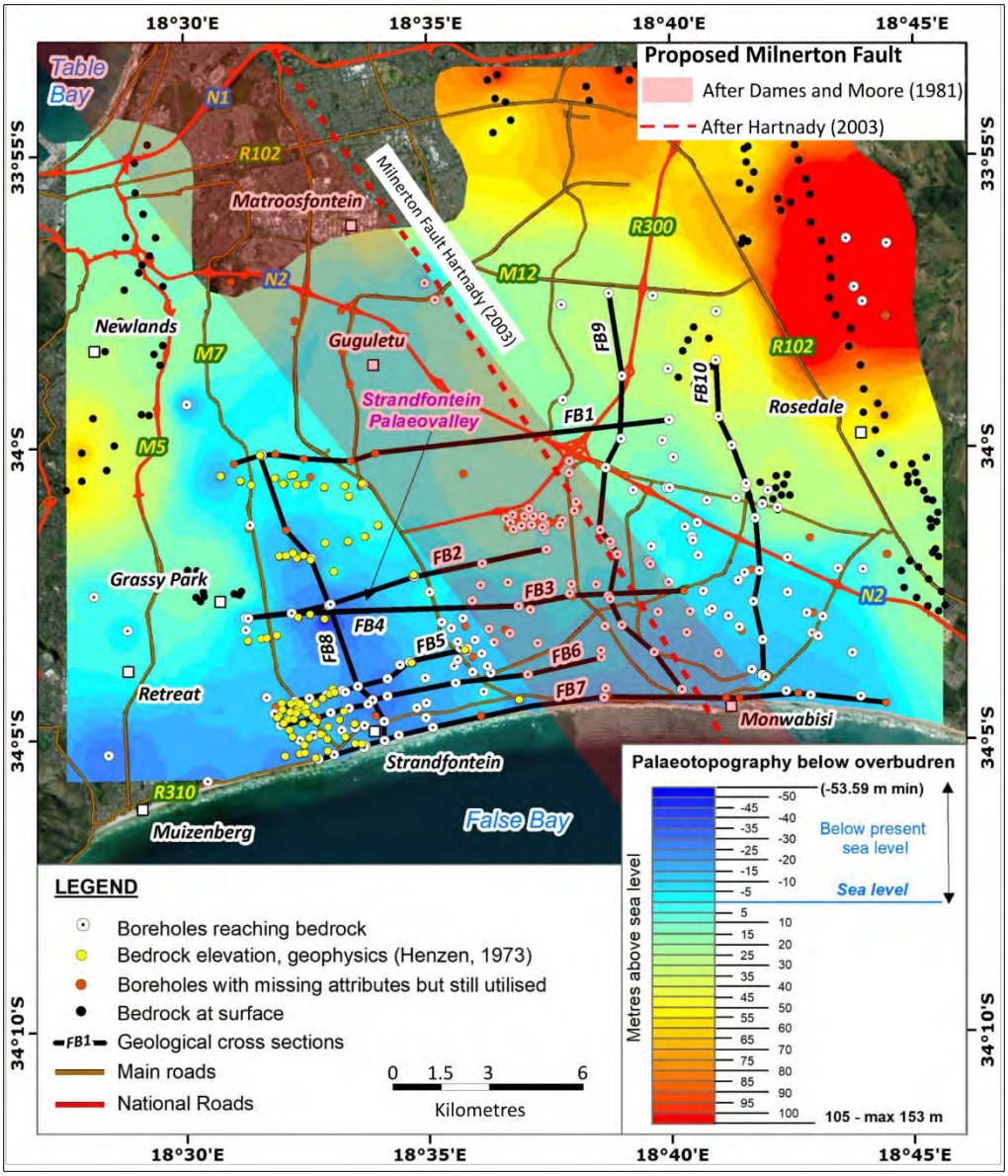

Figure 8-87. Palaeobedrock topography interpolated from borehole data for the Cape Flats. Note the large palaeovalley located towards the west. The valley reaches depths of 53.59 m bmsl. Location of geological cross sections are indicated.

During significant marine transgressive periods such as the Pliocene, when sea-level would have been 25 - 30 m higher than current levels, the Cape Flats and Noordhoek Valley would have been submerged, cutting the Cape Peninsula off as a group of islands (Figure 8-86a). As the sea advanced inland, it would have deposited marine sediments, including sands, silts, and clays. These sediments accumulated and formed layers, contributing to the geological composition of the region. The Cape Flats bedrock valley is filled by terrestrial sediments associated with the fluvial Miocene Elandsfontyn Formation (peat layers, sandy clay and clay), with basal gravel/pebble beds filling the lowest parts of the valley, implying an age of either Early Miocene or older for the valley incision. The palaeovalley appears to have developed in a very similar fashion to those at Langebaanweg and Geelbek, also carved during the Oligocene regression at Saldanha (Coetzee and Rogers, 1982; Sciscio et al., 2013; Roberts et al., 2011, 2013, 2017). Hay and Seyler (2008) proposed that the Cape Flats palaeovalley may have been a palaeochannel of the proto-Elsieskraal River that today has a channelised

flow towards the SW. Located slightly to the east of the main valley, a slightly smaller, shallower valley is encountered and interpreted as a small-scale-tributary to the main channel with sediment associated with a flood plain deposit, rather than a main channel deposit (Vandoolaeghe, 1989). Hay (1981) and Wessels and Greeff (1980), however, interpreted this as a muddy marine deposit from a marine transgression overlying a basal fluvial system. The complete sequence therefore would be basal fluvial gravel overlain by finer material as the river systems lost energy at the onset of marine transgression, overlain by marine calcareous sands and gravels (the Elandsfontyn and Varswater Formations). This dynamic geological interaction between land and sea in response to sea-level fluctuations has shaped the Cape Flat morphology and provide a far more detailed and data driven explanation for the morphology of the Cape Flats than a fault origin.

In reviewing geophysical data presented by Cole et al. (2007a), it is clear to the SSM TI Team that only two of the three gravity traverses show the presence of a gravity low, which could be the result of more weathered and brecciated material associated with a fault or a weathered dyke. The geophysical data therefore do not unequivocally prove or disprove the existence of the Milnerton Fault Zone (Raath and Cole, 2007). If the survey anomalies along Traverse 1 and 2 are interpreted as faults, it does not continue along strike to Traverse 3 (Figure 8-86b), making it unlikely to be a large continuous fault such as the proposed Milnerton Fault Zone and more likely a dyke or minor fault.

The SSM TI Team also investigated the suggestion by Dr Hartnady (Sloan, 2022) that high yielding groundwater boreholes drilled into fractured bedrock support the presence of the Milnerton Fault. Geohydrology studies across the area confirms the successful extraction of groundwater from fractured bedrock in the greater Cape Flats area (e.g., Vandoolaeghe, 1989; Wessels and Greeff, 1980; Hay, 1981; Hay and Seyler, 2008). Fractured bedrock is not uncommon in the area, given the region's tectonic history (e.g., summary by De Beer et al., 2008) and the assumption that a fractured bedrock aquifer must be related to a fault may be misleading, especially considering that several other geological features influence the occurrence, flow and concentration of groundwater in the Cape Flats, including the occurrence of numerous dykes, intrusion of granitic bodies, and Malmesbury Group lithologies. In addition, highly productive boreholes are located along the low lying palaeobedrock channels outlined in Figure 8-87, where groundwater is likely to accumulate.

Activity: Data from several boreholes drilled across the Cape Flats were collected as part of a marine terrace study (Claassen et al., 2024). Unfortunately, many of the borings have insufficient downhole lithostratigraphic descriptions to allow correlation. One borehole dataset from Wessels and Greef (1980) did however have excellent descriptions of the Sandveld Group and were spatially distributed across the location of where the Milnerton Fault is proposed to occur. The density of borehole data allowed creation of a 16 km long, N-S, coast perpendicular trending geological cross-section FB9 (Figure 8-88). Possible wave-cut bedrock platforms overlain by marine gravels are identified at three localities along section FB9 at 26 - 28.1 m amsl, 17.2 m amsl and 3 – 3.7 m amsl. Unfortunately, no chronology is available on any of these sediments. Based on altimetry alone, the broad (~ 4 km wide), ~30 m amsl terrace could be tentatively correlated to terraces at similar elevations occurring east and west of the Cape Flats area, as could the ~18-20 m terrace, but this remains uncertain. If the Milnerton Fault Zone is present and in the proposed location, data collected across the Cape Flats cross-

section FB9 show relative consistency in the correlation of marine related sediments, with no recognisable displacement across the proposed fault, for at least 1.3 -3 My.

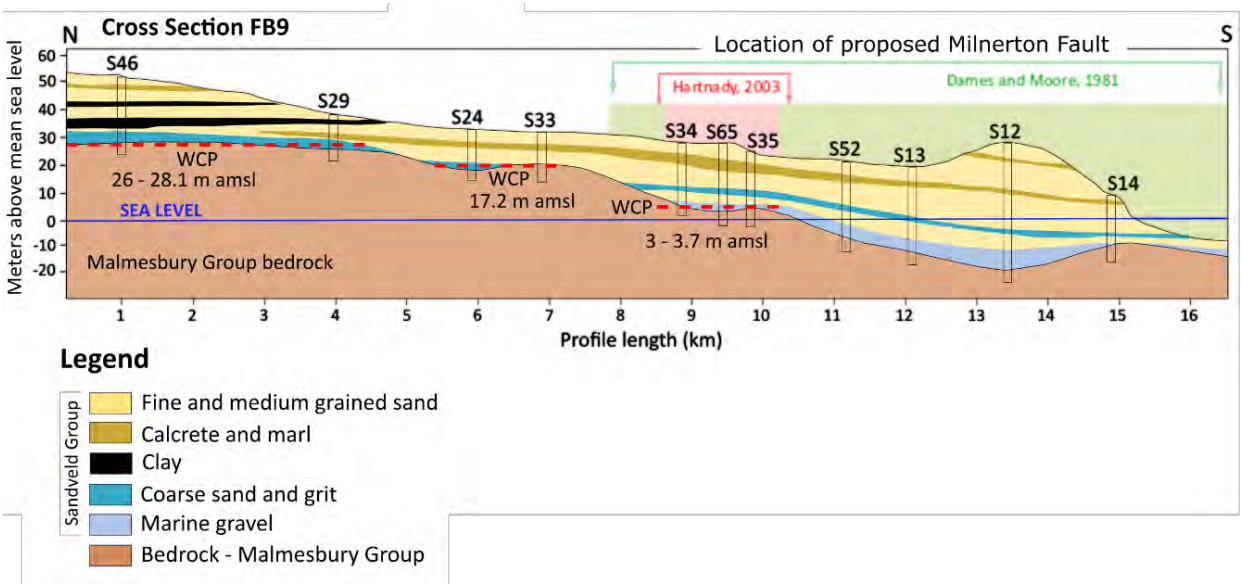

Figure 8-88. N-S orientated geological cross section FB9 along the eastern side of the Cape Flats, derived from borehole data (Wessels and Greef, 1980) with interpreted wave-cut platforms (WCP) (Claassen et al., 2024). The location of the proposed zone of occurance for the Milnerton Fault according to Hartnady (2003) and Dames and Moore (1981) is also indicated.

Deformation at Bloubergstrand

Argument: Dames and Moore (1976) ascribed intense ductile-brittle structural deformation of Malmesbury Group rocks, mapped along a narrow 75 m wide and 800 m long coastal exposure at Bloubergstrand (Figure 8-89), to the occurrence of a larger NW-SE trending fault zone in the area. They proposed that these exposures form part of the proposed Milnerton Fault Zone. Von Veh (1982) mapped the exposures in detail and described them as varying from diffuse zones of attenuation and boudinage, to discrete zones of mylonitisation. Brecciation and fault drag were associated with major strike-slip faults and displacements of a few metres. A conjugate fault pattern of dextral (030°) and sinistral (070°) faults were also documented. Von Veh (1982) ultimately came to the same conclusion as Dames and Moore (1976; 1981), stating that the structural data appears to favour the presence of a single, continuous NW-SE-striking shear zone in the area, but stopped short of correlating it to the proposed Milnerton Fault Zone. During discussions with proponent experts at Workshop 2 the Bloubergstrand exposures (shear zone) may be linked to the proposed Milnerton Fault Zone based on offshore aeromagnetic data (Cole, 2007; Cole et al., 2007a, b), that shows the offset of an interpreted dyke by a NW-SE striking anomaly.

Figure 8-89. (a) Shear zones and faults mapped by Von Veh (1982) at Bloubergstrand. (b) Asymmetrical fold adjacent to a shear zone (S 33°48'7.04"S; E 18°27'32.18") in the Malmesbury Group, and (c) prominent slickensides associated with oblique faulting (Photos provided by Dr T. Dhansay).

Assessment: The SSM TI Team considered that if the exposures at Bloubergstrand are indeed part of a larger fault zone, the shear zone should, if extended along its NW-SE strike, be visible in the onshore and offshore aeromagnetic data (Cole, 2007; Cole et al., 2007a, b). However, the SSM TI Team concluded that not to be the case. There is no evidence of a larger fault zone continuing in either the offshore data or onshore datasets in the location of the proposed Milnerton Fault Zone. The data do however reveal a NW-trending negative anomaly that appears to displace a positive E-W striking anomaly indicating of a possible fault to the east of Bloubergstrand, roughly 16 km south of Duynefontyn (Figure 8-90a). Numerous steeply dipping to near-vertical WNW-ESE to NW-SE-striking dykes occur in the area (Day, 1987) and form part of the False Bay dolerite dyke swarm dated at 132 ± 6 Ma (Reid et al., 1991). These dykes intruded along existing zones of weakness such as faults, fractures, and joints (Backeberg et al., 2011) and mostly occur as positive magnetic anomalies, with a few negative

reversely magnetised anomalies. The change in magnetic polarity indicates intrusion of the dykes over geologic time within at least one reversal of the Earth's magnetic field. Cole (2023) undertook some forward 3D modelling of the NW-trending negative anomaly that appears to displace the positive E-W striking anomaly (Figure 8-90a) with the aim of establishing whether a fault is present east of Bloubergstrand and, if so, model its geometry. The anomalies were modelled in two different ways (Figure 8-90b-e):

- Model 1: The negative anomaly represents a fault that displaced the E-W trending normally magnetised dyke, after which reversely magnetised material intruded along the fault (Figure 8-90b, c).

- Model 2: The second model shows that the NW-striking reversely magnetised dyke intruded first, and that E-W trending dykes were not displaced but are rather intruded *en-echelon* disrupting the NW-striking dyke (Figure 8-90d, e). The perceived offset could simply be related to the general mechanism of dyke propagation and magma flow under shear stress that combines the lateral propagation and magma flow of dyke segments by Currie and Ferguson (1970) and the mode of dyke propagation proposed by Pollard (1987) leading to overlapping dyke tips *en echelon* (Figure 8-91).

Several authors have investigated the structural geology and tectonic history of the Malmesbury Group in the Western Cape Province (e.g., Hartnady, 1969; Theron, 1992; Belcher, 2003; De Beer et al., 2008; Kisters and Belcher, 2018). These studies reveal that structural zones with characteristics similar to those described at Bloubergstrand are not unusual and occur at various other locations across the Saldania Belt without forming part of larger structure such as the scale and length of the proposed Milnerton Fault Zone. In addition, the occurance of mylonitisation and boudinage features are indicative of ductile deformation occurring at significant depths in the crust, suggesting exhumation of the Bloubergstrand shear zones.

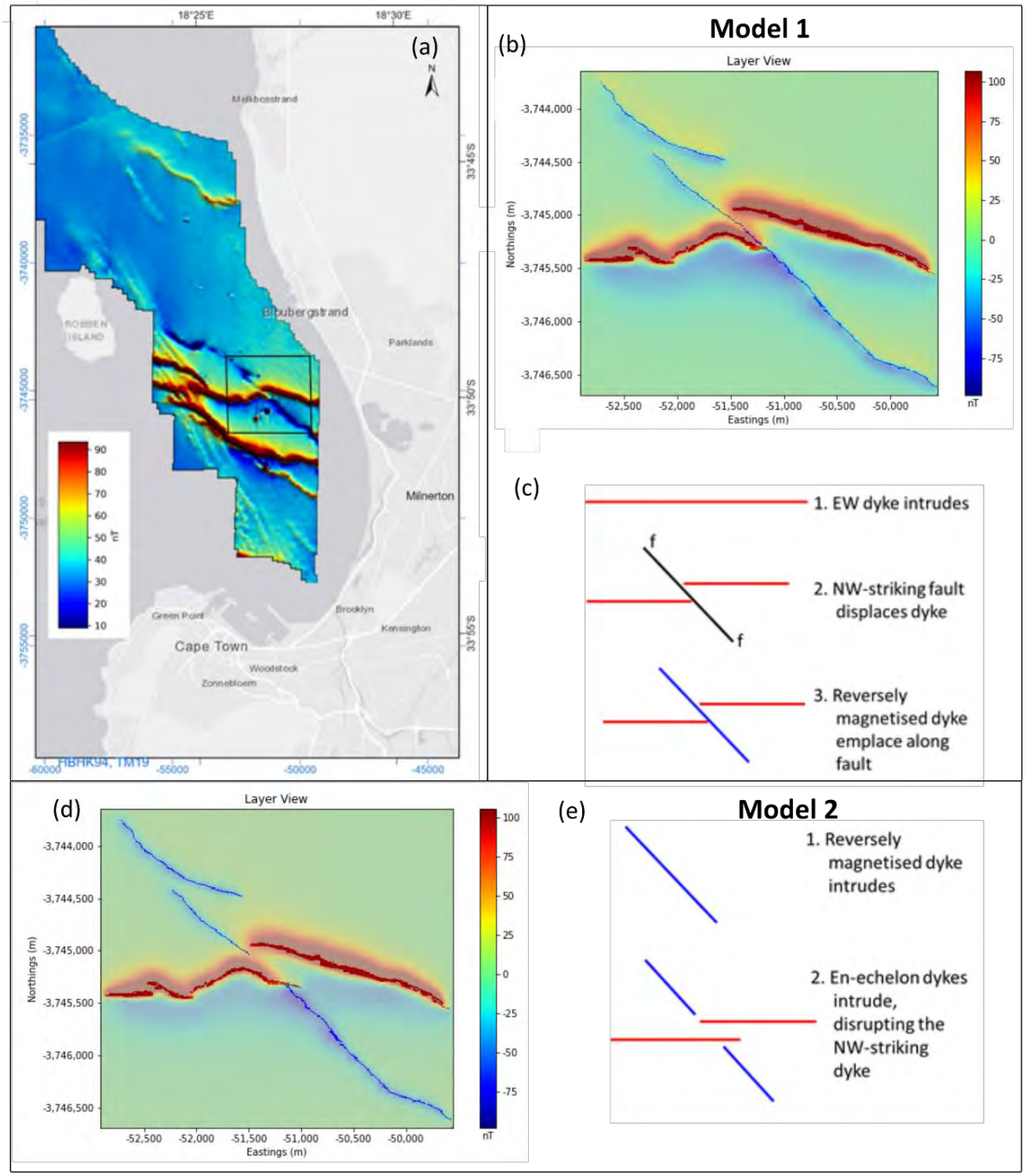

Figure 8-90. (a) Map showing location of offshore marine aeromagnetic data (Cole, 2007). (b and c) Model 1 and (d and e) Model 2 interpretation of a NW-trending negative anomaly that appears to displace a positive E-W striking anomaly.

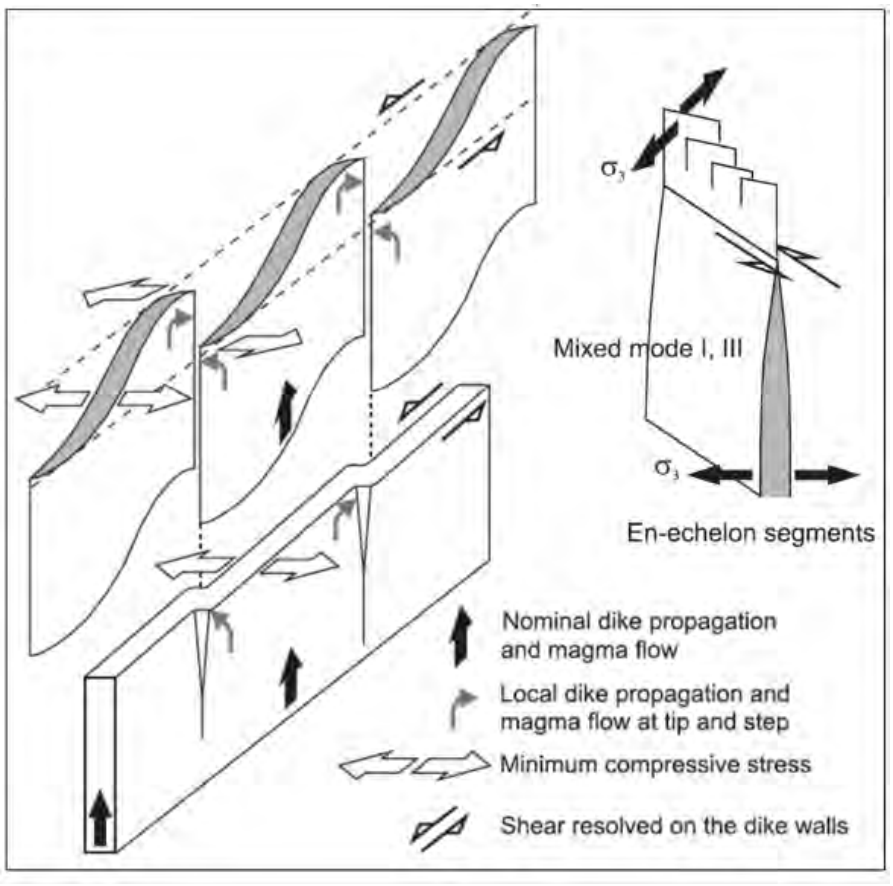

Figure 8-91. General mechanism of dyke propagation and magma flow under shear stress that combines the lateral propagation and magma flow of dyke segments by Currie and Ferguson (1970) and the mode of dyke propagation proposed by Pollard (1987) leading to overlapping *en echelon* dyke tips.

Deformation at Rooi-Els / Hangklip

Argument: East of Hangklip, a lineament identified using LANDSAT imagery was interpreted by Dames and Moore (1976) as a possible shear or fault zone. Although not stated, it is assumed that this lineament corresponds to the Buffels Valley. If the Milnerton Fault is extended along strike from exposures at Bloubergstrand towards the southeast, across the Cape Flats and False Bay, it roughly aligns with the LANDSAT lineament. Dames and Moore (1976, 1981) supposed that this alignment reflects an extension of the proposed fault zone towards the Rooi-Els area (Figure 8-92). They also make reference to observations in de Villiers (1944) that the coast between Cape Hangklip and Cape Agulhas are not in line with the strike of regional folds and may have been truncated by a fault.

Assessment: Geological maps (Söhnge, 1984; Theron, 1990; Siegfried, 2019) and fieldwork (Claassen et al., 2024) around the greater Cape Hangklip area from Gordon's Bay in the north to Betty's Bay in the south, confirm the presence of widespread NW-SE and NE-SW strike-slip, normal and reverse faulting (personal communication Dr T. Dhansay) in accordance with the region's structural and tectonic history (e.g., summary by De Beer et al., 2008). Minor shear zones are not uncommon along coastal exposures in the area (Figure 8-89b, c). It is problematic to try and decipher which one of these faults within the dense network of minor faults in the Hangklip area may be correlated or connected to the Milnerton Fault Zone, if at all, considering the substantial distance of 65 km from the last observed zone of brittle

deformation at Bloubergstrand. Marine terrace studies in the area could not confirm the credibility of the proposed onshore Milnerton Fault in the Hangklip/Pringle Bay area (Claassen et al., 2024).

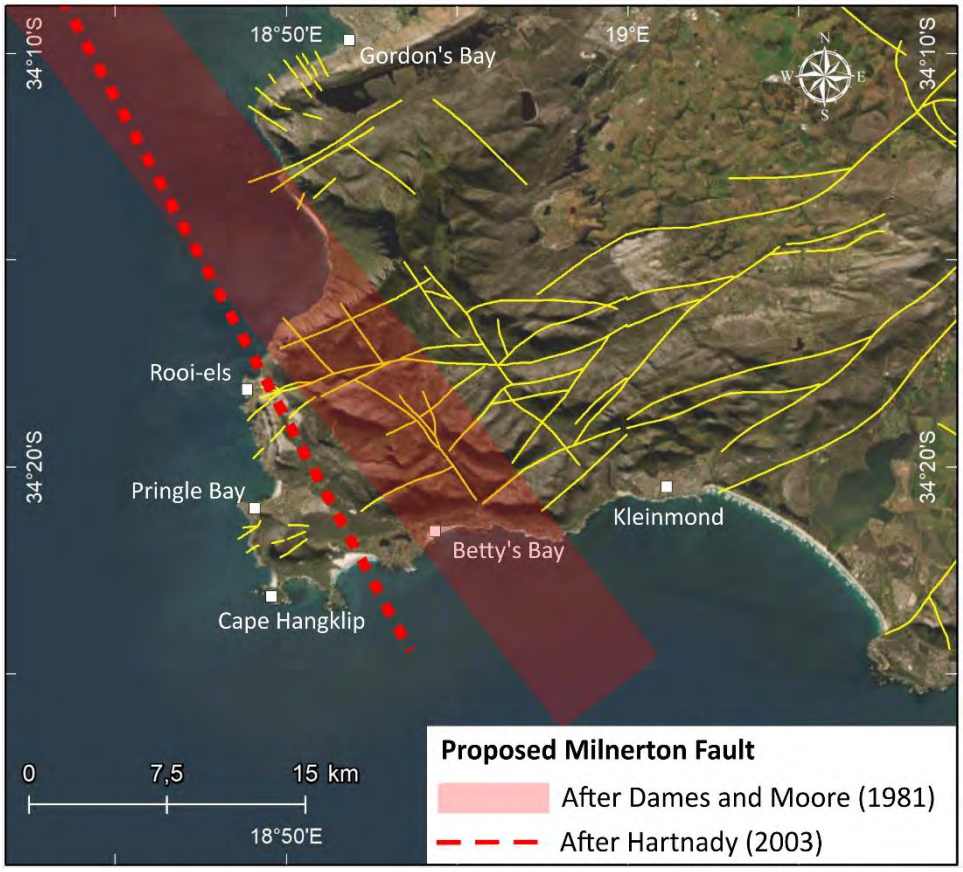

Figure 8-92. Proposed locations of the proposed Milnerton Fault in Cape Hangklip area, southeast of False Bay.

If the argument by Dames and Moore (1976, 1981) holds true, evidence of a fault zone should be present in the eastern offshore area of False Bay. Cawthra and Van Zyl (2023) mapped a northeastern portion of False Bay using various hydroacoustic methods with the intention of imaging any evidence of neotectonic activity on faults that daybreak at the seafloor (Figure 8-93a) or are shallowly buried with sediment (Figure 8-93b). Bathymetry as well as two boomer and pinger sub-bottom profilers (Figure 8-94), confirm the presence of a prominent N-S Malmesbury Group bedrock ridge with a minimal draping of Quaternary cover (<12 m) (Figure 8-94).

Careful consideration and interpretation of these high-resolution bathymetry datasets by Cawthra and Van Zyl (2023) and the SSM TI Team could not find any clear evidence or obvious expression of a NW-SE trending fault in the proposed location of the Milnerton Fault Zone on the seafloor. The False Bay ridge did not appear offset in a NW-SE direction, nor did any of the bedrock exposures that cross the fault path, thereby confirming the lack of evidence to support the occurrence of a large-scale NW-SE trending fracture zone, such as the inferred Milnerton Fault in the False Bay area.

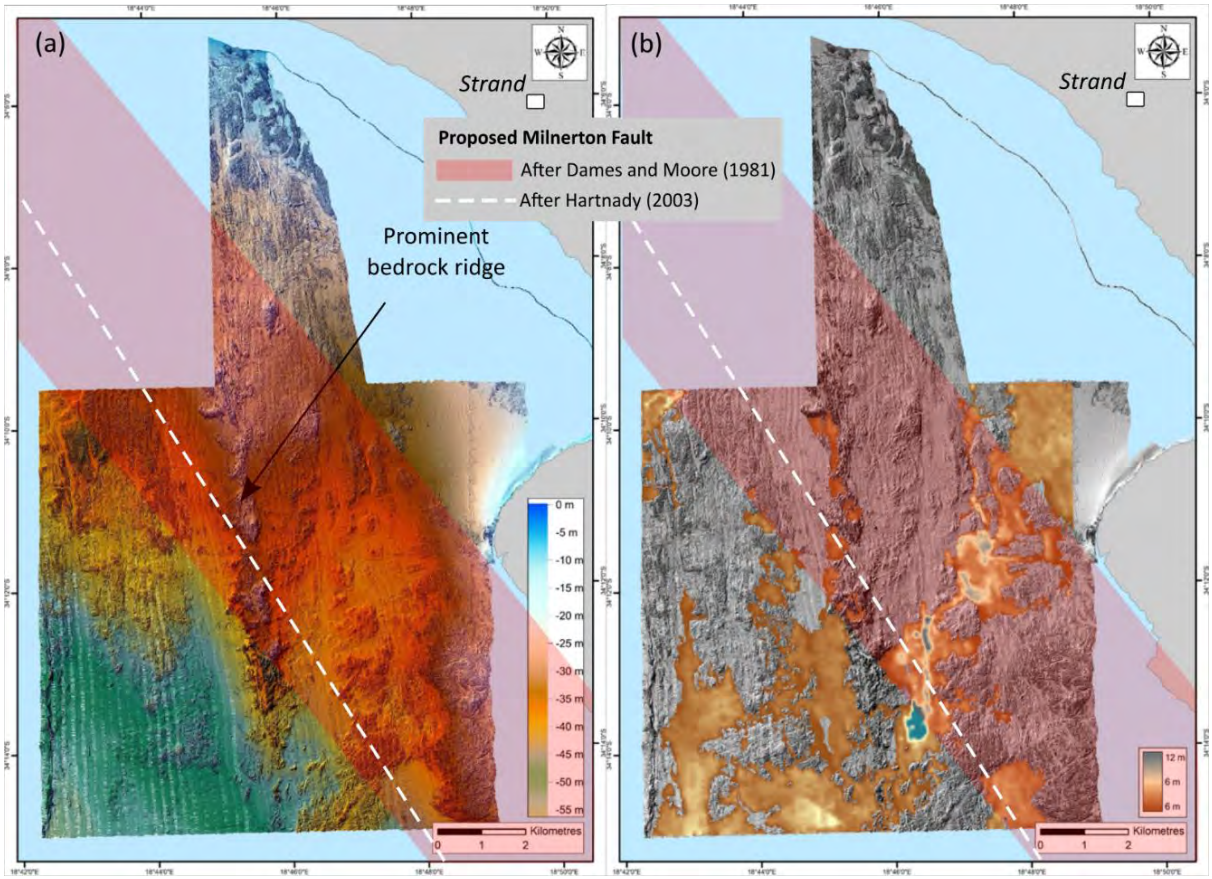

Figure 8-93. Bathymetry maps of the Northeastern portion of False Bay showing the locations of the proposed Milnerton Fault after Dames and Moore (1981) and Hartnady (2003). (a) Multibeam echosounder data in the mapped area of False Bay. Terrain colour shading, 10x vertical exaggeration. (b) Sediment isopach plot for False Bay, based on digitised pinger profiles.

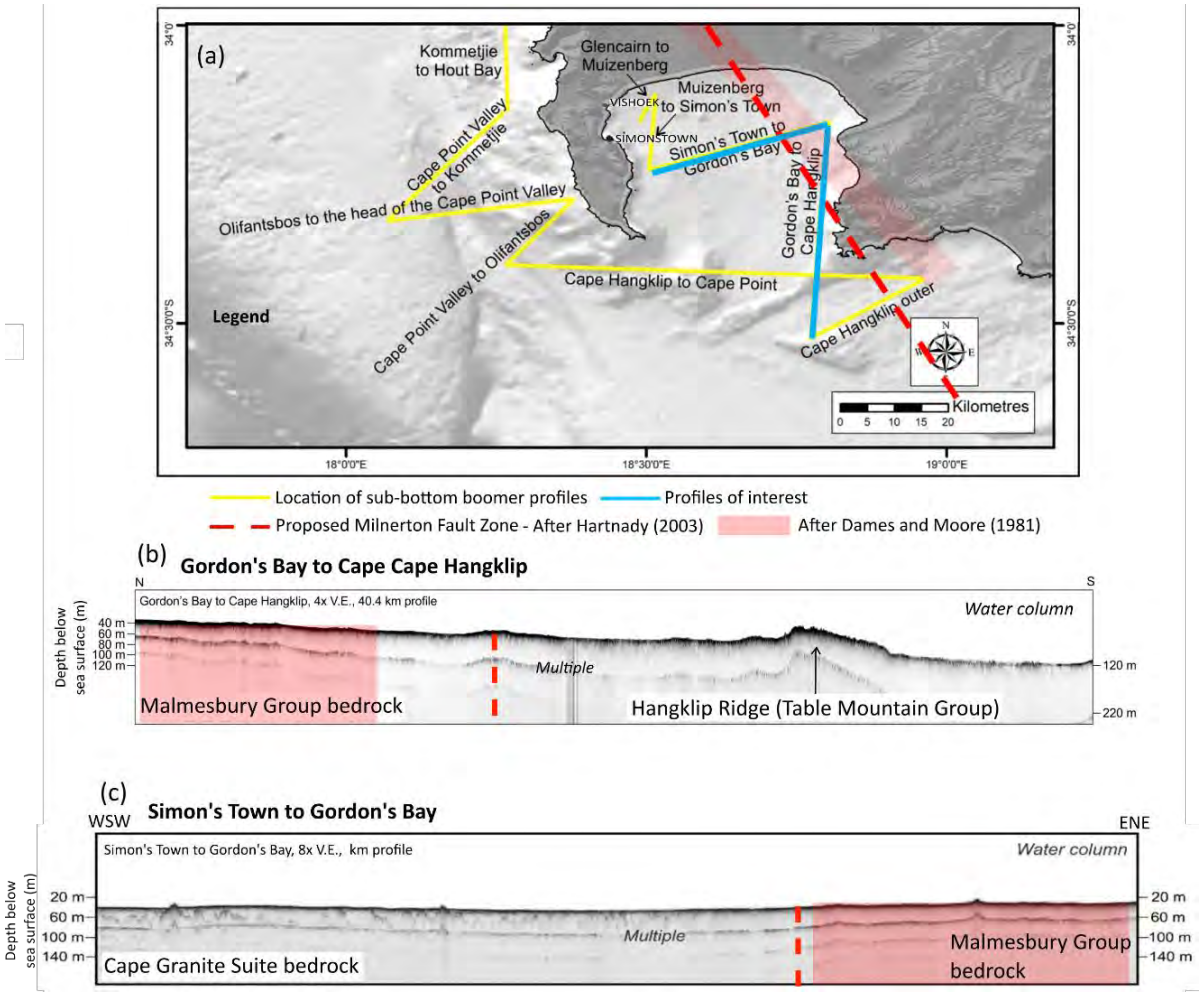

Figure 8-94. (a) Location of sub-bottom boomer profiles within False Bay and West of the Cape Peninsula. The Milnerton lineament is derived from Hartnady (2003). (b) Boomer profiles from the Simon's Town to Gordon's Bay and (c) the Gordan's Bay to Cape Hangklip lines that run across the proposed location of the Milnerton Fault after Hartnady (2003). No fault is indicated, and no offset of younger Quaternary cover was observed (after Cawthra and Van Zyl, 2023).

Activity: Despite the lack of evidence in support of a large-scale NW-SE fault zone in the False Bay area, the SSM TI Team also investigated the possibility of neotectonic activity in the offshore and onshore areas as it might relate to such a feature. The evaluation and conclusion of possible neotectonic activity in the offshore within False Bay were based on:

- Dykes: Day (1986) conducted a marine magnetic survey in False Bay and mapped out several of the NW-SE trending probable and possible dykes that did not appear offset in their alignment (Figure 8-95a, b). Considering the proposed scale and size of the Milnerton Fault (>100 km length, <8 km wide), one would expect significant offset of these dykes if the faults were active since their Early Cretaceous intrusion (Reid et al., 1991), lending credence to a lack of neotectonic offset in the bay.
- Quaternary deposits: Cawthra and Van Zyl (2023) mapped aeolianite and cemented beach deposits towards the northeastern extent of the False Bay bathymetry dataset (Figure 8-95c, d) (Blocks C and E only) similar to those mapped onshore along False Bay by Roberts et al. (2009). Careful evaluation of these probable Neogene or Quaternary deposits reveals that they are intact, unfractured or not displaced within

the 1 m resolution dataset, bolstering the notion of fault inactivity in the area in sediments of probable Neogene/Quaternary age (Cawthra and Van Zyl, 2023). Interpretation by Cawthra and Van Zyl (2023) of two sub-bottom boomer profiles (Simon's Town to Gordon's Bay and Gordan's Bay and Cape Hangklip profiles) conducted across the proposed Milnerton Fault Zone location did not show any offset of cover sediments blanketing bedrock Figure 8-94a-c).

- Incised channels: The bathymetry data generated by Cawthra and Van Zyl (2023) also showed the presence of various paleo-drainages (incised channels) cut into the Malmesbury Group bedrock similar to those observed in the Table Bay area (Figure 8-95e, f). The paleo-drainages would have been incised over multiple cycles of sea-level change and the last time there was active incision of the bedrock was during the last regression from about 125 – 20 ka (e.g., Cawthra et al., 2020). The SSM TI Team could not observe any fault offsets across these drainages.

Ultimately the combined data from these three geophysical datasets reveal no clear evidence to the SSM TI Team of neotectonic activity from faults on the seafloor.

Onshore assessment of any possible neotectonic activity associated with the inferred Milnerton Fault Zone or any other faults in the area by the SSM TI Team was aided by the findings derived from an extensive marine terrace study along the West Cape Coast of South Africa (Claassen et al., 2024). Field work in combination with existing data (Krige, 1927; Haughton 1933a, b; Davies, 1972) conducted at Rooi-Els and Pringle Bay revealed two well-developed wave-cut terraces at ~9-10 m amsl (inferred to correlate to MIS 11, ~400 kya) and at ~15 m amsl (>400 - <800 kya). Although lower terraces at ~3.5 and ~6 m amsl were also encountered, they are far less consistent and/or well-preserved in the area, which limits their effectiveness for correlation. The study found comparative consistency in terrace altimetry across the area of the proposed location of the Milnerton Fault Zone with no obvious or large-scale vertical displacement (Figure 8-96).

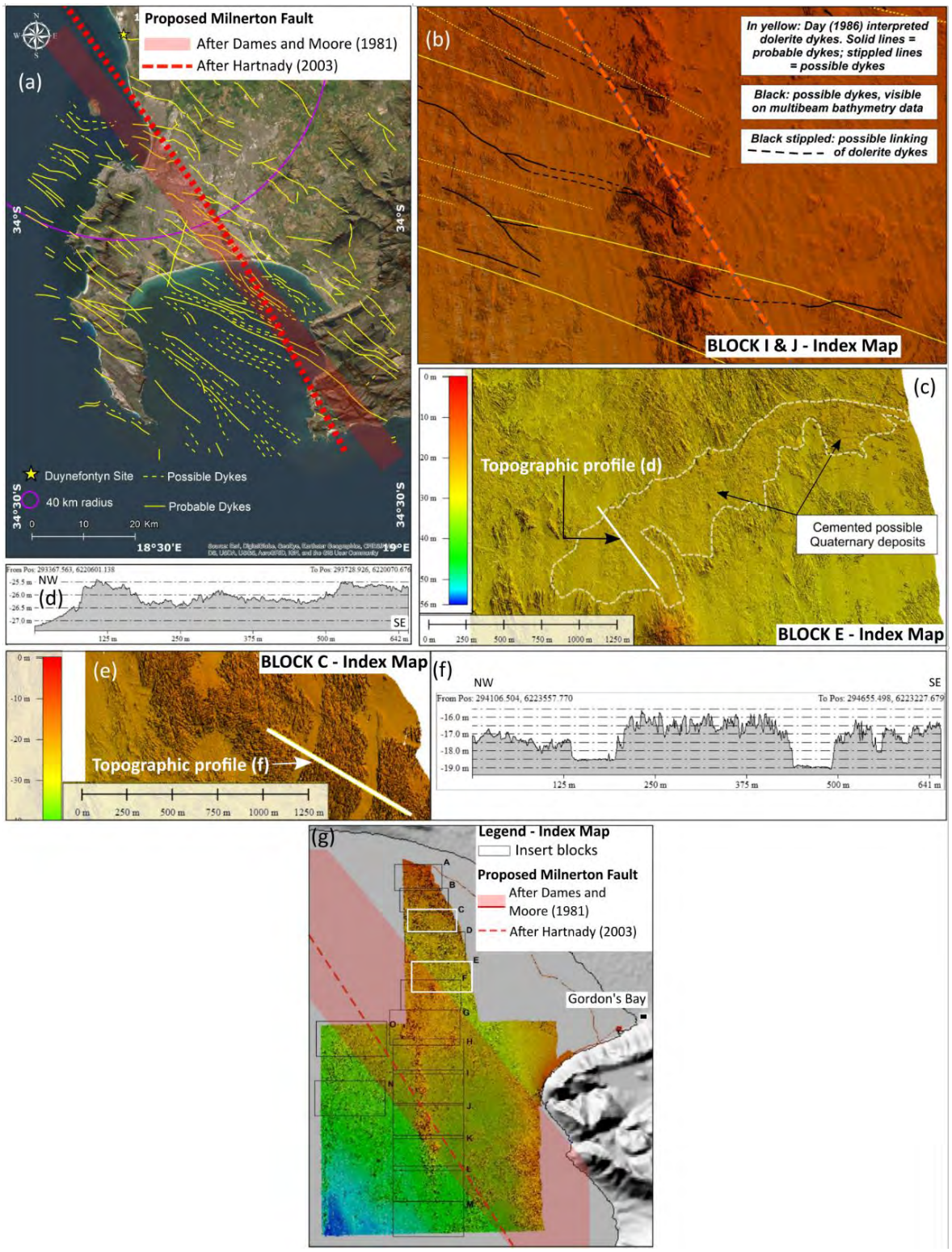

Figure 8-95. (a) Early Cretaceous dykes of the False Bay Dyke swarm (after Day, 1986). (b) Offshore bathymetry data showing the lack of offset of dykes across the proposed locations of the Milnerton Fault. (c) Cemented Quaternary cover draping bedrock exposures on the seafloor are unfractured or show no displacement within the 1 m resolution dataset in block E. (d) Topographic profile across cemented Quaternary cover shown in (c). (e) NNW-SSE trending palaeo-drainages that appear to lack offset in block C. (f) Topographic profile across palaeo-drainages. (g) Index map showing the location of insert blocks in figure (b), (c) and (e).

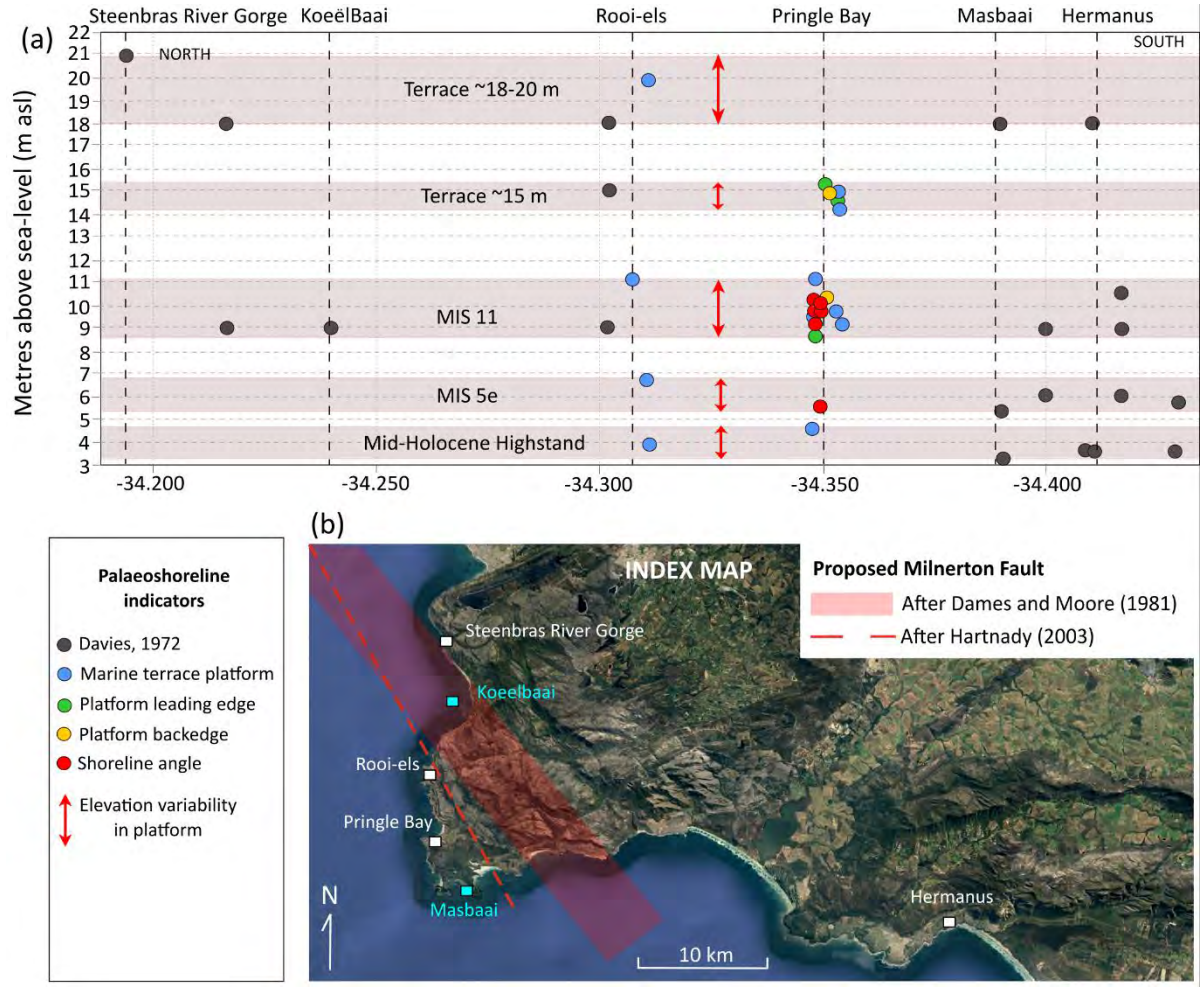

Figure 8-96. (a) Shoreline indicator correlation diagram for the area between Steenbras River Mouth and Hermanus. (b) Index map, showing location of proposed Milnerton Fault as defined by both Dames and Moore (1981) and Hartnady (2003).

Clustered Seismicity-Cape Town Cluster

Argument: The Western Cape exhibits two areas with unusually large concentrations of seismic events known as the Ceres and Cape Town Clusters (e.g., Fernandez and Guzman; 1979; Brandt et al., 2005; Singh et al., 2009) (Figure 8-97). Although seismicity in the Ceres area is largely attributed to the Groenhof Fault (e.g., De Beer, 2005; Smit et al. 2015; Coppersmith, 2023), events in the Cape Town area could not be attributed to any recognised geological fault source. As a way to explain the cluster, the relatively moderate to large magnitude events, and the intensity data in the Cape, several authors (Theron, 1974; Dames and Moore, 1976; Hartnady, 2003; De Beer, 2007; Midzi et al., 2018) argued that the grouped seismicity, which included large events such as the 1809, E[**M**] 6.1 magnitude earthquake, can be explained by the recurrence of slip along a plane of pre-existing crustal weakness, interpreted to be the proposed Milnerton Fault.

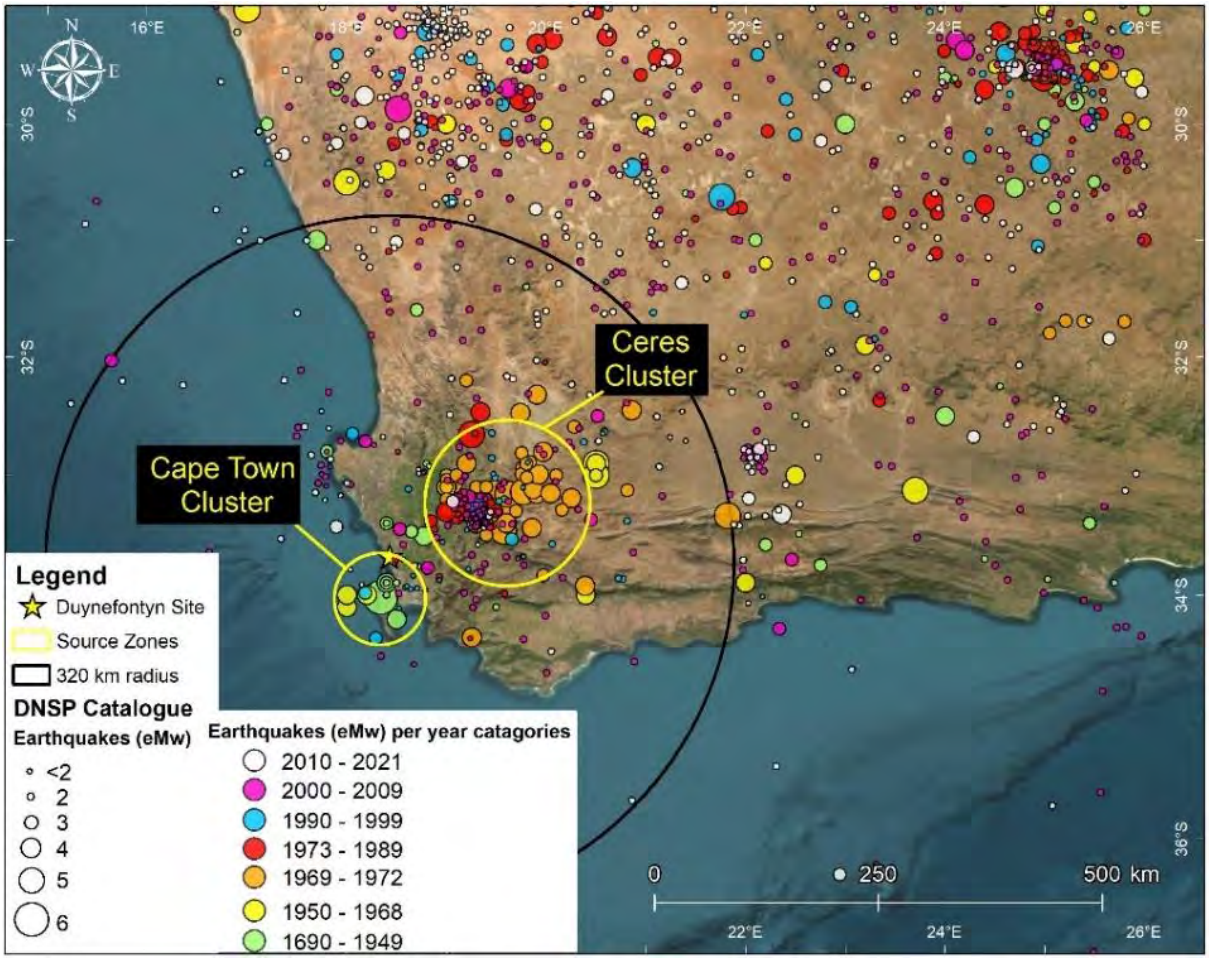

Figure 8-97. Seismic events across the western South Africa within the DNSP catalogue. Two seismic clusters are recognised within the 360 km radius site region.

Assessment and activity: The Cape Town Cluster epicentre locations are primarily comprised of historical events occurring between 1690-1968. The validity into the occurrence of these historical events was carefully investigated and confirmed by Albini and Flint (2023) using archival sources and contemporary narrative sources (e.g., travelling journals and newspaper reports). The epicentre locations of the historical events, are however, not derived from instrumental data, but rather from intensity data points (IDPs) (See Section 4.3, Historical Seismicity) that can have limitations and uncertainties in relation to their distribution in both time and space and which are greatly influenced by a variety of factors linked to the region's infrastructure development. For example, the spatial distribution density of IDPs from a historical earthquake may be much higher near highly populated centres since these areas would have been better at keeping records of such events, than lower population density areas, where fewer data points occur because no records of the earthquake were either made or preserved. This can lead to biased earthquake location estimates. The location of historical IDPs would have been affected by the population density being centred around the Cape Town area and its strategic port and trading posts as opposed to hinterland areas at the time (Albini and Flint, 2023). This may have resulted in a clustering of IDPs in that area and could have biased the epicentre locations calculations. (Figure 8-98). Figure 8-98 shows the 1973 - 2021 period when events have a purely instrumental record. For this time-period the epicentre locations in the area of the supposed Cape Town Cluster are dispersed with no clustering. The SSM TI team has shown in Section 4.3 the large range of location uncertainty/error, of

historical events placing the validity of how the cluster was ultimately defined into question and making it difficult to use the cluster as evidence for the presence of a fault in the positions proposed by Dames and Moore (1976, 1981) and Hartnady (2003). It may be possible that these epicentres occurred outside of the clusters radius and may not all be attributed to a single fault source.

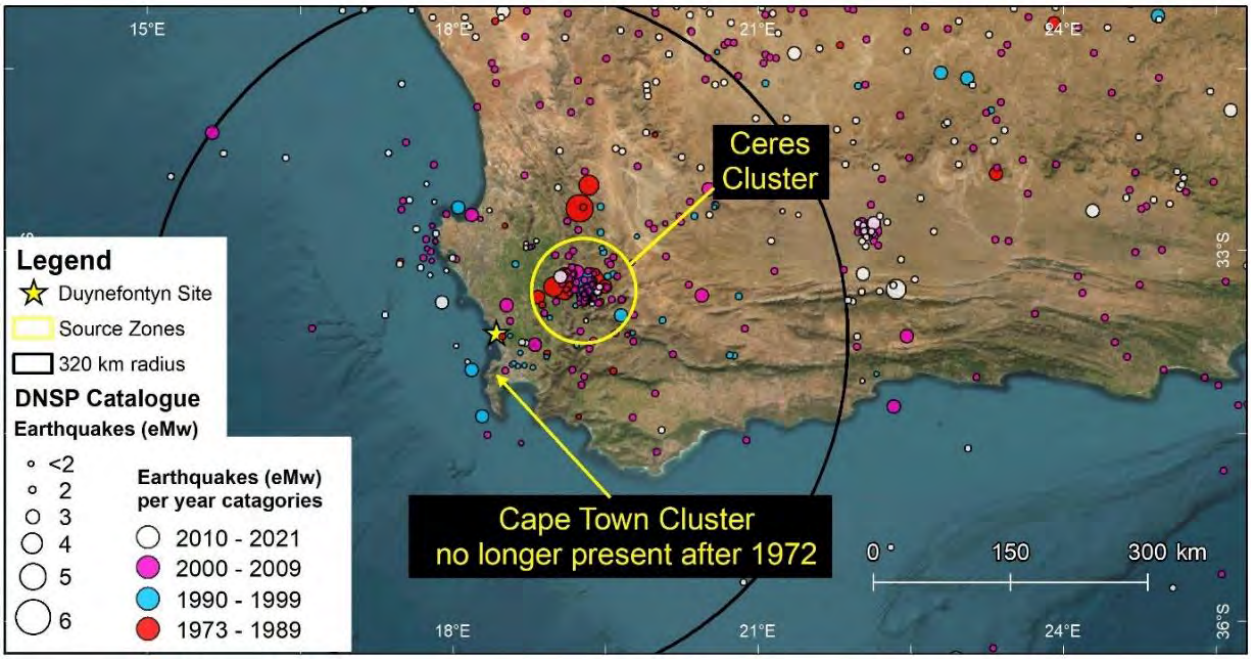

Figure 8-98. Seismic events from DNSP catalogue across western South Africa from 1973 and later.

Certainly, the description and destructive consequences of the largest events like the 1809 earthquake deemed to be close to Cape Town have been well documented, investigated and evaluated by several authors (Hartnady, 2003; De Beer, 2007; Albini and Flint, 2023) (Figure 8-99). These investigations considered vintage records of the events (e.g., Von Buchenröder; 1830) that described the complete destruction of the farmhouse on the farm Jan Biesjes Kraal and the occurrence of an inch to a few feet wide fissures that ran for roughly a mile near modern Milnerton or possibly near the head of Milnerton Lagoon. Although Von Buchenröder (1830) visited the area five days after the earthquake, his written description of the damage only occurred 21 years later, with no description of the type of building integrity of the farmhouse destroyed nor any reference to the local ground conditions that would have allowed for liquefaction. The occurrence of saturated soils in the Milnerton area and especially the vicinity of the lagoon may have been a contributing factor to its sensitivity to deformation in the form of liquefaction (Fouché, 2020; Schoeman, 2018) from an earthquake epicentre that could have originated elsewhere in the region (personal communication, Flint, 2023, Workshop 2).

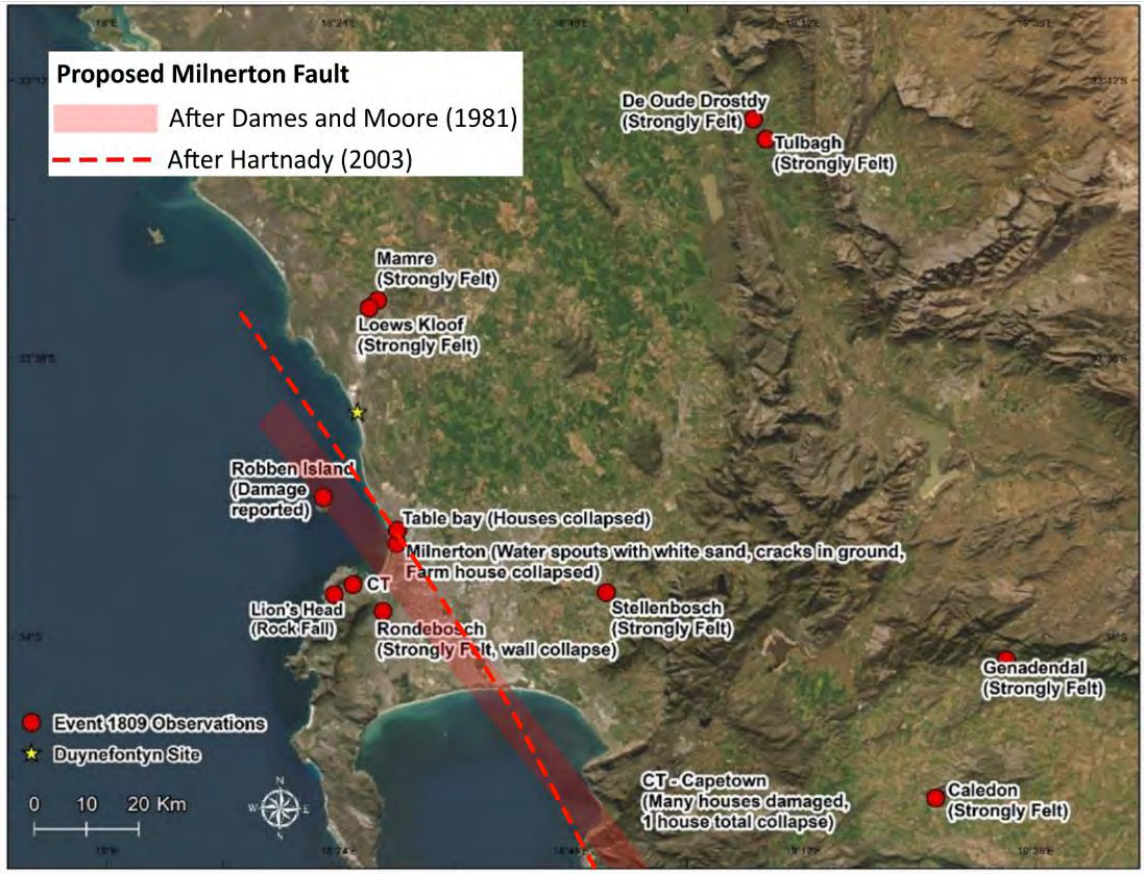

Figure 8-99. Distribution of intensity data points (IDPs) for the 1809 earthquake across the Western Cape.

The offshore Koeberg '8 km feature'

Argument: An offshore magnetic survey conducted by Dames and Moore (1976) identified an NNW-SSE trending anomaly on the seafloor 8 km west of Koeberg (Figure 8-100). The feature has subsequently been informally known as the '8 km feature'. Although these authors interpreted the feature as being either a fault or a lithological boundary, they ultimately concluded that the feature represents a fault. They suggested that if the area of structural deformed exposures at Bloubergstrand (interpreted to be part of a larger NW-SE trending fault zone) is extended offshore along strike, it aligns with the magnetic anomaly, and thus represents the same structural feature/fault, namely the proposed Milnerton Fault.

Assessment: To evaluate the validity of the '8 km feature', the SSM TI Team reviewed data and interpretations of subsequent offshore airborne marine magnetic data and bathymetry in the area (De Beer, 2007; Fugro, 2007; Horwood and Smith, 2007; Cole et al., 2007b; Horwood, 2009). Surveys confirmed anomalies coinciding with the Dames and Moore (1976) feature. In De Beer's (2007) evaluation of offshore data, he referred to the anomaly as the Melkbos Ridge Fault (Figure 8-101a, b) or the KM1 anomaly (Figure 8-102) based on the abrupt termination of a conspicuous NW-trending ridge on the seafloor.

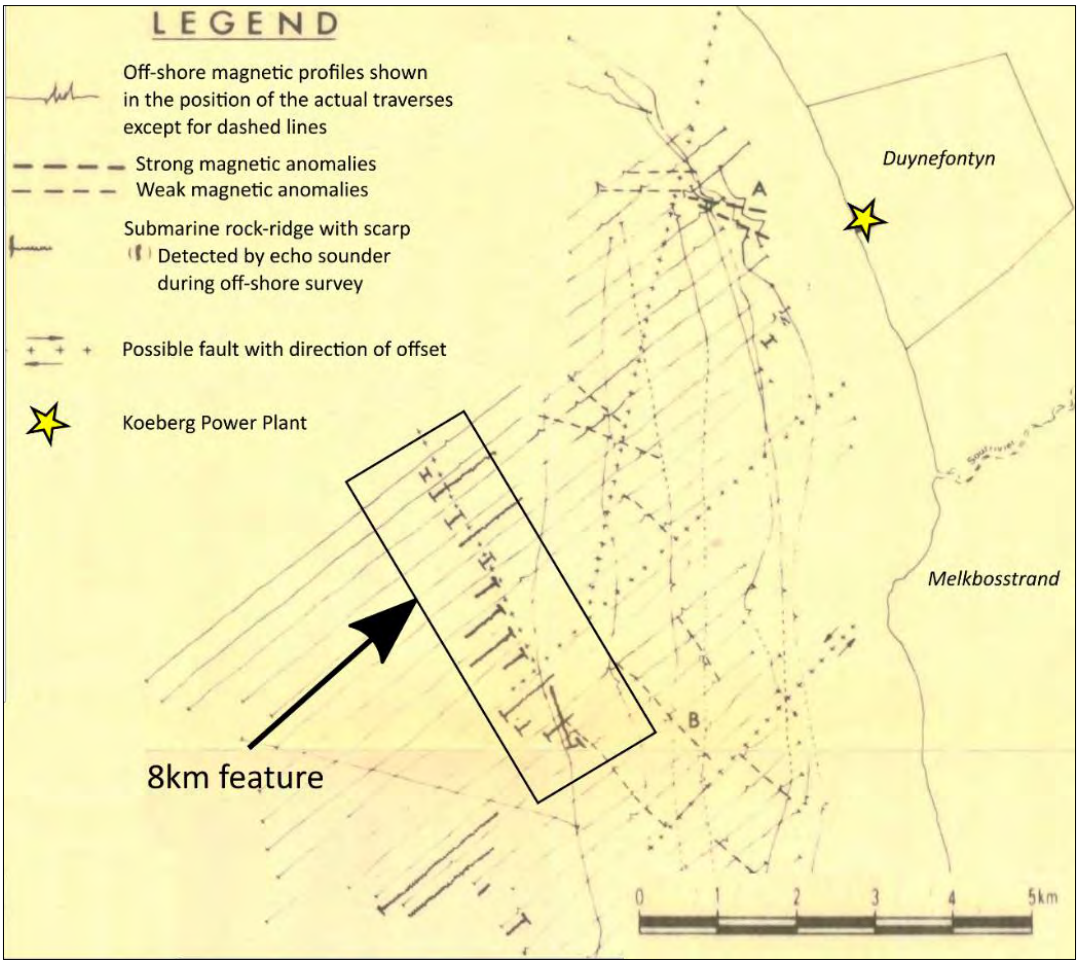

Figure 8-100. Interpreted results from the offshore magnetic survey conducted west of Koeberg by Dames and Moore (1976). The survey identified a feature, informally known as the '8 km feature' and interpreted it to be part of the Milnerton Fault Zone. Apart from the 8 km feature, other anomalies identified by Dames and Moore (1976) in this figure, were not identified in the more recent and high-resolution offshore surveys (Cole et al., 2007b; Horwood and Smith, 2007) Smaller E-W and NW-SE trending faults are interpreted as relict features.

De Beer (2007) describe the anomaly as a NE-facing scarp that is possibly fault related, based on its NW-SE orientation and the abrupt termination of a conspicuous NW-trending whaleback ridge on the seafloor (Figure 8-101a, b). Elongated outcrops may be resistant ridges of silicified fault breccia and vein quartz. Although it has not yet been sampled, the rock type clearly has a high resistance to erosion. The length of 6 km assigned to this inferred fault (Horwood and Smith, 2007) is clearly controlled by the extent of this resistant rock type SW of it, and should be viewed as a minimum value, as the full extent of the feature is unknown. De Beer (2007) also noted that based on its orientation, it may also form part of the same set of regionally structurally persistent features/faults like the relict Table Bay Fault. He concluded that there is, however, not enough evidence to infer that the anomaly is a fault. Horwood (2009) made similar observations and interpretations along the H1 anomaly (figure 8-102), ultimately concluding that the data does not allow for the unequivocal identification of the anomaly as a fault. The SSM TI Team agrees with this assessment and add that the folded bedding of Malmesbury Group strata depicted in Figure 8-101b is also unfaulted.

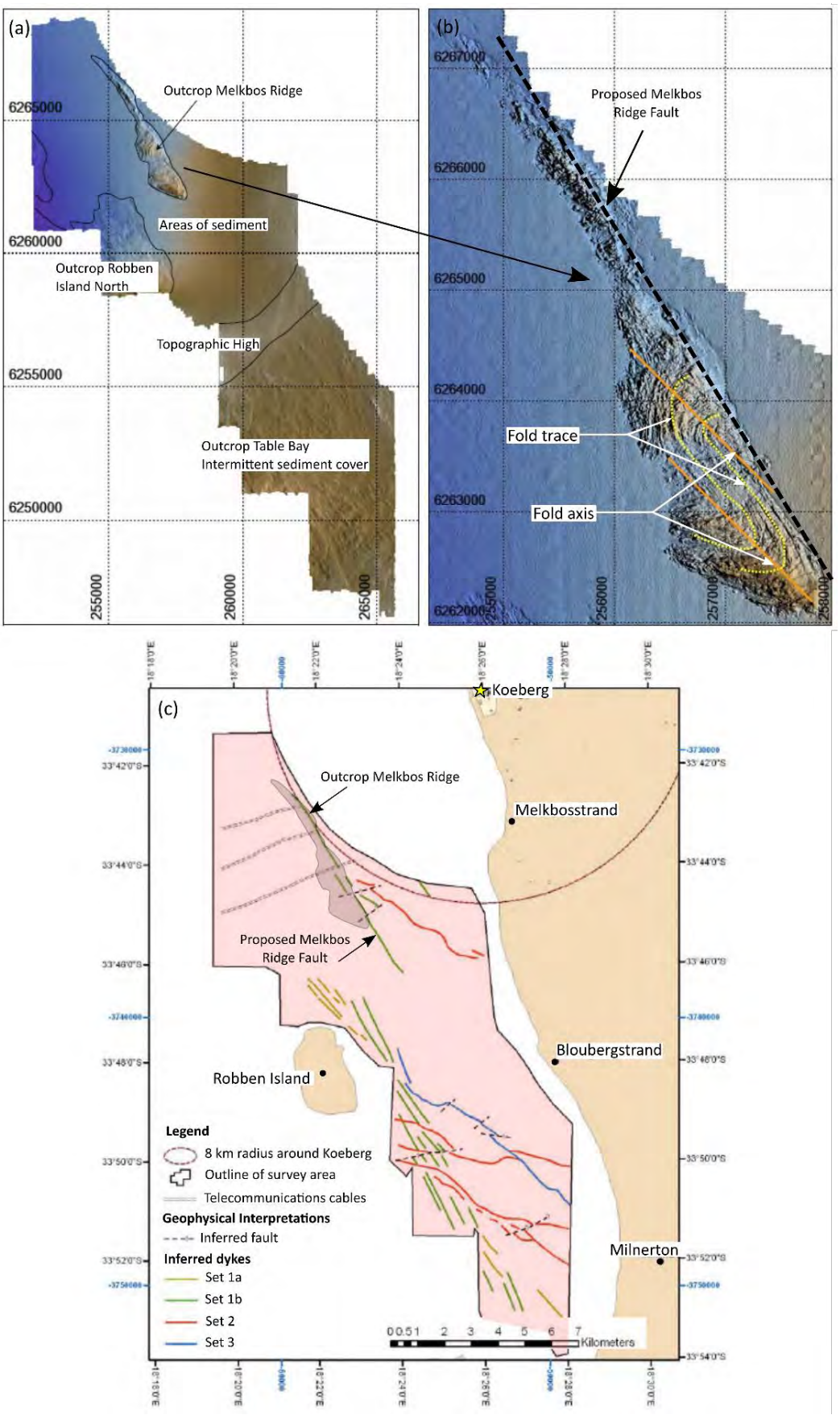

Figure 8-101. Offshore hydroacoustic data depicting the interpreted Melkbos Ridge Fault based on the abrupt termination of a conspicuous NW-trending ridge on the seafloor (Fugro, 2007).

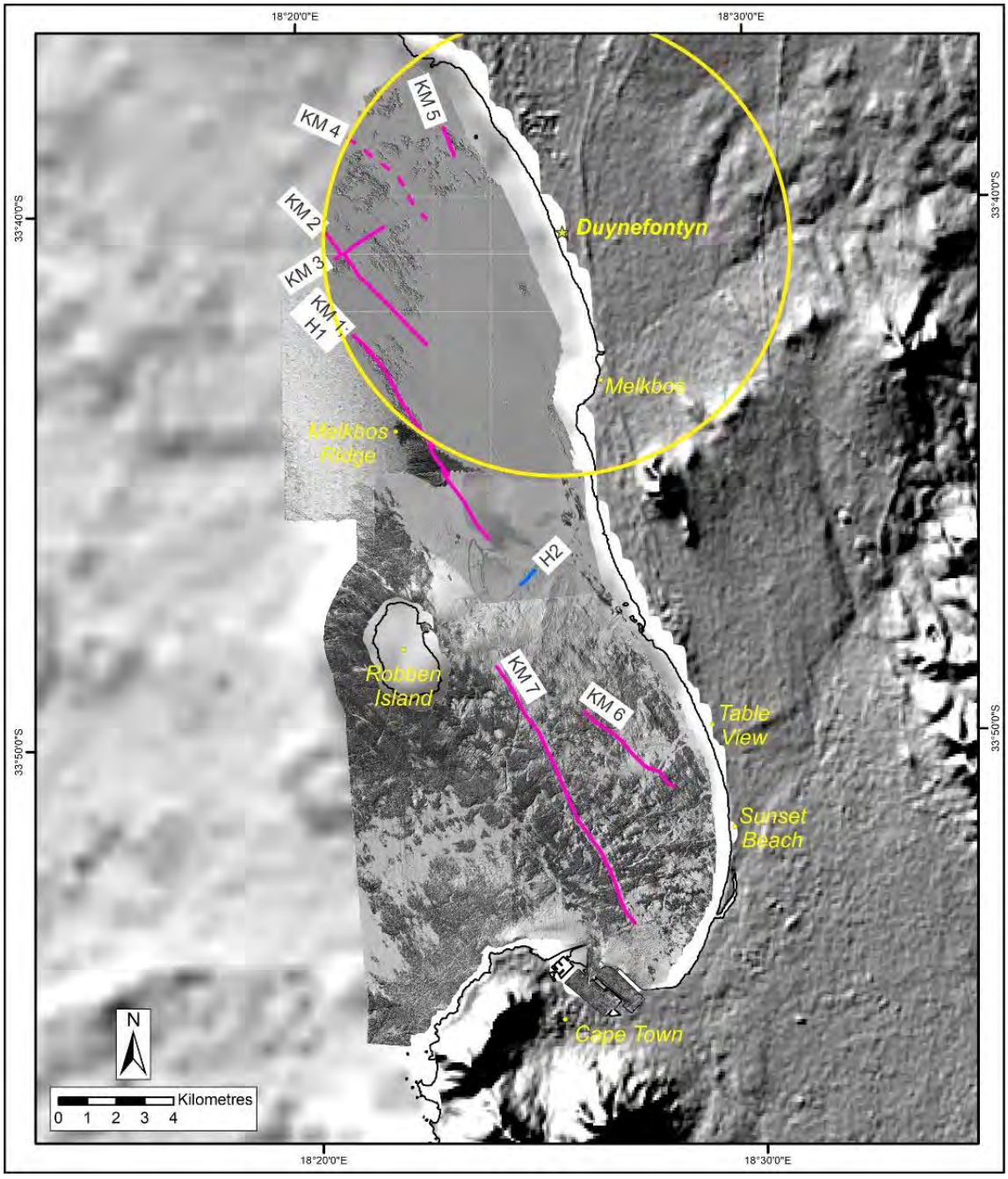

Figure 8-102. Map depicting the location of offshore geophysical datasets along the West Coast between Cape Town and Duynefontyn. Note the KM1/H1 anomaly coincides with the Dames and Moore (1976) 8 km feature (after Cawthra and Van Zyl, 2023).

Cawthra and Van Zyl (2023) conducted two boomer sub bottom profiles (Duynefontyn south and Robben Island to Duynefontyn) across the '8 km feature'. Interpretation and evaluation of the WSW-ENE Duynefontyn south profile suggest that the feature seen as a ridge on the seafloor may be related to bedding rather than fault scarps because there are other buried ridges with similar topographic signatures, and that the NE-facing buried topography thought to be where the Melkbos Ridge Fault or KM1/H1 Fault should be, has gentle slopes rather than a distinct truncated edge. In addition, Quaternary sediments on either side of the ridge remained undisturbed (Figure 8-103).

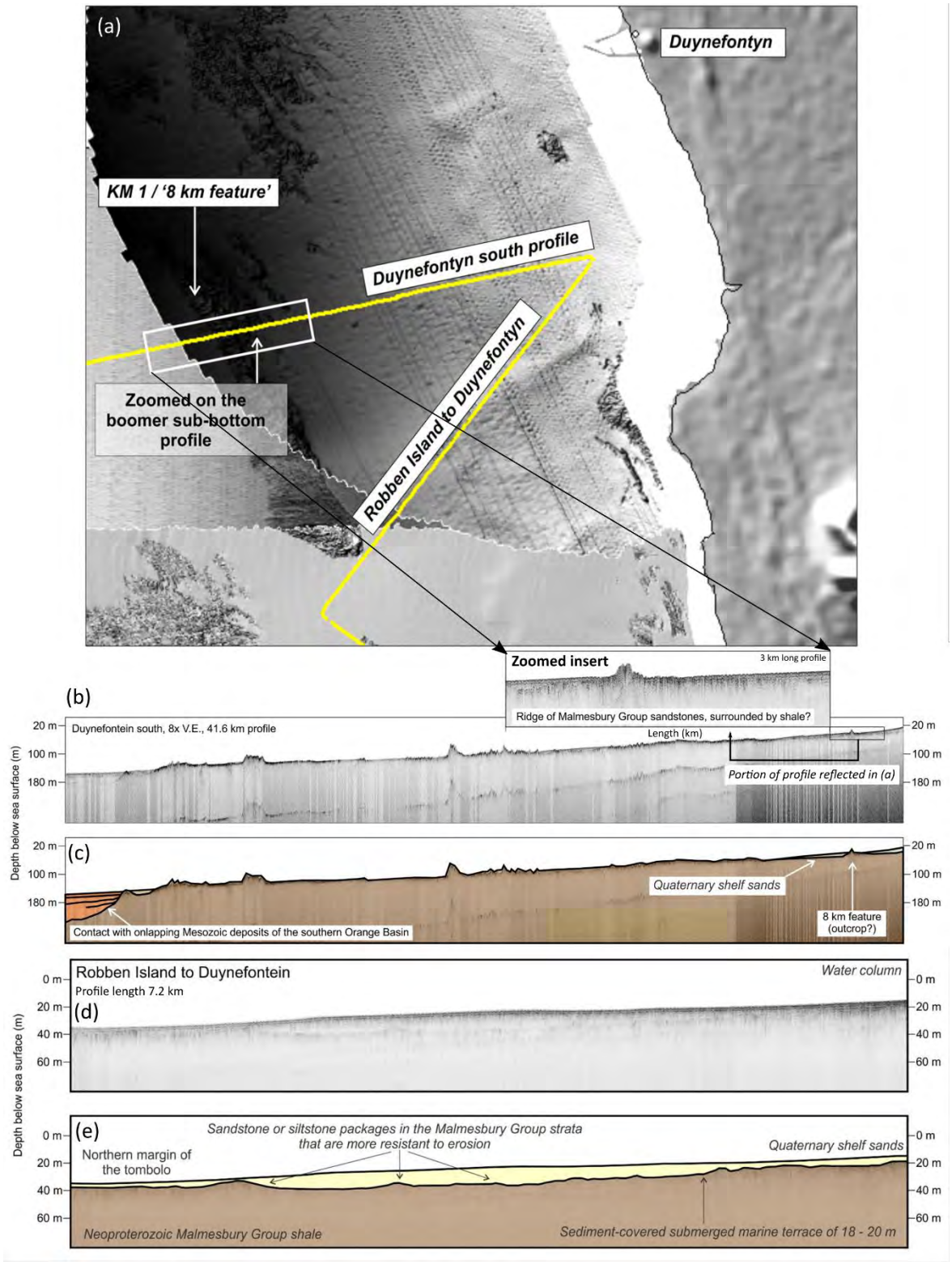

Figure 8-103. (a) Location of boomer sub-bottom profiles across the '8 km feature'. The white rectangle shows the location of the zoomed-in box in figure (b), which depicts the NE portion of the larger NE-SW trending profile 'Duynefontyn South' that extends further towards the SW than depicted in the figure (a). (b) and (c) Show interpreted geology along the 'Duynefontyn South' profile. (d) Sub-bottom raw and (e) interpreted profile 'Robben Island to Duynefontyn'.

8.6 SUMMARY AND CONCLUSIONS

Seismic source models are generally comprised of fault sources and source zones. In practical terms, defining a fault source in a PSHA requires sufficient information of past fault activity in order to develop a defensible representation of the fault geometry and future activity. There needs to be evidence of multiple events localised along the fault. In areas with active faulting, this evidence can be multiple offsets recorded in the soils or alluvial cover along a fault trace. Palaeoseismic techniques can be used to provide evidence of earthquake recurrence. Offset geologic markers such as deflected drainages or displaced bedding contacts can be used to measure the accumulated slip from a collection of past earthquakes. If the age of the offset markers is factored in, then these offset markers can be used to estimate slip rates.

The SSM TI Team found little if any geological evidence of active surficial faulting in the Western Cape. The detailed data collection described in Chapter 5 and the thorough analyses of those data in conjunction with the relevant published literature discussed in Sections 8.5.1 through 8.5.7 confirm this conclusion. The SSM TI Team did not identify any evidence of fault slip within the Pliocene (5.3 – 2.6 Ma) or even within the late Miocene (11.6 – 5.3 Ma). There is no evidence for aligned moderate- to large-magnitude hypocentres along the mapped fault planes. The only exception is the 1969 Ceres earthquake, for which there is a record of aftershocks that clearly defined the fault plane, and some evidence of offset of bedding at the Wakkerstroom site (Figure 8-79).

The field mapping documented in Coppersmith et al. (2024) did not uncover any geologic evidence of active faulting on the large, mapped faults in the Western Cape, nor was there any evidence of geomorphic features commonly associated with active deformation such as pressure ridges, pull-apart grabens, linear scarps, or range-front facets. The lack of observed deformation becomes even more evident when the very slow erosion rates for the Western Cape are factored in (Scharf et al., 2012); meaning that if these features were formed in the recent geologic past, they would be well preserved in the present-day landscape.

Detailed analyses of the hydroacoustic data documented in Cawthra and Van Zyl (2023) also did not reveal any geologically recent fault slip in either Table Bay or False Bay. The comprehensive regional evaluation of the marine terrace data documented in Claassen et al. (2024) shows that there is no vertical offset of the marine terraces that wrap around the southwest Cape coast since at least the Middle Pleistocene (~400 ka) and a lack of any large-scale warping of the coastal margin since at least the Pliocene (~2.6 Ma).

Although the SSM TI Team was aware of the existing geological publications that consider the Colenso Fault and the proposed Milnerton Fault Zone as active because of the potential for a simple spatial correlation with a past earthquake (Dame and Moore, 1976, 1981; Hartnady, 2003), for the purpose of a probabilistic seismic hazard analysis, there was no data on these features that the SSM TI Team could use to include them as fault sources in the SSM. Based on these data and analyses and adhering to the criteria established in Section 8.4.3, the SSM TI assigned a p[S] = 0.0 to all the major faults except for the Groenhof Fault.

The lack of geological evidence for significant repeated events on a single fault surface suggest to the SSM TI Team that future seismicity will also most likely continue to occur on a distributed network of faults in the crust. Even on the Groenhof Fault, where the SSM TI Team reported evidence for repeated deformation, with up to 50m of fault offset, our assessment is

that offset likely occurred over millions or even tens of millions of years, maybe since the Mesozoic or even earlier. This observation leads to the very low slip rates we assessed for the Groenhof Fault (mean of 0.01mm/yr.). This low slip rate translates to one 0.5 m slip event (~**M** 6.3 earthquake) on the Groenhof Fault every 10,000 - 50,000 years.

One way to evaluate how effective the SSM is in characterising future seismicity is to examine how well the source modelling matches current rates of active deformation. This can be done by comparing the seismic moment rate release of future earthquakes with other measures of moment release. The optimal situation is where there are one or more other independent data sets that can be used to estimate (or constrain) moment release rate. These independent constraints on moment release rate can then be compared to the moment release rate from the MFD curve. Three common options used in other hazard studies are (1) strain rates derived from reliable GPS data (e.g., INL, 2022); (2) strain rates derived from plate tectonic rates, where the total strain across the plate margin is known (e.g., PG&E, 2015) or (3) strain rates derived from fault offsets that provide estimates of slip rates or earthquake recurrence rates (e.g., PNNL, 2014). Unfortunately, none of these datasets are available in the Western Cape.

As discussed in Section 4.2.10, the GPS data from southern Africa indicate low rates consistent with the moment release rates in the SSM, but the GPS data are too noisy and underdeveloped to quantify crustal strain. The study area is far from any plate margin and, as documented in Section 8.4 and summarised above, there is hardly any geologic evidence of Quaternary or even Miocene fault slip that the SSM TI Team could have used to assess slip rates and no palaeoseismic data to model earthquake recurrence.

Based on Figure 8-26, the annual cumulative mean rate for **M**≥5 across the Western Cape is approximately 0.02 and the annual cumulative mean rate for **M**≥6 across the Western Cape is approximately 0.002-0.003. These rates are consistent with the rates modelled by the Thyspunt SSHAC 3 (Bommer et al., 2013) for the Syntaxis source zone, as shown in Figure 8-18 of the Thyspunt final report and are also generally consistent with the rates modelled for the most stable parts of CEUS by EPRI/DOE/NRC (2012). Figure 6.4.1-1 of EPRI/DOE/NRC (2012) presents a map of the mean annual rate for **M**≥5 earthquakes normalised by area (1x1 degree cells) in the CEUS Study Region for magnitude case A (recurrence rates computed from E[**M**] 2.9). In the figure, areas of the northwestern CEUS with the lowest seismicity have mean annual rates per unit area ranging from 1×10^{-5} to 1×10^{-6}. To allow for a direct comparison, the mean annual rates per unit area are converted to mean annual rates of approximately 0.01 to 0.1, which are consistent with the values obtained for the host zone SDZ.

Most importantly, given the limited data available, the SSM TI Team's integration in developing the MFDs for the source zones included a full accounting of epistemic uncertainty that was propagated through the SSM. This was accomplished by rigorously following the SSHAC process and responding to the many comments, suggestions, and technical challenges of our work from the PPRP. As described in Chapter 6, The SSM TI Team carefully developed a reliable project earthquake catalogue that included a thorough evaluation of the historic earthquake record going back to 1620. The SSM TI Team used two options for evaluating completeness and two options for estimating *b*-values that yield four MFD curves for each source zone. All methods applied to completeness and *b*-value estimation are well established in the seismological community. The SSM TI Team deemed that these four options were

sufficient to capture the epistemic uncertainty in the data and the methods. These uncertainties were then carried through to the final hazard calculation. Given all these considerations, the SSM TI Team's final conclusion is that the SSM is an accurate and objective representation of the seismic hazard at the Duynefontyn site and fully captures the CBR of TDI.

8.7 REFERENCES

Aki, K. and Richards, P.G. (1980). Quantitative Seismology, Theory and Methods. Freeman, San Francisco, USA.

Albini, P. and Flint, N. (2023). Investigating the Earthquake Records from 1620 to 1969 of interest for the Duynefontyn area, South Africa. CGS Report 2022-0127 (Rev. 0). Council for Geoscience, Pretoria, South Africa, 400 pp.

Baby, G.; Guillocheau, F.; Braun, J.; Robin, C. and Dall'Asta, M. (2020). Solid sedimentation rates history of the Southern African continental margins: Implications for the uplift history of the South African Plateau. Terra Nova 32(1). 53-65.

Backeberg, N.R.; Reid D.L.; Trumbull, R.B. and Romer, R.L. (2011). Petrogenesis of the False Bay dyke swarm, Cape Peninsula, South Africa: evidence for basement assimilation. South African Journal of Geology 114(3/4). 335-352.

Baron, J.H. (1990). Aquifer characteristics and recommended water allocation in the Grootwater aquifer unit, Yzerfontein sub-terranean government water control area. Technical report GH 3715. Department of Water Affairs.

Becker, P. (2020). Eskom secretive about its study into seismic activity and Koeberg nuclear station. Mail and Guardian. https://mg.co.za/thoughtleader/opinion/2020-12-03-eskom-secretive-about-its-study-into-seismic-activity-and-koeberg-nuclear-station/ (accessed on 2 November 2023).

Belcher, R.W. (2003). Tectonostratigraphic evolution of the Swartland region and aspects of orogenic lode-gold mineralisation in the Pan-African Saldania Belt, Western Cape, South Africa. PhD thesis, University of Stellenbosch. 318-333.

Bierman, P.R. (2023). Cosmogenic ^{10}Be and ^{26}Al analysis of Western Cape sediment samples, South Africa. Report prepared by Dr Paul Bierman, Geologist and Geochronologist for the Council for Gesocience, 2023/12/22.

Bierman, P.R.; Coppersmith, R.; Hanson, K.; Neveling, J.; Portenga, E.W. and Rood, D.H. (2014). A cosmogenic view of erosion, relief generation, and the age of faulting in southern Africa. GSA Today 24(9). 4-11.

Bommer, J.J.; Coppersmith, K.J.; Coppersmith, R.; Hanson, K.; Mangongolo, A.; Neveling, J.; Rathje, E.; Rodriguez-Marek, A.; Scherbaum, F.; Shelembe, R.; Stafford., P. and Strasser, F. (2013). Probabilistic Seismic Hazard Analysis for the Thyspunt Nuclear Site, South Africa. CGS Report 2013-0190 (Rev 0). Council for Geoscience, Pretoria, South Africa, 821 pp.

Bommer, J.J. and Montaldo Falero, V. (2020). Virtual fault ruptures in area-source zones for PSHA: Are they always needed?. Seismological Research Letters 91(4). 2310-2319.

Bommer, J.J. and Stafford, P.J. (2009). Seismic hazard and earthquake actions. Chapter 2 of Seismic Design of Buildings to Eurocode 8. Editor: Elghazouli, A.Y., Spon Press, Oxon, UK. Pages: 6-46, ISBN: 978-0-415-44762-1.

Botha, W.J. and Thompson, M.W.H. (1977). Geophysical survey for the Saldhana groundwater project of the Department of Water Affairs. Department of Mines Report GH 3212/2417.

Brandt, M.B.C.; Bejaichund, M.; Kgaswane, E.M.; Hattingh, E. and Roblin, D.L.R. (2005). Seismic History of Southern Africa. Seismological Series of the Council for Geosciences 37, Pretoria, South Africa.

Broad, D.S.; Jungslager, E.H.A.; McLachlan, I.R. and Roux, J. (2006). Offshore Mesozoic Basins. In: Johnson, M.R.; Annhaeusser, C.R.; Thomas, R.J. (eds.). The Geology of South Africa. Geological Society of South Africa, Johannesburg/Council for Geoscience, Pretoria, South Africa. 553-572.

Broad, D.S.; Jungslager, E.H.A.; McLachlan, I.R.; Roux, J. and Van der Spuy, D. (2012). South Africa's offshore Mesozoic basins. In: Roberts, D.G.; and Bally, A.W. (eds.). Phanerozoic Passive Margins, Cratonic Basins and Global Tectonic Maps. Elsevier, Rotterdam, Netherlands. 535-564.

Boyd, O.S. (2020), Temperature model in support of the U.S. Geological Survey National Crustal Model for seismic hazard studies: U.S. Geological Survey Open-File Report 2,019-1,121.

Cawthra, H.C.; MacHutchon, M.R. and Van Zyl, W. (2019). Cruise Report: Pinger and Boomer sub-bottom profiling surveys on Rietvlei. CGS Report 2019-0109 (Rev. 1). Council for Geoscience, Pretoria, South Africa, 19 pp.

Cawthra, H.C.; Anderson, R.J.; De Vynck, J.C.; Jacobs, Z.; Jerardino, A.; Kyriacou, K. and Marean, C.W. (2020). Migration of Pleistocene shorelines across the Palaeo-Agulhas Plain: Evidence from dated sub-bottom profiles and archaeological shellfish assemblages. Quaternary Science Reviews 235. 106107.

Cawthra, H.C. and Van Zyl, F.W. (2023). Duynefontyn Data Collection for Offshore Faults. CGS Report 2023-0116 (Rev. 0). Council for Geoscience, Pretoria, South Africa, 126 pp.

Chiou, B.J. and Youngs, R.R. (2008). An NGA model for the average horizontal component of peak ground motion and response spectra. Earthquake Spectra 24(1). 173-215.

Chisenga, C.; Van der Meijde, M.; Yan, J.; Fadel, I.; Atekwana, E.A.; Steffen, R. and Ramotoroko, C. (2020). Gravity derived crustal thickness model of Botswana: Its implication for the Mw 6.5 April 3, 2017, Botswana Earthquake. Tectonophysics 787. 228479.

Claassen, D.; Mthembi, P. and Black, D.E. (2024). Marine Terrace Studies. CGS Report 2022-0140 (Rev. 0). Council for Geoscience, Pretoria, South Africa, 148 pp.

Coetzee, J.A. (1978a). Climatic and biological changes in South Western Africa during the Late Cenozoic. In: van Zinderen Bakker, E.M. and Coetzee, J.A. (eds.). Palaeoecology of Africa and the surrounding islands 10/11. Balkema, Rotterdam, Netherlands. 13-29.

Coetzee, J.A. (1978b). Late Cenozoic palaeoenvironments of Southern Africa. In: van Zinderen Bakker, E.M. and Coetzee, J.A. (eds.). Antarctic glacial history and world palaeoenvironments. Balkema, Rotterdam, Netherlands.

Coetzee, J.A. and Rogers, J. (1982). Palynological and lithological evidence for the Miocene palaeoenvironment in the Saldanha region (South Africa). Palaeogeography, Palaeoclimatology, Palaeoecology 39. 71-85.

Cole, J. (2007). Survey report for the Koeberg site extension Eskom site surveys, South Africa.

Cole, J. (2022). Geophysical investigations of structures in the Western Cape Fold Belt. PowerPoint presentation at SSHAC Enhanced Level 2 Workshop 2, June 20, Cape Town, South Africa.

Cole, J. (2023). 3D Magnetic modelling of dykes in the area around Duynefontyn. CGS Report 2023-0002 (Rev. 0). Council for Geoscience, Pretoria, South Africa, 34 pp.

Cole, J.; Raath, C.J. de W. and Maré, L.P. (2007a). Final report: Airborne survey of Koeberg. CGS Report 2007-0028. Council for Geoscience, Pretoria, South Africa.

Cole, J.; Cole, P. and De Beer, C.H. (2007b). Geophysical interpretation of the marine magnetic data collected in the offshore site area (8 km radius) of Koeberg. NSIP Report NSIP-NSI-020265#P1-7. CGS Report 2007-0187. Council for Geoscience, Pretoria, South Africa.

Compton, J. S. (2004). The Rocks and Mountains of Cape Town. Double Storrey Books, United Kingdom.

Compton, J.S.; Franceschini, G. and Wigley, R. (2006). A Proposed Neogene Synthesis of the West Coast and West Coast Fossil Park. African Natural History 2.

Conrad, J. (2013a). Geohydrological Assessment – Erf 2176 Arnelia Farms, Hopefield. GEOSS Report 2012/01-05.

Conrad, J. (2013b). Geohydrological Assessment – Erf 2177 Arnelia Farms, Hopefield.

Coppersmith, R.; Slack, C.; Moabi, N.; Dhansay, T.; Cawthra, H.; Claassen, D. and Sethobya, M. (2024). Duynefontyn onshore fault mapping investigation. CGS Report 2023-0001 (Rev. 0). Council for Geoscience, Pretoria, South Africa, 67 pp.

Cornell, C.A. and Van Marke, E. H. (1969). The major influences on seismic risk. Proceedings of Third World Conference on Earthquake Engineering, Santiago, Chile A-I. 69-93.

Currie, K.L. and Ferguson, J. (1970). The mechanism of intrusion of lamprophyre dikes indicated by ‘‘offsetting’’ of dikes. Tectonophysics 9. 525-535.

Dames and Moore (1976). Geologic Report. Koeberg Power Station, Cape Province, South Africa, for The Electricity Supply Commission. Job 9629-014-45.

Dames and Moore (1981). Seismic Design Requirements, Koeberg Nuclear Power Station Johannesburg, South Africa, for the Electricity Supply Commission. Job 9629-041-45.

Davies, O. (1972). Pleistocene shorelines in the southern and south-eastern Cape Province (Part 2). Annals of the Natal Museum 21(2). 225-279.

Day, R.W. (1986). Magnetometric mapping of the False Bay dolerites. Joint Geological Survey/University of Cape Town Marine Geoscience Technical Report 16. 217-227.

Day, R.W. (1987). False Bay dolerites. Annals of the Geological Survey of South Africa 21. 1- 7.

De Beer, C.H. (2002). The stratigraphy, lithology and structure of the Table Mountain Group. 8-18. In: Pietersen, K. and Parsons, R. (eds.). A synthesis of the hydrogeology of the Table Mountain Group - Formation of a Research strategy. WRC Report TT 158/01. Water Research Commission.

De Beer, C.H. (2004). Investigation into evidence for neotectonic deformation within onland Neogene to Quaternary deposits between Alexander Bay and Port Elizabeth – Desk Study Report. CGS 2004-0226. Council for Geoscience, Pretoria, South Africa.

De Beer, C.H. (2005). Investigation into evidence for neotectonic deformation within onland Neogene to Quaternary deposits between Alexander Bay and Port Elizabeth – South Coast Report. NSIP-SHA-016311. CGS Report 2005-0180. Council for Geoscience, Pretoria, South Africa. 1-197.

De Beer, C.H. (2007). Potential onshore and offshore geological hazards for the Koeberg nuclear site, Cape Town, South Africa: A review of the latest airborne and marine geophysical data and their impact on the existing geological model for the Site Vicinity area. CGS Report 2007-0275 (Rev. 1). Council for Geoscience, Pretoria, South Africa.

De Beer, C.H.; Roberts, D.L.; Cole, J.; Engelbrecht, J.; and Dondo, C. (2008). The geology of the site and site vicinity areas of Koeberg, and an update on onland geological hazards. CGS Report 2008-0239. Council for Geoscience, Pretoria, South Africa.

De Villiers, J. (1944). A review of the Cape orogeny: Annals of the University of Stellenbosch XXII A. 185-208.

De Villiers, J.E. (1979). Note on deformation and metasomatism in rocks of the Koringberg-Hermon area. Transaction of the Geology Society, South Africa 82. 179-181.

Dhansay T.; Musekiwa, C.; Ntholi, T.; Chevallier, L.; Cole, D. and de Wit, M.J. (2017). South Africa's geothermal energy hotspots inferred from subsurface temperature and geology. South African Journal of Science 113.

Dingle, R.V.; Siesser, W.G. and Newton, A.R. (1983). Mesozoic and tertiary geology of Southern Africa. AA Balkema, Rotterdam, Netherlands.

Electric Power Research Institute/ Department of Energy/United States Nuclear Regulatory Commission (EPRI/DOE/USNRC) (2012). Central and Eastern United States Seismic Source Characterization for Nuclear Facilities, NUREG-2115. US Nuclear Regulatory Commission, Washington DC, USA.

Electric Power Research Institute (EPRI); Johnston, A.C.; Coppersmith, K.J.; Kanter, L.R. and Cornell, C.A. (1994). The earthquakes of stable continental regions 1-5. Schneider, J.F. (ed.). Palo Alto, California, USA.

Electric Power Research Institute – Seismicity Owners Group (EPRI-SOG) (1988). Seismic hazard methodology for the central and Eastern United States, 11 volume proprietary report. EPRI Technical Report NP-4726-A.

Ellsworth, W.L. (2003). Magnitude and area data for strike slip earthquakes. In: Working Group On California Earthquake Probabilities (2013). Appendix D.

Fadel, I.; Paulssen, H.; Van Der Meijde, M.; Motsamai, T.; Ntibinyane, O. and Nyblade, A.A. (2020). Crustal and upper mantle shear wave velocity structure of Botswana: the April 3, 2017, central Botswana earthquake linked to the East African Rift System. Geophysical Research Letters 47.

Fagereng, Å. and Toy, V.G. (2011). “Geology of the earthquake source: an introduction.” Geological Society, London, Special Publications. Fagereng, A.; Toy, V. G. and Rowland, J. V. (eds.). Geology of the Earthquake Source: A Volume in Honour of Rick Sibson. Geological Society, London. Special Publications 359. 1-16.

Fairhead, J.D. and Girdler, R.W. (1971). The Seismicity of Africa. Geophysical Journal 24(3), 271-301.

Fouché, N. (2020). The liquefaction potential of the upper quaternary sands of the Cape Flats, Western Cape, South Africa. Journal of the South African Institution of Civil Engineering. 63, (2), 22-30.

Schoeman, N. (2018). The Liquefaction potential of soils on the Cape Flats established by means of empirical correlation. MSc. Thesis, Stellenbosch University.

Fernandez, L.M. and Guzman, J.A. (1979). Seismic history of Southern Africa. Geological Survey of South Africa, Seismologic Series 9.

Field, E.H.; Arrowsmith, R.J.; Biasi, G.P.; Bird, P.; Dawson, T.E.; Felzer, K.R.; Jackson, D.D.; Johnson, K.M.; Jordan, T.H.; Madden, C.; Michael, A.J.; Milner, K.R.; Page, M.T.; Parsons, T.; Powers, P.M.; Shaw, B.E.; Thatcher, W.R.; Weldon, R.J. II and Zeng, Y. (2014). Uniform California Earthquake Rupture Forecast, Version 3 (UCERF3) - The Time-Independent Model. Bulletin of the Seismological Society of America 104(3). 1122-1180.

Foster, A.N. and Jackson, J.A. (1998) Source parameters of Large African earthquake: Implications for crustal rheology and regional kinematics. Geophysical Journal International 134, 422-448.

Frankel, A. (1995). Mapping Seismic Hazard in the Central and Eastern United States. Seismological Research Letters 66(4). 8-21.

Frimmel, H.E.; Basei, M.A.S.; Correa, V.X. and Mbangula, N. (2013). A new lithostratigraphic subdivision and geodynamic model for the Pan-African western Saldania Belt, South Africa. Precambrian Research 231. 218-235.

Fugro (2007). Survey report for the Koeberg site extension. Eskom site surveys, South Africa. Report NZ647za. NSIP-NSI-020603. 1-105.

Gosling, M. (2011). Koeberg sitting alongside fault line. IOL News article. https://www.iol.co.za/news/koeberg-sitting-alongside-fault-line-1042362 (accessed 2 November 2023).

Goulet, C.A.; Bozorgnia, Y.; Abrahamson, N.; Kuehn, N.; Al Atik, L.; Youngs, R.; Graves, R.W. and Atkinson, G. (2018). Central and eastern North America ground–motion characterization–NGA-East final report. Pacific Earthquake Engineering Research Center. PEER Report 2018/08.

Green, R.W.E. and Bloch, S. (1971). The Ceres, South Africa, earthquake of September 29, 1969: I. Report on some aftershocks. Bulletin of the Seismological Society of America 61(4). 851-859.

Green, R.W.E. and McGarr, A. (1972). A comparison of the focal mechanism and aftershock distribution of the Ceres, South Africa earthquake of September 29, 1969. Bulletin of the Seismological Society of America 62(3), 869-871.

Gresse, P.G. and Theron, J.N. (1992). The Geology of the Worcester Area Sheet Explanation 3319 Worcester. 1:250,000 scale. Geological Survey of South Africa, Pretoria, South Africa.

Gresse, P.G. (1997). 3319 Worcester geological map. 1:250,000-scale. Geological Survey of South Africa, Pretoria, South Africa.

Gresse P.G.; von Veh, M.W. and Frimmel, H.E. (2006). Namibian (Neoproterozoic) to Early Cambrian Successions. In: Johnson, M.R.; Anhaeusser, C.R. and Thomas, R.J. (eds.). The Geology of South Africa. Geological Society of South Africa, Johannesburg/Council for Geoscience, Pretoria, South Africa. 395-421.

Gulia, L. and Wiemer, S. (2010). The influence of tectonic regimes on the earthquake size distribution: A case study for Italy. Geophysical Research Letters 37(10). L10305.

Gutenberg, B. and Richter, C.F. (1954). Seismicity of the earth and associated phenomena. Second edition. Princeton University Press. Princeton, New Jersey, USA.

Hagedorn, J. (1988). Silcretes in the western Little Karoo and their relation to geomorphology and palaeoecology. Paleoecology of Africa 19. 371-375.

Hanks, T.C. and Bakun, W.H. (2002). A bilinear source-scaling model for M-log A observations of continental earthquakes. Bulletin of the Seismological Society of America 92. 1841-1846.

Hanks, T.C. and Bakun, W.H. (2008). M-logA Observations for Recent Large Earthquakes. Bulletin of the Seismological Society of America 98. 490-494.

Hanks, T.C. and Bakun, W.H. (2014). M–log A models and other curiosities. Bulletin of the Seismological Society of America 104(5). 2,604-2,610.

Hanson, K.; Coppersmith, R. and Slack, C. (2012). Thyspunt Geological Investigations – Kango Fault Study. CGS Report 2012-0035. Council for Geoscience, Pretoria, South Africa.

Hamel, K. (2015). A structural and geochemical traverse across the NW outcrop of the Colenso Fault Zone, Saldanha, South Africa. MSc Dissertation, University of Cape Town.

Hartnady, C.J.H. (1969). Structural analysis of some Pre-Cape formations in the Western Province. Unpublished MSc thesis, University of Cape Town.

Hartnady, C.J.H. (2003). Cape Town Earthquakes: Review of the historical record. Draft Vers030522. Umvoto Africa, Muizenberg, South Africa.

Hartnady, C.J.H.; Newton, A.R. and Theron, J.N. (1974). The stratigraphy and structure of the Malmesbury Group in the southwestern Cape. Bulletin Precambrian Research Unit, University Cape Town 15. 193-213.

Haq, B.U.; Hardenbol, J. and Vail, P.R. (1987). The new chronostratigraphic basis of the Cenozoic and Mesozoic sea level cycles. Special Publications – Cushman Foundation for Foraminifera Research 24. 7-13.

Haughton, S.H. (1931). The late Tertiary and Recent deposits of the West Coast of South Africa. Transactions Geological Society South Africa 34 (1931). 19-58.

Haughton, S.H. (1933a). Geological Map of the Cape Town Area Sheet 427. 1:148,000 scale. Cape Town. Union of South Africa, Department of Mines, Geological Survey.

Haughton, S.H. (1933b). The Geology of Cape Town and Adjoining Country, An Explanation of Sheet 247. Union of South Africa, Department of Mines, Geological Survey.

Hay, E.R. (1981). A stratigraphic and sedimentological analysis of borehole data from a portion of the Cape Flats. Umvoto Africa. Honours thesis, University of Cape Town.

Hay, R. and Seyler, H. (2008). The assessment of water availability in the Berg Catchment (WMA 19) by means of water resource related Models: Groundwater Model Report 5. Cape Flats Aquifer Model P WMA 19/000/00/0408.

Hecker, S.; Abrahamson, N.A. and Wooddell, K.E. (2013). Variability of displacement at a point: Implications for earthquake-size distribution and rupture hazard on faults. Bulletin of the Seismological Society of America 103(2A). 651-674.

Hendey, Q.B. (1981). Geological Succession at Langebaanweg, Cape Province, and Global Events of the Late Tertiary. South African Journal of Science 77. 33-38.

Henzen, M.R. (1973). Die herwinning opberging en onttrekking van gesuiwerde rioolwater in die Kaapse skiereiland 1-2 [English: The recycling storage and extraction of treated sewage in the Cape Peninsula 1-2].

Horwood, S. and Smith, K. (2007). Marine Geophysical Survey Report, Eskom Site Surveys, South Africa. Koeberg. Volume 1A - Survey Results. Council for Geoscience, Marine Geoscience Unit, Bellville, South Africa.

Horwood, S. (2009). Marine Structural Geology Report, Koeberg Extended Geophysical Site Survey, Table Bay, Cape Town, South Africa. Council for Geoscience Report 2009-0005.

Idaho National Laboratory (INL) (2022). Idaho National Laboratory Sitewide SSHAC Level 3 Probabilistic Seismic Hazard Analysis INL/RPT-22-70233. prepared for the US Department of Energy office of Nuclear Energy, Science, and Technology under DOE Idaho Operations Office Contract DE-AC07-05ID14517.

Johnston, A.C.; Coppersmith, K.J.; Kanter, L.R. and Cornell, C.A. (1994). The Earthquakes of Stable Continental Regions: Final Report Submitted to Electric Power Research Institute (EPRI): TR-102261. 5-volume proprietary report prepared for Electric Power Research Institute, Palo Alto, California, USA.

Kafka, A.L. (2002). Statistical analysis of the hypothesis that seismicity delineates areas where future large earthquakes are likely to occur in the central and eastern United States. Seismological Research Letters 73(6). 990-1001.

Kafka, A.L. (2007). Does seismicity delineate zones where future large earthquakes will occur in intraplate environments?. Special Paper of the Geological Society of America 425. 35-48.

Kafka, A.L. and Levin, S.Z. (2000). Does the spatial distribution of smaller earthquakes delineate areas where larger earthquakes are likely to occur?. Bulletin of the Seismological Society of America 90(3). 724-738.

Kafka, A.L. and Walcott, J.R. (1998). How well does the spatial distribution of smaller earthquakes forecast the locations of larger earthquakes in the northeastern United States?. Seismological Research Letters 69(5). 428-439.

Keefer, D.L., and Bodily, S.E. (1983). Three-point approximations for continuous random variables, Management Science, 29(5). 595-609.

Keyser, A.W. (1974). Introduction, and some microseismic observations in the meizoseismal area of the Boland earthquake of 29th September 1969. In: van Wyk and Kent (1974). The Earthquake of 29 September 1969 in the Southwestern Cape Province, South Africa. Seismological Series 4, Geological Survey (now the Council for Geoscience), Department of Mines, Pretoria, 53 pp excluding Maps, Appendices and Photographs.

Kijko, A. (2004). Estimation of the maximum earthquake magnitude, Mmax. Pure and Applied Geophysics 161. 1655-1681.

Kijko, A.; Graham, G. and Retief, S.J.P. (1999). Seismic hazard assessment of the Koeberg Nuclear Power Plant as a re-evaluation of the seismic design level. CGS Report 1999-0158. Council for Geoscience, Pretoria, South Africa.

Kisters, A. (2016). What Lies Beneath Table Mountain or All Models Are Wrong, But Some Are Useful. Lecture delivered on August 2.

Kisters, A. and Belcher, R. (2018). The Stratigraphy and Structure of the Western Saldania Belt, South Africa and Geodynamic Implications. In: Siegesmund, S.; Basei, M.; Oyhantçabal, P. and Oriolo, S. (eds.). Geology of Southwest Gondwana. Regional Geology Reviews. Springer, Cham, Switzerland. 387-410.

Kisters, A.F.M.; Belcher, R.W.; Armstrong, R.A.; Scheepers, R.; Rozendaal, A. and Jordaan, L.S. (2002). Timing and kinematics of the Colenso Fault, The Early-Paleozoic shift from collisional to extensional tectonics in the Pan-African Saldania Belt, South Africa. South African Journal of Geology 105. 257-270.

Krige, A.V. (1927). An examination of the Tertiary and Quaternary changes of sea-level in South Africa, with special stress on the evidence in favour of a recent world-wide sinking of ocean-level. Annals of the University of Stellenbosch 5(A1). 1-81.

Krüger F., Reichmann, S. & Scherbaum, F. (2011). Moment tensor solution for the 29.9.1969 Ceres earthquake. Presentation at TNSP Workshop 1, April 2011.

Kruger, F. and Scherbaum, F. (2014). The 29 September 1969, Ceres, South Africa, Earthquake: Full Waveform Moment Tensor Inversion for Point Source and Kinematic Source Parameters. Bulletin of the Seismological Society of America 104(1). 576-581.

Lecea, A.M.; Green, A.N. and Cooper, J.A.G. (2016). Environmental change during the Pleistocene and Holocene: Estuaries and lagoons of southern Africa. In: Knight, J. and Grab, S.W. (eds.). Quaternary Environmental Change in Southern Africa: Physical and Human Dimensions. Cambridge University Press. 219-233.

Leonard, M. (2010). Earthquake fault scaling: self-consistent relating of rupture length, width, average displacement, and moment release. Bulletin of the Seismological Society of America 100(5A). 1971-1988.

Leonard, M. (2012). Erratum: Earthquake fault scaling: relating rupture length, width, average displacement, and moment release, Bull. Seismol. Soc. Am. 102, 2,797.

Leonard, M. (2014). Self-consistent earthquake fault-scaling relations: update and extension to stable continental strike-slip faults. Bulletin of the Seismological Society of America 104(6). 2953-2965.

Luden, C. (2015). Investigation into the Ceres-Tulbagh fault line – trying to understand intraplate seismicity. Unpublished BSc Honors, University of Cape Town, South Africa.

Maasha, N. and Molnar, P. (1972). Moment tensor solution for the 29.9.1969 Ceres earthquake. Presentation at TNSP Workshop 1, April 2011.

MacHutchon, M.R.; De Beer, C.H.; van Zyl, F.W. and Cawthra, H.C. (2020). What the marine geology of Table Bay, South Africa can inform about the western Saldania Belt, geological evolution and sedimentary dynamics of the region. Journal of African Earth Sciences 162. 103699.

Maggi, A.; Jackson, J. A.; McKenzie, D. and Priestley, K. (2000). Earthquake focal depths, effective elastic thickness, and the strength of the continental lithosphere. Geology 28(6). 495-498.

Mai, P.M.; Aspiotis, T.; Aquib, T.A.; Cano, E.V.; Castro-Cruz, D.; Espindola-Carmona, A.; Li, B.; Li, X.; Liu, J.; Matrau, R.; Nobile, A.; Palgunadi, K.H.; Ribot, M.; Parisi, L.; Suhendi, C.; Tang, Y.; Yalcin, B.; Klinger, Y. and Jónsson, S. (2023). The Destructive Earthquake Doublet of 6 February 2023 in South-Central Türkiye and Northwestern Syria: Initial Observations and Analyses. The Seismic Record 3(2). 105-115.

Manzunzu, B.; Midzi, V.; Mangongolo, A. and Essrich, F. (2017). The aftershock sequence of the 5 August 2014 Orkney earthquake (ML 5.5), South Africa. Journal of Seismology 21(6). 1323-1334.

Manzunzu, B.; Midzi, V.; Mulabisana, T.F.; Zulu, B.; Pule, T.; Myendeki, S. and Rathod,G.W. (2019). Seismotectonics of South Africa. Journal of African Earth Sciences 149. 271-279.

Maud, R.R. (1996). The macro-geomorphology of the Eastern Cape. In: The geomorphology of the Eastern Cape, South Africa, (ed: C.A. Lewis), Grocott & Sherry, Grahamstown, p. 1-18.

Midzi, V.; Saunders, I.; Manzunzu, B.; Kwadiba, M.T.; Jele, V.; Mantsha, R.; Marimira, K.T.; Mulabisana, T.F.; Ntibinyane, O.; Pule, T.; Rathod, G.W.; Sitali, M.; Tabane, L.; van Aswegen, G. and Zulu, B.S. (2018). The 03 April 2017 Botswana M6.5 earthquake: preliminary results. Journal of African Earth Sciences 143. 187-194.

Midzi, V.; Manzunzu, B.; Mulabisana, T.; Zulu, B.S.; Pule, T. and Myendeki, S. (2020). Probabilistic seismic hazard maps for South Africa. Journal of African Earth Sciences 162. 103689.

Miller, K.G.; Wright, J.D. and Fairbanks, R.G. (1991). Unlocking the Ice House: Oligocene–Miocene oxygen isotopes, eustasy, and margin erosion. Journal of Geophysical Research 96. 6,829-6,848.

Moabi, N. and Dhansay, T. (2021). Fault Studies. PowerPoint presentation at SSHAC Enhanced Level 2 Workshop 1, 24 February, Cape Town, South Africa.

Morris, A.P.; Ferrill, D.A. and Henderson, D.B. (1996). Slip tendency analysis and fault reactivation. Geology 24. 275-278.

Mulabisana, T.; Meghraoui, M.; Midzi, V.; Saleh, M.; Ntibinyane, O.; Kwadiba, T.; Manzunzu, B.; Seiphemo, O.; Pule, T. and Saunders, I. (2021). Seismotectonic analysis of the 2017 Moiyabana earthquake (Mw 6.5; Botswana), insights from field investigations, aftershock and InSAR studies. Journal of African Earth Sciences 182. 104297.

Mulabisana, T. (2023). Microseismicity monitoring along the Colenso Fault. CGS Report 2023-0082 (Rev. 0). Council for Geoscience, Pretoria, South Africa.

Nazareth, J. J. and Hauksson, E. (2004). The seismogenic thickness of the southern California crust. Bulletin of the Seismological Society of America 94(3). 940-960.

Pacific Gas & Electric (PG&E) (2015). Seismic Source Characterization for the Diablo Canyon Power Plant, San Luis Obispo County, California. Revision A. Avila Beach, CA.

Pacific Northwest National Laboratory (PNNL) (2014). Hanford Sitewide Probabilistic Seismic Hazard Analysis. PNNL-23361. Pacific Northwest National Laboratory, Richland, Washington, USA.

Petroleum Agency of South Africa (PASA) (2021). Brochure: Petroleum exploration potential of the Orange Basin. https://www.petroleumagencysa.com/index.php/petroleum-geology-resources/brochures (Accessed 15 May 2022).

Paton, D. A.; Pindell, J.; McDermott, K.; Bellingham, P. and Horn, B. (2017). Evolution of seaward-dipping reflectors at the onset of oceanic crust formation at volcanic passive margins: Insights from the South Atlantic. Geology 45(5). 439-442.

Paton, D.A. (2022). Can (should?) Thick/Thin skinned tectonics concepts be applied to understanding the Western Cape. PowerPoint presentation at PSHA Duynefontyn Workshop 2, 21 June, Stellenbosch, South Africa.

Pether, J. (1994). The sedimentology, palaeontology and stratigraphy of coastal-plain deposits at Hondeklip Bay, Namaqualand, South Africa. MSc thesis, University of Cape Town.

Pether, J.; Roberts, D.L. and Ward, J.D. (2000). Deposits of the West Coast. In: Partridge, T.C. and Maud, R.R. (eds.). The Cenozoic of Southern Africa, Oxford Monographs on Geology and Geophysics 40. Oxford University Press, New York, USA. 33-55.

Pickford, H. (1998). Onland Tertiary marine strata in southwestern Africa: Eustacy, local tectonics and epeirogenesis in a passive continental margin. South African Journal of Science 94. 5-8.

Pollard, D.D. (1987). Elementary fracture mechanics applied to the structural interpretation of dykes. In: Halls, H.C. and Fahrig, W.F. (eds.). Geological Association of Canada Special Paper 34, Mafic Dyke Swarms. 5-24.

Raath, C.J. de W. and Cole, J. (2007). Ground geophysical surveys investigating features identified during the airborne geophysical study of the area around Koeberg. CGS Report 2007-0155 (Rev. 0). Council for Geoscience, Pretoria, South Africa.

Raath, C.J. de W., Cole, J. and De Beer, C.H. (2007). Ground geophysical surveys investigating features identified during the airborne geophysical study of the area around Koeberg. CGS Report 2007-0155 (Rev. 1). Council for Geoscience, Pretoria, South Africa.

Rabie, L.P. (1948). Geological map of the Moorreesburg-Wellington area. University of Stellenbosch (printed but not issued).

Rabie, L.P. (1974a). Structural map of the Moorreesburg-Wellington area. Annals of the University of Stellenbosch 49A(5).

Rabie, L.P. (1974b). Geological Map of the Moorreesburg-Wellington Area. Annals of the University of Stellenbosch 49A(5).

Reid, D.L.; Erlank, A.J. and Rex, D.C. (1991). Age and correlation of the False Bay dolerite dyke swarm, south-western Cape, Cape Province. South African Journal of Geology 94(2/3). 155-158

Paul C Rizzo Associates Inc. (Rizzo) (2008). Definition of Design ground motions for the PBMR Demostration Power Plant, Plant PBMR Project PBMR003224 Koeberg, South Africa. Prepared for Project 07-3835. PBMR, Centrion, South Africa.

Roberts, D.L.; Bateman, M.D.; Murry-Wallace, C.V.; Carr, A.S. and Holmes. P.J. (2009). West coast dune plumes: Climate driven contrasts in dunefield morphogenesis along the western and southern South African coasts. Palaeogeography, Palaeoclimatology, Palaeoecology 271. 24-38.

Roberts, D.L. and Siegfried, H.P. (2009). 3217DB and DD Vredenburg Geological Map. 1:50,000 scale. Council for Geoscience, Pretoria, South Africa.

Roberts, D.L.; Matthews, T.; Herries, A.I.R.; Boulter, C.; Scott, L.; Dondo, C.; Mthembi, P.; Browning, C.; Smith, R.M.H.; Haarhoff, P. and Bateman, M.D. (2011). Regional and global context of the Late Cenozoic Langebaanweg (LBW) paleontological site: West Coast of South Africa. Earth-Science Reviews 106. 191-214.

Roberts, D.L.; Cawthra, H.C. and Musekiwa, C. (2013). Dynamics of late Cenozoic aeolian deposition along the South African coast: a record of evolving climate and ecosystems. Geological Society, London, Special Publications 388. 353-387.

Roberts, D.L.; Neumann, F.H.; Cawthra, H.C.; Carr, A.S.; Scott, L.; Durugbo, E.U.; Humpries, M.S.; Cowling, R.M.; Bamford, M.K.; Musekiwa, C. and MacHutchon, M. (2017). Palaeoenvironments during a terminal Oligocene or early Miocene transgression in a fluvial system at the southwestern tip of Africa. Global and Planetary Change 150. 1-23.

Roberts, D.L. and Brink, J.S. (2002). Dating and correlation of Neogene coastal deposits in the Western Cape (South Africa): Implications for neotectonism. Journal of Geology 105. 337-352.

Rodriguez-Marek, A., Rathje, E., Ake, J., Munson, C., Stovall, S., Weaver, T., Ulmer, K., and Juckett, M. (2021). Documentation Report for SSHAC Level 2: Site Response. US Nuclear Regulatory Commission, RIL 2021-15.

Rogers, J. (1980). First report on the Cenozoic sediments between Cape Town and Eland's Bay. Geological Survey of South Africa Report 1980-136.

Rogers, J. (1982). Lithostratigraphy of Cenozoic sediments between Cape Town and Eland's Bay. Palaeoecology of Africa 15. 121-137.

Rogers, A.W. (1905). An Introduction to the Geology of the Cape Colony. Longmans, Green, and Co, London, United Kingdom.

Rogers, A.W. (1906). A raised beach deposit near Klein Brak River. Annual Report Geological Comm. Cape Good Hope for 1905 (10). 293-296.

Rogers, A.W. and Schwarz, E.H.L. (1907). Geological map of the colony of the Cape of Good Hope, Sheet II. Geological Commission.

Rowe, C.D.; Backeberg, N.R.; Van Rensburg, T.; Maclennan, S.A.; Faber, C.; Curtis, C. and Viglietti, P.A. (2010). Structural geology of Robben Island: implications for the tectonic environment of Saldanian deformation. South African Journal of Geology 113(1). 57-72.

Rozendaal, A.; Gresse, P.G.; Scheepers, R. and Le Roux, J.P. (1999). Neoproterozoic to Early Cambrian crustal evolution of the Pan-African Saldania Belt, South Africa. Precambrian Research 97. 303-323.

Scharf, T.E.; Codilean, A.T.; de Wit, M.J. and Kubik, P.W. (2011). Denudation rates and geomorphic evolution of the Cape Fold Belt determined through the use of in-situ produced cosmogenic 10Be. Poster presentation at Geosynthesis 2011, Integrating the Earth Sciences, 8th Annual Inkaba Workshop, August 28–September 2, Cape Town, South Africa.

Scharf, T.E.; Codilean, A.T.; De Wit, M., Jansen, J.D., and Kubik, P.W. (2013). Strong rocks sustain ancient postorogenic topography in southern Africa. Geology 41(3). 331-334.

Scholz, C.H. (1988). The brittle-plastic transition and the depth of seismic faulting. Geologische Rundschau 77. 319-328.

Schwartz, D.; Coppersmith, K.; Swan, F.H.; Somerville, P. and Savage, W.U. (1981). Characteristic earthquakes on intraplate normal faults (Abstract). Earthquake Notes 52.

Schwartz, D.P. and Coppersmith, K.J. (1984). Fault behavior and characteristic earthquakes: examples from the Wasatch and San Andreas fault zones. Journal of Geophysical Research 89(B7). 5,681-5,698.

Sciscio, L.; Neumann, F.H.; Roberts, D.; Tsikos, H.; Scott, L. and Bamford, M. (2013). Fluctuations in Miocene climate and sea levels along the south-western South African coast: Inferences from biogeochemistry, palynology and sedimentology. Palaeontologia Africana 48. 2-18.

Shaw, B.E. (2013). Earthquake surface slip-length data is fit by constant stress drop and is useful for seismic hazard analysis. Bulletin of the Seismological Society of America 103(2A). 876-893.

Shudofsky, G.N. (1985). Source mechanism and focal depths of East African earthquakes using Rayleigh-wave inversion and body-wave modeling. Geophysical Journal of the Royal Astronomical Society 83(3), 563-614.

Siegfried, H.P (2014). 3317BB and 3318AA Saldanha Geological Map. 1:50,000 scale. Council for Geoscience, Pretoria, South Africa.

Siegfried, H.P. (2019). 3418BB Somerset West and 3418BD Hangklip Geological map. 1:50,000 scale. Council for Geoscience, Pretoria, South Africa.

Singh, M.; Kijko, A. and Durrheim, R. (2009). Seismotectonic models for South Africa: Synthesis of geoscientific information, problems, and the way forward. Seismological Research Letters 80(1). 71-80.

Slabber, N. (1995). The geology and geochemistry of the Bridgetown Formation of the Malmesbury Group, Western Cape province. MSc. thesis (Unpublished), University of Stellenbosch.

Silverman, B.W. (1986). Density estimation for statistics and data analysis. Chapman and Hall, London, England.

Sloan, A.R. (2022). Geomorphology and seismological investigations of potential neotectonic faults in South Africa and Namibia. PowerPoint presentation PSHA Duynefontyn workshop 2, June 21, Stellenbosch, South Africa.

Smart, K.J.; Cawwood, A.J and Ferrill, D.A. (2023). Geological Stress Analyses to Support a Probabilistic Seismic Hazard Analysis (PSHA) for a Critical Site in South Africa. SwRI® Project 15.27360.

Smit, L.; Fagereng, A.; Braeuer, B. and Stankiewicz, J. (2015). Microseismic Activity and Basement Controls on an Active Intraplate Strike-Slip Fault, Ceres–Tulbagh, South Africa. Bulletin of the Seismological Society of America 105(3). 1,540-1,547.

Söhnge, A.P.G. (1984). Glacial diamictite in the Peninsula Formation near Cape Hangklip. Transactions of the Geological Society of South Africa 87. 199-210.

Söhnge, P.G. (1934). The Worcester Fault. South African Journal of Geology 38(1). 253-277.

Somerville (2011). Scaling Relations between Seismic Moment and Rupture Area of earthquakes in Stable Continental Regions". Draft Report; Pacific Earthquake Engineering Research Center, University of California, Berkeley, California, USA.

Somerville, P. (2014). Scaling Relations between Seismic Moment and Rupture Area of earthquakes in Stable Continental Regions". PEER Report 2014/14, Pacific Earthquake Engineering Research Center, University of California, Berkeley, California, USA.

Stafford, P.J. (2014). Source-scaling relationships for the simulation of rupture geometry within probabilistic seismic-hazard analysis. Bulletin of the Seismological Society of America 104(4). 1620-1635.

Stankiewicz, J.; Ryberg, T.; Schulze, A.; Lindeque, A.; Weber, M.H. and De Wit, M. J. (2007). Initial results from wide-angle seismic refraction lines in the southern Cape. South African Journal of Geology 110(2-3). 407-418.

Stamatakos, J.; Watson-Lamprey, J.; Cawthra, H.; Claassen, D.; Coppersmith, R.; Johnson, C.; Largent, M.; Manzunzu, B.; Midzi, V.; Mulabisana, T.; Murphy, D.; Rathje, E. and Wooddell, K. (2022). Baseline PSHA for the Duynefontyn site and the Koeberg Nuclear Power Station. CGS Report 2022-0009 (Rev. 1). Council for Geoscience, Pretoria, South Africa.

Stamatakos, J.; Dasgupta, B.; Pensado, O.; Chokshi, N.; Budnitz, R. and Ravindra, M.K. (2023). Proposed Enhancements to the Risk-Informed and Performance-Based Regulatory Framework for Seismic Hazard Design at NRC-Regulated Nuclear Power Plants. Nuclear Science and Engineering. 1-8.

Stepp, J. (1972). Analysis of completeness of the earthquake sample in the Puget Sound area and its effect on statistical estimates of earthquake hazard. Proceedings of the 1st International Conference on Microzonation, Seattle 2. 897-910.

Stirling, M.; Goded, T.; Berryman, K. and Litchfield, N. (2013). Selection of earthquake scaling relationships for seismic-hazard analysis. Bulletin of the Seismological Society of America 103(6). 2993-3011.

Stock, C. and Smith, E.G., (2002). Adaptive kernel estimation and continuous probability representation of historical earthquake catalogs. Bulletin of the Seismological Society of America 92(3). 904-912.

Tanaka, A. (2004). Geothermal gradient and heat flow data in and around Japan (II) Crustal thermal structure and its relationship to seismogenic layer. Earth, Planets and Space 56(12). 1195-1199.

Tanaka, A. and Ishikawa, Y. (2002). Temperature distribution and focal depth in the crust of northeastern Japan. Earth, Planets and Space 54. 1109-1113.

Tanaka, A. and Ito, H. (2002). Temperature at the base of the seismogenic zone and its relationship to the focal depth of the western Nagano Prefecture area (in Japanese with English abstract). Journal of the Seismological Society of Japan 55. 1-10.

Tankard, A.J. (1976a). Pleistocene history and coastal morphology of the Ysterfontein–Eland's Bay area, Cape Province. Annals of the South African Museum 69. 73-119.

Tankard, A.J. (1976b). Cenozoic sea level changes: a discussion. Annals of South Africa Museum 71. 1-17.

Tankard, A.J. (2022). Western Cape crustal thickness/composition. PowerPoint presentation at SSHAC Enhanced Level 2 Workshop 2, June 21, Cape Town, South Africa.

Tankard, A.; Welsink, H.; Aukes, P.; Newton, R. and Stettler, E. (2009). Tectonic evolution of the Cape and Karoo basins of South Africa. Marine and Petroleum Geology 26(8). 1379-1412.

Theron, J.N. (1974). The seismic history of the Southwestern Cape Province. Geological Survey of South Africa, Seism. Ser. 4. 12-18.

Theron, J.N. (1984a). 3318 DC Bellville geological map. 1:50,000 scale. Geological Survey of South Africa, Pretoria.

Theron, J.N. (1984b). 3318 CD Cape Town geological map. 1:50,000 scale. Geological Survey of South Africa, Pretoria.

Theron, J.N. (1984c). 3418 BA Mitchells Plain geological map. 1:50,000 scale. Geological Survey of South Africa, Pretoria.

Theron, J.N. (compiler). (1990). Sheet 3318 Cape Town geological map series. 1:250,000 scale. Council for Geoscience, Pretoria, South Africa.

Theron, J.N. (1992). Geological map sheet explanation 3318 Cape Town geological map. 1:250,000 scale. Geological Survey of South Africa, Pretoria,

Theunissen, G. (2020). Cape Town is due another earthquake, an expert says – and it will be a big, expensive one. News24. https://www.news24.com/news24/bi-archive/cape-town-is-due-an-earthquake-2020-9 (accessed 22 May 2023).

Thingbaijam, K.K.S.; Mai, P.M. and Goda, K. (2017). New empirical earthquake source-scaling laws. Bulletin of the Seismological Society of America 107(5). 2,225-2,246.

Timmerman, L.R.A. (1985a). Preliminary report on the geohydrology of the Grootwater Primary Aquifer Unit between Yzerfontein and the Madder River. Report (Unpublished). South African Department of Water Affairs.

Timmerman, L.R.A. (1985b). Preliminary report on the geohydrology of the Cenozoic sediments of part of the coastal plain between the Berg River and Elands Bay (southern section). Report Gh 3370.

Van der Elst, N.J. (2021). B-positive: A robust estimator of aftershock magnitude distribution in transiently incomplete catalogs. Journal of Geophysical Research, Solid Earth 126(2).

Van Zyl, M. (1997). Landscape evolution of the Garden Route between the Bloukrans River and Mossel Bay. MSc. Thesis, University of Port Elizabeth.

Vandoolaeghe, M.A.C. (1989). The Cape Flats groundwater development pilot abstraction scheme. Technical report Gh 3655. Directorate Geohydrology, Cape Town, South Africa.

Veneziano, D. and Van Dyck, J. (1985). Statistical discrimination of aftershocks and their contribution to seismic hazard. In: Seismic Hazard Methodology for Nuclear Facilities in the Eastern U.S. 2, Appendix A-4, EPRI/SOG Draft 85-1.

Visser, H.N. and Schoch, A.E. (1972). Map Sheet 255: 3217D & 3218C St Helena Bay, 3317B and 3318A Saldanha Bay. Geological Survey of South Africa.

Visser, H.N. and Schoch, A.E. (1973). The geology and mineral resources of the Saldanha Bay area. Memoir, Geological Survey of South Africa 63.

Visser, H.N. and Theron, J.N. (1973). 3218 Clanwilliam Geological Map. 1:250,000-scale. Department of Mines, Geological Survey.

Visser, H.N.; De Villiers, J.E.; Theron, J.N. and Hill, R.S. (1981). Die geologie van die gebied tussen Ceres en Moorreesburg. [English: The geology of the area between Ceres and Mooreesburg]. Explanation of Sheets 3318B Malmesbury and 3319A Ceres. Geological Survey of South Africa.

Von Buchenröder, W.L. (1830). The Cape Town Earthquake of 1809. South African Quarterly Journal, Cape Town.

Von Veh, M.W. (1982). Aspects of sedimentation, structure and tectonic evolution in the Tygerberg terrane, southwestern Cape Province. Bulletin of the Precambrian Research Unit, University of Cape Town, South Africa 32. 1-88.

Wagner, G.S. and Langston, C.A. (1988). East African earthquake body wave inversion with implications for continental structure and deformation. Geophysical Journal 94(3), 503-518.

Weichert, D.H. (1980). Estimation of the earthquake recurrence parameters for unequal observation periods for different magnitudes. Bulletin of the Seismological Society of America 70(4). 1,337-1,346.

Wells, D.L. and Coppersmith, K.J. (1994). New empirical relationships among magnitude, rupture length, rupture width, rupture area, and surface displacement. Bulletin of the Seismological Society of America 84(4). 974-1,002.

Weng, H. and Yang, H. (2017). Seismogenic width controls aspect ratios of earthquake ruptures. Geophysical Research Letters 44. 2,725-2,732.

Werner, M.J.; Helmstetter, A.; Jackson, D.D. and Kagan, Y.Y. (2011). High-resolution long-term and short-term earthquake forecasts for California. Bulletin of the Seismological Society of America 101(4). 1,630-1,648.

Wesnousky, S.G.; Scholz, C.H.; Shimazaki, K. and Matsuda, T. (1983). Earthquake frequency distribution and mechanics of faulting. Journal of Geophysical Research 88. 9331-9340.

Wesnousky, S.G.; Scholz, C.H.; Shimazaki, K. and Matsuda, T. (1984). Integration of geological and seismological data for the analysis of seismic hazard: A case study of Japan. Bulletin of the Seismological Society of America 74(2). 687-708.

Wesnousky, S.G. (1986). Earthquakes, Quaternary faults, and seismic hazard in California. Journal of Geophysical Research, Solid Earth 91(B12). 12,587-12,631.

Wesnousky, S.G. (2008). Displacement and Geometrical Characteristics of Earthquake Surface Ruptures: Issues and Implications for Seismic-Hazard Analysis and the Process of Earthquake Rupture. Bulletin of the Seismological Society of America 98(4). 1,609-1,632.

Wessels, W.P.J. and Greeff, G.J. (1980). N Ondersoek na die optimale benutting van Eersterivierwater deur opberging in sandafsetting of ander metodes. [English: Investigation into the optimal utilisation of Eerste River water through storage in sand deposits or other methods]. University of Stellenbosch, Department of Civil Engineering.

Wheeler, R.L. (2009). Methods of Mmax estimation east of the Rocky Mountains. Open File Report 2009-1018. United States Geological Survey.

Wiemer, S. and Wyss, M. (2000). Minimum Magnitude of Completeness in Earthquake Catalogs: Examples from Alaska, the Western United States, and Japan. Bulletin of the Seismological Society of America 90(4). 859-869.

Wooddell, K.E. and Abrahamson, N.A. (2013). Constraints on magnitude-frequency distributions for evaluating the hazard of multi-segment ruptures. Seismological Research Letters 84(2).

Wooddell, K.E.; Abrahamson, N.A.; Acevedo-Cabrera, A.L. and Youngs, R.R. (2014). Hazard implementation of simplified seismic source characterization allowing for linked faults. Seismological Research Letters 85(2).

Yen, Y.-T. and Ma, K.F. (2011). Source-scaling relationship for M 4.6–8.9 earthquakes, specifically for earthquakes in the collision zone of Taiwan. Bulletin of the Seismological Society of America 101(2). 464-481.

Youngs, R.R. and Coppersmith, K.J. (1985). Implications of fault slip rates and earthquake recurrence models to probabilistic hazard estimates. Bulletin of the Seismological Society of America 75. 939-964.

CHAPTER 9: GROUND MOTION MODEL

9. GROUND MOTION MODEL

9.1 OVERVIEW OF GROUND MOTION MODEL

The ground motion model (GMM) for the PSHA at the Duynefontyn site has been designed to meet the Senior Seismic Hazard Analysis Committee (SSHAC) objective of capturing the CBR of TDI. This objective is met by developing a GMM logic-tree that captures the best estimates and associated epistemic uncertainty of ground-motion predicted for all seismic sources defined in the SSM. The GMM logic-tree is formed by the GMM TI Team through objective evaluation of the available ground-motion data (see Chapter 7), potentially applicable models, and site data (see Section 4.6). The GMM TI Team then integrated the information from their evaluation to produce a single logic-tree that represents the CBR of TDI.

9.1.1 Applicability

The GMM applies to all sources defined in the SSM, including the magnitude and distance ranges implied by the model, and other features such as style-of-faulting, as they are the inputs to the GMM.

For the Duynefontyn site, the seismic sources in the SSM are related to crustal seismicity and are predominantly modelled as seismic source zones, except for the Groenhof Fault Source which is modelled as a fault. The SSM defines distributions of seismogenic thickness, style-of-faulting, hypocentre depth, strike, dip, and maximum magnitude (Mmax) for each of the seismic source zones.

The hazard is controlled by the host zone, the Saldania Zone (SDZ) (see Chapter 10). The SSM in SDZ is composed of 80% strike-slip ruptures and 20% normal ruptures and has a maximum magnitude range from moment magnitude (**M)** 6.2 to **M** 7.8, with a mode of **M** 6.6. Additional information about the SSM can be found in Chapter 8.

The GMM is applicable for **M** 5 through **M** 7.8 and the distance ranges defined in the SSM (0 km to 320 km). The GMM is defined for both normal and strike-slip ruptures. The median reference rock model was developed by the GMM TI Team for the Western Cape using South Africa wide ground-motions, and thus its applicability should extend throughout South Africa. The sigma model adopted by the GMM TI Team is based on a worldwide dataset and evaluated for use in the Western Cape. The site-specific nature of the site amplification model means that the full GMM is only applicable at the Duynefontyn site.

9.1.2 Required outputs

The PSHA for the Duynefontyn site was conducted to obtain seismic hazard estimates at two site locations: the existing KNPS, and the new build site at Duynefontyn (Figure 1-2). For each location at the Duynefontyn site, the owner specified a control point defined by a set of coordinates and an elevation at the base of the sand layer (Table 9-1).

Table 9-1. Control points.

Site Name	Latitude	Longitude	Elevation
Koeberg Nuclear Power Station	-33.676894	18.431397	Bottom of sand layer
New Build Site at Duynefontyn	-33.661108	18.428319	Bottom of sand layer

At each control point, the required outputs from the PSHA are expressed in terms of 5%-damped pseudo-spectral acceleration at a range of oscillator frequencies (Table 9-2). The GMM provides predictions of the horizontal component of ground-motion using RotD50, the median-component ground motions (Boore, 2010).

Table 9-2. Target oscillator frequencies and periods covered by the GMM.

Frequency (Hz)	Period (sec)
0.5	2
1	1
2.5	0.4
5	0.2
10	0.1
20	0.05
25	0.04
33	0.03
50	0.02
100	0.01

9.1.3 Backbone GMPE approach

The traditional approach for developing a GMM has been to select a number of ground motion prediction equations (GMPEs) and assign weights to reflect the confidence of the GMM TI Team in each of the models regarding their applicability to the target region and site. In general, GMPEs from one region are not perfectly applicable to another, and thus adjustments are made to the GMPEs to make them more applicable to the target region or site.

The objective of the GMM logic-tree is to capture the CBR of TDI, which is the CBR of possible ground-motions at a site given the earthquake scenarios in the SSM. The traditional approach for developing a GMM does not directly provide the CBR, and for some earthquake scenarios in the SSM may not capture the CBR at all. An example of this from Bommer (2022) and shown in Figure 9-1 demonstrates how there can be magnitude-distance combinations where GMPEs predict results that are extremely similar and thus the epistemic uncertainty is too low.

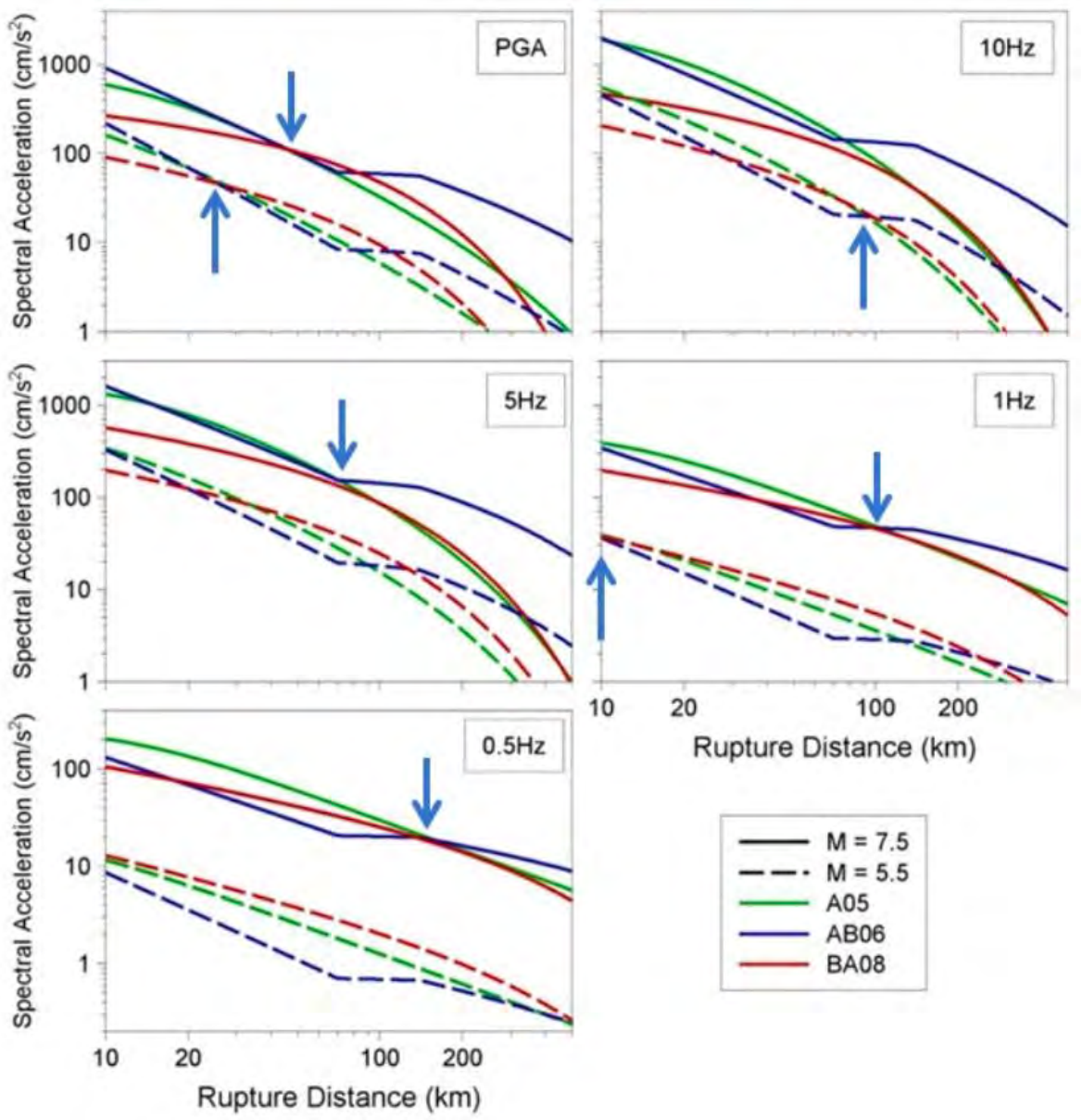

Figure 9-1. Example of three GMPEs used to populate a GMM at different frequencies for earthquakes of M 5.5 and M 7.5. Arrows indicate magnitude-distance combinations where the GMPEs predict ground-motions that are very similar and epistemic uncertainty is low (Bommer, 2022).

Even when the GMPEs in a traditional logic-tree approach are not predicting extremely similar ground-motions, it is generally not the case that they sample the range of possible ground-motions. To capture the full CBR and address issues such as limited data availability for hazard-critical earthquake scenarios that tend to have large magnitudes and short distances and the limitations of the approach used to estimate site response difference between the host and target sites, epistemic uncertainty needs to be added (Al Atik and Youngs, 2014).

The GMM TI Team adopted a 'backbone' approach for the development of the median reference rock model to represent the CBR of TDI. This approach addresses the issues with the traditional logic-tree approach by creating a logic-tree where each branch is occupied by a modified version of a single GMPE (Atkinson et al., 2014). The alternative branches were obtained by applying scale factors to the backbone GMPE, where the scale factors account

for differences in host-to-target seismic parameter adjustments. This approach has been used on multiple SSHAC Level 3 PSHAs for sites in South Africa, Spain, and the United States, and is becoming standard of practice for such projects.

The GMM TI Team decided to follow the recommendations of Bommer and Stafford (2020) by selecting the Chiou and Youngs (2014) GMPE, referred to as CY14, as the backbone GMPE and making host-to-target adjustments as described in Section 9.2.1. The GMM TI Team adopted a host-to-target adjustment approach that is conceptually similar to the hybrid empirical method (HEM) of Campbell (2003) and requires seismic parameter sets to be available for both the 'host' and 'target' regions, where these parameters are those defined as part of the point-source stochastic model (Boore, 2003). Stafford et al. (2022) previously derived host region seismic parameters for the CY14 GMPE that were utilised on this project.

For the target region, the host-to-target adjustment approach requires seismic parameters consistent with the point-source stochastic model that describe the source and path characteristics of the rupture scenarios that are relevant for the Duynefontyn site. Two approaches were considered by the GMM TI Team for estimating the target parameters, one based on Fourier amplitude spectra, the other based on elastic response spectra. Following these approaches, the GMM TI Team and a specialty contractor developed seven suites of target-region parameters that each predict the ground-motion in South Africa while making different assumptions about data, the treatment of the site decay parameter (κ_0), regression process, and additional issues outlined in Section 9.2.2.

The GMM TI Team developed host-to-target source and path adjustments for each of the seven suites of target parameters and applied them to the CY14 GMPE (Section 9.2.3). To capture the CBR of TDI with mutually exclusive branches, the GMM TI Team decided to develop a meta-model that is a combination of the seven adjusted GMPEs (Section 9.2.4). The epistemic uncertainty of the meta-model is then a combination of the model-to-model variability, near-source saturation uncertainty, and additional epistemic uncertainty (Section 9.2.5).

9.1.4 Sigma approach

The aleatory variability (sigma) describes the expected deviation from the mean ground-motion that can occur at a given site. To estimate this variability, the GMM TI Team generally relies on the ergodic assumption, which states that variability in space (between different locations) can be used as a substitute for variability over time at one location (Anderson and Brune, 1999). Using this assumption, global datasets are considered applicable for estimating the variability of the ground-motion at a given site.

Recent decades have seen a large increase in the number of ground-motion recordings that are available for use and numerous projects have made significant efforts to collect the available recordings. This has allowed for repeatable site effects at some stations to be determined and removed from the aleatory variability. This allows the development of models for aleatory variability for single stations, referred to as "single-station sigma" (Atkinson, 2006). The GMM TI Team decided to use single-station sigma because a site-specific amplification model was developed for this project, thus the site-to-site aleatory variability is not needed, and the epistemic uncertainty of the site-specific amplification model is considered using a logic-tree approach (Section 9.3).

To evaluate the use of global single-station-sigma models, the GMM TI Team examined the residuals from the inversions performed to estimate target seismic parameters to determine whether there was sufficient data to deviate from global models. The GMM TI Team decided the data was insufficient for this purpose and to use the single-station sigma model developed by Al Atik (2015) to represent aleatory variability at the Duynefontyn site. The mixture model was also applied to capture the widening of the tails of the aleatory variability that is observed in large ground-motion datasets (Section 9.3.4).

9.1.5 Site amplification model approach

Two general approaches are available to develop site adjustments for the site-specific subsurface conditions: a one-step approach and a two-step approach, as shown in Figure 9-2. The one-step approach computes the frequency-dependent site adjustment factors (SAF) as the ratio of the surface response spectra from two separate site response analyses: one for the site condition associated with the reference GMPE and one for the site-specific reference condition plus the near-surface condition. The alternative is the two-step approach in which a shear-wave velocity (V_S) and κ_0 adjustment is first applied to the GMPE to correct for the site-specific reference condition and then site response analyses are used to derive amplification factors that represent the site-specific near-surface condition.

The two-step approach creates a challenge since it depends on the characterisation of the buried reference rock horizon. This is a required input to the V_S-κ_0 adjustment and is needed to define the base of the column for which the site response calculations are performed. The challenge is that until site characterisations have been completed, neither the reference rock model nor the amplification model can be developed. This challenge is resolved by the one-step approach in which the site adjustments for the effects of both the deep and shallow portions of the site profile are captured in a single step. The GMM TI Team adopted the “one-step approach” recommended by Rodriguez-Marek et al. (2021) and Williams and Abrahamson (2021) (See Section 9.4.1).

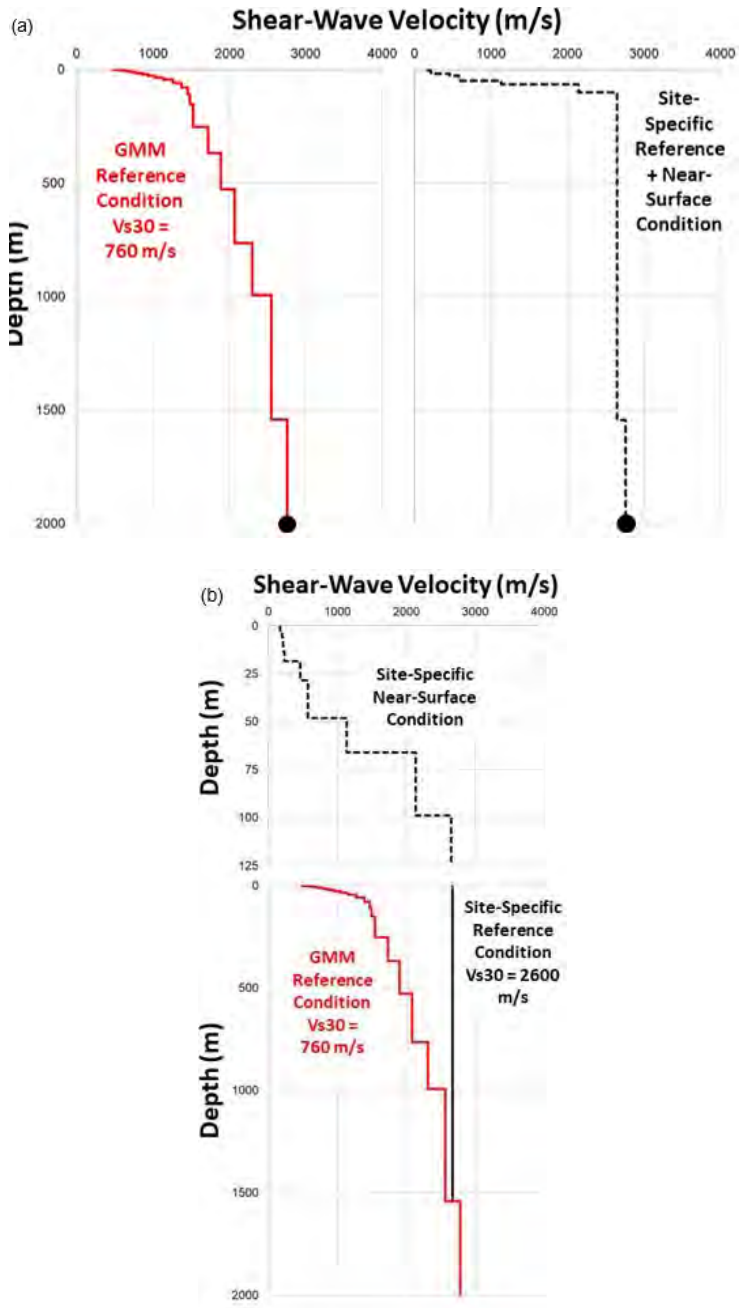

Figure 9-2. The (a) one-step and (b) two-step approaches to develop site adjustment factors. From Rodriguez-Marek et al. (2021).

The GMM TI Team quantified the epistemic uncertainty associated with the site adjustment factors (SAF) using a site response logic-tree that defines alternative site properties (e.g., V_S profiles, κ_0) with associated weights and performed site response analyses for each combination of site properties in the logic-tree (See Section 9.4.2 through 9.4.4). Typical logic-trees contain many branches, thus fully sampling the logic-tree potentially requires performing several thousand site response analyses. Incorporating this many results into the hazard calculation is computationally difficult, so Rodriguez-Marek et al. (2021) proposed an approach to re-sample the weighted distribution of computed SAF into a manageable number of SAF (usually between five and seven) that together capture the distribution associated with

the full logic-tree (Section 9.4.1). The standard deviation of the SAF, representing the epistemic uncertainty associated with the logic-tree (σ_{ep}), is also computed (Figure 9-3) and quantifies the epistemic uncertainty associated with the site response logic-tree. Often σ_{ep} becomes small and approaches zero at periods larger than the natural period of the site due to the inherent limitations of one-dimensional site response analysis, but recorded ground-motions do not indicate smaller ground-motion variability at long periods, thus σ_{ep} must be adjusted at long periods to address these limitations. Model error is another component of σ_{ep} that is addressed separately from the standard deviation of the SAF. The GMM TI Team evaluated the variability due to the model error associated with one-dimensional site response and integrated it into the model (Bahrampouri and Rodriguez-Marek, 2023; Stewart and Afshari, 2021) (See Section 9.4.5).

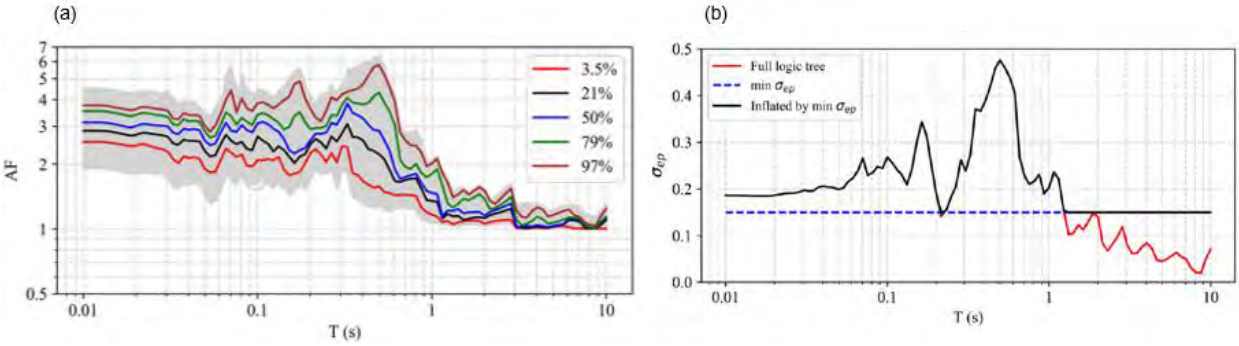

Figure 9-3. (a) Median SAF (light gray lines) for full logic-tree capturing all sources of uncertainty along with the resampled, five-point discrete SAF (colour lines), and (b) the standard deviation of the SAF from the logic-tree (σ_{ep}) compared with the minimum epistemic uncertainty. From Rodriguez-Marek et al. (2021).

The site adjustment factors are incorporated into the hazard following Approach 4 (NUREG/CR-6728), where the surface hazard curves are developed by combining the site amplification model with the reference rock model inside the hazard calculations. The site amplification model considers the influence of the intensity of the reference motion, as quantified by Sa_{ref}, and the earthquake magnitude on the SAF, as well as the epistemic uncertainty. The GMM TI Team performed site response analyses for a range of reference motion intensities and earthquake magnitudes to develop the final site amplification model.

9.2 MEDIAN REFERENCE ROCK MODEL

9.2.1 Selection of backbone GMPE and host-region source and path characteristics

9.2.1.1 Selection of backbone GMPE

The selection of a seed backbone GMPE is dependent on several practical requirements and criteria for applicability. The GMM TI Team summarise the main attributes in the present section and Bommer and Stafford (2020) discuss these in more detail. For a start, any candidate GMPE must meet the practical requirements of the PSHA. Such practical requirements include:

- the ability of the model to make predictions for the range of periods for which hazard calculations will be performed.
- the ability of the model to make predictions for the relevant rupture mechanisms dictated by the seismic source model.
- having an appropriate range of applicability in magnitude and distance space (or having robust support for extrapolation).
- passing other exclusion criteria such as those presented by Cotton et al. (2006) and Bommer et al. (2010).

Application of these criteria limits the suite of candidate seed GMPEs, and adaptability criteria are then used to identify GMPEs that are well-suited to work as seed models. The criteria of Bommer and Stafford (2020) related to adaptability can be summarised in three key issues, each discussed briefly in the following subsections.

9.2.1.1.1 Robust host-region parameterisation

To compare target-region seismic parameters with host-region seismic parameters it is important to be able to associate the seed GMPE with a particular host region, or to have access to seismic parameters that are known to represent the seed model. In the traditional HEM framework, the ‘host region’ literally was some spatial or geographic region, but in more recent studies we look to identify parameters that are directly linked to the seed GMPE (Al Atik and Abrahamson, 2021; Stafford et al., 2022). In the context of assessing adaptability, it is important to understand what seismic parameters are representative of the seed GMPE (the host GMPE) so that the GMM TI Team can make like-for-like comparisons with similar parameters obtained for the target region. Some GMPEs are more difficult to obtain seismic parameter sets for than others. Bommer and Stafford (2020) use the example of models that treat site response using generic site classes, versus models that include V_{S30} as a predictor, versus models that have site scaling that is linked to a known velocity/crustal profile. It is far easier to separate the effects of impedance and damping if one knows the crustal profile than if one only has a generic site class to work with.

In this context, the recent work of Al Atik and Abrahamson (2021) has been important as they derive model-specific crustal profiles that reproduce the linear site response effects of a few GMPEs. Rather than selecting a generic crustal model that the GMM TI Team thinks is consistent with a candidate seed GMPE, it becomes possible to work with a crustal model that is known to replicate the implicit site scaling within a candidate GMPE. Stafford et al. (2022) demonstrated how the assumed impedance effects can vary between a generic crustal model and a GMPE-specific crustal model. The use of GMPE-specific information enables a better

mapping of scaling effects within the candidate seed model to physical scaling effects within the Fourier spectral model. The approach of Al Atik and Abrahamson (2021) assumes that the linear site response embedded within a ground-motion model can be replicated through the use the quarter-wavelength approach in which impedance effects are attributed to 1D changes in velocity (and density, but with the velocity being the dominant contributor). When the resulting velocity profile is subsequently used in 1D equivalent linear site response computations the site response that is obtained should be similar to that implied by the quarter-wavelength approach. The consistency of the 1D assumption is guaranteed, but the equivalent linear site response method can indicate resonant effects that would not be captured by the quarter-wavelength approach. Internal testing indicates that the discrepancies on response spectra are relatively minor (see Section 9.4.7) because the velocity profiles of Al Atik and Abrahamson (2021) are both finely discretised and relatively smoothly varying. The GMM TI Team has confidence in the internal consistency of this approach as a result.

9.2.1.1.2 Isolated influence of individual scaling factors

GMPEs tend to have functional terms that try to represent different scaling characteristics. For example, terms that involve the earthquake magnitude will typically relate to the strength of motions leaving the source, terms that involve source-to-site distance will reflect either geometric spreading or anelastic attenuation effects, and so on. In the example of the work of Scasserra et al. (2009) one can attribute the trends in ground-motion residuals to geometric spreading rather than anelastic attenuation because most of the data considered by those authors was within 100 km of the source (where anelastic effects are mild) and because the distance (R) dependence is consistent with the theoretical expectation that ground-motions scale as $R^{-\gamma}$, where γ is the geometric attenuation rate, due to geometric spreading.

This approach of directly comparing the seed GMPE predictions to empirical data does not always give such clear insight into what corrections are required. Many GMPEs do not have functional terms that uniquely relate to identifiable physical processes. For example, the NGA-West2 ground-motion model of Abrahamson et al. (2014), that builds on a similar functional form used in Abrahamson and Silva (1997, 2008), and has been extensively used in many applications, defines their core magnitude and distance scaling, for magnitudes above $M_2 = 5$, as:

9-1

$$\ln SA = \begin{cases} a_1 + a_5(\boldsymbol{M} - M_1) + a_8(8.5 - \boldsymbol{M})^2 + [a_2 + a_3(\boldsymbol{M} - M_1)]\ln R + a_{17}R_{RUP} & \boldsymbol{M} > M_1 \\ a_1 + a_4(\boldsymbol{M} - M_1) + a_8(8.5 - \boldsymbol{M})^2 + [a_2 + a_3(\boldsymbol{M} - M_1)]\ln R + a_{17}R_{RUP} & M_2 \le \boldsymbol{M} \le M_1 \end{cases}$$

With M_1 varying with period but taking its lowest value of 6.75 at short periods and being as high as 7.25 at long periods. In Equation 9-1, $\boldsymbol{M}$ is the moment magnitude, $lnSA$ is the natural log of spectral acceleration for a given period, R is a distance metric that combines the rupture distance and a model parameter in the form $R = \sqrt{R_{RUP}^2 + h\text{^}2}$, R_{RUP} is rupture distance, and a_1, a_2, a_3, a_5, a_8 and a_{17} are coefficients.

On face value the model has quadratic magnitude scaling, consistent with what one expects from Fourier source spectral theory (Fukushima, 1996), magnitude-dependent geometric spreading, and magnitude-independent anelastic attenuation (the $a_{17}R_{RUP}$ term). These functional terms are widely used in other GMPEs and have been used for decades. If one

looks at the actual coefficients, one sees that the coefficients a_4 and a_5 are constant for all periods and are equal to -0.1 and -0.41, respectively, and that a_8 varies with period but is always negative. While the functional terms 'look' reasonable, the fact that a_5 and a_8 are both negative initially suggests that spectral accelerations decrease with increasing magnitude (above M_1) and do so at quite a high rate. When one considers the additional interaction term ($a_3 \boldsymbol{M} \ln R$) we see that spectral acceleration will increase with magnitude provided that[1]:

9-2

$$a_5 - 2a_8(8.5 - \boldsymbol{M}) + a_3 \ln R > 0$$

This suggests that for certain combinations of magnitude and distance the model will have amplitudes that increase with magnitude, but for others they will decrease. At very short distances, the term R is limited to be no smaller than 4.5 and this means that in practice the gradient with magnitude remains positive over the range of applicability of the model.

The specific details of the Abrahamson et al. (2014) GMPE are not important for the current context. What is important is the fact that this model will provide similar predictions to CY14 in many instances (both models are essentially unbiased with respect to the data they were calibrated against, and there is significant overlap between the data used in each study). To illustrate this point further, any of the other NGA West2 models (Boore et al., 2014; Campbell and Bozorgnia, 2014; or Idriss, 2014) could have been discussed in this section. To first order, these models, along with Chiou and Youngs (2014) and Abrahamson et al. (2014), all provide similar predictions for many scenarios. Each of the alternatives have characteristics that complicate model adjustments when compared to Chiou and Youngs (2014). The magnitude-scaling of the Boore et al. (2014) model has a period-dependent hinge magnitude, but slopes above and below this hinge that vary with period (and even become negative for some periods). The magnitude-scaling of the Campbell and Bozorgnia (2014) model has multiple period-independent hinge magnitudes and slopes freely vary between these hinges. While this is a flexible parameterisation in many respects, stress parameter adjustments become complicated to implement precisely because of the large number of degrees of freedom within the response spectral model. Finally, the Idriss (2014) model uses quadratic magnitude scaling with no control on the slopes or the effective transition from steep magnitude scaling (associated with frequencies below the source corner frequency) and shallow slopes (associated with frequencies above the source corner frequency).

Returning to the extended comparison of the Abrahamson et al. (2014) and Chiou and Youngs (2014) models, in terms of how applicable the two models are to a given region, they will have similar quantitative performance. In terms of how easily one can associate source scaling and path scaling to particular functional expressions within the models, there are significant differences. This has implications for how adaptable these models are (Bommer and Stafford, 2020). To make this clear, if these two models were compared to a dataset like that used by Scasserra et al. (2009) it is possible that both sets of residuals that were obtained would exhibit a trend with distance. It is very clear which terms within CY14 could be adjusted to accommodate that difference in scaling. For the Abrahamson et al. (2014) GMPE, the trend

[1] This discussion just focusses upon the core magnitude-distance scaling of this model, the real situation is more nuanced than what is presented here as there is additional magnitude dependence in other parts of the model, such as within the nonlinear site response scaling.

could also be removed, but it may not be as clear which terms should be targeted given that the model has more complex magnitude-distance interactions.

It is helpful in the context of adaptability for the candidate GMPE to also isolate these terms clearly within the functional form of the model because the point-source stochastic model has distinct terms for source scaling, path scaling, and site scaling. This means that particular terms of a ground-motion model can be targeted for adjustment. The CY14 GMPE has clear separation between the source and path scaling terms (Bommer and Stafford, 2020; Chiou and Youngs, 2014).

9.2.1.1.3 Theoretical consistency of functional form

In addition to having functional terms that clearly relate to a particular physical process (such as source scaling or geometric spreading), it further helps if these functional terms closely mimic the functional expressions of the point-source stochastic model. Fourier and response spectral ordinates do not scale in the same way, but for many periods the nature of the scaling is very similar (Bora et al., 2016). If we consider the magnitude scaling of the Abrahamson et al. (2014) GMPE presented in Equation 9-1 we can see that it has particular slopes ($\partial \ln SA / \partial \boldsymbol{M}$) above and below M_1 and that M_1 varies with period. It is not immediately clear what these slopes are because you must consider both the a_4 and a_5 coefficients as well as the interaction term with distance, and there is also the quadratic magnitude-scaling term that complicates matters.

We can contrast Equation 9-1 with the primary magnitude scaling of CY14 shown in Equation 9-3:

9-3

$$\ln SA \propto c_2(\boldsymbol{M} - 6) + \frac{c_2 - c_3}{c_n} \ln\left[1 + e^{c_n(c_M - \boldsymbol{M})}\right]$$

In Equation 9-3, $\boldsymbol{M}$ is the moment magnitude, SA is the spectral acceleration for a given period, and c_2, c_3, c_n and c_M are coefficients (the latter two of which are period dependent). When $\boldsymbol{M}$ is very large (compared to c_M) the exponential term becomes very small, and the magnitude scaling is essentially $\ln SA \propto c_2\boldsymbol{M}$. In contrast, when $\boldsymbol{M} \ll c_M$ we have $\ln SA \propto c_3\boldsymbol{M}$, so the coefficients c_2 and c_3 define the slopes for large and small magnitudes (with large and small being relative to the coefficient c_M), respectively. The coefficient c_n controls how quickly the scaling transitions from having one slope to another.

The same scaling is exhibited by Fourier spectral amplitudes due to the characteristics of the Ω-squared source spectrum (Fukushima, 1996; Chiou and Youngs, 2008). Importantly, from Fourier spectral theory (Boore, 2003), the coefficient c_M can be related to the source corner frequency (and hence stress parameter) and so changes to $\Delta\sigma$ can be related to changes in c_M (Bommer and Stafford, 2020; Boore et al., 2022). Figure 9-4 illustrates this behaviour and shows how a single parameter of a ground-motion model can be used to represent changes in an underlying FAS parameter if the functional expressions are theoretically consistent. The

figure shows the magnitude scaling that is adopted by the Chiou and Youngs (2008)[2] GMPE, and that also underpins the scaling found within CY14.

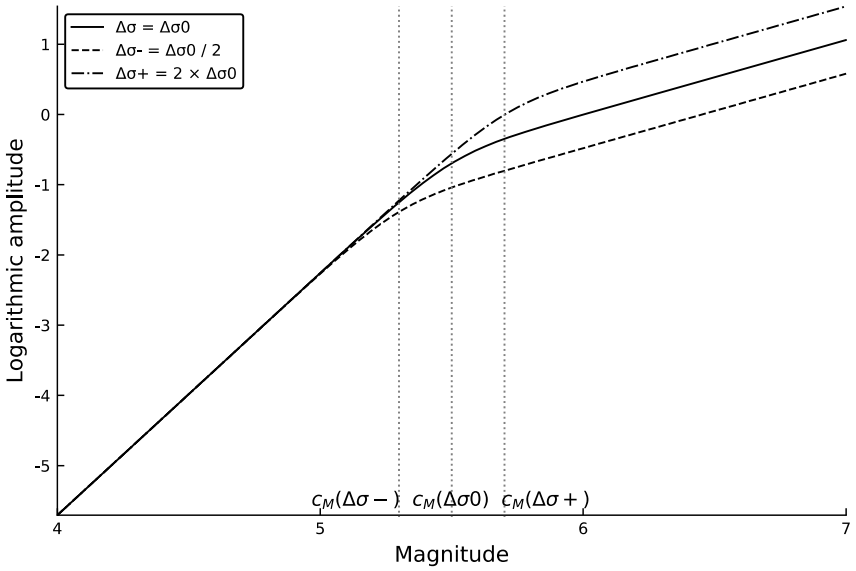

Figure 9-4. Influence of changes to the stress parameter $\Delta\sigma$ on the magnitude scaling of logarithmic spectral amplitudes. The curves shown correspond to a functional form that replicates the scaling implied by an Ω-squared source spectrum (Aki, 1967), with corner frequency linked to the stress parameter (Brune, 1970, 1971). The vertical dotted lines identify the locations where the magnitude scaling transitions from a steep slope at small magnitudes to a shallower slope for large magnitudes. In the Chiou and Youngs (2014) GMPE, this location is specified through the coefficient c_M, and varies with response period (Bommer and Stafford, 2020).

In the example just discussed we have a physical model that defines how source spectral amplitudes vary with magnitude, and this model has one key parameter which is $\Delta\sigma$. In the case of Chiou and Youngs (2008, 2014) the functional form that was adopted for magnitude scaling replicates the scaling of the physical model and this means that $\Delta\sigma$ can be related to the coefficient c_M. This is a particular feature of the Chiou and Youngs (2008, 2014) GMPEs and is not a feature shared by most other GMPEs. Those other GMPEs, such as the earlier example of Abrahamson et al. (2014), will still exhibit magnitude scaling that is relatively steep for small magnitudes and relatively shallow for larger magnitudes, but the functional form and parameterisation of that GMPE does not have such a direct link to the underlying physical model. The implication is that adjustments can still be made to reflect differences in $\Delta\sigma$ but those adjustments will involve changes to multiple parameters or terms of the GMPE or else will require a more elaborate approach to be adopted, such as the HEM of Campbell (2003) (which, as published, involves consideration of complete Fourier parameter sets).

Bommer and Stafford (2020) explained that using the standard point-source stochastic model we expect to see response spectral ordinates that scale with magnitude as shown in Figure 9-5. We have now seen, through consideration of the Abrahamson et al. (2014) and Chiou and Youngs (2014) GMPEs, that there are different ways to represent this scaling in a GMPE. We can identify the coefficient c_M as relating to the role of $\Delta\sigma$, and it is possible to target just

[2] Note that Chiou and Youngs (2008) actually forced the coefficient c_3 to equal the theoretical value of 3.45, but relaxed that constraint in their Chiou and Youngs (2014) update to enable better agreement with observations from smaller magnitude events (where the influence of κ_0 becomes important).

that term when adjusting for stress parameter differences, because CY14 has greater theoretical consistency in its parameterisation (Boore et al., 2022).

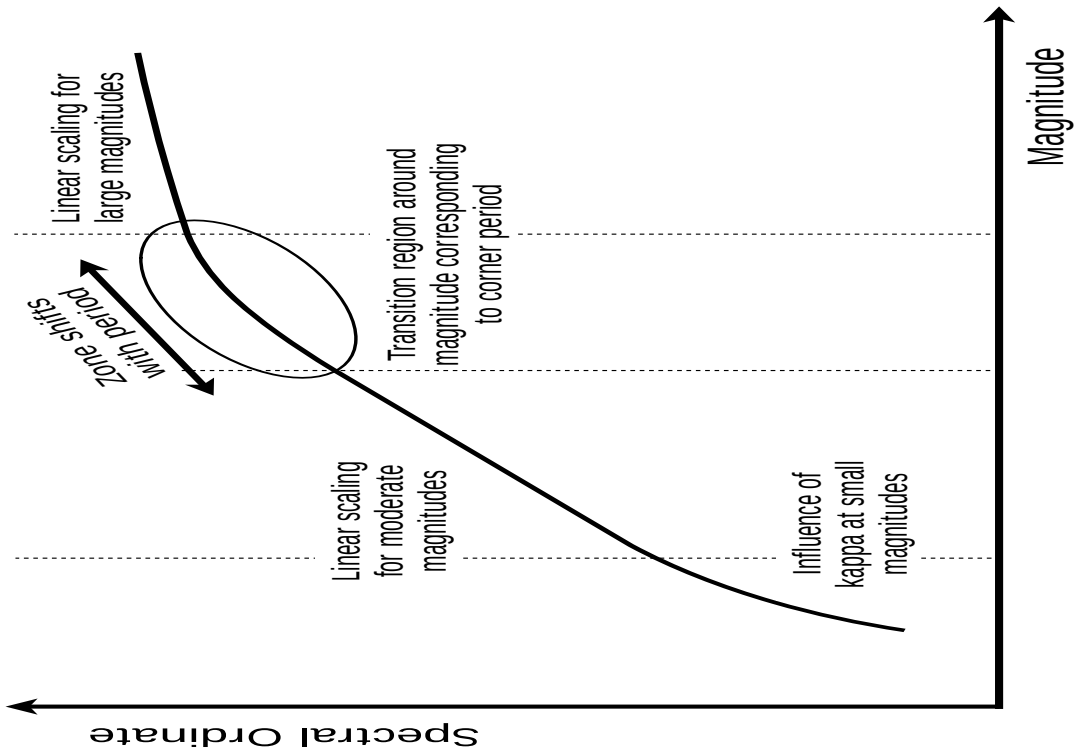

Figure 9-5. Schematic illustration of theoretically consistent magnitude scaling. From Bommer and Stafford (2020).

After considering the desirable attributes of the candidate seed GMPEs, CY14 was adopted by the GMM TI Team as the seed GMPE for the present study. This decision was heavily influenced by the issues outlined in the previous section and discussed in more detail in Bommer and Stafford (2020) and was also taken in the knowledge that Stafford et al. (2022) had already obtained seismic parameter sets (and related components) that can be used as underlying 'host region' parameters in conjunction with CY14.

9.2.1.2 Host-region source and path characteristics

To perform the host-to-target adjustment, seismic parameters for the host GMPE must be estimated. Stafford et al. (2022) previously derived a set of seismic parameters that broadly replicate the predictions of the CY14 GMPE. Stafford et al. (2022) specify a loss function that measures the extent to which a set of seismic parameters, and other relevant RVT components, provide predictions of response spectral ordinates that match those of the CY14 GMPE. The seismic parameters fix the site scaling to be equal to the results from Al Atik and Abrahamson (2021) and use functional components for the source and path scaling that are designed to mimic the functional terms of the CY14 GMPE. The general performance of the Stafford et al. (2022) inversion results can be seen in Figure 9-6 (for magnitude scaling) and Figure 9-7 (for distance scaling).

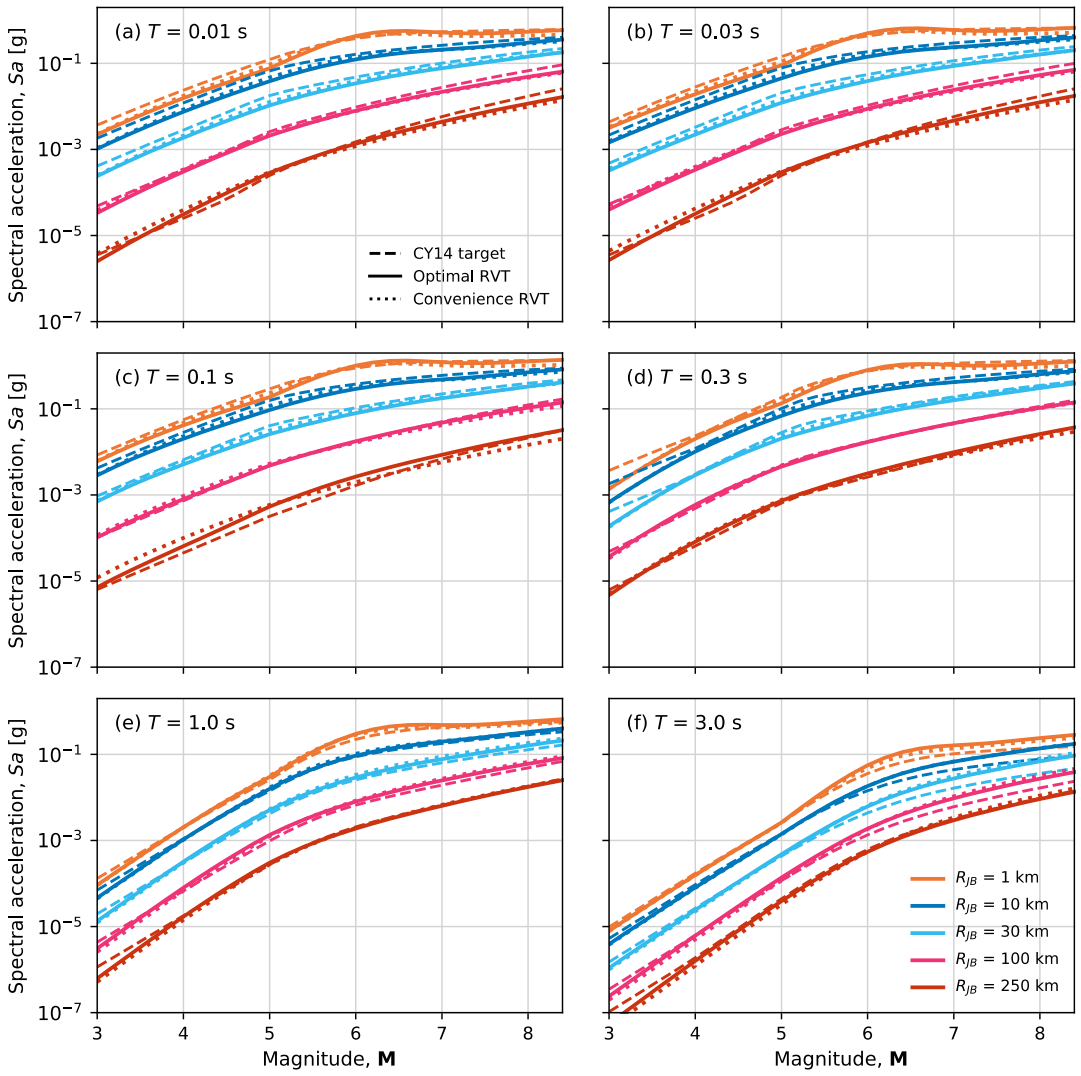

Figure 9-6. Comparison of the predictions of Chiou and Youngs (2014), dashed line, and the RVT-based predictions of Stafford et al. (2022) for two of the parameter sets they derive with respect to magnitude. The solid lines correspond to the 'optimal' parameter sets obtained by those authors, and used for the present study, while the dotted lines correspond to the 'convenience' parameter sets (the convenience parameter set corresponds to a FAS parameterisation that is entirely consistent with the model presented in Boore, 2003). Each panel corresponds to the response period annotated in the upper left of the panel, and the coloured lines correspond to the distances specified in the legend of panel (f). From Stafford et al. (2022).

While the results shown in Figure 9-6 and Figure 9-7 indicate that the seismic parameter sets found by Stafford et al. (2022) do not perfectly reproduce the CY14 predictions, it is clear that for a very broad range of magnitudes, distances, and response periods, the agreement is good. Furthermore, the agreement shown in these figures is far superior to what would be obtained if representative 'host region' parameters were simply adopted from the literature, as suggested within the original HEM framework of Campbell (2003).

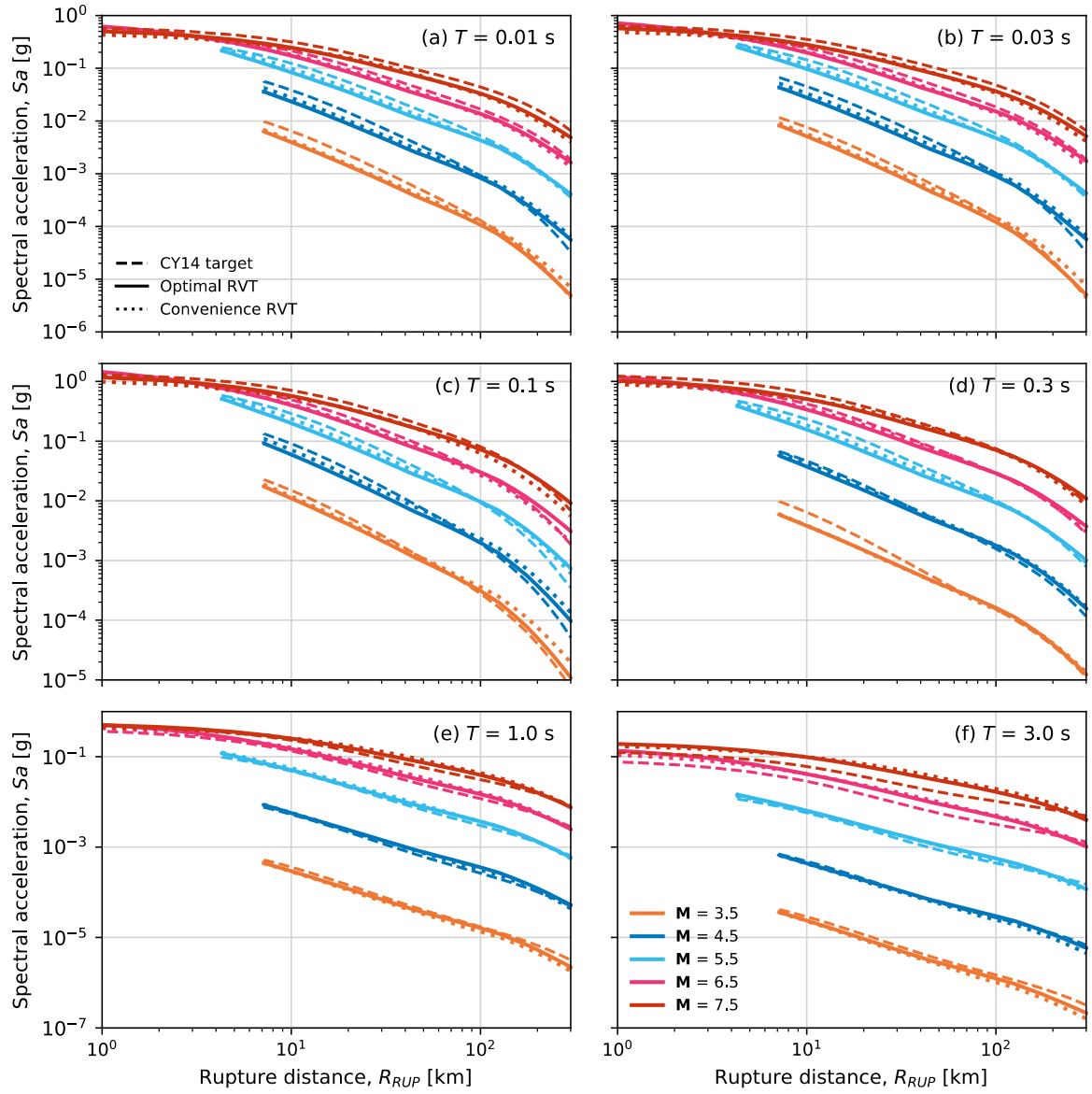

Figure 9-7. Comparison of the predictions of Chiou and Youngs (2014), dashed line, and the RVT-based predictions of Stafford et al. (2022) for two of the parameter sets they derive with respect to distance. The solid lines correspond to the 'optimal' parameter sets obtained by those authors, and used for the present study, while the dotted lines correspond to the 'convenience' parameter sets. Each panel corresponds to the response period annotated in the upper right of the panel, and the coloured lines correspond to the magnitudes specified in the legend of panel (f). From Stafford et al. (2022).

The purpose of the article of Stafford et al. (2022) was to enable studies like the present project to adopt their parameter sets instead of attempting to invert the CY14 GMPE themselves. The parameter sets are therefore ready to use as published to represent the host model. The necessary components that remained to be specified for the target region are a model for stress parameter, the geometric spreading function (including near-source saturation effects), and the anelastic attenuation model, because the site response scaling is fixed to the results from Al Atik and Abrahamson (2021) for an average shear-wave velocity of 760 m/s.

For the stress parameter, Stafford et al. (2022) found the function in Equation 9-4 that includes dependence upon both $\boldsymbol{M}$, and the relative depth to the top of rupture (ΔZ_{TOR}):

9-4

$$\ln \Delta\sigma(\boldsymbol{M}, \Delta Z_{TOR}) = s_\alpha + s_\beta \min(\boldsymbol{M} - 5, 0) + \left(s_\gamma + s_\delta \operatorname{sech}[2 \max(\boldsymbol{M} - 4.5, 0)]\right)\Delta Z_{TOR}$$

The coefficients s_α, s_β, s_γ and s_δ are provided in Table 9-3, along with the other coefficients of the model yet to be defined.

Table 9-3. Estimates and standard errors of the optimal FAS parameters found by Stafford et al. (2022) to represent the Chiou and Youngs (2014) GMPE.

Parameter	Estimate	Standard error
s_α	2.296	0.031
s_β	0.4624	0.0311
s_γ	0.0453	0.0136
s_δ	0.109	0.0166
γ_1	1.1611	0.00601
h_α	-0.8712	0.373
h_β	0.4451	0.0474
h_γ	1.1513	0.0
h_δ	5.0948	0.725
h_ε	7.2725	0.0566
Q_0	205.4	5.53
η_α	0.6884	0.0131
η_β	0.1354	0.00654
η_γ	5.1278	0.0794

The geometric spreading function is defined by Equation 9-5:

9-5

$$\ln g(R_{PS}, R_{RUP}) = -\gamma_1 \ln(R_{PS}) + \frac{(\gamma_1 - \gamma_f)}{2} \ln\left(\frac{R_{RUP}^2 + r_t^2}{r_0^2 + r_t^2}\right)$$

with the equivalent point source distance (R_{PS}) defined in terms of the rupture distance (R_{RUP}) and the near-source saturation distance ($h[\boldsymbol{M}]$) according to Equation 9-6:

9-6

$$R_{PS} = R_{RUP} + h(\boldsymbol{M})$$

The near-source saturation distance is then defined using Equation 9-7:

9-7

$$\ln \boldsymbol{h}(\boldsymbol{M}) = \boldsymbol{h_\alpha} + \boldsymbol{h_\beta M} + \frac{\boldsymbol{h_\beta} - \boldsymbol{h_\gamma}}{\boldsymbol{h_\delta}} \ln\left[1 + \boldsymbol{e}^{-\boldsymbol{h_\delta}(\boldsymbol{M}-\boldsymbol{h_\varepsilon})}\right]$$

Finally, the anelastic attenuation filter is defined as $Q(f) = Q_0 f^{\eta(\boldsymbol{M})}$. The quality factor Q_0 is provided in Table 9-3, and the magnitude-dependent quality exponent $\eta(\boldsymbol{M})$ is defined in Equation 9-8.

9-8

$$\eta(\boldsymbol{M}) = \eta_\alpha + \eta_\beta \tanh\left(\boldsymbol{M} - \eta_\gamma\right)$$

All coefficients for this model are presented in Table 9-3. In addition to the coefficients in Table 9-3, the prediction of response spectral ordinates requires models for excitation and root-mean-square durations, as well as a model for the peak factor (the ratio of the peak to root-mean-square oscillator response). Stafford et al. (2022) specify that the recommendations of Boore and Thompson (2015) should be followed for these components, i.e. the excitation duration uses the reciprocal of the corner frequency for the source duration combined with the path duration model of Boore and Thompson (2014, 2015), and the root-mean-square duration uses the factors from Boore and Thompson (2015). The peak factor model uses the Der Kiureghian (1980) modification of the Vanmarcke (1975) formulation.

9.2.2 Target-region source and path characteristics

For the target 'region,' the host-to-target adjustment approach requires seismic parameters consistent with the point-source stochastic model that describe the source and path characteristics of the rupture scenarios that are relevant for the Duynefontyn site. These are then used as the target parameters for adjustments to the CY14 GMPE. Two approaches were considered by the GMM TI Team for estimating the target parameters.

The first approach identifies the target parameters directly from FAS of ground-motion recordings, and the target parameters are obtained using an inversion over a dataset of relevant recordings. Making inferences about how the seismic parameters influence response spectral ordinates requires either assumptions about the equivalence of the scaling in the Fourier and response spectral domains or the specification of additional model components to allow the computation of response spectral ordinates from the Fourier parameters. A drawback of this approach is that it does not necessarily need to consider how the seismic parameters are linked to corresponding response spectral ordinates, and, in principle, do not even need to look at the response spectra. This can lead to a misfit with the response spectra in application.

An alternative approach is to mirror the method used by Stafford et al. (2022) to invert the CY14 GMPE, but instead invert the response spectral ordinates computed from the empirical data rather than the predicted response spectral ordinates from the GMPE. With this approach, each model component related to the full RVT framework is specified from the outset and response spectral ordinates are inverted directly to find the seismic parameters that act together with the RVT components.

Proponent experts advocated for each of the described approaches at Workshop 2. Professors Andreas Rietbrock and Ben Edwards advocated for the Fourier approach, while Professor Peter Stafford advocated for the response spectral approach. The GMM TI Team decided to adopt both approaches to obtain multiple estimates of the target parameters that collectively define the best estimates of these parameters and to gain insight regarding the epistemic uncertainty in these target parameter sets. To obtain results for both approaches, the GMM TI Team followed the response spectral approach to develop target parameters, and a specialty contractor (Prof. Edwards) was contracted by the CGS to follow the Fourier approach to develop target parameters.

Datasets compiled for the target region inversions ideally have significant overlap with the rupture scenarios of interest for the hazard calculations. In areas of low seismicity like this project, the empirical data is heavily dominated by recordings of relatively small-magnitude events, many of which occur at significant distances from the target site. As a result, the seismic parameters obtained from inverting the empirical data, regardless of the approach adopted, may not be directly comparable with those from Stafford et al. (2022) given that the latter parameters are obtained for a very different range of rupture scenarios. This introduces epistemic uncertainty into the process that needs to be accounted for.

Another key challenge when performing inversions of the available empirical data is to understand the extent to which the dataset meets the ideal requirements for the project and how seismic parameter estimates from the rupture scenarios represented in the dataset can be mapped to the rupture scenarios of interest. Figure 9-8 shows the complete set of records available for inversion and demonstrates that many of the records in the inversion database are from earthquakes hundreds of kilometres from the target site, and that very few events are located within the host seismic zone that dominates the preliminary seismic hazard calculations. This also introduces epistemic uncertainty into the process that needs to be accounted for (see further discussion in Section 9.2.6.1). The actual subsets used by these analysts will be presented later in this section in terms of magnitude-distance distributions, but the magnitude-distance distribution of the events in Figure 9-8 is shown in Figure 9-9.

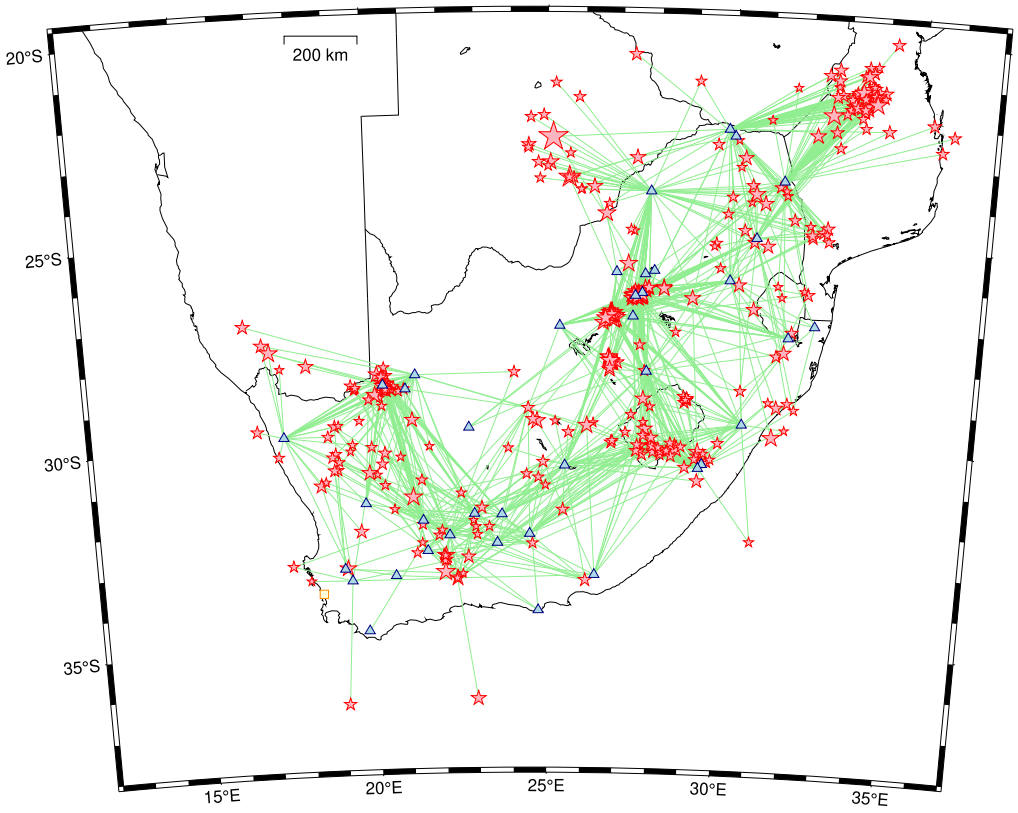

Figure 9-8. Ray-path coverage from the empirical database compiled for target region inversions. Red stars indicate earthquake events, blue triangles show recording stations, and light green lines between events and stations relate to individual accelerograms.

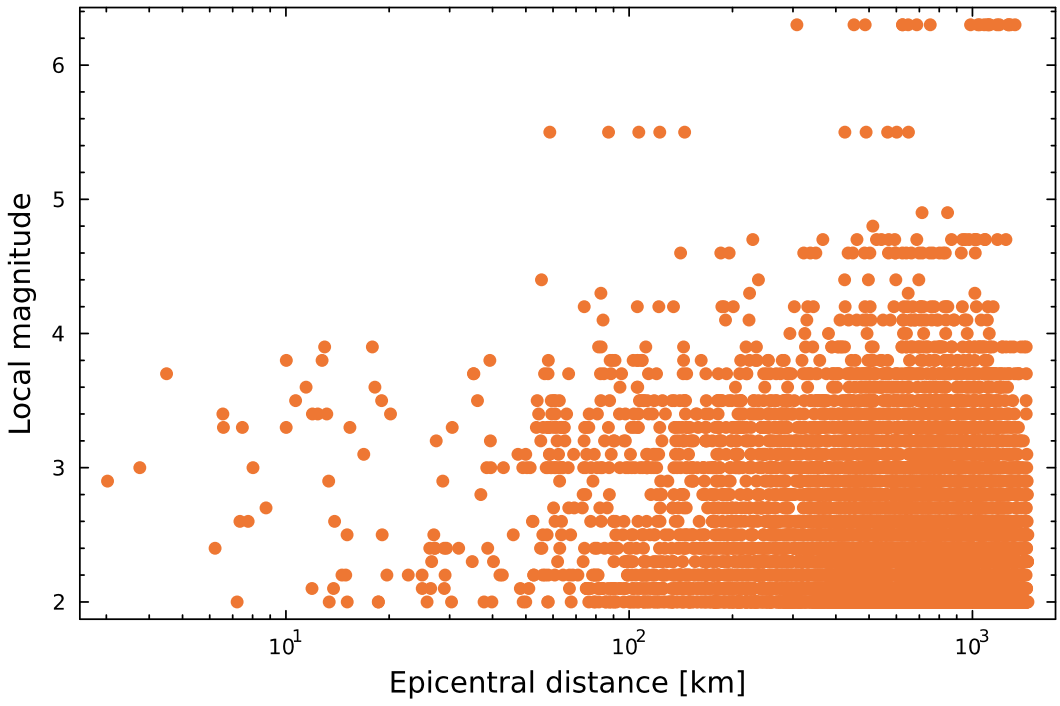

Figure 9-9. Magnitude-distance distribution of the empirical database compiled for target region inversions. The points shown in this figure relate to the ray paths shown in Figure 9-8.

The GMM TI Team and Prof. Edwards used the same initial database, called the Inversion Ground-motion Database (GMDB) including processed waveforms, computed Fourier spectra (of both assumed signal and noise), computed response spectra, and associated metadata (Section 7.3.2). Each analyst selected a subset of the Inversion GMDB as deemed appropriate for their inversions, and the differences in the selected datasets are considered to reflect the epistemic uncertainty. Differences between the datasets can arise because different records are deemed useable for each of the two inversion approaches. For example, issues with high-frequency noise contaminating the Fourier amplitude spectra may not pose significant problems for estimating short-period response spectral ordinates (Douglas and Boore, 2011).

Within each inversion approach, alternative parameter suites were obtained depending on the assumptions made during the inversion process, and the parameterisation of the point-source stochastic model. For example, the first step in the inversion approach of Edwards was to estimate κ, a parameter characterising the high-frequency spectral shape for each recording. In this step, alternative assumptions about which frequency range to consider, the location of the source corner frequencies, what smoothing to apply to the FAS, what signal-to-noise ratio to adopt, and whether to use linear- or log-spaced frequencies, all influenced the parameter estimates that were obtained, and consequently influenced the downstream estimates of other FAS parameters. For most of these decisions, there is no 'correct' option but rather the analyst must often make compromises about what they might ideally like to do vs what the available data allow them to do. Or the analyst simply must decide to adopt a set of justifiable criteria and then proceed on that basis.

Similar issues are encountered with the GMM TI Team approach. For example, there is no one-to-one mapping between the Fourier spectral ordinate at a frequency equal to a given oscillator frequency and the response spectral ordinate at the same oscillator frequency (Bora et al., 2016). Rather, there is a many-to-one relationship whereby multiple frequencies in the Fourier domain contribute to a single ordinate in the response spectral domain. When inverting the response spectra, the GMM TI Team specified a particular set of periods for performing the inversions and this imposed some implicit weighting on the underlying Fourier spectral ordinates. This, in turn, affected the relative influence that different FAS parameters had within the inversion, meaning that the use of a different set of periods could impact the FAS parameter estimates that are found from the GMM TI Team inversions.

The overall inversion problem is non-unique, so constraints are imposed upon model components that lead to alternative parameter sets. The non-uniqueness arises because different parameters can influence response spectral ordinates for the same scenarios, e.g., both the stress parameter and kappa exert a strong influence upon the amplitude of high-frequency FAS ordinates. For small-magnitude scenarios it is difficult to decouple the effect of these parameters and many combinations can give a similar match to observed spectra. It is important to note that when these alternative parameter combinations are used for predicting motions from larger magnitude scenarios the predictions can vary considerably. The constraints that are imposed can be in terms of the parameter values, as in the GMM TI Team approach, or in terms of the inversion stages, as in the Edwards approach. In either case, the alternative parameter sets can each describe the empirical data in a similar manner. Since the objective is to identify parameters that reflect the underlying properties of response spectral ordinates in the target region, rather than the specific details of the compiled database, one cannot assert which of the alternative sets is unambiguously superior. The consequence is

that Edwards and the GMM TI Team each provided multiple sets of seismic parameters that were considered as part of the evaluation process, with the expectation that the alternative parameter sets collectively led to response spectral predictions that represent the CBR of the TDI.

Upon obtaining seismic parameters for the target region, the GMM TI Team compared these (or the response spectral predictions associated with these parameters) with the parameters and predictions of CY14 in order to identify whether adjustments need to be made to the CY14 model (as explained in Section 9.2.2.1). Where adjustments are deemed necessary, the objective is to modify the CY14 predictions to centre them for the target site and to define the backbone of the distribution for all rupture scenarios of interest.

The following section first describes some common challenges that are relevant for both the Fourier and response spectral inversions, and subsequent sections then detail the approaches applied and results found by Edwards and the GMM TI Team.

In summary, seven sets of FAS parameters and the associated components for RVT computations arise from the inversions of the Inversion GMDB. Three of these models come from Edward's Fourier-based inversions with parameters presented in Section 9.2.2.2, and four of the models come from the GMM TI Team response spectral-based inversions with parameters presented in Section 9.2.2.3. The GMM TI Team developed seven sets of adjustments to the CY14 model from the seven FAS parameter sets (Section 9.2.2.4).

9.2.2.1 Common challenges related to site response

Both Edwards and the GMM TI Team needed to constrain how site effects were considered because the metadata provided to the analysts had extremely limited information regarding the site characteristics. The GMM TI Team assigned each site an approximate shear-wave velocity over the top 30 m (V_{S30}) values using slope topographic proxies for either active crustal or stable crustal regions, giving each site an estimated value of V_{S30} that could potentially be taken into consideration within the inversions. This was done with the caveat that the slope-topographic proxies that were used are not calibrated for South African conditions. The team also had four stations — Grahamstown (GRHM), Matjiesfontein (MATJ), Elim (ELIM), and Ceres (CER) — that had a velocity profile for the top tens of metres and had recorded earthquakes. Even though none of these profiles was sufficiently deep to permit the calculation of an impedance function over the full frequency range of interest, they did have sufficient depth to compute a site-specific value for V_{S30}. Table 9-4 provides a comparison of the estimated and computed values of V_{S30} for these stations. The two proxies used, utilize topography to estimate the V_{s30} with two different relationships: active and stable regions. The table shows that the values computed from the velocity profiles do not fall within the predicted active proxy ranges, but three of the four are close to the predicted range. The stable proxy relationship results in two stations, GRHM and MATJ, having predictions that technically include the computed value, but this is partly a reflection of the limited resolution of the predicted ranges for the stiffer sites. It is clear from Table 9-4 that even with data for four stations, the proxy V_{S30} values have a limited correlation with computed equivalents. Differences do not appear to be systematic, and while the proxy for active regions has better resolution in the sense that it does not predict the same site classification for all four sites, it can also provide grossly inaccurate predictions. An example of this being the very stiff GRHM station falsely predicted to be the softest site.

Table 9-4. Computed and estimated V_{S30} values for stations with measured profiles and some recordings. Note that 'total records' in this table relate to the records shown in Figure 9-8, not to the number of records actually used by Edwards and the GMM TI Team in their inversions (many of the records reported in this table relate to events recorded at very large distances).

Station Code	Total Records	Max. Profile Depth [m]	Computed V_{S30} [m/s]	Active Proxy V_{S30} [m/s]	Stable Proxy V_{S30} [m/s]
GRHM	308	41	1652	360-490	>760
MATJ	338	96	766	620-760	>760
ELIM	64	42	634	490-620	>760
CER	346	104	455	490-620	>760

The inversions for the seismic parameters aim to identify the source and path characteristics of the rupture scenarios that are important for the Duynefontyn site. The GMM TI Team models the site response for a very-deep velocity profile within this project. The obtained source and path properties from the Fourier and response spectral inversions should also relate to crustal properties at the deepest point in the velocity profile used for the site response. Edwards and the GMM TI Team used spectra computed from surface recordings and therefore need to account for any site effects existing in the empirical data. Edwards and the GMM TI Team took different approaches to account for site effects in the records.

Edwards does not explicitly account for frequency-dependent site effects[3], but rather assumes that the combined effect of site impedance and damping are reflected in his computed κ values that are found within the first stage of his inversions. This process is illustrated in Figure 9-10.

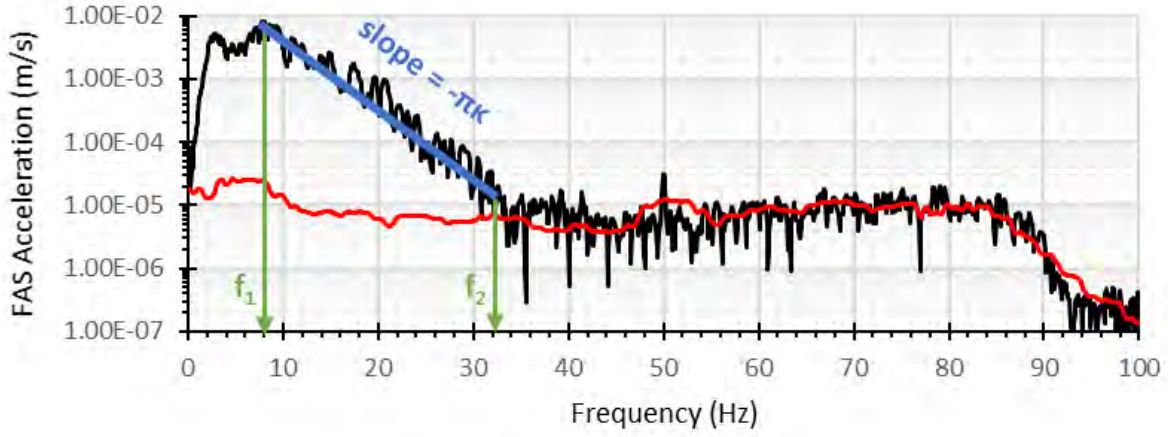

Figure 9-10. Example of high-frequency slope estimation used by Edwards. The black line shows the FAS of a record, the red line shows the FAS of the pre-event noise. Frequency limits that define the frequency range used to fit the blue linear trend line are denoted by f_1 and f_2. From Edwards (2023).

[3] When computing moment magnitudes from signal moments Edwards does obtain an estimate of the average site amplification for each site over all frequencies. This amplification is relative to the unknown network average site response—which is assumed to relate to some stiff rock condition.

Edwards first obtains an estimate of the high-frequency slope for each recording, and these lead to zero-distance κ_0 estimates for each station (the average $\delta\kappa$ – which is the slope of the κ versus distance line -- over all records is found along with station-specific intercepts are identified). As these slopes were computed directly from the recorded FAS, the estimates implicitly include the effects of both impedance and damping. In subsequent inversion steps, he then assumed that site effects had been addressed. Following this assumption, the stress parameter and geometric spreading will relate to some network-averaged site condition that Edwards assumes will correspond to some generic stiff rock site with essentially zero impedance effects. That underlying profile is not explicitly known. Edwards also recognises that most seismograph stations are likely to be located on hard/stiff rock sites as a routine matter of site selection during installation. For this reason, the effects of site impedance were assumed to be relatively minor. Following his inversions, Edwards also computed average station residuals for each station to look for any atypical behaviour.

The GMM TI Team made use of the provided V_{S30} proxies in order to make a nominal correction of all data to some common reference condition. As shown in Table 9-4, these proxies have limitations, but it is assumed that, on average and over all sites, they will be able to add some information. Both active crustal and stable crustal relations were considered, and the active crustal relations were adopted. This decision was not informed by the results of Table 9-4. Rather, the GMM TI Team first assumed that the estimated V_{S30} values were correct, and then used the site response scaling within the CY14 GMM to correct response spectral amplitudes to a reference condition of V_{S30} = 760 m/s, via Equation 9-9:

9-9

$$SA_{reference} = SA_{computed} \times \frac{SAF(V_{S30} = 760)}{SAF(V_{S30})}$$

in which $SAF(V_{S30})$ represents the site adjustment factor of CY14 for a given average shear-wave velocity value. After making that correction, referenced empirical regression analyses were performed on the corrected response spectral ordinates, and the GMM TI Team looked at the residuals from these regressions against the average shear-wave velocity values implied from the proxy relations. Figure 9-11 shows the residuals for the active crustal topographic proxy. If the proxy relationship was systematically biased, or if the site adjustment factors in the CY14 GMPE were grossly inappropriate for use in South Africa, then the process of applying Equation 9-9 would lead to trends in the residuals. Figure 9-11 shows that when a given site class has a reasonable amount of data, the mean residuals in each class are close to being unbiased.

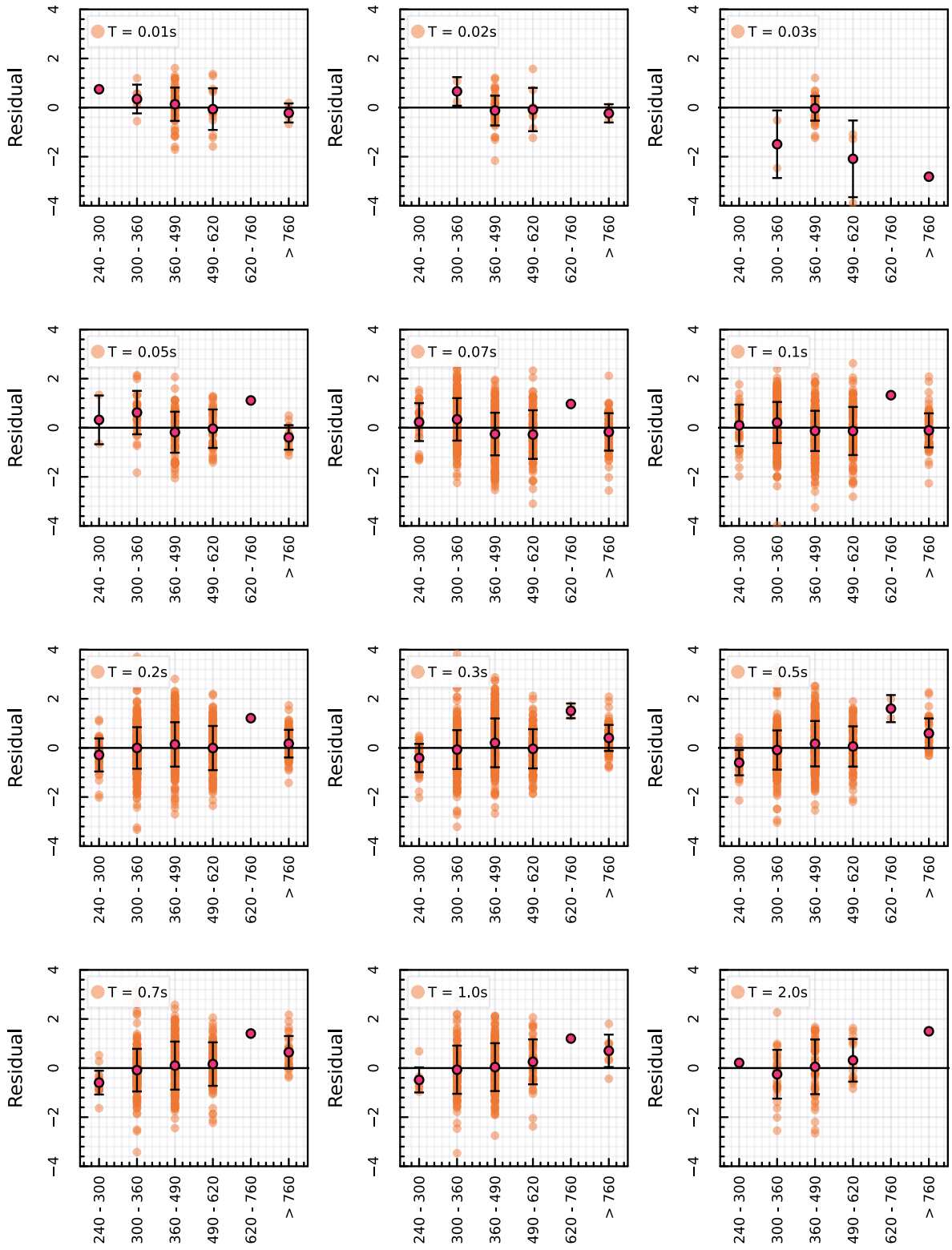

Figure 9-11. Residuals, Δ, of reference-corrected spectral amplitudes against proxy-based site classification. The residuals shown here were obtained by the GMM TI Team from referenced-empirical corrections to the South African data – with a constant amplitude offset and a distance scaling correction, *i.e.* $\Delta = \beta_0 + \beta_1 R_{RUP}$, and $\Delta = \ln SA_{reference} - \ln SA_{CY}$, with the latter being the predictions of CY14.

On this basis, the GMM TI Team used Equation 9-9 to make corrections to a reference V_{S30} of 760 m/s for most of the inversions, but also used a slight modification of the same equation to consider a stiffer reference site condition of 1130 m/s corresponding to the case where the CY14 GMPE effectively predicts no site response. That is, if one increased the V_{S30} to higher values, the predictions of the CY14 GMPE would not change. Hence, predictions for 1130 m/s are equivalent to predictions for source level velocities. Once all motions were adjusted to a common reference site condition, and the general validity of the CY14 site response scaling was observed, it was consequently assumed by the GMM TI Team that the implicit crustal profile within the CY14 GMPE was reasonable to represent impedance effects over the South African network. These impedance effects were adopted from the inversions of Al Atik and Abrahamson (2021).

Ideally, complete crustal profiles would be known for every recording station in the Inversion GMDB. The expected effects of impedance could then be identified and used to adjust the observed surface recordings to amplitudes that are representative of crustal depths, and the inversions on these site-corrected recordings would enable more accurate estimates of the crustal source and path scaling in South Africa to be made. For this project, the approaches of Edwards and the GMM TI Team represent different attempts to infer source and path scaling properties using the limited information that is available. The differences between the two approaches have an impact on the estimated target seismic parameters and contribute to the overall estimate of epistemic uncertainty.

The inversions of Edwards and the GMM TI Team both require either the specification or estimation of a network average κ_0 value along with the source and path parameters. The source is represented either by a best estimate of the stress parameter for the available dataset or by parameters of a magnitude-dependent stress parameter function. The path scaling involves a geometric spreading function and parameters of an anelastic attenuation filter. The parameters are statistically correlated because certain parameters have a similar impact on the Fourier spectral shape in the frequency range where the signal is visible. A particularly strong trade-off exists between κ_0 and the stress parameter $\Delta\sigma$, but the κ_0 is only estimated in this study for the purpose of isolating other seismic parameters related to source and path scaling. This is potentially problematic as different assumptions or estimates related to κ_0 will influence the estimate of $\Delta\sigma$, but we are ultimately only interested in the $\Delta\sigma$ values going forward.

9.2.2.2 Summary of Edwards' Fourier spectral inversions

Edwards submitted a report to the CGS detailing his inversions and presented to the GMM TI Team at Workshop 2 (Edwards 2022, 2023). This section provides a summary of the Edwards inversions with the pertinent information regarding the GMM TI Team evaluation and integration of his inversions. In particular, it is important to note the differences between the Edwards and GMM TI Team inversions as they contribute to the GMM TI Team assessment of model-to-model epistemic uncertainty.

From the Inversion GMDB, Edwards selected a subset to use for his inversions based upon visual inspection of the processed noise and signal waveforms and their Fourier spectra. He inspected the usable frequency limits provided within the metadata for the ground-motion database and concluded that these were reasonable. He took the processed records and FAS provided, and worked with these for his inversions. Figure 9-12 shows the records selected

by Edwards in the context of the complete set of records provided for consideration. The figure shows that the majority of records within 300 km of a site were selected, but that some records within this distance range were discarded due to concerns regarding their quality. Figure 9-13 then shows a refined view of the magnitude-distance distribution of the data finally selected by Edwards. The maximum considered distance is limited to 300 km, and this is reflects a modelling decision of Edwards to focus upon the data assumed to be of greatest relevance for the hazard and also appreciating that the assumptions he makes regarding path scaling start to break down at greater distances (i.e., anelastic attenuation terms do not continue to scale linearly with distance).

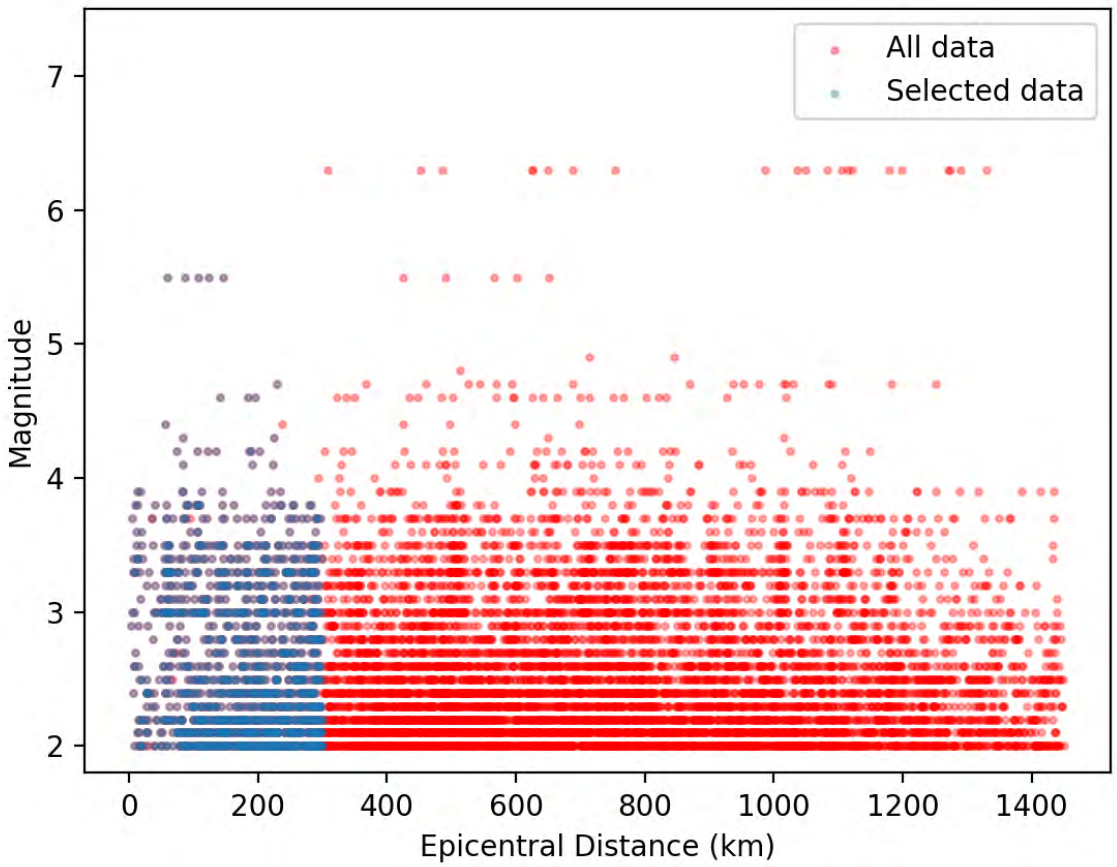

Figure 9-12. Magnitude-distance distribution of the complete database provided to Edwards and the GMM TI Team for their inversions along with the subset selected by Edwards. From Edwards (2023).

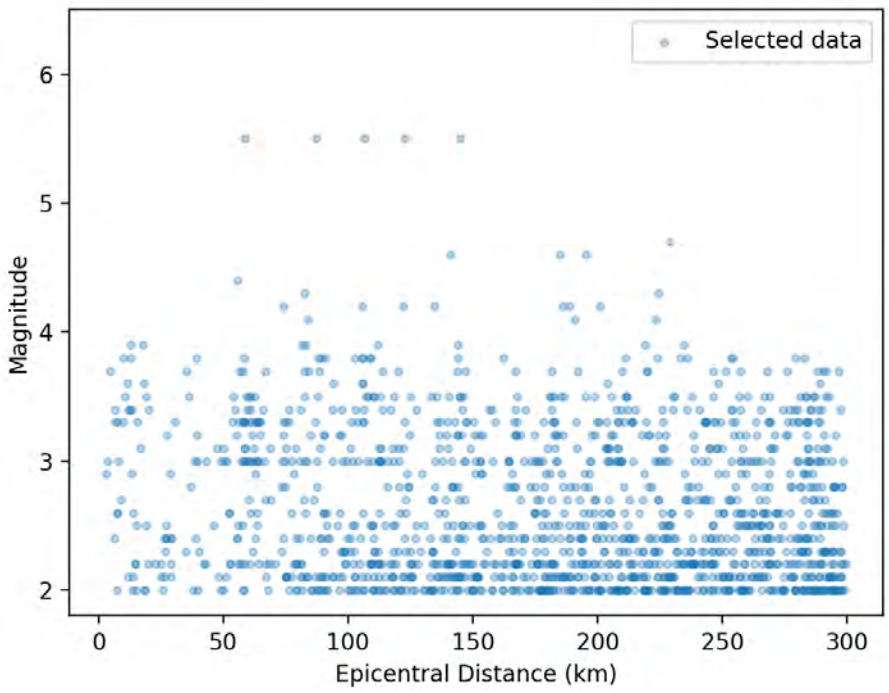

Figure 9-13. Magnitude-distance distribution of the selected records used by Edwards in his FAS inversions. From Edwards (2023).

Note that while Figure 9-13 shows the complete set of records used by Edwards, not all of the records shown in this figure were considered at every step in his inversions. As will be discussed in what follows, Edwards adopts a multi-stage approach to his inversions. In some stages he was primarily interested in behaviour at high frequencies, and this limits which records can be used in those stages. In other stages his focus was upon relatively near-source recordings and so the distance range was restricted to maximum values lower than 300 km maximum used to obtain the initial subset. Figure 9-13 shows the maximum amount of constraint in terms of magnitude-distance space that is available from the subset of records selected by Edwards.

Edwards performed Fourier-based inversions in two distinct phases of the project. In the initial phase, performed prior to the hazard sensitivity analyses being conducted, Edwards focussed exclusively on the scaling of Fourier spectral ordinates without considering the response spectral amplitudes that the obtained sets implied. Those initial inversions gave rise to the best estimates of the stress parameter, geometric spreading, anelastic attenuation, and site kappa for the Inversion GMDB. Both the GMM TI Team and Edwards found that the seismic parameters he had obtained during this initial phase led to a systematic underprediction of response spectral amplitudes by more than a factor of two. This bias was identified by the GMM TI Team when they looked to map the seismic parameter sets into response spectral predictions within the RVT framework. That process required a set of duration and peak factor models to be selected that could have been partly responsible for the observed bias. Once alerted to the problem, Edwards performed his own response spectral computations using a different set of duration and peak factor models and found an even greater bias.

To address this problem, in the second phase of his inversions, Edwards allowed certain seismic parameters ($\Delta\sigma$ and κ_0) to vary from the optimal values identified in his initial inversions. Alternative sets of $\Delta\sigma$ and κ_0 pairs were proposed to centre the overall parameter

sets in the Inversion GMDB. In this phase, the geometric spreading and anelastic attenuation scaling were held fixed at the values previously found in the FAS-only inversions, with the anelastic spreading having only a weak contribution in the Edwards parameters sets since Q_0 is estimated to be very high.

Table 9-5 summarises the Edwards results across two phases of investigation. The column 'FAS inversions' shows the results from the initial phase focusing exclusively on the computed Fourier amplitude spectra, while the column 'PSA calibration' shows the results following the second phase where a calibration was made against the response spectral data. The latter column also provides details about the elements of the RVT procedure that are required to predict response spectral ordinates from the FAS parameters.

Table 9-5. FAS parameter sets obtained by Edwards. Note that for the PSA calibration column, the three values of stress parameter are paired with the three values of site kappa (in the order shown). Items marked with an asterisk (*) signify model components that were fixed in the inversions.

Parameter	FAS inversions	PSA calibration
Magnitude scaling	$\boldsymbol{M} \equiv M_L$ $(M_L \geq 2.5)$	$\boldsymbol{M} \equiv M_L$ $(M_L \geq 2.5)$*
Stress parameter $\Delta\sigma$ [bar]	21 $(\sigma_{\log_{10}\Delta\sigma} = 0.59)$	15, 30, 60
Source velocity β_S [km/s]	3.5*	3.5*
Geometric spreading model $\{R_{ref}, \gamma\}$	$\gamma = 1.0$ $R_{hyp} < 10$ $\gamma = 1.06$ $10 \leq R_{hyp} < 60$ $\gamma = 0.670$ $60 \leq R_{hyp} < 150$ $\gamma = 0.905$ $R_{hyp} \geq 150$	$\gamma = 1.0$ $R_{hyp} < 10$ $\gamma = 1.06$ $10 \leq R_{hyp} < 60$ * $\gamma = 0.670$ $60 \leq R_{hyp} < 150$ $\gamma = 0.905$ $R_{hyp} \geq 150$
Quality Factor Q_0	3314	3314*
Site kappa κ_0 [s]	0.015	0.01, 0.02, 0.03
Site amplification	Assumed equal to unity	Boore et al. (2014) @ V_{S30} of 760 m/s
Excitation duration	NA	$D_{ex} = 1/f_c + 0.13\, R_{hypo}$
RMS duration	NA	Liu & Pezeshk (1999)
Peak factor	NA	Cartwright & Longuet-Higgins (1956)

Edwards obtained the results in Table 9-5 using a multi-stage process. In the first step, the high-frequency spectral shape of each record was parameterised in terms of the Fourier acceleration spectra, $|A(f)|$, using:

9-10

$$\ln|A(f)| = A_0 - \pi\kappa f$$

over a frequency range that was assumed to span from some point above the source corner frequency of an assumed ω^2 spectrum, f_{lo}, to an upper frequency constrained by the signal-to-noise ratio, f_{hi} (as previously depicted in Figure 9-10 as $f_1 = f_{lo}$ and $f_2 = f_{hi}$). In Equation

9-10, the offset A_0 was of no interest for the initial phase, and only the parameter κ was retained. This model assumes that the logarithmic FAS ordinates will scale linearly with frequency over a particular frequency range. The general model for FAS can be expressed as:

9-11

$$|A(f)| = \frac{\mathbb{C}M_0 f^2}{1 + (f/f_c)^2} g(R) \exp\left[-\frac{\pi f R}{Q(f) c_Q}\right] S(f) \exp(-\pi \kappa_0 f)$$

with $\mathbb{C}$ encapsulating physical and geometric parameters related to the source and domain boundaries, M_0 being the seismic moment, f_c being the source corner frequency, $g(R)$ being the geometric spreading function, where R is usually an equivalent point-source distance metric (like hypocentral distance, or the so-called 'equivalent point-source distance'), $Q(f)$ being the quality factor, c_Q being a velocity used to estimate $Q(f)$, $S(f)$ representing the site impedance relative to the source properties encapsulated within $\mathbb{C}$, and κ_0 being the site kappa. Many of these terms were previously defined, but it is convenient to repeat these here.

Under the assumption that site impedance effects are either negligible or have been removed from observations, and further assuming that anelastic attenuation is frequency independent, i.e.,. $Q(f) = Q_0$, Equation 9-11 can be written as:

9-12

$$|A(f)| \propto A_0 \frac{f^2}{1 + (f/f_c)^2} \exp\left[-\pi \left(\frac{R}{Q_0 c_Q} + \kappa_0\right) f\right]$$

Furthermore, when $f \gg f_c$, the first fractional term tends to f_c^2 so that:

9-13

$$|A(f)| \propto A_0 f_c^2 \exp\left[-\pi \left(\frac{R}{Q_0 c_Q} + \kappa_0\right) f\right]$$

Taking the natural logarithm of both sides leads to:

9-14

$$\ln|A(f)| = A_0' - \pi \left(\frac{R}{Q_0 c_Q} + \kappa_0\right) f$$

Hence, Edwards first computes a value of k for each record. Given Equation 9-14, this parameter is equivalent to:

9-15

$$\kappa \equiv \frac{R}{Q_0 c_Q} + \kappa_0$$

Plotting estimates of κ from each record against distance and fitting a straight line to the data yields a slope equal to $\kappa \delta k = 1/(Q_0 c_Q)$ with an intercept at κ_0. Edwards adopted this framework in the first stage of his inversions.

This framework assumes $f \gg f_c$, so that the contribution to the spectral shape from the assumed omega-squared source spectrum is negligible. To address this requirement, Edwards assumed a stress parameter of 10 MPa and equivalence between local and moment magnitude to define the lower frequency to have values of $f_{lo} = \{15, 10, 5\}$ Hz for magnitudes of $M_L = \{2.75, 3.1, 3.7\}$, respectively. The implication is that the usable frequency range for estimating k is more limited for the smaller earthquake recordings than for larger earthquakes. The spectral decay of most records is estimated from a range that begins from 10-15 Hz, because the average magnitude of the selected dataset was around $M_L = 3$. Figure 9-14 shows that the influence of the corner frequency within the omega-squared spectrum is relatively broadband and is not localised around f_c.

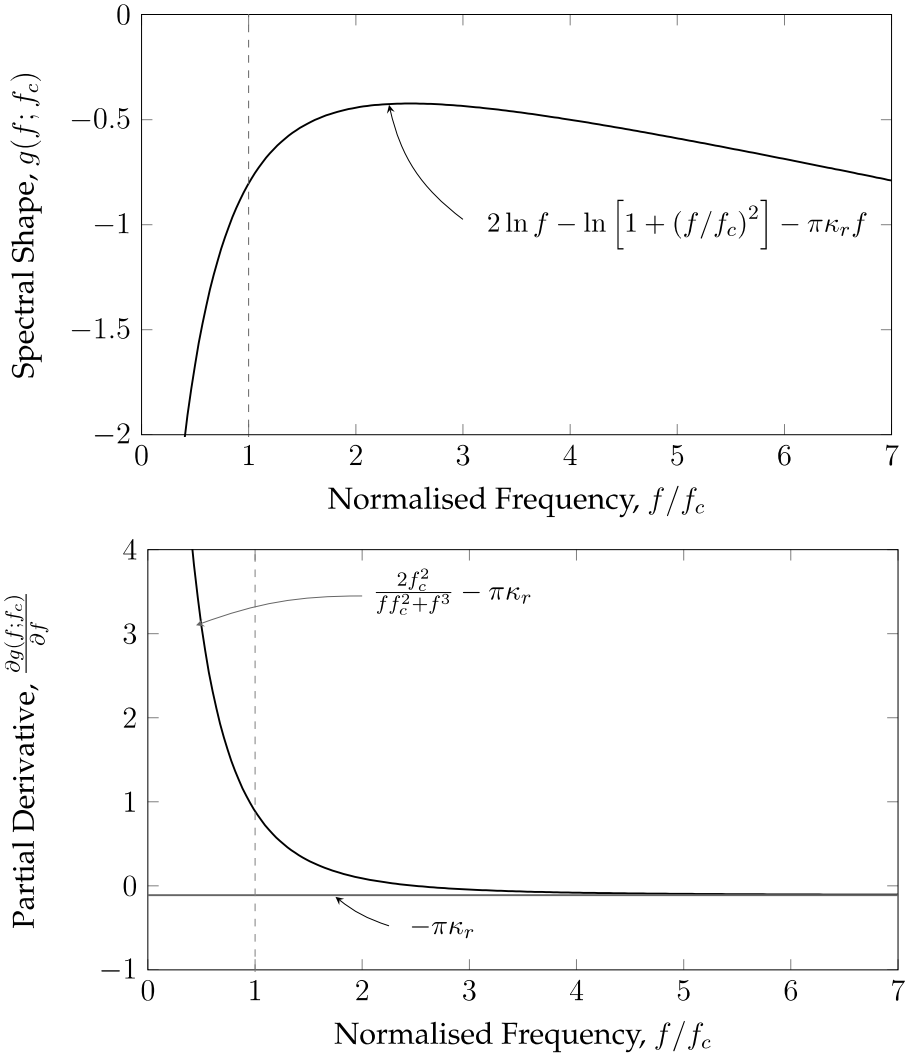

Figure 9-14. Shape of logarithmic Fourier amplitude spectrum against normalised frequency (upper panel) and its derivative with respect to frequency (lower panel), for a particular $k = 0.04$ s. The vertical dashed line identifies the relative position of the source corner frequency f_c. The function $g(f; f_c)$ is essentially the logarithm of Equation 9-12 with the constant term $\ln A_0$ omitted.

In subsequent inversion steps, as noted in Table 9-5, Edwards found an average stress parameter of 21 bars, which is much lower than the 100 bars used to define f_{lo}. For an average magnitude for the selected dataset of around $M_L = 3$, assuming 100 bar gives $f_c = 11.9$ Hz, while assuming 21 bar gives $f_c = 7$ Hz. The higher stress parameter initially adopted by

Edwards leads to values of f_{lo} that are conservatively higher than his best estimate f_c values (by a factor of around 1.7). Figure 9-14 shows that the source corner frequency should still influence estimates of k when adopting these values. This is a common problem in estimating high-frequency spectral shape from recordings of small-magnitude events, and there will always need to be some compromise between adhering to the theoretical framework and enabling a sufficient frequency range in order to obtain a stable slope k for each record.

Once a systematic approach to defining f_{lo} and f_{hi} has been adopted, this approach leads to as many estimates of k as there are records within the database. While Equation 9-15 suggests that a linear relationship should exist between k and distance, Edwards believes that different ray paths dominate the FAS over different distance ranges leading to estimates of Q_0 that vary with distance, and he uses the framework of Equation 9-15 to make estimates of κ_0 using two different distance ranges. Edwards considers a short distance range, with distances less than 150 km, and a longer distance range with distances out to 300 km. The shorter distance range is more consistent with the assumption of linearity in Equation 9-15 (a plot of kappa against distance shows a nonlinear trend as one considers greater distances, Edwards, 2023), but it also leads to a smaller dataset with far fewer records per station.

The estimates of κ_0 for the stations considered by Edwards are presented in Table 9-6, where the numbers of records reflect the longer distance range case that extends out to 300 km. This is the preferred distance given that the 300 km distance range incorporates 674 records, while the 150 km range leaves only 304 records. Also, the Lephepe (LEPH) station has 51 records for the 300 km distance and zero records once the restriction to 150 km is imposed. It should also be noted that the Edwards database incorporates only a small number of records recorded on stations with an associated velocity profile (Table 9-4).

For distances out to 300 km in the Edwards analysis, the average κ_0 value is 0.019 s, and it is 0.014 s for the closer distance range of 150 km. The corresponding average values of $\delta\kappa$ are $\delta\kappa = 2.25 \times 10^{-5}$ s/km for the 300 km, and $\delta\kappa = 8.62 \times 10^{-5}$ s/km for the 150 km distance ranges, but the values of $\delta\kappa$ are not retained. Rather, once the individual station κ_0 estimates for the < 150 km distance range are found, they are held fixed for each station, and a new broadband fit is made in order to re-estimate $\delta\kappa$ as well as corner frequencies, f_c, for each event and signal moments, Ω_0 (essentially the $\mathbb{C}M_0$ combination from Equation 9-11 combined with the average station amplification over all frequencies).

The values of $\delta\kappa$ above are found from high-frequency fitting with linear frequency spacing, but the re-computed broadband fits are made using a logarithmic frequency spacing that aims to give similar weighting to the spectrum over the log-frequency space. The broadband fitting leads to a new $\delta\kappa 102 = 8.62 \times 10^{-54}$ s/km. For a crustal velocity of 3.5 km/s, this corresponds to $Q_0 = 3314$. It also yields corner frequencies that are used to estimate the stress parameter and the signal moments that are used to infer the magnitude scaling relation as well as the geometric spreading function. Examples of the broadband fits that are made are shown in Figure 9-15.

Table 9-6. Estimates of κ_0 for individual stations from the inversions of Edwards. 'Nrec' is the number of records. Entries in the rightmost column of '—' represent stations that have no recordings within 150 km of events.

Station	R < 300 km			R < 150 km
	κ_0 (s)	Error (s)	Nrec	κ_0 (s)
AUGR	0.001148	0.003975	8	0.001262
BFON	0.019702	0.004590	6	0.007107
BRAK	0.031396	0.004590	6	0.024689
BUFB	0.016320	0.005622	4	--
CER	0.016573	0.003555	10	0.007948
CRLN	0.016313	0.001544	53	0.015336
CVNA	0.025231	0.007950	2	0.017332
ELIM	-0.006112	0.007950	2	--
FRAZ	0.024522	0.004590	6	--
GRAF	0.023927	0.004590	6	--
GRAN	0.027555	0.003118	13	0.022938
GRHM	0.009981	0.007950	2	0.008036
HRAO	0.019318	0.001205	87	0.014051
HVD	0.024195	0.002903	15	0.014190
KEIM	0.001925	0.004590	6	-0.001637
KLOF	0.040899	0.002811	16	0.038338
KOMG	0.015109	0.002811	16	0.003289
KSD	0.015629	0.003975	8	0.009729
KSR	0.012033	0.002397	22	0.007247
KSTD	0.012275	0.003246	12	-0.004307
LEPH	0.019559	0.001574	51	--
MATJ	0.041746	0.004249	7	0.032151
MERW	0.019216	0.004590	6	0.019000
MOPA	0.021880	0.002453	21	0.019453
MSNA	0.004969	0.007950	2	--
MUSN	0.013468	0.003975	8	0.011836
NECS	0.013853	0.002727	17	0.006981
PILG	0.028984	0.003246	12	0.024028
PMBG	0.010747	0.004590	6	--
POGA	0.017049	0.003555	10	0.016020
PRTV	0.039754	0.007950	2	--
PRYS	0.006446	0.001658	46	0.001149
ROOI	0.029324	0.004590	6	0.025730

Station	R < 300 km			R < 150 km
	κ_0 (s)	Error (s)	Nrec	κ_0 (s)
SEK	0.005856	0.011243	1	--
SNKL	0.048928	0.001257	80	0.036507
SWZ	0.014875	0.001824	38	0.010394
TEMB	0.039508	0.007950	2	--
UPI	0.011147	0.005622	4	0.001358
WDLM	0.020879	0.001516	55	0.017488

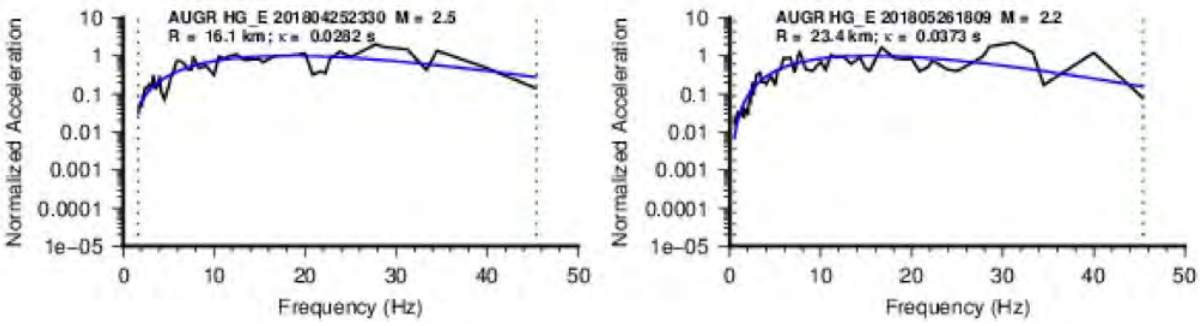

Figure 9-15. Example of the broadband spectral fits performed by Edwards to estimate κ, f_c and Ω_0. The results shown here are for two different earthquakes recorded at station AUGR.

Edwards plotted the signal moments against distance and looked for any deviations away from a theoretical spherical spreading of $1/R$. Figure 9-16 shows the signal moments compared with alternative geometric spreading functions. The left panel compares the signal moments with spherical spreading and identifies a deviation from this scaling around 60 km, as annotated in the figure. The right panel shows that the deviation can be removed with a segmented distance scaling function.

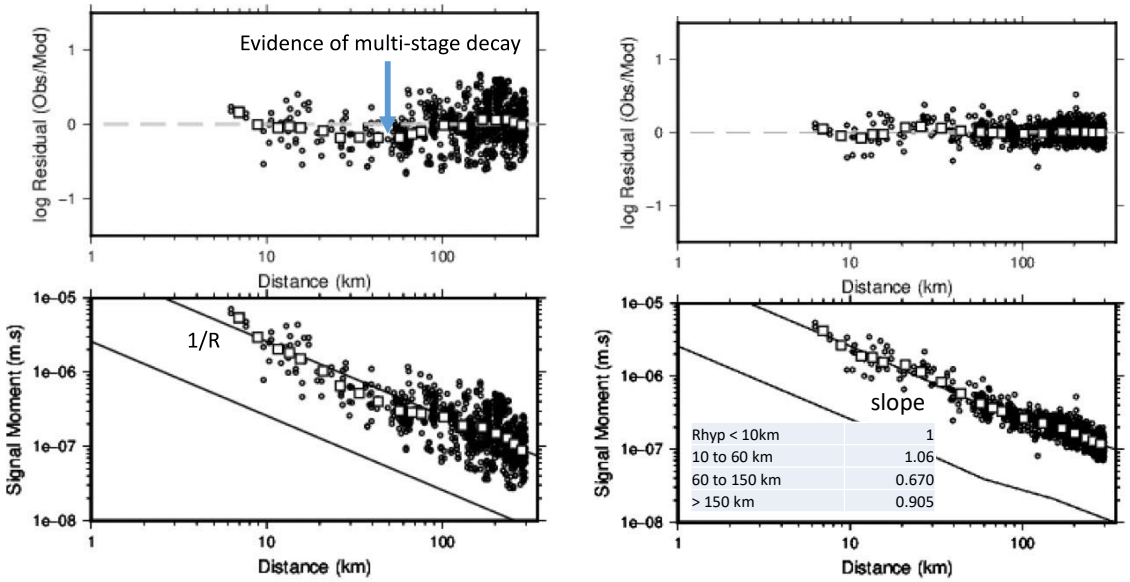

Figure 9-16. The left column shows estimated signal moments compared with a theoretical $1/R$ geometric spreading functions. Deviations from a zero-residual trend are highlighted. The right column shows the estimated signal moments fitted with a segmented piecewise linear distance scaling function. Geometric spreading rates, and critical distances are shown in the lower right panel inset. Square markers show binned values.

The signal moments relate to the earthquake magnitude when extrapolated back to zero distance. Edwards explores the relationship between the local magnitude values provided in the metadata for the inversions and the estimated **M** from consideration of these signal moments. Figure 9-17 shows the relation he found between local and moment magnitude and compares these to the European magnitude conversion equation of Grünthal and Wahlström (2003). Based on the comparison, Edwards suggests that local and moment magnitudes are essentially equivalent for local magnitudes of 3.7 and above.

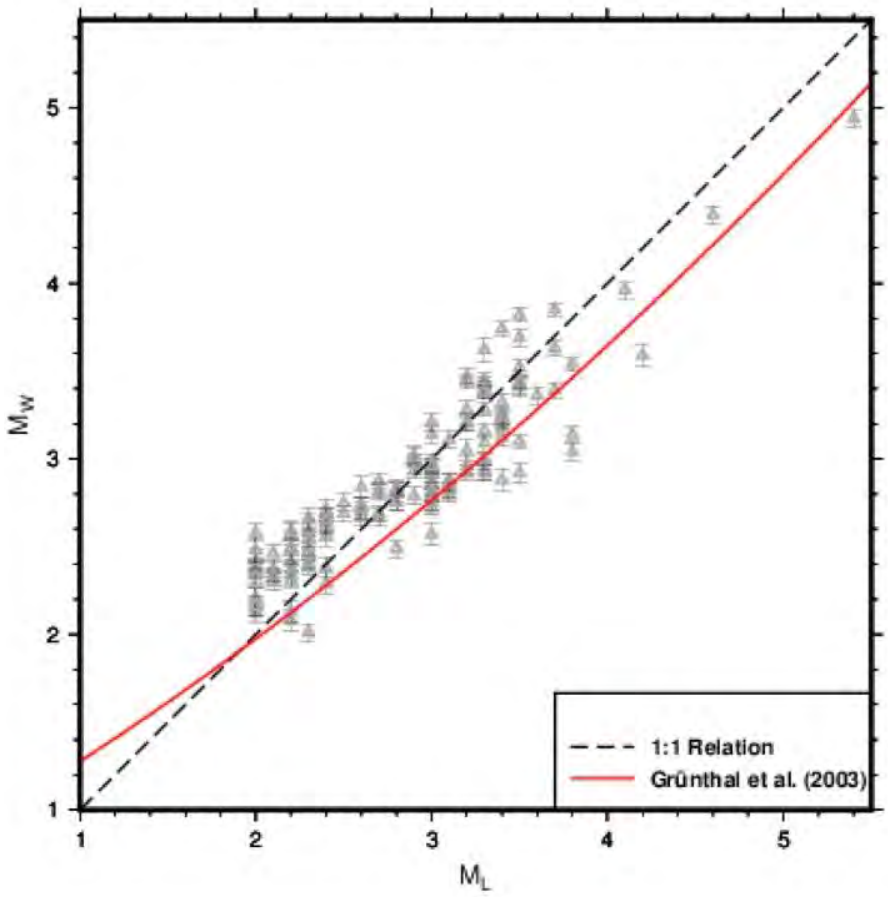

Figure 9-17. Estimated moment magnitudes against provided local magnitudes for the South African database. Note that the red line is the Grünthal and Wahlström (2003) model. Figure from Edwards (2023).

Edwards converted the estimates of corner frequency for each event into an associated estimate of the stress parameter using the assumed equivalence between local and moment magnitudes. Figure 9-18 shows the results of this conversion and superimposes model fits to the data. On the left, the model is constrained to have self-similar scaling (so the coefficient for the magnitude scaling is set to 0.5); on the right, the magnitude scaling is free to vary, but the data still suggests that self-similar scaling is appropriate, i.e. there is no evidence for magnitude dependence of the stress parameter over the dataset used by Edwards in his inversions. The value of the intercept in the fitted lines in Figure 9-18 is related to the average stress parameter. Edwards finds this to be 21 bars with a $\log_{10}$ standard deviation of 0.59 units, and this is computed from 134 events with a mean magnitude of just under 2.9. This level of variability is clearly dominated by the relatively high variability at smaller magnitudes.

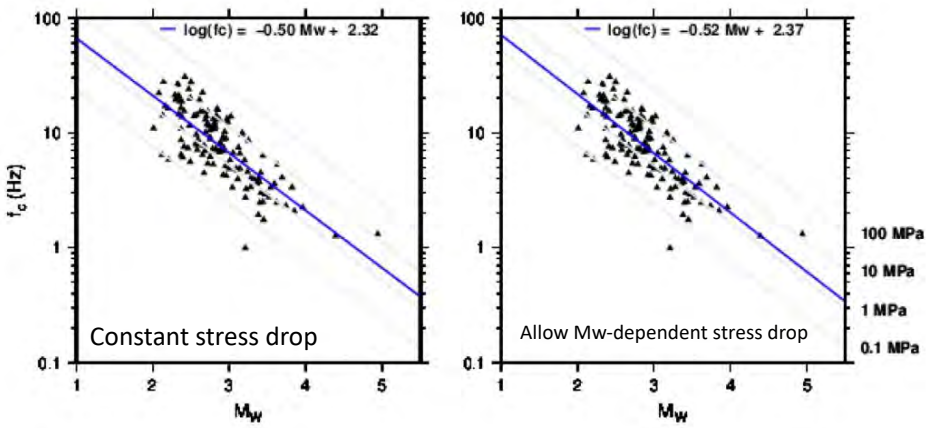

Figure 9-18. Corner frequency against moment magnitude and associated levels of stress parameter shown with diagonal grey lines. The left panel shows a blue line fitted assuming self-similarity, while the slope of the blue line in the right panel is free to vary.

Edwards computed residuals of the point-source stochastic model for each station using the previously defined seismic parameters. Aggregating these residuals by station led to relative estimates of a site parameter ($S[f]$) for each station. Figure 9-19 shows examples of the station residual trends that are not representative of general patterns, but rather highlight that several stations have significant low-frequency offsets that would usually be expected to tend to unity. It is also worth noting that the slopes of these residual functions at high frequencies, where κ_0 is estimated in the first stage of the inversions, can have non-trivial slopes, both positive or negative. This can be related to either the frequency band used to compute κ, the approach to constrain κ_0 for a particular distance range or the use of different records for different stages of the inversion.

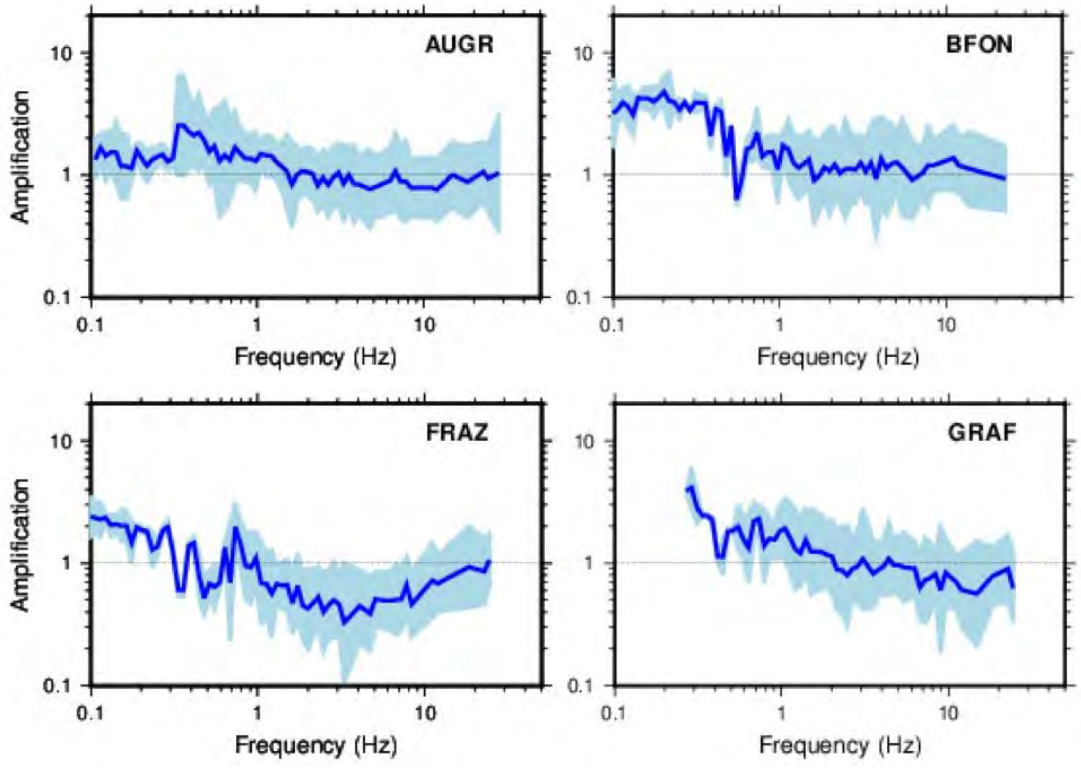

Figure 9-19. Examples of residual trends of FAS against frequency for four stations.

The second phase of Edwards' inversions was to check the FAS parameter set for its ability to reproduce levels of response spectral ordinates for the Inversion GMDB. This step required assumptions about duration models and the selection of components within an RVT framework (Boore, 2003). Table 9-5 lists the model components, noting that the final three rows were not required for the checks Edwards made against the small magnitude data but are required when making forward predictions of response spectral amplitudes for larger earthquakes. Edwards used the model components to compute residuals like those shown in Figure 9-20. The residuals suggested an overall bias of 0.38 $\log_{10}$ units, corresponding to an average bias over magnitude and distance space equal to a factor of 2.4.

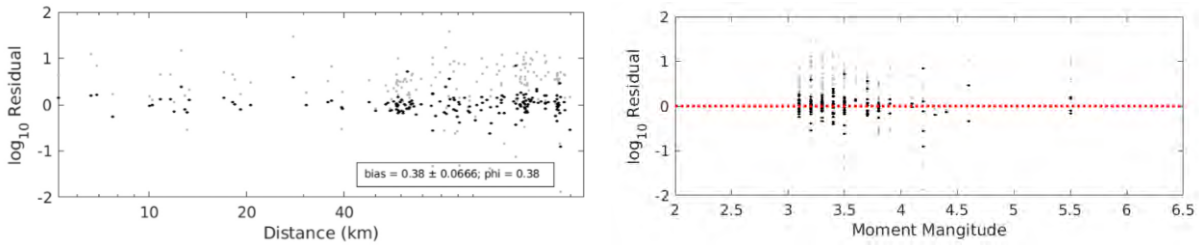

Figure 9-20. Example of residuals in response spectral space found from the seismic parameters of Edwards listed in the 'FAS inversion' column of Table 9-5. Grey dots are actual residuals, while the black dots are the residuals obtained following removal of the average bias.

Figure 9-20 suggests that the distance and magnitude scaling are relatively flat, i.e. the bias is not arising from a grossly erroneous path scaling function. To remove the overall offset, Edwards kept the path scaling elements of the FAS model fixed and allowed values of $\Delta\sigma$ and κ_0 to vary in a way that changed the average amplitudes of the spectra, particularly at short response periods. Edwards based the adjustments primarily upon the average spectral acceleration[4] (Sa_{avg}) but also evaluated the performance of individual spectral ordinates. Figure 9-21 shows how the average bias varies as a function of $\Delta\sigma$ and κ_0. The contours, particularly in the case of the average spectral acceleration, show a well-defined minima trough where various combinations of these parameters lead to a similar low level of bias. To represent epistemic uncertainty, Edwards first identified a best estimate model with a stress parameter of 30 bar and an average κ_0 of 0.02 seconds, and then identified levels of stress parameter that were a factor of 2 higher or lower than this central value while also selecting compatible values of κ_0 that have similar levels of bias. Figure 9-21 shows these three sets of parameters with red markers.

[4] The geometric mean of spectral ordinates over a range of periods: $SA_{avg} = (\prod_{i=1}^{n} SA(T_i))^{1/n}$

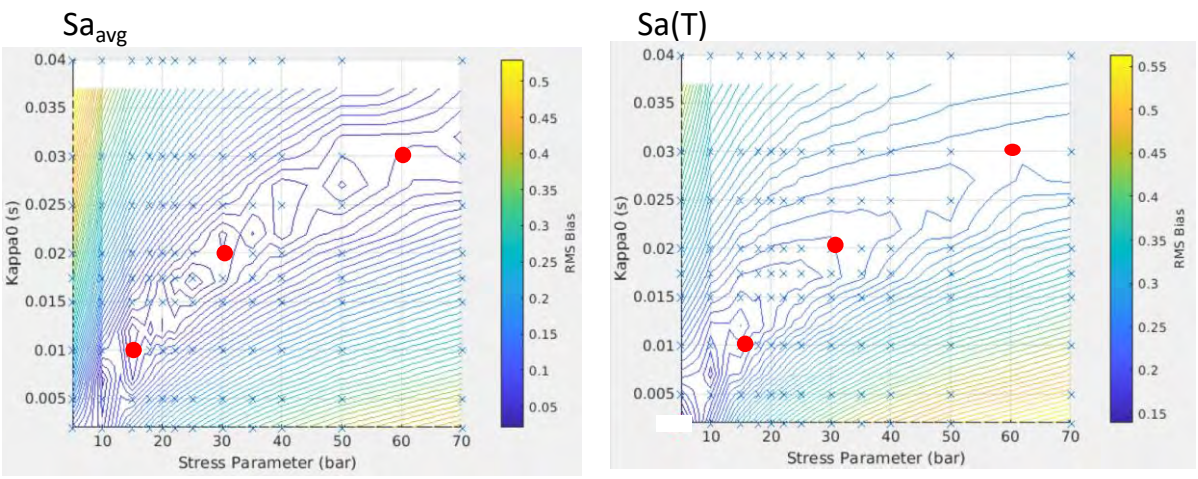

Figure 9-21. Bias contours for average spectral acceleration (Sa_{avg}) (left) and an individual spectral ordinate (right). The red dots show the three combinations of $\Delta\sigma$ and κ_0 that were identified by Edwards to centre the FAS parameter set predictions against South African response spectral data.

The final set of seismic parameters proposed by Edwards is provided in the right-most column of Table 9-5 and includes the three distinct levels of stress parameter along with the associated values of the average site kappa. Since the overall objective is to find seismic parameters that reflect crustal source and path scaling, the specific values of the site kappa are not particularly important. It is important to note that these parameters are correlated with the stress parameter and that all three pairs of parameters provide a similar level of bias with respect to the response spectra in the Inversion GMDB.

9.2.2.3 Summary of GMM TI Team response spectral inversions

The GMM TI Team started with the Inversion GMDB but used different criteria than Edwards to obtain the subset used. Figure 9-22 shows the complete magnitude-distance distribution from the Inversion GMDB, along with the subset of records selected for the inversions. Figure 9-23 then shows a closer view of the distribution of the selected subset. Of the 9586 records that were made available, the GMM TI Team selected a subset of 1045 records for the inversions.

The first point of difference between the subsets selected by Edwards and the GMM TI Team is that the GMM TI Team initially allowed records as far as 500 km from a site to be considered. After this initial filtering based on distance, the GMM TI Team determined whether individual records could be used or not from a re-evaluation of the usable frequency range in both Fourier and response spectral space. The details of this re-evaluation are provided later in this section, but from comparison of Figure 9-12 and Figure 9-22 it can be appreciated that the GMM TI Team rejects more records than Edwards after their initial distance-based filtering of the database. For example, many of the records at distances of around 100 km that are rejected by the GMM TI Team are used by Edwards. As noted previously, these differences in data selection reflect epistemic uncertainty as well as the different requirements of Fourier and response spectral inversions. The selection criteria for response spectral ordinates are more forgiving (i.e. more records are deemed usable) than for Fourier spectral ordinates.

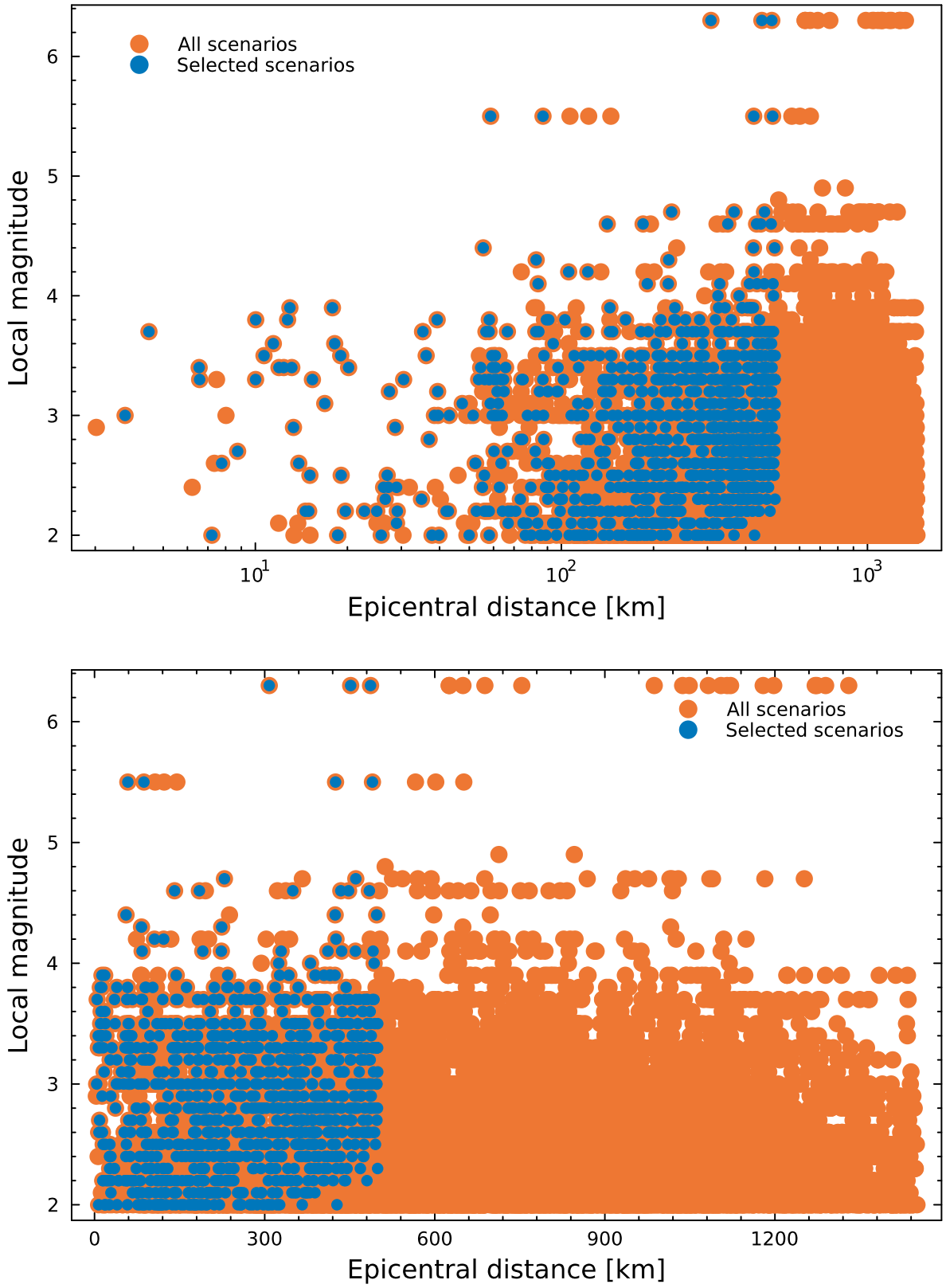

Figure 9-22. Magnitude-distance distribution of the Inversion GMDB (corresponding to the ray paths previously shown in Figure 9-8) and the subset of selected records used by the GMM TI Team. The same data are plotted in both panels, but the upper uses a logarithmic distance axis, while the lower panel uses a linear axis to aid comparison with the similar figures from Edwards (2023; Figure 9-12).

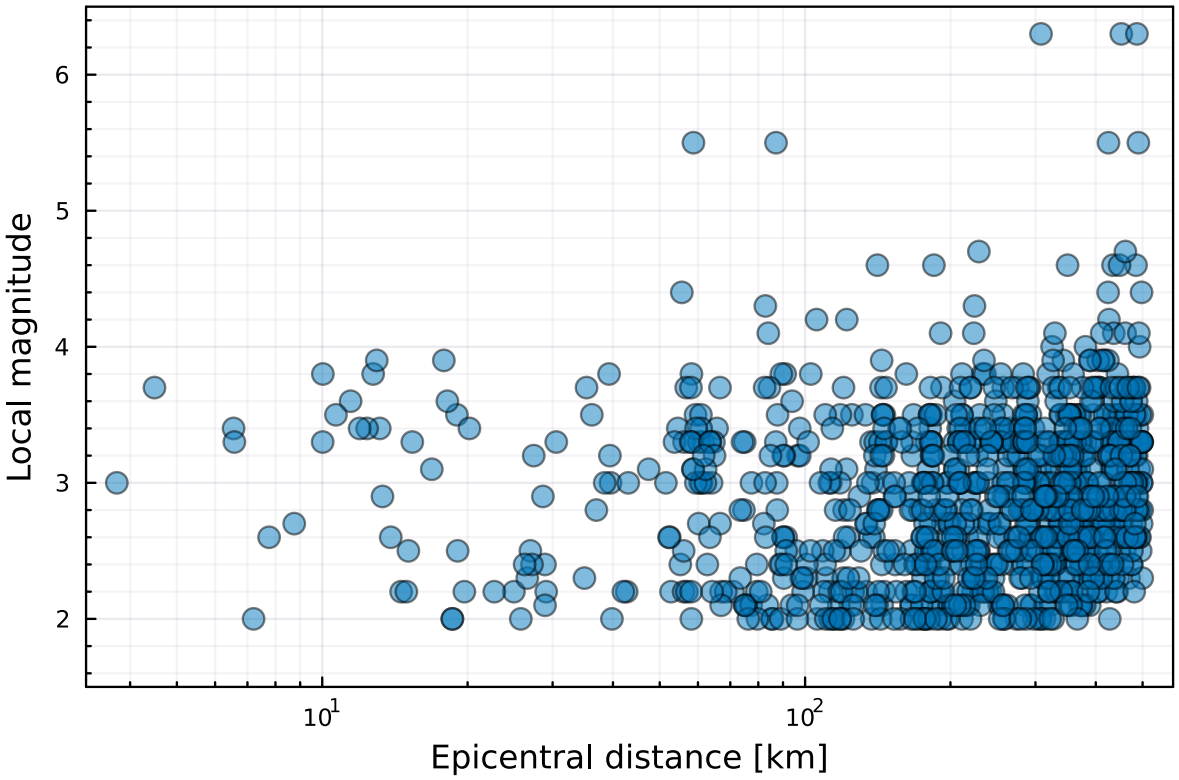

Figure 9-23. Magnitude-distance distribution of the records selected by the GMM TI Team for the response spectral inversions.

The GMM TI Team inversions work directly with response spectral data, but elements of the model development also make use of Fourier spectral amplitudes. For example, the GMM TI Team re-evaluated the usable frequency range of the Fourier ordinates and the usable period range of the response spectral ordinates from analyses that worked with the Fourier spectra. Specifically, for the FAS frequency limits the GMM TI Team used a noise spectrum that was defined as the maximum of the record-specific pre-event noise and the geometric mean of the noise spectra for all records at the recording station (this is more conservative than just using the pre-event noise spectra for each record). They also made use of broadband fits to Fourier amplitude spectra to obtain initial estimates of some parameters and to obtain an $M_L - \boldsymbol{M}$ relationship. Figure 9-24 provides an example where the broadband fit is found from a parameterisation of Equation 9-12 resulting in a shape that is a combination of an $\omega^2\Omega$ source spectrum and a κ filter. The FAS, for both acceleration and displacement, are plotted along with the noise spectra for the signal, a broadband fit, and vertical lines denoting usable frequency limits. The absolute amplitude is related to the source strength in terms of the seismic moment and signal moment, geometric spreading, and any average site impedance effects.

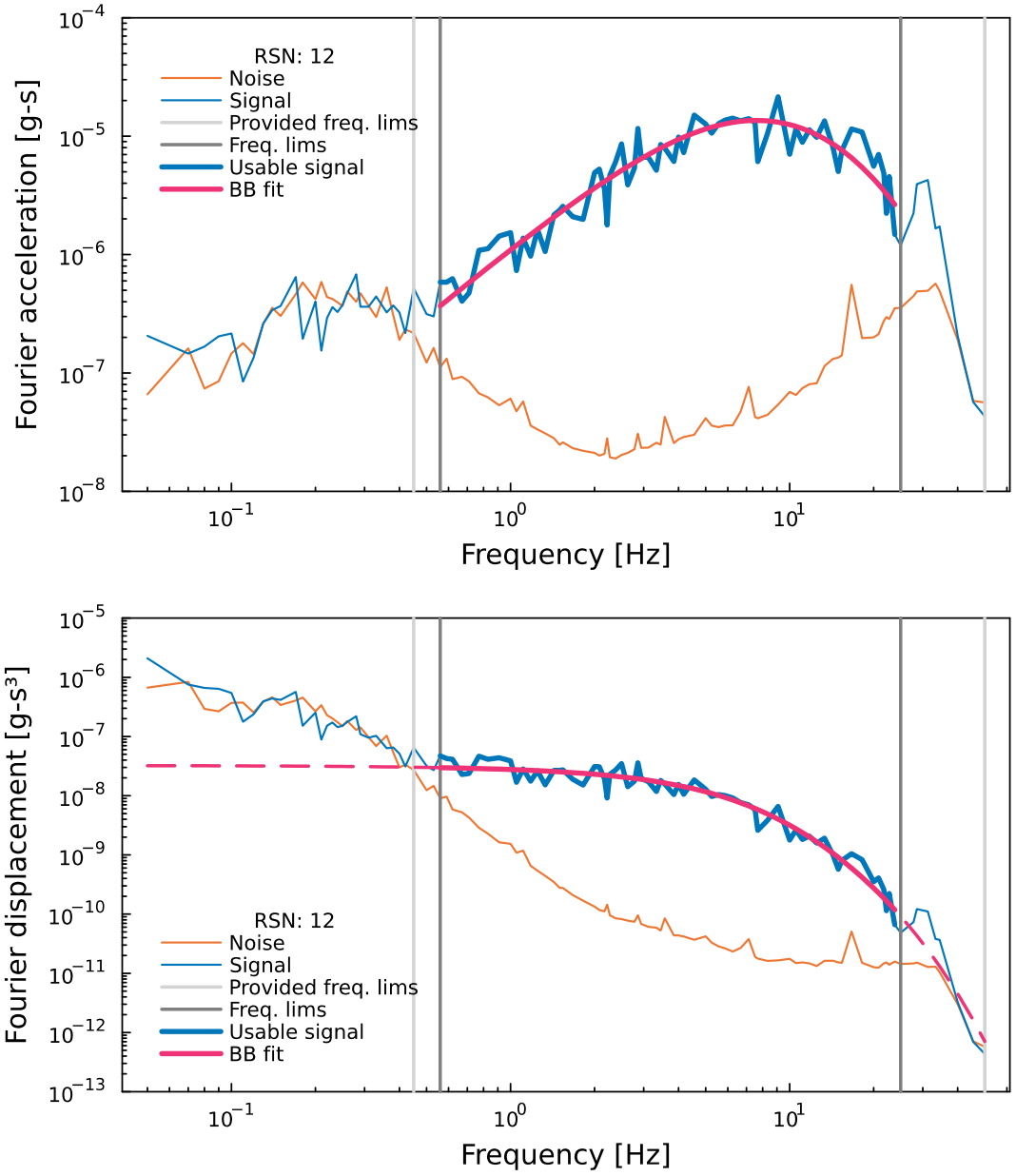

Figure 9-24. Example broadband fits to Fourier amplitude spectra (acceleration shown in the upper panel, and displacement in the lower panel) for one record (RSN 12). The 'provided freq. lims' are the limits of the usable frequency range provided in the meta data of the ground motion database. The 'freq. lims' are the re-evaluated limits obtained by the GMM TI Team using the more conservative definition of the noise spectrum (the maximum of the station mean noise and the pre-event noise for the record).

Like Edwards, the GMM TI Team used the absolute amplitudes of the broadband model fits, like those shown in Figure 9-24, to obtain an independent estimate of the moment magnitudes for the various events considered within the database. The dashed extrapolation of the model fit to low frequencies in the lower panel of Figure 9-24 tends to the signal moment and this was converted to an effective estimate of seismic moment.

The GMM TI Team also took the broadband fits obtained for each record and used them as the basis for identifying periods where response spectral ordinates could be reliably estimated. The GMM TI Team obtained their own estimates of the usable frequency ranges of each record in both Fourier and response spectral space. In contrast, Edwards adopted the usable

frequency limits that were provided as part of the automated processing from the Inversion GMDB.

The GMM TI Team first limited the maximum usable frequency in the Fourier domain to 25 Hz given that a pre-filter with a corner frequency at this value was applied during the record processing. Then, the GMM TI Team borrowed concepts from RVT to formulate Equation 9-16.

9-16

$$SA(T;\zeta) \propto \sqrt{m_0(T,\zeta)} = \sqrt{2\int_0^{\infty} |H(f;T,\zeta)|^2 |A(f)|^2 df}$$

In this equation SA is the spectral amplitude for period T and damping ratio ζ, m_0 is the zeroth spectral moment for this period and damping ratio, and is defined as a function of the FAS $|A(f)|$ and the frequency-response function of a single-degree-of-freedom oscillator $|H(f;T,\zeta)|$ as shown by the term under the radical on the right-hand-side of the equation. The integral in Equation 9-16 is evaluated over all positive frequencies. The frequency response function, $|H(f;T,\zeta)|$, tends to unity at low frequencies, and attenuates very strongly for frequencies above the reciprocal of the period T.

To determine whether the spectral ordinate at a given period was usable for the response spectral inversions we start with the expression in Equation 9-16 and replace the limits of the integral with the frequency limits identified on the basis of signal-to-noise ratio considerations provided in the database. Equation 9-17 then provides an estimate of the spectral amplitude given a finite bandwidth in the frequency domain:

9-17

$$SA(T;\zeta) \approx \sqrt{2\int_{f_{lo}}^{f_{hi}} |H(f;T,\zeta)|^2 |A(f)|^2 df}$$

For a given pair of f_{lo} and f_{hi}, the computed spectral amplitude obtained from Equation 9-17 will differ from that obtained using Equation 9-16 by an amount that depends upon how much of a contribution the omitted frequency ranges (frequencies above f_{hi} and below f_{lo}) make to the spectral ordinate at period T. For each record the $|A(f)|$ was represented by a broadband fit to the Fourier spectrum (fit between f_{lo} and f_{hi}). This broadband model was then assumed to be valid for all frequencies and was used in both Equation 9-16 and Equation 9-17. If, for a given period T, the result from Equation 9-17 was within 1% of the result from Equation 9-16 then the spectral ordinate at that period was considered usable for the response spectral inversions.

Figure 9-25 shows the record processing that the GMM TI Team performed for the record whose FAS was previously shown in Figure 9-24. The right-hand panel of the middle row shows the acceleration response spectrum. The dark grey vertical lines in this panel represent the usable frequency limits based on signal-to-noise ratios of the FAS. The heavy pink line shows the usable response spectral ordinates for this record. The figure shows that the periods are within the bounds associated with these vertical lines.

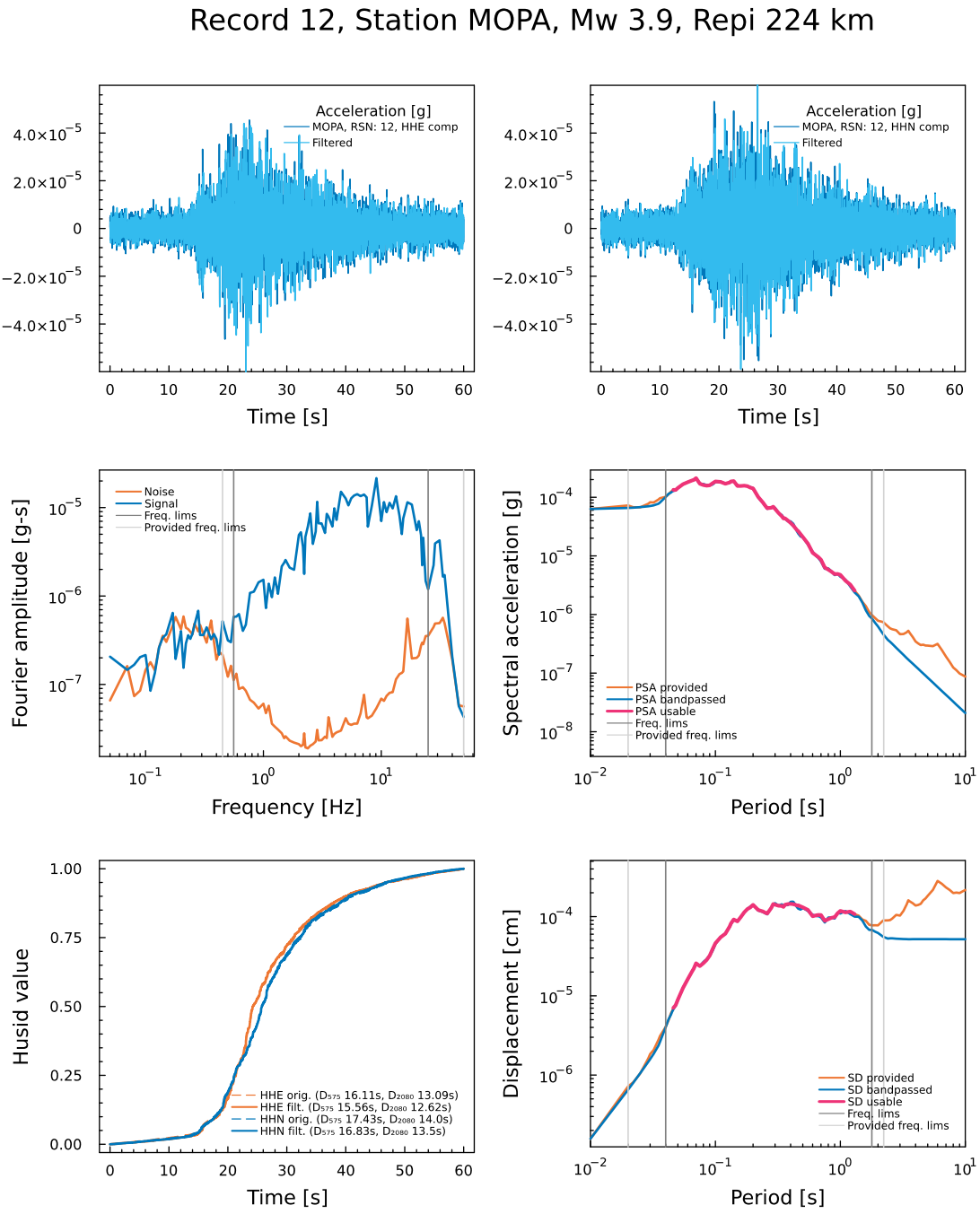

Figure 9-25. Example of individual record processing performed by the GMM TI Team to identify usable response spectral ordinates. The various panels in this figure all relate to the same record (RSN 12) as previously shown in Figure 9-24. The upper left panel shows the HHE component accelerogram provided in the GMDB (dark blue) and bandpass filtered version of this signal (light blue) using the frequency limits found by the GMM TI Team. The upper right panel is similar to the upper left panel but relates to the HHN component. The central left panel shows the FAS of the signal and noise (the quadratic mean is used for both), and the vertical lines show the limits of the usable frequency range defined in the GMDB and by the GMM TI Team. The central right panel shows the response spectra of the provided and bandpass filtered accelerograms using the GMRot50 component. The vertical lines show the usable period limits from the GMDB and those found by the GMM TI Team. The bottom right panel is similar to the central right butpanel but shows displacement response spectra rather than acceleration response spectra. Finally, the lower left panel shows Husid curves for the provided and bandpass filtered signals.

The GMM TI Team performed the inversion on the response spectral data directly (using the approach detailed later in this section). They obtained estimates of the moment magnitudes for each event from Fourier domain considerations and identified which spectral ordinates could be used within the inversions from evaluating spectral shapes for individual records within the Fourier domain. The GMM TI Team **M** estimates are plotted against the corresponding M_L in Figure 9-26 where the observed trends observed in Figure 9-26 are similar to those Edwards identified (see Figure 9-17). This result is not surprising because the process to estimate the signal moments from broadband fits in the Fourier domain is similar in both studies, but whereas Edwards used these results to assume a 1:1 equivalence between the local and moment magnitudes (for $M_L \geq 2.5$), the GMM TI Team fit the quadratic model shown in Figure 9-26 to these data using a random effects regression analysis.

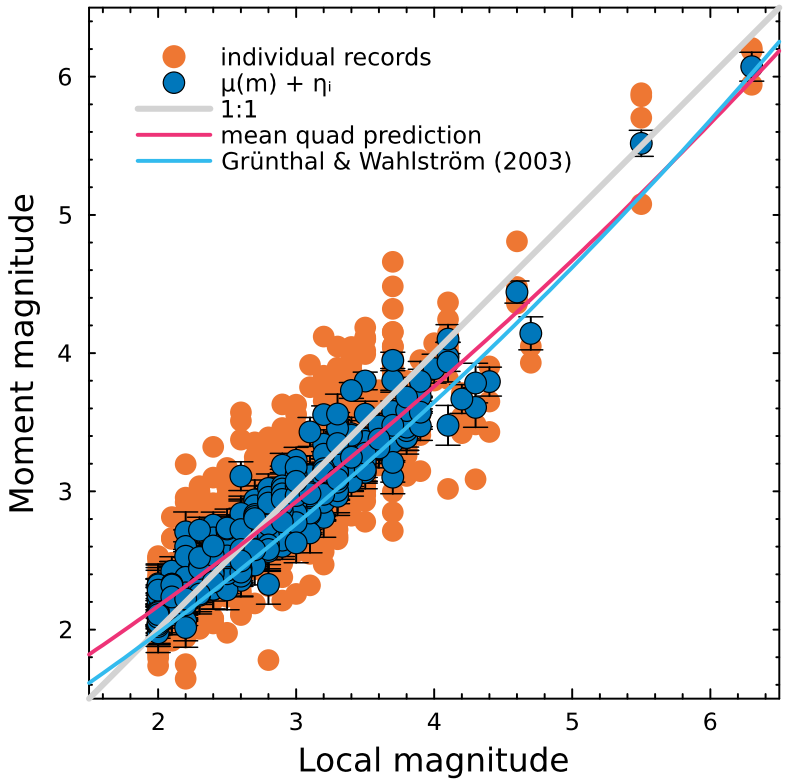

Figure 9-26. Comparison of estimated moment magnitudes and provided local magnitudes for the data analysed by the GMM TI Team. Orange markers relate to individual signal moment estimates for records, while the blue markers are the mean plus event random effects from a random effects regression on these individual values (the pink fitted line plus the random effects give an individual blue point, and the error bars on those blue points reflect the error in the random effects). The model of Grünthal and Wahlström (2003) (previously shown in Figure 9-17) is also shown for comparison.

The GMM TI Team derived the relationship shown in Equation 9-18 to map local magnitudes to moment magnitudes. Estimates of moment magnitude within the final inversions were then made using this relationship.

9-18

$$\boldsymbol{M} = 0.890 + 0.561\, M_L + 0.039\, M_L^2$$

Note that Edwards shows the relationship of Grünthal and Wahlström (2003) in Figure 9-17, which is derived from 164 well-constrained central European earthquakes. Their relationship

is $\boldsymbol{M} = 0.67(\pm 0.11) + 0.56(\pm 0.08)M_L + 0.046(\pm 0.013)M_L^2$, and is very similar to the result obtained by the GMM TI Team for the Inversion GMDB. This model is also shown in Figure 9-26.

The GMM TI Team also performed analyses on Fourier spectral amplitudes to guide the parameterisation of the inversion models in the response spectral domain but did not adopt any other elements directly. For example, starting estimates of κ_0 came from Fourier-based analyses similar to those performed by Edwards, but the κ_0 values were not explicitly used in the inversions themselves. Additionally, the functional form for geometric spreading was investigated in the Fourier spectral domain. Figure 9-27 shows the signal moments obtained by the GMM TI Team against distance (for both raw signal moments in the upper panel, and signal moments corrected so that each marker is equivalent to what would have been observed if all records had a magnitude equal to the mean magnitude of the dataset in the lower panel). As signal moments are proportional to the seismic moment, and the moments relate to amplitudes below the source corner frequency, a positive one-unit change in magnitude corresponds to a positive $3/(2\ln 10)$ change in the signal moment. Therefore, the signal moment for each record was adjusted using this scaling and the degree to which the magnitude of the event differed from the mean magnitude of the database. The lower panel of this figure was used to parameterise the geometric spreading function within the response spectral inversions.

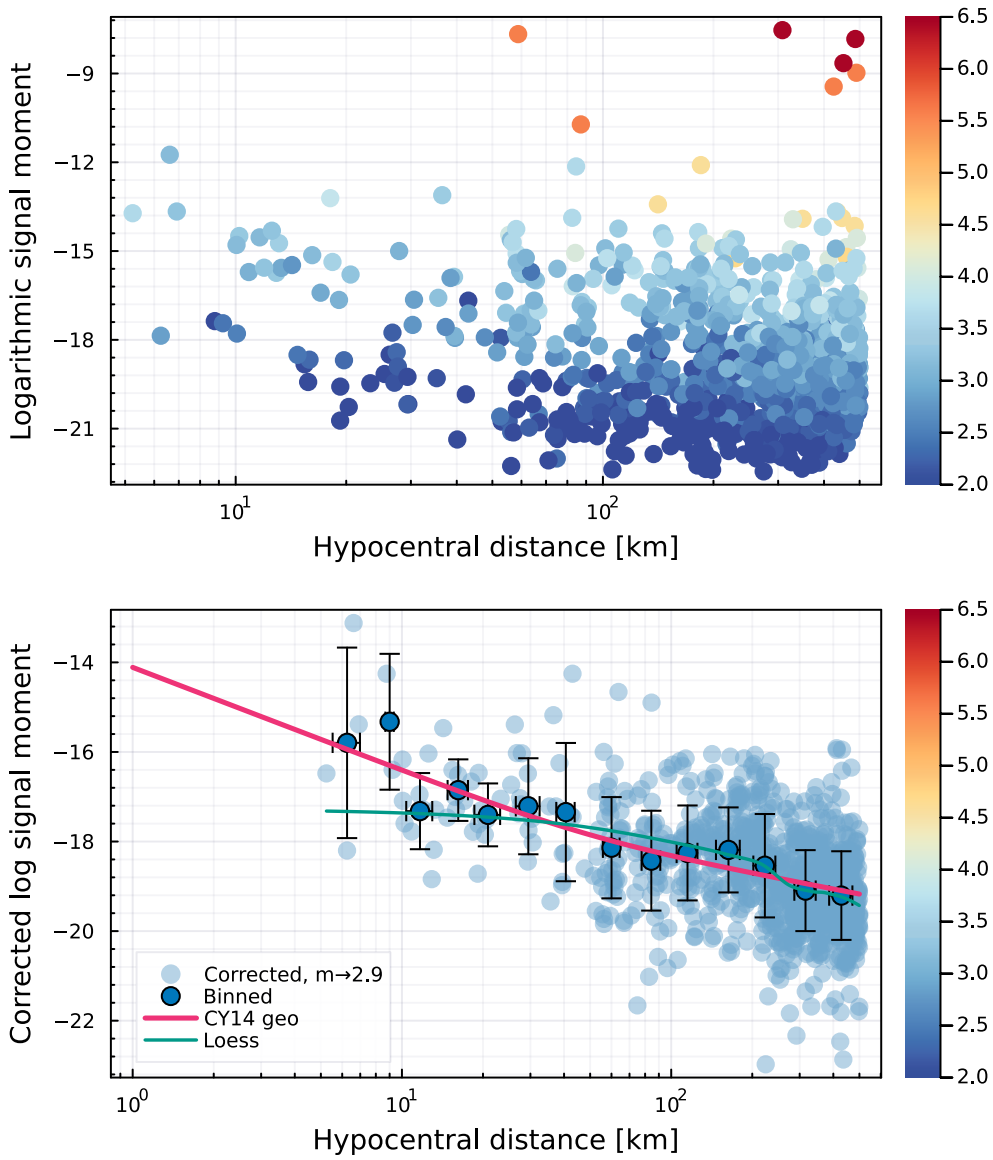

Figure 9-27. Logarithmic signal moments plotted against distance for the records analysed by the GMM TI Team. The upper panel shows actual amplitudes, and colours markers by magnitude, while the lower panel converts all moments to the level associated with the mean magnitude of the data. The green line shows a loess fit to the data while the geometric spreading function of CY14 is shown with the heavy pink line.

While Edwards observed evidence to support the use of piecewise segmented scaling in Figure 9-16, the GMM TI Team started by assuming that the smooth geometric spreading function used within the CY14 GMPE was appropriate and then checked for systematic deviations that might reject that assumption. Based upon Figure 9-27, the GMM TI Team decided that the deviations that could be identified were too small to justify modifying the scaling within CY14. Deviations from the solid pink line are apparent in the binned corrected moments in the lower panel of Figure 9-27. Some of these deviations are also represented in Edwards's segmented distance scaling. It is also clear that these deviations from the smooth parametric form of CY14 are generally very small in comparison with the degree of variability that exists within the data. Again, this is an example of how epistemic uncertainty and TDI can be captured using multiple independent analyses.

In addition to looking at the scaling of the Fourier spectral ordinates, the GMM TI Team performed some referenced empirical analyses (Atkinson, 2008). These analyses assumed that the Inversion GMDB response spectral data could be well-described using the CY14 GMPE with simple empirical adjustment terms. It is assumed that a simple source-related offset coupled with a linear distance scaling to account for differences in anelastic attenuation would be sufficient. A regression was performed on the response spectral data, period-by-period, using the regression model:

9-19

$$\Delta_{ij} = \ln SA_{ij}^{SA} - \ln SA_{ij}^{CY} = \beta_0 + \beta_1 R_{RUP,ij} + \eta_i + \eta_j + \varepsilon_{ij}$$

In Equation 9-19, β_0 and β_1 are fixed effects regression coefficients, and η_i and η_j are random effects that reflect event and station effects respectively. The term ε_{ij} is the event-and station-corrected residual. The superscripts SA and CY represent the Inversion GMDB empirical data and the CY14 predictions, respectively.

Figure 9-28 shows the model fits to the total residuals. The level of the pink fitted lines as distances tend to zero is equivalent to β_0 in Equation 9-19, and for many periods β_0 is close to zero, suggesting that significant adjustments to the source scaling of CY14 are unlikely to be required to match the Inversion GMDB. At the same time, as the distance increases, we see that the total residuals are significantly above zero ($\beta_1 > 0$), and that the CY14 GMPE is significantly underpredicting the Inversion GMDB. The use of a simple linear distance correction, as per Equation 9-19, does a good job explaining these residuals trends, meaning that the differences in path scaling at large distances are functionally related to differences in anelastic attenuation. A simple correction for differences in the attenuation rates may account for a significant amount of the difference between the CY14 predictions and the Inversion GMDB.

As with many of the Fourier-based considerations, the results based on these referenced empirical analyses were not directly used within the subsequent inversions, but they were used to inform how the FAS model should be parameterised. In the GMM TI Team's first inversion model, the source scaling of CY14 was assumed to be valid for the Inversion GMDB, reflecting the findings of these referenced empirical regressions. At the same time, the actual period dependence of the non-zero offsets (the β_0 values) were investigated to ascertain whether these were likely to be associated with differences in the stress parameter or due to differences in the average κ_0. These considerations influenced whether the GMM TI Team fixed κ_0 or allowed κ_0 to be a free parameter in certain inversions.

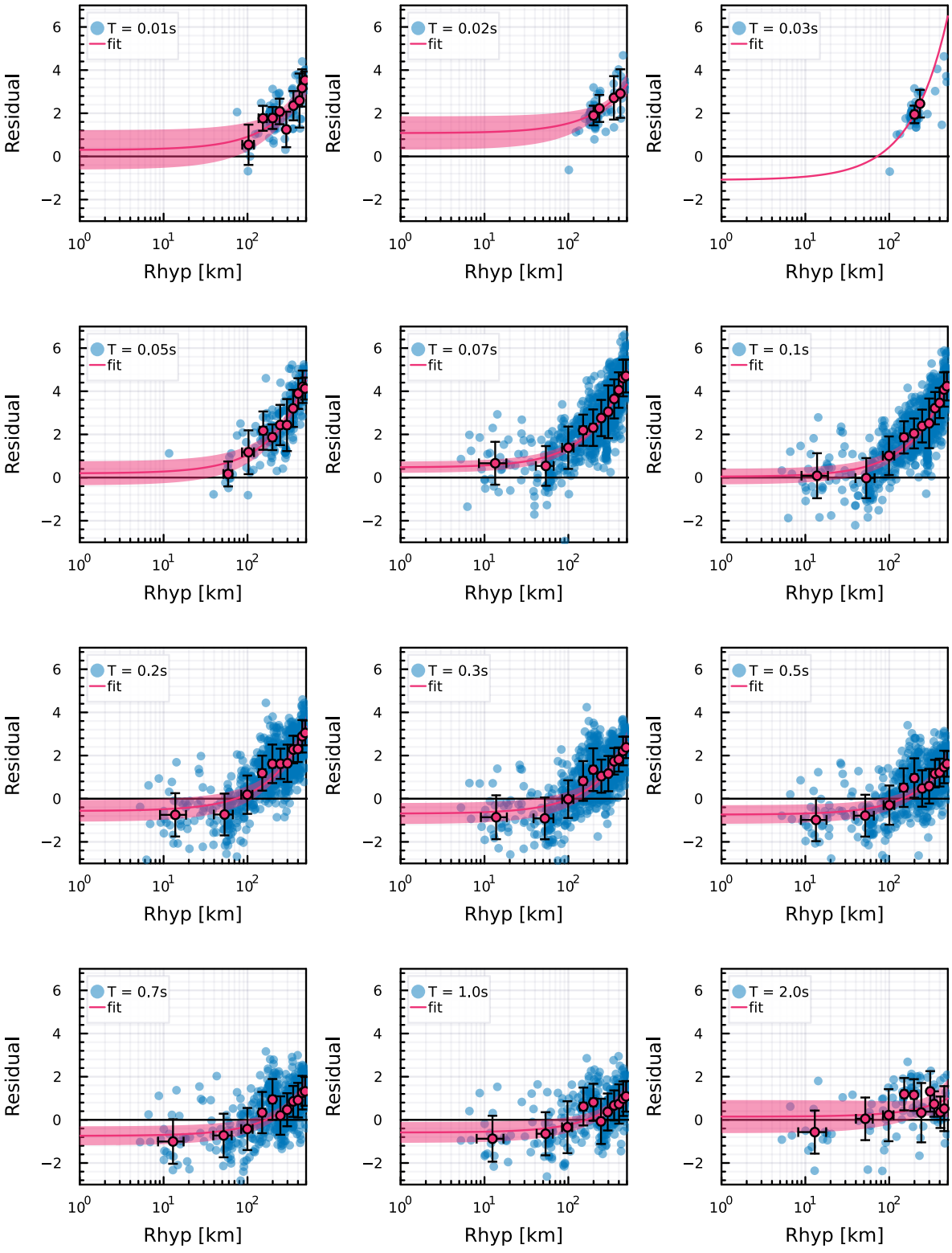

Figure 9-28. Total residuals (blue markers) computed using the published CY14 GMM along with binned residuals and model fits using the function in Equation 9-19. The pink markers show binned residuals and associated error bars.

The GMM TI Team method for response spectral inversions involves a nonlinear optimisation of a loss function in a single step. The loss function is defined in Equation 9-20:

9-20

$$L(\boldsymbol{\theta}; \boldsymbol{rup}) = \sum_{i=1}^{n_{rup}} \sum_{j=1}^{n_{T_i}} \left[\ln SA_{ij}^{SA}\left(T_j, rup_i\right) - \ln SA_{ij}^{RVT}\left(T_j, rup_i; \boldsymbol{\theta}\right)\right]^2$$

where $\boldsymbol{\theta}$ is the vector of seismic parameters that includes both constraints and free parameters, $\boldsymbol{rup}$ is a vector/list of all rupture scenarios within the database, n_{rup} is the total number of ruptures, n_{T_i} is the number of response spectral ordinates for rupture scenario rup_i, SA^{SA} is a spectral ordinate computed from a South African ground-motion recording, and SA^{RVT} is a predicted spectral ordinate obtained via RVT. Parameter estimates and their covariances are computed from the optimisation of this generic function, and various constraints on the parameters, or relationships between parameters are enforced. The minimisation is performed using the Julia programming language (https://julialang.org) and associated packages. In particular, the NLopt.jl package (https://github.com/JuliaOpt/NLopt.jl) is used that provides an interface to the NLopt C library (Johnson, 2007). The optimisation itself starts with a derivative-free global algorithm – the DIRECT-L algorithm of Gablonsky and Keller (2001), which works by progressively subdividing hyper-rectangles (DIRECT stands for DIvision of RECTangles) over a bounded domain in order to identify a global minimum to within some prescribed tolerance or until a maximum number of function evaluations have been performed. With the global minima found using a relatively coarse tolerance, a gradient-based local optimisation algorithm is then applied to find the final minimum. The starting estimates for the local optimisation are the final estimates from the global optimisation. The local algorithm is the SLSQP algorithm of Kraft (1994). For the local optimisation, gradients are computed exactly using the ForwardDiff.jl package (Revels et al., 2016) along with StochasticGroundMotionSimulation.jl (Stafford, 2021).

It is necessary in the GMM TI Team inversions to specify how durations (excitation and root-mean-square [RMS]) and peak-factors will be computed within the RVT framework. Table 9-5 lists these elements along with the seismic parameters obtained by the GMM TI Team for the four inversion models that they ultimately proposed. These four inversion models are referred to either as ‘inversion model X’ or ‘inversion X’ in the rest of the report with ‘X’ being a number from 1-4. As noted above, the details of each of these different inversion models is provided in Table 9-5.

The GMM TI Team adopted the recommendations from Boore and Thompson (2015) regarding how to undertake RVT simulations within the stochastic method. In the Stafford et al. (2022) inversions of CY14, it was assumed that excitation durations are comprised of a source duration equal to the reciprocal of the source corner frequency, and the path duration for active crustal regions from Boore and Thompson (2014, 2015). When processing the Inversion GMDB, the durations (significant duration for the accumulation of 20-80% of the final Arias intensity) of the waveforms were computed and compared with the alternative active or stable crustal region path duration models from these authors (the path durations are $2 \times D_{20-80\%}$). Figure 9-29 compares these computed durations from the Inversion GMDB with the path model predictions of Boore and Thompson (2014, 2015). Figure 9-29 shows that the path duration model for stable crustal regions is more consistent with the Inversion GMDB than the active crustal counterpart.

The decision to adopt the stable crustal region (SCR) model of Boore and Thompson (2015) appears obvious from Figure 9-29, but it does result in deriving more complicated model adjustments. In the case where the same RVT elements are relevant for both the Inversion GMDB and the CY14 inversions of Stafford et al. (2022), one only needs to adjust for the FAS parameters. When differences in duration also need to be accounted for, path adjustments become more challenging because the piecewise linear nature of the Boore and Thompson (2014, 2015) path duration models is so different from the smooth path scaling of the CY14 GMPE. In addition, the segmented active crustal and stable crustal path duration models have different reference distances (the distances defining the segments of the path scaling models) that make the derivation of an analytical adjustment function very difficult.

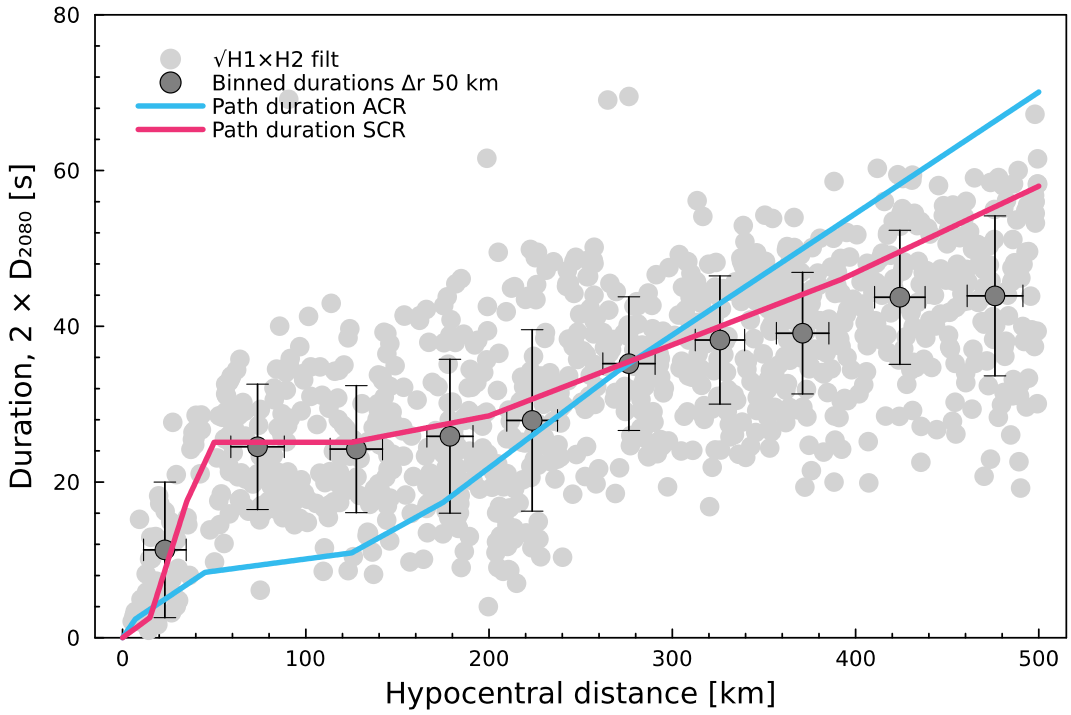

Figure 9-29. Durations computed from the Inversion GMDB and path durations for stable crustal regions (SCR, pink) or active crustal regions (ACR, blue) from Boore and Thompson (2014, 2015). Note that the duration is computed as twice the significant duration between 20 and 80% accumulation of Arias intensity (see Boore and Thompson, 2014).

Table 9-7. Seismic parameters obtained by the GMM TI Team from response spectral inversions. Under each inversion model, the free parameters are denoted by an asterisk (*), and all other model components are fixed/constrained. BT15 is Boore and Thompson (2015).

Component	Inversion 1	Inversion 2	Inversion 3	Inversion 4
Stress parameter	Fixed to CY14 (Stafford et al., 2022)	Linear scaling of CY14 (Stafford et al., 2022)	Magnitude dependence of CY14 (Stafford et al., 2022)	Linear scaling of CY14 (Stafford et al., 2022)
$\Delta\sigma(\boldsymbol{M})$ scale factor	--	1.057*	--	0.993*
$\delta \ln \Delta\sigma(\boldsymbol{M})$ slope	--	--	0.256*	--
Reference site condition	$V_{S30} = 760$ m/s, Al Atik & Abrahamson (2021)	$V_{S30} = 760$ m/s, Al Atik & Abrahamson (2021)	$V_{S30} = 760$ m/s, Al Atik & Abrahamson (2021)	$V_{S30} = 1130$ m/s, Al Atik & Abrahamson (2021)
Near-field geometric rate γ_1	1.08*	1.0*	1.0*	1.084*
Far-field geometric rate γ_f	0.5	0.5	0.5	0.5
Quality factor Q_0	579.3*	377.3*	381.0*	1979.6*
Quality exponent η	0.461*	0.759*	0.718*	0.0
Site kappa κ_0 [s]	0.0164*	0.039	0.039	0.0
Excitation duration	BT15 – SCR	BT15 – SCR	BT15 – SCR	BT15 – SCR
RMS duration	BT15	BT15	BT15	BT15
Peak factor	Vanmarcke (1975)	Vanmarcke (1975)	Vanmarcke (1975)	Vanmarcke (1975)
Near-source saturation	BT15	BT15	BT15	BT15
Free parameters	4	4	4	3
Minimum loss function	33871.3	34824.2	34678.2	35558.3

When differences in excitation duration also need to be accounted for, the adjustments become necessarily more elaborate in part due to the multi-segmented path scaling functions of Boore and Thompson (2015). For this project, model adjustments are developed in a manner that directly accounts for any differences in excitation duration, both for the ACR versus SCR issue encountered for the GMM TI Team inversion models, and for the bespoke excitation duration model adopted by Edwards.

Many model diagnostics are obtained from each of the alternative GMM TI Team inversion models. Examples of the performance of inversion model 1 are shown in Figure 9-30 to Figure 9-32. The performance of the other three inversion models is visually similar, as implied by the relatively similar minimum loss function values reported in Table 9-7. In particular, all models show a positive residual trend for the longer periods considered. This trend is likely the result of signal quality issues at lower frequencies. Boore et al. (2022) developed correction factors to account for this sort of effect, but with the trend existing at longer periods. While it is not necessarily clear from Figure 9-30, the number of available spectral ordinates drops quite strongly for the longer periods considered in these inversions and so the overall fit (the loss function) is driven more strongly by shorter periods where there are more data. Note also that the magnitude distribution of the data also changes with period, with the longer periods being associated with larger events (in general). The trend can therefore also be influenced by the assumed mapping between local and moment magnitudes (and how well that mapping behaves over the magnitude range).

Figure 9-31 shows this issue related to the magnitude range changing with period clearly. At the longer periods the records are clearly from larger events and there starts to be a systematic bias toward positive residuals for these longer periods. It is also clear that the bias is driven by the smaller events at these periods. This is consistent with the idea that data quality issues are contributing to the trend at longer periods seen in Figure 9-30. The data at longer periods from the smaller events are probably censored such that only the higher-than average motions are being considered at these periods.

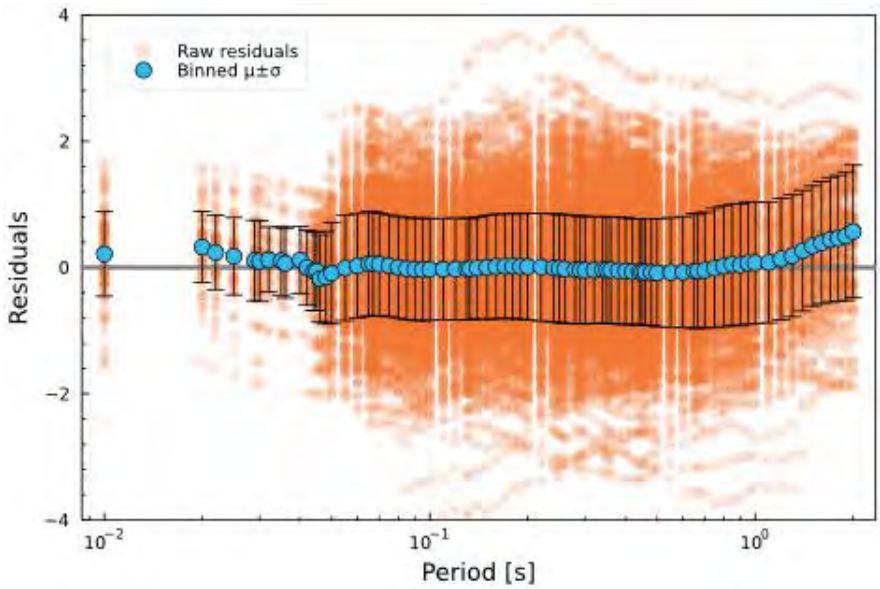

Figure 9-30. Response spectral residuals for GMM TI Team inversion model 1 plotted against period. Light orange points are individual response spectral ordinates, while blue markers and associated error bars show the mean residuals for each considered period and the standard deviation of these residuals at each period.

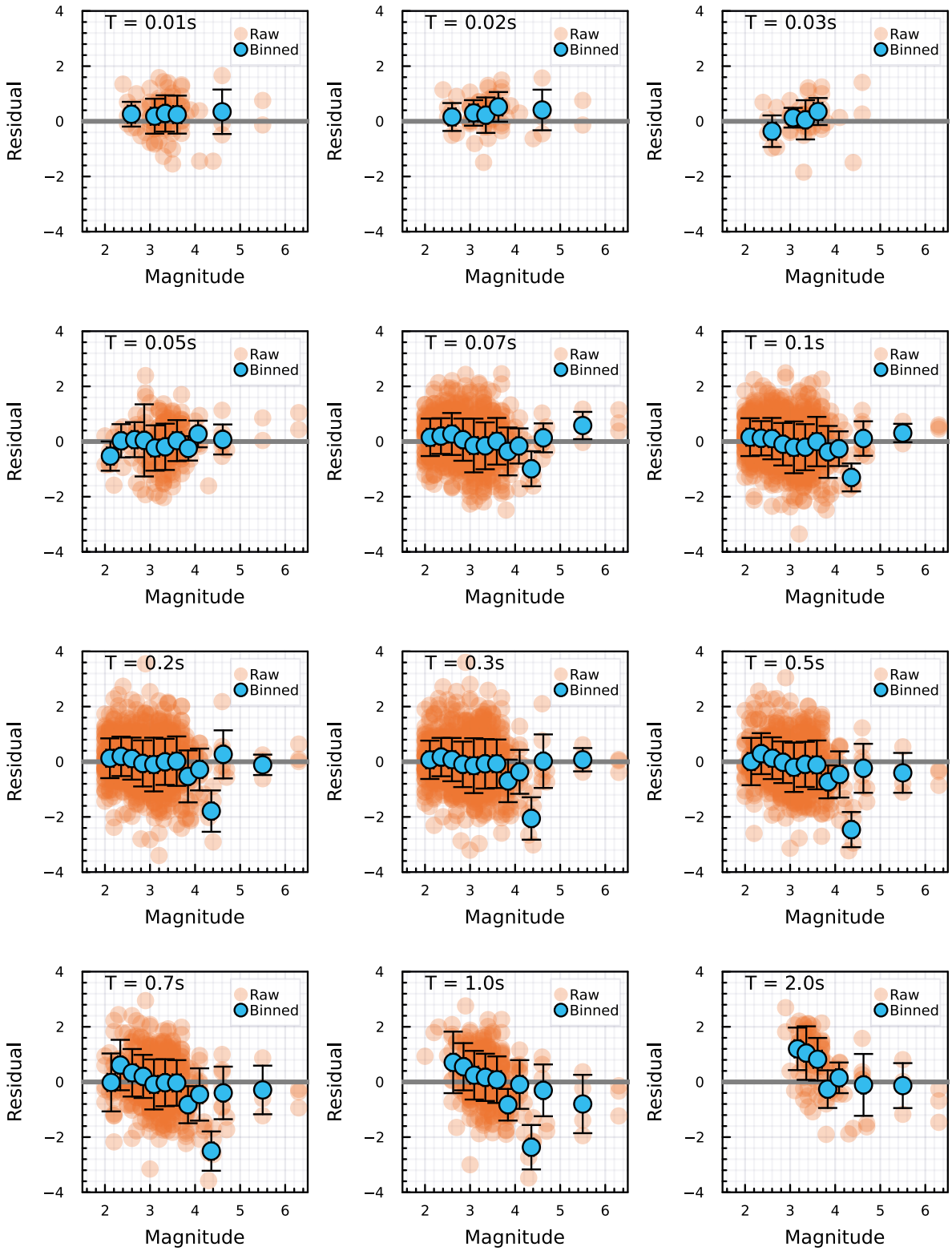

Figure 9-31. Response spectral residuals for GMM TI Team inversion model 1 plotted against magnitude. Light orange points are individual response spectral ordinates, while blue markers and associated error bars show the mean residuals for each considered period. Each panel shows results for a given period, annotated in the upper left of the panel.

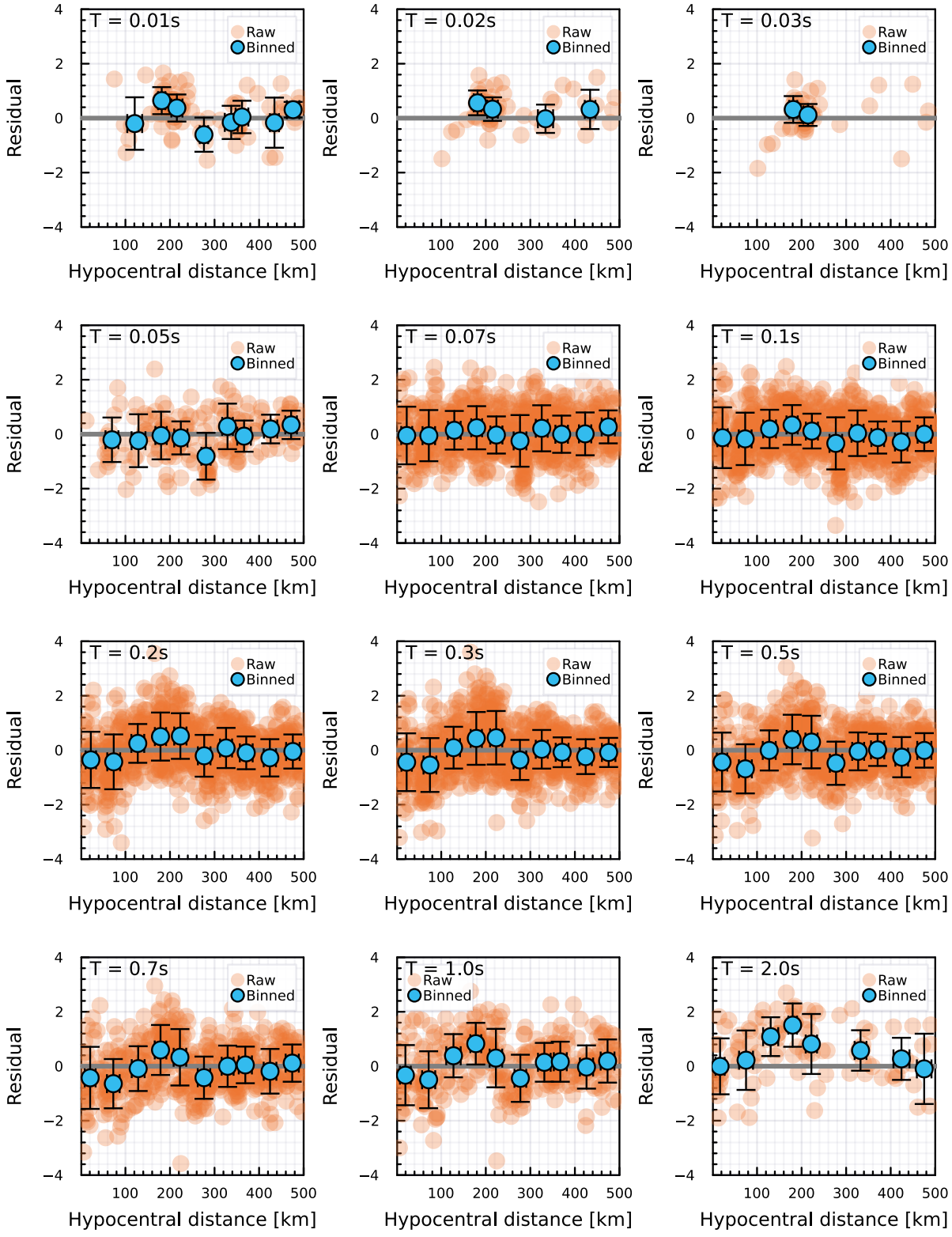

Figure 9-32. Response spectral residuals for GMM TI Team inversion model 1 plotted against distance. Light orange points are individual response spectral ordinates, while blue markers and associated error bars show the mean residuals for each considered period. Each panel shows results for a given period, annotated in the upper left of the panel.

9.2.3 Host-to-target source and path adjustments

Seven sets of seismic parameters and the associated components for RVT computations arise from the inversions of the Inversion GMDB. Three of these models come from Edward's Fourier-based inversions with parameters presented in Table 9-5, and four of the models come from the GMM TI Team response spectral-based inversions with parameters presented in Table 9-5.

The GMM TI Team developed model adjustments for each of the seven seismic parameter sets. Adjustments for differences in the stress parameter were made using the approach described in detail by Boore et al. (2022). Adjustments for path differences were developed to meet the requirements of this project, as explained in detail throughout the rest of this section.

The approach for developing adjustments is based upon the RVT method of defining response spectral ordinates for a given period T and damping ratio ζ_n as shown in Equation 9-21.

9-21

$$SA(T,\zeta_n) = \psi(T,\zeta_n)\sqrt{\frac{m_0(T,\zeta_n)}{D_{rms}(T,\zeta_n)}}$$

The term $\psi(T,\zeta_n)$ is the peak factor that is not very important within the context of model adjustments (because it is relatively insensitive to magnitude and distance and does not vary strongly with Fourier spectral parameters). Both the zeroth spectral moment, $m_0(T,\zeta_n)$, and the root-mean-square duration, $D_{rms}(T,\zeta_n)$ can play an important role in influencing what adjustments are required.

The zeroth spectral moment is defined by Equation 9-22:

9-22

$$m_0(T,\zeta_n) = 2\int_0^\infty |H(f;T,\zeta_n)|^2 |A(f)|^2 df$$

with $H(f;T,\zeta_n)$ being the frequency response function of a single-degree-of-freedom oscillator and $|A(f)|$ being the Fourier amplitude spectrum. The frequency response function for the oscillator is solely a function of period and damping and so will be the same in any host and target combination. Differences in the zeroth spectral moment only arise through the FAS, either through changes in magnitude or distance, or through changes to the seismic parameters, like $\Delta\sigma$ or Q_0. An important feature of the frequency response function, especially for low damping ratios, is that the modulus of this function is strongly peaked at the frequency corresponding to $1/T$, tends to unity as the frequency tends to zero, and decays rapidly for frequencies above $1/T$. This nature of $|H(f;T,\zeta_n)|$, combined with the fact that $|A(f)| \propto f^2$ at frequencies below the corner frequency, means that contributions to the integral of Equation 9-22 are dominated by frequencies around $1/T$ when f_c is above this frequency. As such, the equality in Equation 9-22 can be used to define the approximate proportionality shown in Equation 9-23:

9-23

$$m_0(T) \propto |H(1/T\,;T,\zeta_n)|^2 |A(1/T)|^2$$

This relationship provides a reasonable approximation for periods longer than the peak of the response spectrum (Bora et al., 2016) and it implies that the scaling of response spectral ordinates and Fourier spectral ordinates is similar for those periods. For applications in a region where the peak factor and duration models are the same (for example, adjusting an active crustal model for use in another active crustal location) then the adjustment framework only needs to focus upon accounting for the relative differences in the FAS parameters.

In the case where we have a different duration relation for the host (e.g., active crustal) and target (e.g., stable crustal) regions, even if the seismic parameter sets were identical, we would still require model adjustments because response spectral ratios would become:

9-24

$$\frac{SA_{SCR}A^{SCR}}{SA^{ACR}A_{ACR}} \equiv \sqrt{\frac{D_{rms,ACR}^{ACR}}{D_{rms,SCR}^{SCR}}} \approx \sqrt{\frac{D_{ex,ACR}^{ACR}}{D_{ex,SCR}^{SCR}}}$$

where D_{ex} is an excitation duration (with the subscript denoting the region).

Therefore, for the same seismic parameter sets in an active and stable crustal region the adjustment that would be required for logarithmic spectral ordinates is given in Equation 9-25 and plotted in the lower panel of Figure 9-33.

9-25

$$\Delta \ln SA_D = \frac{1}{2} \ln \left(\frac{D_{ex,ACR}^{ACR}}{D_{ex,SCR}^{SCR}} \right)$$

Due to the complicated piecewise linear nature of the path duration models from Boore and Thompson (2014, 2015), the adjustment implied by Equation 9-25 is also complicated.

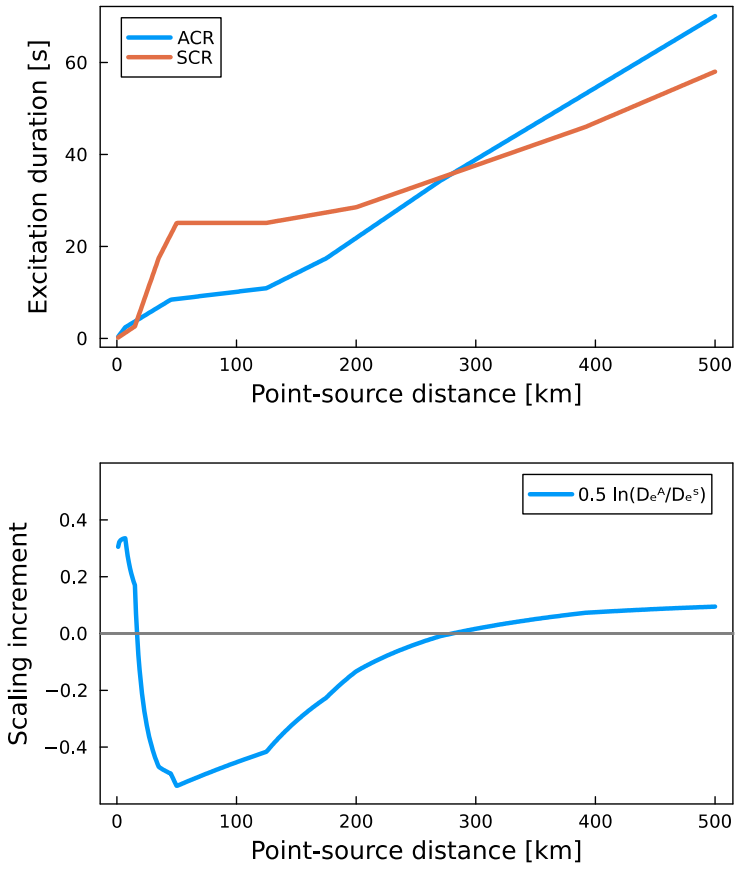

Figure 9-33. Differences in excitation duration between active and stable crustal regions (upper panel) and the logarithmic adjustment that is implied by Equation 9-25 in the lower panel.

The path differences in the present project arise due to three contributions: geometric spreading, anelastic attenuation, and path duration. As geometric spreading and excitation duration are frequency-independent, they effectively scale the FAS and response spectra in the same way, so adjustments are defined as direct ratios of the relevant components. If the geometric spreading function and anelastic attenuation filter in the host region are denoted by $g(r)_h$ and $q(r,f)_h$, with a subscript t used in place of the h to represent the equivalent terms for the target region, then the overall path correction associated with differences in m_0 is defined by:

9-26

$$\Delta \ln SA_P A^P = \ln g(r)_t(r)^t - \ln g(r)_h g(r)^h + \ln q(r,f)_t q(r,f)^t - \ln q(r,f)_h q(r,f)^h$$

Equation 9-26 can also be written as:

9-27

$$\Delta \ln SA_P A^P = \Delta \ln g\,(r) + \Delta \ln q(r,f)$$

For the seismic parameter sets obtained by Edwards, $g(r)_t$ is a piecewise trilinear function while $g(r)_h$ is the smooth function defined in Equation 9-5. It is not possible to write a compact analytical expression for $\Delta \ln g$ for the Edwards inversion models. As the GMM TI Team adopted the same functional expression as CY14, the $\Delta \ln g$ for the inversion models is relatively simple.

9-28

$$\Delta \ln g(r) = -\Delta\gamma_1 \ln(R_{PS}) + \frac{\Delta\gamma_1}{2} \ln\left(\frac{R_{RUP}^2 + c_R^2}{1 + c_R^2}\right)$$

where $\Delta\gamma_1 = \gamma_{1,t}^t - \gamma_{1,h}^h$ as the GMM TI Team and CY14 both fix $\gamma_f = -0.5$. As this expression is independent of frequency, this $\Delta \ln g(r)$ will apply to all periods. The effects of these adjustments (along with other source and path adjustments are shown later in Figure 9-38).

The anelastic adjustment is more complicated because of the frequency dependence of the filter. Although the anelastic filter was defined previously, for convenience define it again here as:

9-29

$$q(r, f) = \exp\left[-\frac{\pi f r}{Q(f) c_Q}\right]$$

Equivalently, in its logarithmic form we have:

9-30

$$\ln q(r, f) = -\frac{\pi f r}{Q(f) c_Q}$$

Differences in anelastic attenuation at a given frequency are then obtained as:

9-31

$$\Delta \ln q(r, f) = -\frac{\pi f r}{c_Q}\left[\frac{1}{Q(f)^t} - \frac{1}{Q(f)^h}\right]$$

The mapping of $q(r, f)$ into m_0 involves broadband integration. As we know that for many periods this integration is strongly dominated by contributions near the oscillator frequency, we can make a first-order correction by using the oscillator frequency within Equation 9-31 and obtaining a function that only depends upon distance.

9-32

$$\Delta \ln q(r) = -\frac{\pi r}{T c_Q}\left[\frac{1}{Q(1/T)^t} - \frac{1}{Q(1/T)^h}\right]$$

The expression in Equation 9-32 will not work well for short periods. We therefore introduce an empirical correction that accounts for the deficiency of the approximation in Equation 9-32 and absorbs assumptions related to the equivalence between the RMS and excitation durations. This empirical correction is represented as in Equation 9-33:

9-33

$$\Delta \ln q'(r) = -\delta\gamma_q(T, \boldsymbol{M}) r$$

The broadband nature of $q(r, f)$ means that Equation 9-32 will work for some periods (generally the moderate-to-long periods) and that it is influenced by magnitude because the

$q(r, f)$ will interact with the source spectrum that varies with magnitude. The $\delta\gamma_q$ term is therefore a correction to the anelastic attenuation rate that addresses these problems. For the long periods $\delta\gamma_q \approx 0$, but for shorter periods there is both period and magnitude dependence.

The calibration of the $\delta\gamma_q$ function is obtained using the HEM framework. RVT predictions are made using host- and target-region seismic parameter sets for a large number of magnitude, distance and period combinations. For each combination of magnitude and period, the GMM TI Team computed response spectral ratios from the RVT predictions. We then accounted for the known effects of excitation duration (using Equation 9-25), the known effects of geometric spreading (using Equation 9-28 for the GMM TI Team parameter sets, or the explicit $\Delta \ln g(r)$ values for the Edwards parameter sets), and used Equation 9-32 to remove the first-order effects of anelastic attenuation. Any $\Delta \ln SA$ that is not yet accounted for will tend to have a linear dependence upon distance (given that it is primarily an anelastic attenuation effect) and so the GMM TI Team calibrated the value of $\delta\gamma_q$ for that period and magnitude using 200 log-spaced distances going from short distances all the way out to 700 km. This process is repeated for each period of interest and for magnitudes from 2.0 to 8.0, inclusive, in steps of $\Delta\boldsymbol{M} = 0.25$.

Figure 9-34 shows the results of these regression analyses for the many considered combinations of period and magnitude. The figure demonstrates that the magnitude dependence is complex and varies with period. For many periods it is also clear that the value of $\delta\gamma_q$ is numerically low, but it must be kept in mind that these $\delta\gamma_q$ values are multiplied by distance and that some very distant rupture scenarios arise from the seismic source model.

An empirical approach is taken to develop an analytical function that can replicate the behaviour seen in Figure 9-34. The functional form is guided by our expectation that the $\delta\gamma_q$ values should be relatively large for short periods, and that they should tend to zero for the longer periods where the first-order correction of Equation 9-32 is expected to work well. The form chosen is shown in Equation 9-34:

9-34

$$\delta\gamma_q(T, \boldsymbol{M}) = \alpha_1(\boldsymbol{M}) \exp[-\alpha_2 \ln(T/0.01)] + \alpha_3(\boldsymbol{M})$$

This function has a value of approximately $\alpha_1(\boldsymbol{M})$ at short periods and then exponentially decays toward a plateau of $\alpha_3(\boldsymbol{M})$ at long periods. The rate of decay is controlled by α_2, while the short-period offset is defined as:

9-35

$$\alpha_1(\boldsymbol{M}) = \beta_1 + \frac{\beta_2}{1 + \exp[-\beta_4(\boldsymbol{M} - \beta_3)]}$$

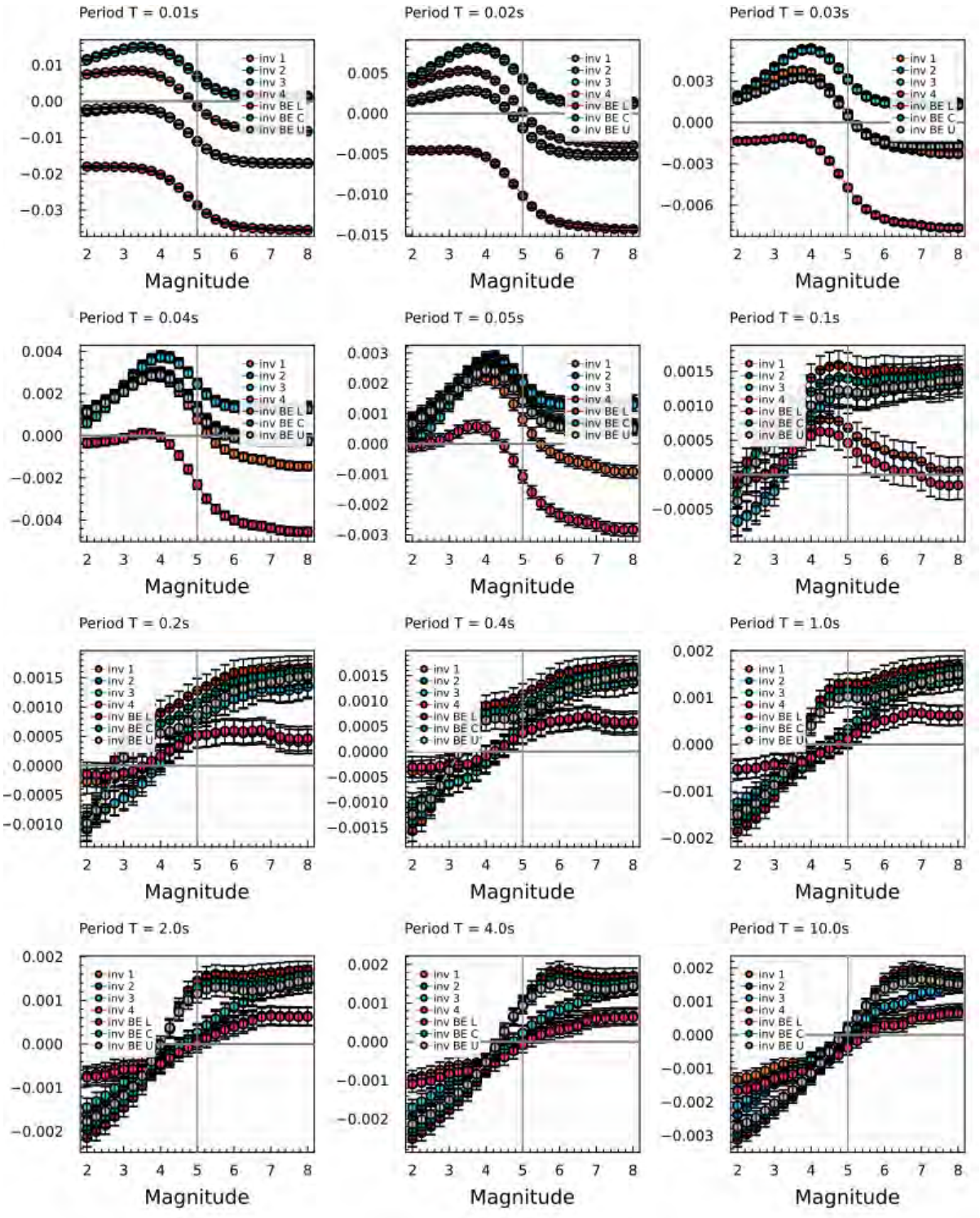

Figure 9-34. Values of $\delta\gamma_q$ plotted against magnitude for each of the seven seismic parameter sets. Each panel corresponds to the period annotated above the panel. Error bars show the uncertainty associated with the estimate of $\delta\gamma_q$ obtained from the regression analysis performed for the corresponding magnitude and period using 200 log-spaced distance values.

The long-period plateau is defined by:

9-36

$$\alpha_3(\boldsymbol{M}) = \beta_6 + \beta_7 \tanh[\beta_8(\boldsymbol{M} - \beta_9)]$$

The performance of this model is demonstrated in Figure 9-35 by comparing the computed $\delta\gamma_q$ values obtained from the regressions on the HEM results with the predictions of the model represented in Equation 9-33. As Figure 9-35 plots the $\delta\gamma_q$ values against period, it is readily apparent that the greatest corrections are required at short periods and that the intermediate-to-long periods require very little additional correction beyond the first-order correction made using Equation 9-32. The coefficients of the model in Equation 9-34 (and Equations 9-35 and 9-36) are provided in Table 9-8, with the model index corresponding to the underlying inversion results according to the mapping shown later in Table 9-11.

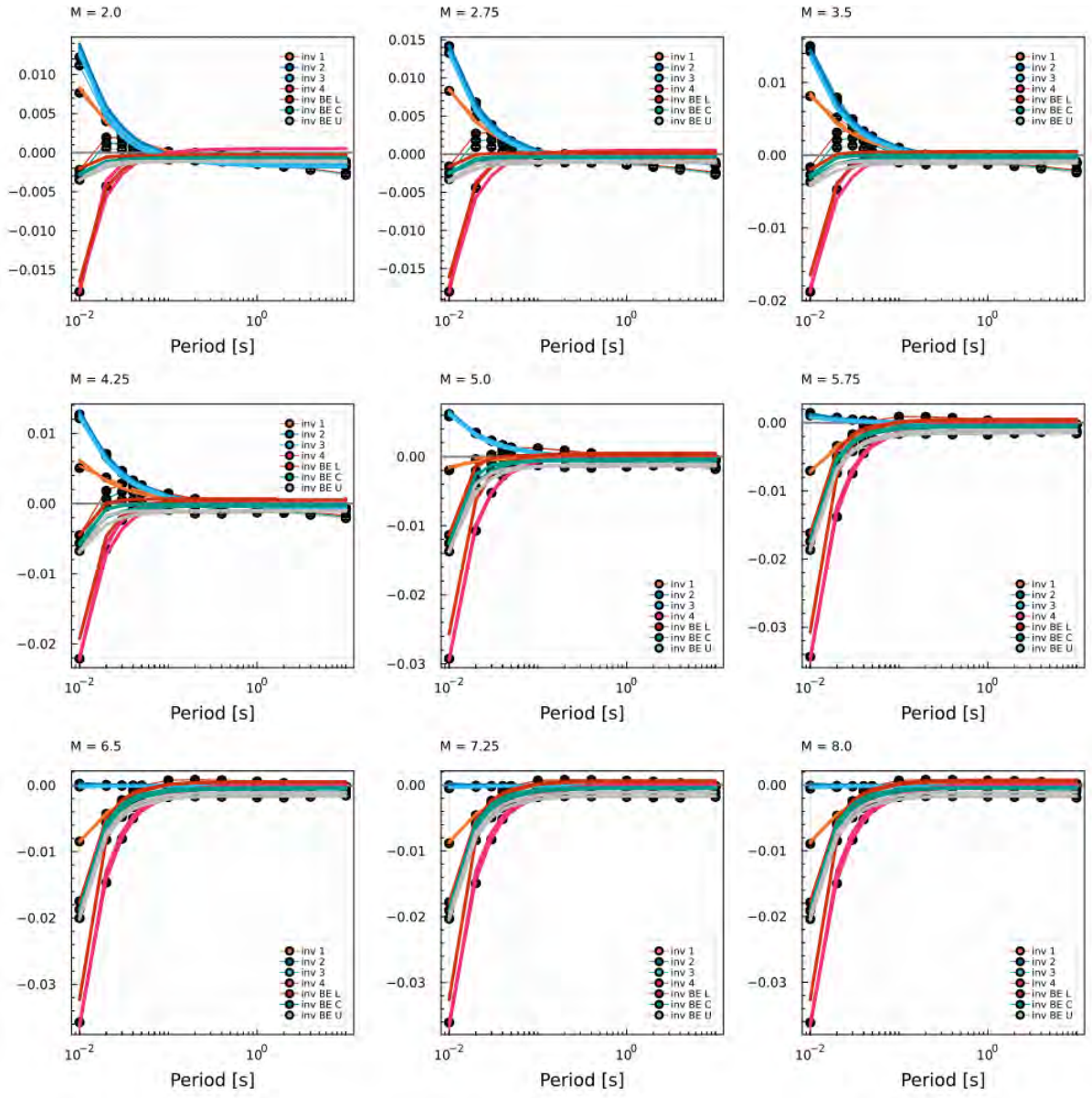

Figure 9-35. Comparison between the computed values of $\delta\gamma_q$ and the modelled values $\delta\gamma_q(T, M)$ using Equation 9-33. In contrast to Figure 9-34, this figure plots the $\delta\gamma_q$ values and predictions against period for a selection of magnitude values.

Table 9-8. Coefficients of the anelastic attenuation correction function defined in Equation 9-34 (and hence Equation 9-35 and 9-36). The model index relates to the seven inversion models with indices $j \in \{1, \ldots, 4\}$ corresponding to the FAS parameter sets from Stafford, and $j \in \{5, 6, 7\}$ corresponding to the FAS parameter sets from Edwards. See Table 9-11 for the explicit mapping between inversion model and index.

	Individual Model Index, j						
	$j = 1$	$j = 2$	$j = 3$	$j = 4$	$j = 5$	$j = 6$	$j = 7$
β_1	0.0093246	0.015448	0.015028	-0.017576	-0.0021433	-0.0019286	-0.0016799
β_2	-0.018101	-0.014822	-0.014326	-0.018907	-0.016334	-0.016575	-0.016871
β_3	4.8799	4.9293	4.8938	4.7881	4.7957	4.7912	4.7821
β_4	2.7549	3.1261	3.3810	2.2447	2.4132	2.3907	2.3552
α_2	0.93194	0.9680	0.99014	1.5298	1.8052	1.8109	1.8134
β_6	-0.00017736	-0.002213	-0.0017315	0.00033613	0.00039617	0.00039302	0.00039768
β_7	0.0011394	0.0037614	0.0030441	0.00011596	0.0010975	0.00098946	0.00087575
β_8	0.57743	0.31348	0.3674	3.8524	1.2166	1.2723	1.3640
β_9	3.7991	2.2479	2.5628	2.7907	2.9621	2.9653	2.9647

The overall expression for the path adjustment can now be written as:

9-37

$$\Delta \ln SA^R = \Delta \ln SA^D + \Delta \ln g(r) + \Delta \ln q(r) - \delta\gamma_q(T, \boldsymbol{M}) R_{RUP}$$

with $\Delta \ln SA^D$ coming from Equation 9-25, $\Delta \ln g(r)$ either coming from Equation 9-28 (for the GMM TI Team seismic parameters) or from explicit ratios of geometric spreading functions (for Edwards' seismic parameters), $\Delta \ln q(r)$ coming from Equation 9-32, and $\delta\gamma_q(T, \boldsymbol{M})$ from Equation 9-34.

To obtain a complete ground-motion model associated with seismic parameter set j, we define:

9-38

$$\ln SA_j(T, rup) = \ln SA_{CY}\left(T, rup; \Delta\sigma_j\right) + \Delta \ln SA^R\left(T, rup; \boldsymbol{\gamma}_j, \Delta\sigma_j, Q_{0,j}, \eta_j\right)$$

In Equation 9-38, the model is defined for a given period and the variable rup is used to encapsulate magnitude $\boldsymbol{M}$ and all necessary distance metrics. The stress parameter $\Delta\sigma_j$, geometric spreading rates $\boldsymbol{\gamma}_j$, quality factor $Q_{0,j}$ and quality exponent η_j are all given subscripts to match the individual model index. That model index identifies which seismic parameter set is used and what the underlying inversion model is.

Equation 9-38 includes two key components. The path correction $\Delta \ln SA^R$ has already been described, but this path correction must be applied to the other key component which is

$\ln SA_{CY}(T, rup;\ \Delta\sigma_j)$. This term is the CY14 GMPE with adjustments made to account for stress parameter differences and is defined in Equation 9-39. The modifications that have been made to this function are highlighted in red font and relate to the enforcement of linear site response for a reference shear-wave velocity of $V_{S30} = 760$ m/s, and a stress parameter adjustment that is made through the coefficient Δc_M.

9-39

$$\begin{aligned}\ln SA_{CY} = c_1 &+ \left\{c_{1a} + \frac{c_{1c}}{\cosh[2\max(\boldsymbol{M} - 4.5, 0)]}\right\} F_{RV} + \left\{c_{1b} + \frac{c_{1d}}{\cosh[2\max(\boldsymbol{M} - 4.5, 0)]}\right\} F_{NM} \\ &+ \left\{c_7 + \frac{c_{7b}}{\cosh[2\max(\boldsymbol{M} - 4.5, 0)]}\right\} \Delta Z_{TOR} \\ &+ \left\{c_{11} + \frac{c_{11b}}{\cosh[2\max(\boldsymbol{M} - 4.5, 0)]}\right\} (\cos\delta)^2 + c_2(\boldsymbol{M} - 6) \\ &+ \frac{c_2 - c_3}{c_n} \ln\left[1 + e^{c_n(c_M + \Delta c_M - \boldsymbol{M})}\right] - (c_2 - c_3)\Delta c_M \\ &+ c_4 \ln\{R_{RUP} + c_5 \cosh[c_6 \max(\boldsymbol{M} - c_{HM}, 0)]\} + (c_{4a} - c_4) \ln\left(\sqrt{R_{RUP}^2 + c_{RB}^2}\right) \\ &+ \left\{c_{\gamma 1} + \frac{c_{\gamma 2}}{\cosh\left[\max\left(\boldsymbol{M} - c_{\gamma 3}, 0\right)\right]}\right\} R_{RUP} \\ &+ c_9 F_{HW} \cos\delta \left[c_{9a} + (1 - c_{9a}) \tanh\left(\frac{R_X}{c_{9b}}\right)\right] \left(1 - \frac{\sqrt{R_{JB}^2 - Z_{TOR}^2}}{R_{RUP} + 1}\right) + \phi_1 \ln\left(\frac{760}{1130}\right)\end{aligned}$$

Note that other standard requirements regarding the application of the CY14 GMPE remain in place. Specifically, for periods less than or equal to 0.3 seconds, if the spectral acceleration predicted by Equation 9-39 falls below the corresponding level of peak ground acceleration, then the peak ground acceleration value should be used.

The adjustment for stress parameter effects that appears in Equation 9-39 via Δc_M is defined in two steps. First, we define the change $\Delta c_{M,FS}$ that would theoretically apply in the Fourier spectral domain. This change is found from Equation 9-40:

9-40

$$\Delta c_{M,FS} = \frac{2}{3} \log_{10}\left(\frac{\Delta\sigma_{SA}}{\Delta\sigma_{CY}}\right)$$

where $\Delta\sigma_{SA}$ is the estimate of target region (South Africa) stress parameter that is consistent with one of the individual models arising from the inversions of the Inversion GMDB, and $\Delta\sigma_{CY}$ is the level of stress parameter implicit within the CY14 GMPE. This latter value was found by Stafford et al. (2022) to be a function of magnitude and ΔZ_{TOR} as previously shown in Equation 9-4. Given the extremely limited information about depths of South African earthquakes, we assume that $\Delta Z_{TOR} = 0$ for all rupture scenarios. Equation 9-41 can therefore be used to define $\Delta\sigma_{CY}$ for use in Equation 9-40.

9-41

$$\ln \Delta\sigma_{CY} = 4.5994 + 0.46241 \min(\boldsymbol{M} - 5.0, 0.0)$$

The values of $\Delta\sigma_{SA}$ to be used within Equation 9-40 are defined in Table 9-9, and the theoretical change to c_M in the Fourier domain is also provided as $\Delta c_{M,FS}$.

Table 9-9. Values of stress parameter $\Delta\sigma_{SA}$ associated with individual models for use in Equation 9-40. These values are constant when used for M of 5 and above.

Model Index *j*	Underlying Inversion	Stress parameter, $\Delta\sigma_{SA}$ (bar)	Parameter change in Fourier domain $\Delta c_{M,FS}$
1	GMM TI Team 1	99.4	0.0000
2	GMM TI Team 2	105.1	0.0161
3	GMM TI Team 3	99.4	0.0000
4	GMM TI Team 4	98.7	-0.0020
5	Edwards L	38.7	-0.2731
6	Edwards C	77.4	-0.0724
7	Edwards U	154.8	0.1283

The values in Table 9-9 relate to the case where **M** are at least 5, and, in this case, we just have constant adjustment terms. More generally, the stress parameters in the target region, $\Delta\sigma_{SA}$, are computed as:

9-42

$$\Delta\sigma_{SA} = \psi_0 \exp[4.5994 + \psi_1 \min(\boldsymbol{M} - 5.0, 0.0)]$$

Table 9-10 provides the values of ψ_0 and ψ_1 for the seven different models.

Table 9-10. Values of stress parameter $\Delta\sigma_{SA}$ associated with individual models for use in Equation 9-42. Note that for magnitudes of at least 5, these parameters lead to stress parameter values that match those in Table 9-9.

Model Index *j*	Underlying Inversion	Parameter ψ_0	Parameter ψ_1
1	GMM TI Team 1	1.0	0.46241
2	GMM TI Team 2	1.05743	0.46241
3	GMM TI Team 3	1.0	0.25596
4	GMM TI Team 4	0.99283	0.46241
5	Edwards L	0.38930	0.46241
6	Edwards C	0.77860	0.46241
7	Edwards U	1.55719	0.46241

The second step in defining Δc_M for use in Equation 9-39, is to then adjust the values of $\Delta c_{M,FS}$ for the Fourier domain (in Table 9-9) to their corresponding values in the response spectral

domain. For that process we require the coefficients c_2 and c_3 from CY14 (the same coefficients that are used in the GMPE). Note that the first of these is period-independent and equal to $c_2 = 1.06$ while c_3 varies with period as tabulated in CY14.

Using these values of c_2 and c_3, we can then define:

9-43

$$\Delta c_M = \chi \times \Delta c_{M,FS}$$

where χ is found from Equation 9-44:

9-44

$$\chi = \begin{cases} \dfrac{c_{3,FS} - c_2}{c_3 - c_2} & \text{for } \Delta c_{M,FS} < 0 \\ \dfrac{c_{3,FS} - c_{2,FS}}{c_3 - c_{2,FS}} & \text{for } \Delta c_{M,FS} \geq 0 \end{cases}$$

in which $c_{2,FS}$ and $c_{3,FS}$ are the theoretical values of these parameters in the Fourier spectral domain with values equal to $c_{2,FS} = \frac{1}{2}\ln(10) = 1.15$ and $c_{3,FS} = \frac{3}{2}\ln(10) = 3.45$. Again, the values of c_2 and c_3 in Equation 9-44 are the published values from CY14 that are also used in Equation 9-39.

It must be noted that the stress parameter values presented in Table 9-9 for the models of Edwards do not match the values previously presented in Table 9-5 for the same parameter sets. The reason for this is that Edwards only estimated stress parameter values for the empirical data and did not find any magnitude dependence of the stress parameter within the limited magnitude range covered by that data.

When making predictions for the rupture scenarios of interest for the hazard calculations, the magnitude-independence of the Edwards stress parameters is problematic. The GMM TI Team did not receive any actionable recommendation from Edwards regarding how his stress parameters obtained for the recordings of small-magnitude earthquakes could be mapped into values relevant for larger events. Edwards did comment upon the fact that his models underpredicted the stress parameter for the largest event in the dataset he considered, which was the only event within the magnitude range of interest for the hazard calculations. The GMM TI Team assumed that the magnitude-dependence of the CY14 GMPE (as inverted by Stafford et al., 2022) was valid in South Africa, so stress parameters for the Edwards inversion models are obtained by *pro rata* scaling of this function after assuming that Edwards' stress parameters reflect the mean magnitude of the South African database.

9.2.4 Technical basis for weights

Within the logic tree used for the preliminary hazard calculations, each of the models associated with the distinct FAS parameter sets was assigned a weight, but for the final hazard calculations, the seven individual models are combined into a single model so that no logic tree node is devoted to these FAS parameter sets. The combined model is defined and described within Section 9.2.5, but some comments upon the basis of the weights that are used in that section are warranted here.

The seven models are not weighted equally when combined, as defined in Section 9.2.5. Between the FAS inversions model from Edwards and response spectral inversion models of the GMM TI Team, the team had a slight preference for the latter. Although the GMM TI Team's approach of directly inverting response spectral data within the RVT framework has far less precedent than the Fourier spectral inversions performed by Edwards, the former approach is designed with GMM adjustments in mind. In contrast, we have explained that the original FAS parameters obtained by Edwards did not work well for predicting response spectral amplitudes, and Edwards' subsequent calibration was required to centre his final models. This calibration step was done while retaining the path scaling elements obtained in the initial FAS inversions. Edwards' final FAS parameter sets are not the result of a complete inversion specifically designed to match the South African response spectral data. In addition, to make forward predictions using Edwards' FAS parameter sets, the GMM TI Team needed to make assumptions regarding the magnitude scaling of the stress parameter, the method for accounting for near-source saturation, and distance metrics to be used within duration models. In contrast, GMM TI Team's inversion models were developed in a framework that was directly designed for developing host-to-target model adjustments, and no additional decisions were required from the GMM TI Team (those decisions still had to be made, but the inversions are conditionally dependent upon the decisions rather than being independent). The strong historical precedent of Edwards' approach to obtaining FAS parameters was therefore offset by the practical challenges of adapting his results for use within the model adjustment framework of this project, and this resulted in the GMM TI Team having a slight preference for the response spectral inversion models. To reflect this slight preference, the GMM TI Team collectively gave the response spectral models a weight of 4/7 and the Fourier spectral models a weight of 3/7.

Within the response spectral inversion models of the GMM TI Team, all four models were given equal weight – so a final weight of 1/7 each. For the Fourier-based inversion models from Edwards, a slightly different approach was adopted. If uniform weights were used for the three Edwards stress parameter alternatives, then the implied variability of stress parameter is larger than the value Edwards obtained during his FAS inversions. Table 9-5 shows the logarithmic standard deviation for the stress parameter is $\sigma_{\log_{10}\Delta\sigma} = 0.59$ computed from 134 events with a mean magnitude of just under 2.9. These numbers led to a standard error in the estimate of the mean logarithmic stress parameter of $s.e.[\log_{10}\Delta\sigma] = \frac{0.59}{\sqrt{134}} = 0.051$. Note that adopting equal weights for the three stress parameter values implies a standard error of 0.142, which is almost three times larger than the statistical standard error of 0.051.

The value of 0.051 is not an appropriate target against which to calibrate weights on the stress parameter alternatives for multiple reasons:

- The variability of 0.59 is clearly dominated by variations among the smallest events. The stress parameter estimates for these events are inherently more variable due to:
  - issues with local-to-moment magnitude conversion (Edwards assumes equivalence of the scales for $M_L \geq 2.5$, but uses data from smaller events to define his stress parameter distribution);
  - less spatial averaging arising from the smaller source dimensions, and greater depth variability, of the smaller events; and,

  - corner frequencies are harder to estimate given that the broadband fitting used to determine these is conditional on the site kappa that is found from a limited spectral bandwidth, *i.e.*, κ_r values that lead to κ_0 are less reliable for the smaller events, and this has a knock-on effect for the reliability of the f_c estimates.

- All of the events have magnitudes $< M_{min}$ considered for the hazard calculations.
- The GMM TI Team has to make assumptions regarding the magnitude dependence of the stress parameter to move from Edwards' best estimate of stress parameter for the South African data, to estimates relevant for the hazard calculations. If we were certain that stress parameter values were constant across magnitude, the 134 events would provide robust constraint for the stress parameter for events of any magnitude. When uncertainty exists regarding how stress parameter values vary, the effective sample size is greatly reduced.

For the above reasons, the GMM TI Team believes that the 0.051 target is too low, but an approach of equal weighting also gives a level of uncertainty in the mean logarithmic stress parameter of 0.142 which is too high. The weighting of the Edwards alternative stress parameter branches is therefore specified to provide an effective uncertainty of the logarithmic stress parameter that lies roughly between these values at a level that is approximately double the statistical value of 0.051. Specifying relative weights of 0.2, 0.6, 0.2 on the lower, central and upper values of the stress parameter (of 15, 30 and 60 bar) leads to an implied logarithmic standard deviation of 0.11 $\log_{10}$ units.

The weights on the three FAS-based inversion models from Edwards are therefore non-uniform, and they are assigned values of 0.086, 0.256 and 0.086 for the lower, central and upper branches. These weights come from the weight of 3/7 assigned to the FAS-based inversion models, multiplied by the relative weights of 0.2, 0.6 and 0.2.

Table 9-11 provides the final set of weights assigned to the individual models associated with the seven FAS parameter sets.

9.2.5 Development of single host-to-target adjusted GMPE

Edwards and the GMM TI Team collectively proposed seven sets of seismic parameters that were used to make host-to-target adjustments to the CY14 GMPE. These seven candidate models could either be used individually, as was done for the preliminary hazard calculations, or could be combined into a meta-model. The GMM TI Team took the latter option and constructed a meta-model that is comprised of a model for the best estimate of the logarithmic mean and a model for epistemic uncertainty in this mean. These components collectively characterise the centre of the ground-motion distribution and its uncertainty, while the aleatory variability model defined in Section 9.3 completes the specification of the overall meta-model. Hazard results should not be sensitive to the choice to use a meta-model over the seven individual models and the computational demands are similar as well (because, as explained in the following sections, the GMM TI Team did not derive a new parametric model within the meta-model, but rather used the weighted combination of individual predictions from the seven individual models). From a conceptual viewpoint the meta-model better describes the reality that we believe that there is some central level of logarithmic spectral acceleration for each rupture scenario and some associated uncertainty. The use of mean and uncertainty in the meta-model is more descriptive of that conceptual model than the use of seven individual

models. The reason being that any one of those individual models does not provide information about the distribution of logarithmic spectral ordinates. The information related to the distribution only arises when the seven are considered collectively.

The development of the components related to the logarithmic mean and its uncertainty are described in Sections 9.2.2 and 9.2.3, but these depend directly upon the seven sets of seismic parameters developed by Edwards and the GMM TI Team. Each of the seven models developed from the seismic parameters was assigned a weight that is specified in Table 9-11. The justification for these weights is provided in 9.2.4. The first four models relate to the response spectral inversions from the GMM TI Team, while the last three relate to the FAS-based inversions from Edwards.

Table 9-11. Weights assigned to the individual models associated with FAS parameter sets presented in this section.

Model Index j	Underlying Inversion	Weight, w_j	Collective Weight
1	GMM TI Team 1	0.143	0.571
2	GMM TI Team 2	0.143	
3	GMM TI Team 3	0.143	
4	GMM TI Team 4	0.143	
5	Edwards L	0.086	0.429
6	Edwards C	0.256	
7	Edwards U	0.086	

9.2.5.1 Final specification of mean backbone model

The mean backbone model is defined as the weighted average over the seven adjusted versions of CY14 using the individual seismic parameter sets described in Sections 9.2.2.2 through 9.2.2.4. The mathematical expression for the weighted mean is shown in Equation 9-45 and is evaluated for each rupture scenario, rup, represented within the seismic source model.

9-45

$$\mu_{\ln SA}(rup) = \sum_{j}^{7} w_j \times \ln SA_j(rup)$$

The $\ln SA_j(rup)$ terms represent the individual model predictions for model j and rupture scenario rup. The first four models, $j \in \{1, \ldots, 4\}$, correspond to the response spectral inversions from the GMM TI Team, while the final three models, $j \in \{5, \ldots, 7\}$, correspond to the FAS-based inversions from Edwards (Table 9-11). The weights for the individual models were previously defined in Table 9-11. Figure 9-36 shows the weighted mean predictions for several scenarios. The weighted model-to-model standard deviations, depicted as shaded bands in Figure 9-36, are shown separately in Figure 9-37.

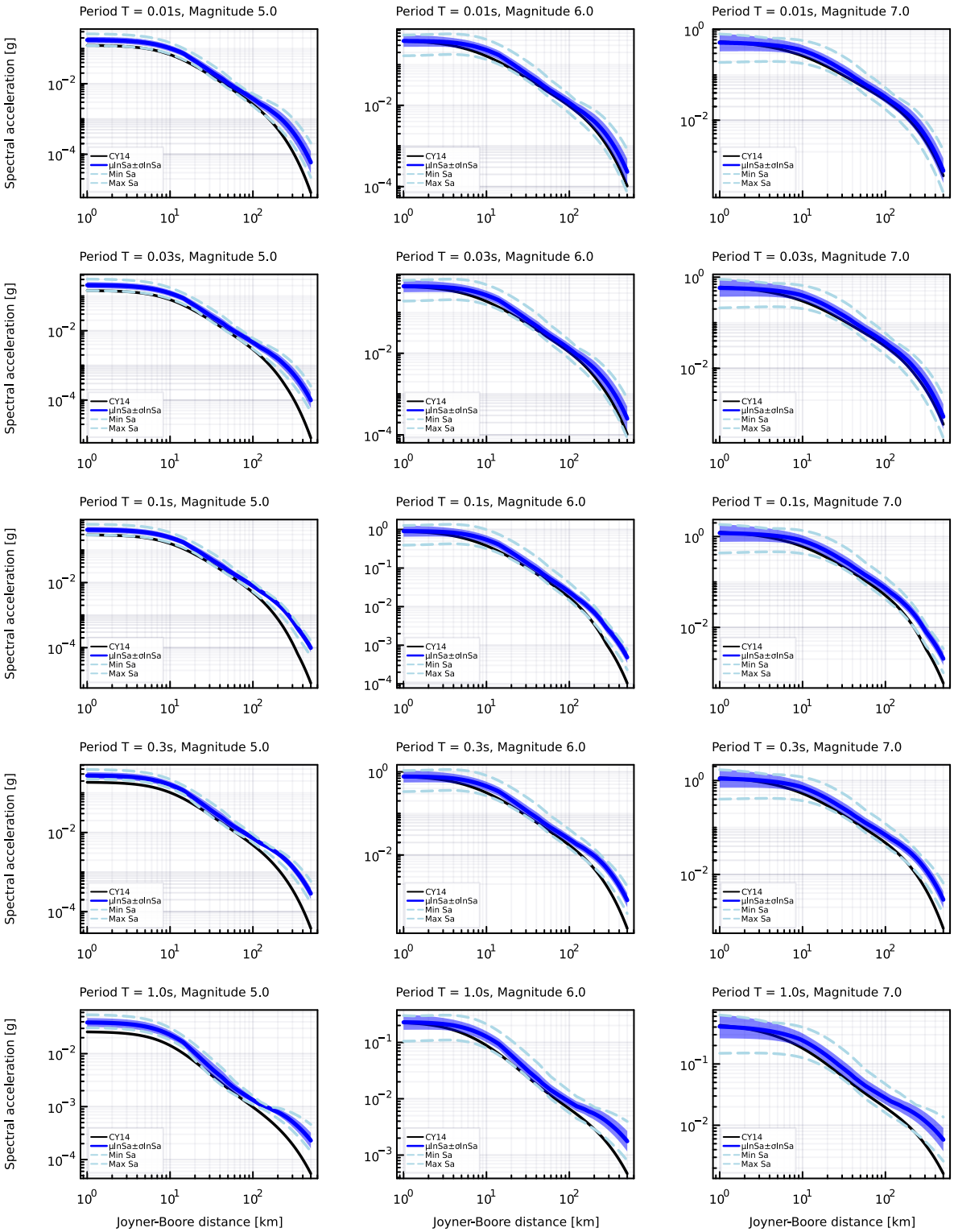

Figure 9-36. Weighted logarithmic mean spectral amplitudes associated with Equation 9-45 and comparison with the unadjusted CY14 GMPE (solid black lines). The model-to-model variability is shown by the shaded regions while the most extreme predictions from individual models are shown with dashed light blue lines. Rows correspond to distinct periods, annotated in the upper left of each panel, while columns correspond to magnitudes 5, 6 and 7, from left-to-right respectively.

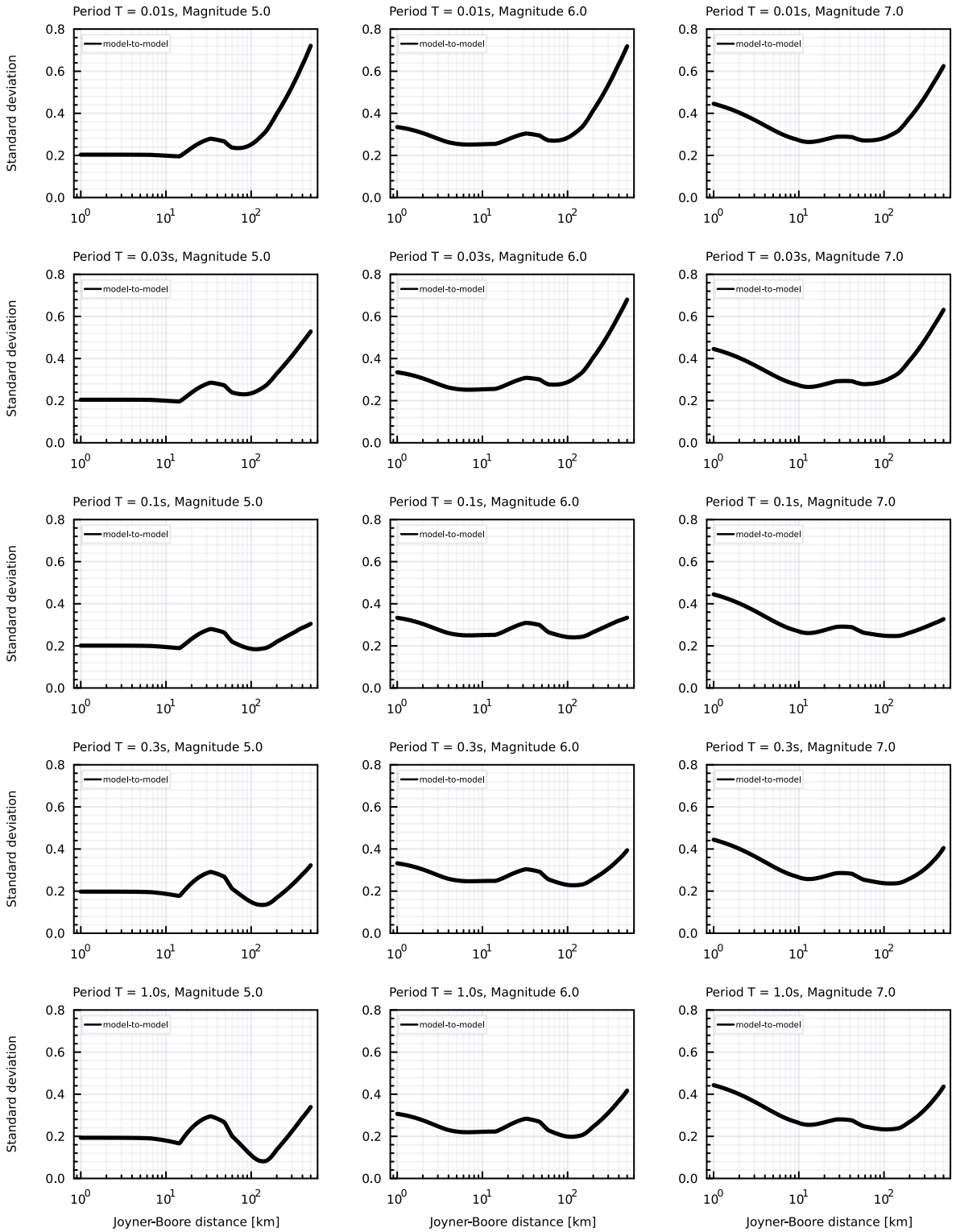

Figure 9-37. Weighted model-to-model standard deviation around the logarithmic mean spectral amplitude associated with Equation 9-45. The standard deviations shown in this figure correspond to the shaded regions of Figure 9-36. Rows correspond to distinct periods, annotated in the upper left of each panel, while columns correspond to magnitudes 5, 6 and 7, from left-to-right respectively.

9.2.5.2 Evaluation of the final model

The GMM TI Team provides an evaluation of the adjusted models in terms of visual comparisons of the predictions for scenarios of interest. There are no data from rupture scenarios of hazard significance to judge the model predictions against, but the individual models are known to match the South African data well for the rupture scenarios represented within the Inversion GMDB. Figure 9-38 shows the predictions of the seven individual models along with the weighted mean model from Equation 9-45, and the unadjusted predictions from CY14. The figure shows the distance scaling for a range of periods and magnitudes that cover most scenarios of interest for the hazard calculations. Figure 9-39 shows the same predictions in a less congested manner and the lines are coloured in accordance with the underlying inversion approach.

Both figures show the expected trends that had been suggested from the GMM TI Team's referenced empirical analyses, i.e. that relatively modest adjustments are required for the source scaling (the amplitudes at very short distance are similar to, or a little higher than, the CY14 predictions), and that the amplitudes at large distances for the adjusted models are significantly greater than those for the unadjusted CY14 GMPE.

The source-related adjustments to the logarithmic mean are relatively mild and the distance scaling adjustments increase in significance as the distance itself increases, thus the scaling of the logarithmic mean amplitudes for near-source scenarios do not vary greatly. This is consistent with the modelling framework in which we assume that the Chiou and Youngs (2014) model already captures the main features of scaling for these scenarios (and we are implicitly assuming that the Chiou and Youngs (2014) model provides predictions for these scenarios that are representative of the global distribution of amplitudes from these scenarios). As there are no data to validate this assumption the final model has increased levels of epistemic uncertainty for near-source scenarios. The basis of this epistemic uncertainty model is detailed in Section 9.2.69.2.6.3 in particular. In Bommer and Stafford (2020), before models are judged on the basis of adaptability they are first screened for applicability. In that context, the Chiou and Youngs (2014) is regarded as having functional terms that represent the key attributes of ground-motion scaling for scenarios of interest to the hazard (this includes near source saturation effects, and other factors related to near-source amplitudes from moderate-to-large magnitude rupture scenarios). For the site conditions relevant for this project (i.e., stiff sites), Gregor et al. (2014) shows that the Chiou and Youngs (2014) model is commonly near the centre of the distribution of predictions from the NGA West2 ground-motion models. This is true for near-source saturation scaling and finite-fault scaling such as hanging wall effects. While we cannot prove that the model is centred with respect to data from moderate-to-large magnitude events, it is reasonable to assume that the model is at least approximately centred with respect to global ground-motion levels given its central position amongst the NGA West2 models.

As the definition of the mean is the weighted average over the seven individual models, it does not require any branching within the logic-tree. Rather, it simply represents the aggregation of the seven individual models that correspond to the FAS inversions from Edwards and the GMM TI Team.

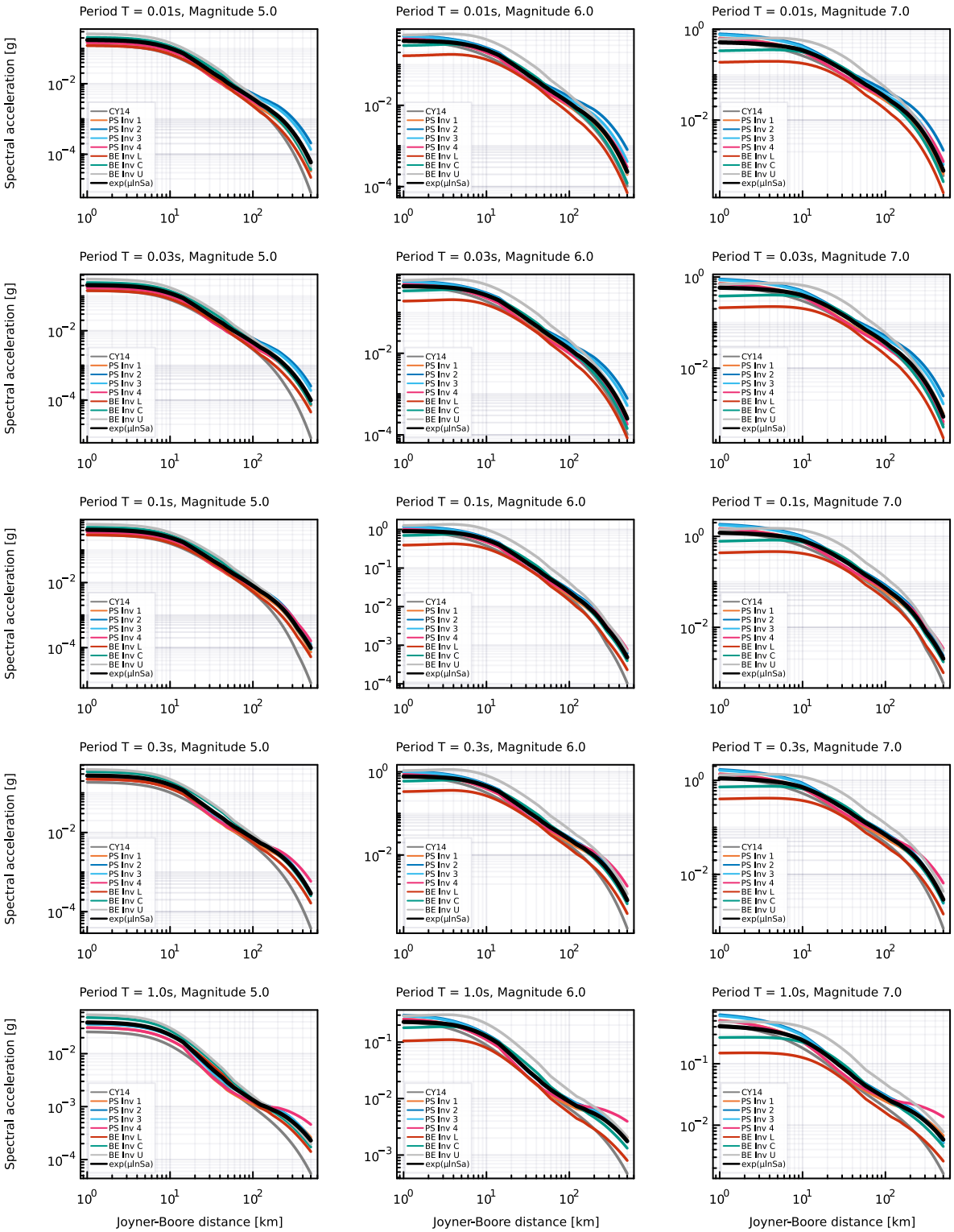

Figure 9-38. Comparison of the predictions for the individual models, the weighted mean model, and the unadjusted CY14 GMPE. Rows correspond to distinct periods, annotated in the upper left of each panel, while columns correspond to M 5, 6 and 7, from left-to-right respectively. 'PS Inv – X' represents the 'Pseudo-Spectral' (response spectral) inversions of the GMM TI Team (with $X \in \{1, \ldots, 4\}$); 'XX; BE Inv – X' represents the FAS inversions of 'Ben Edwards' (with $X \in \{L, C, U\}$).XX

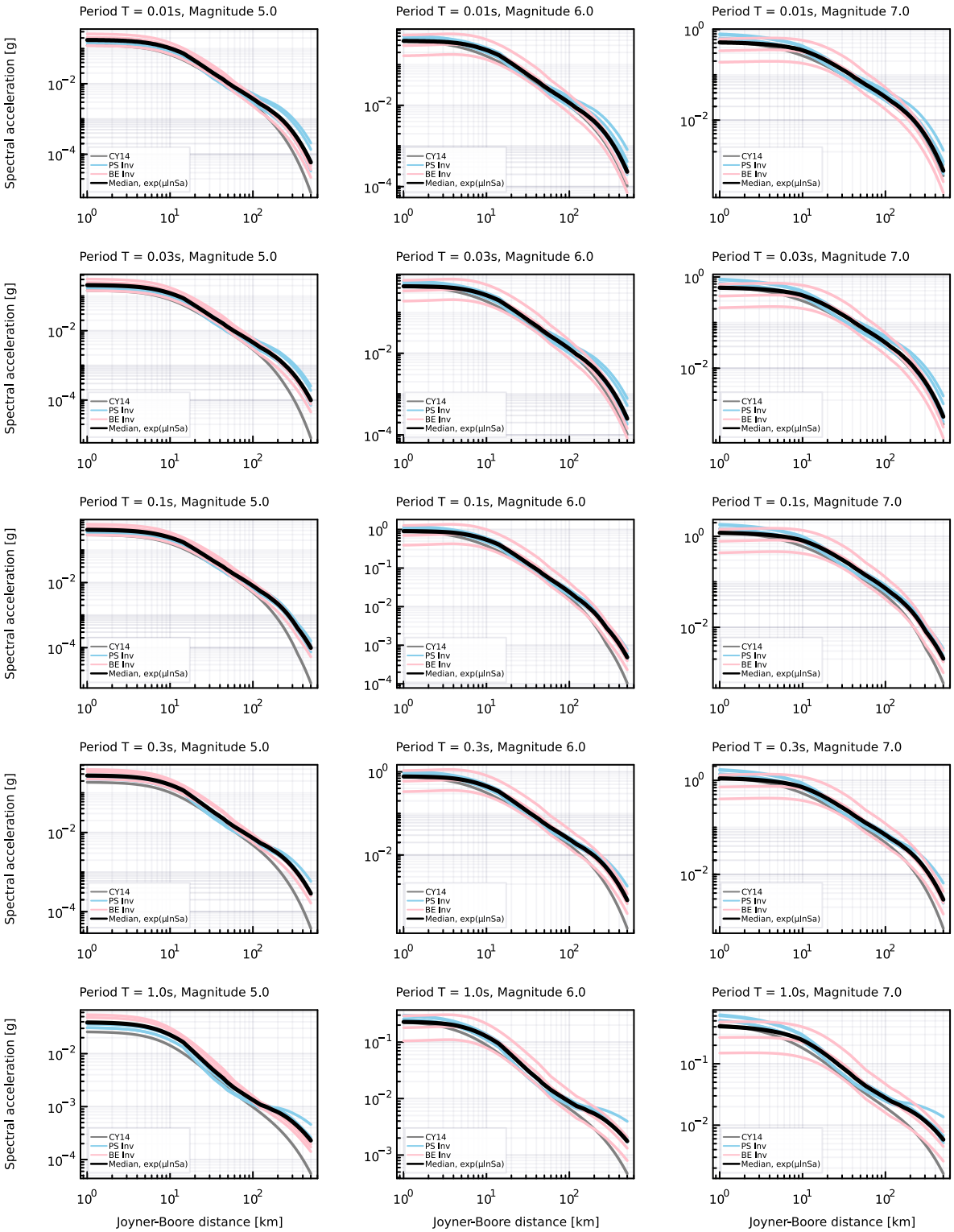

Figure 9-39. Comparison of the predictions for the individual models and the unadjusted CY14 GMPE. Models are grouped according to the underlying inversion approach, with pink lines used for the FAS-based inversion models from Edwards ('BE Inv'), and light blue used for the response spectral models from the GMM TI Team ('PS Inv'). Rows correspond to distinct periods, annotated in the upper left of each panel, while columns correspond to M 5, 6 and 7, from left-to-right respectively.

9.2.6 Development of epistemic uncertainty for median reference rock

9.2.6.1 Background and sources of epistemic uncertainty

There are numerous sources of epistemic uncertainty within a GMM. Some of these sources of epistemic uncertainty are discussed by Baker et al. (2021) as summarised in Figure 9-40.

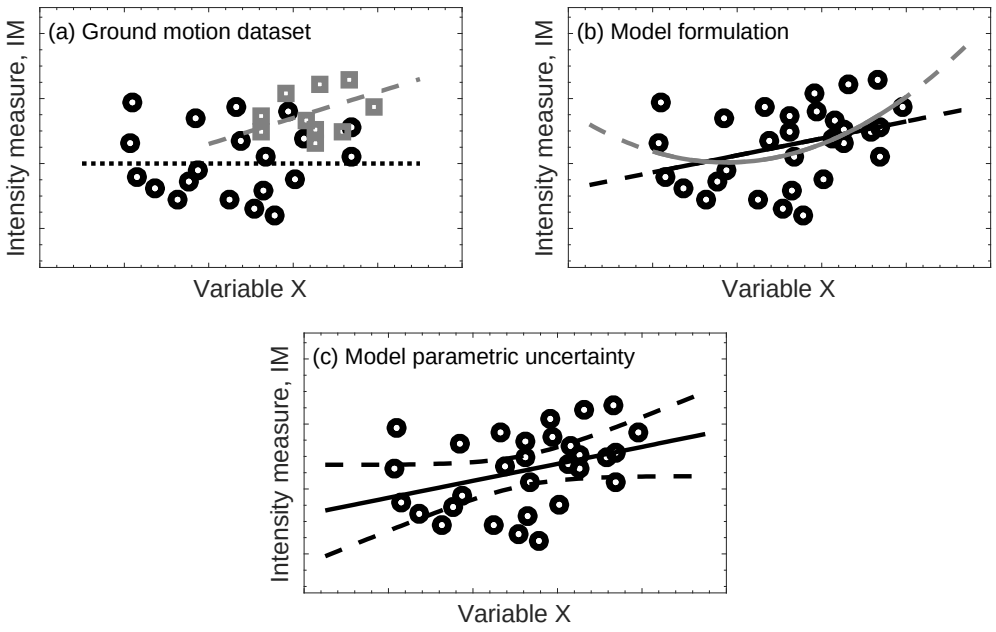

Figure 9-40. Contributions to epistemic uncertainty in ground-motion modelling. Panel (a) represents epistemic uncertainty associated with dataset compilation and selection. Panel (b) represents epistemic uncertainty associated with functional form specification, and (c) represents the within-model parametric uncertainty associated with a given dataset and functional form. From Baker et al. (2021).

Figure 9-40 a represents the epistemic uncertainty that arises from analysts selecting different subsets of data from a ground-motion database. The black circles and grey squares represent subsets of a database selected by model developers. This is similar to the present project, where Edwards and the GMM TI Team started with a common database but used different criteria and judgement to obtain their individual datasets. The differences between the black dotted and grey dashed lines fitted to those subsets reflects epistemic uncertainty that is attributed to database compilation and selection issues.

Figure 9-40 b represents the epistemic uncertainty that comes from having multiple models that do a similarly good job of matching a given dataset. The black and grey lines in the figure represent two alternative functions that provide similar predictions over the range of variable X for which there is empirical support. In the context of the current project, Edwards and the GMM TI Team each derived corrected logarithmic signal moments and used these to select (and calibrate) models for geometric spreading. For the same set of signal moments, a number of alternative parameterisations of the geometric spreading models could have been proposed that would have had similar statistical performance. When purely empirical curve-fitting is performed, differences in functional forms can be quite large and can lead to large model-to-model differences, especially when extrapolating. As more physical considerations are used to inform the selection of functional forms, the smaller the model-to-model differences tend to be (Baker et al., 2021).

Figure 9-40 c shows that for any finite dataset, and any functional form chosen, the statistical calibration of the model coefficients will include best estimates of fixed effects as well as parametric uncertainties (and covariances) of those fixed effects. When performing a regression analysis, the objective is usually not to simply fit the data as well as possible, but rather to reveal the characteristics of the underlying process that generated the data. The 'fixed effects' are model parameters associated with the underlying process that would not be sensitive to the specific composition of the finite dataset used to calibrate the model. We contrast 'fixed effects' with 'random effects', where the latter are the apparently random deviations away from the fixed effects. In the context of ground-motion modelling, we generally want a model that will predict ground-motions for any future earthquake, but our datasets only contain recordings for a particular set of past events. Each of those events will have their own specific features so we use fixed effects to represent the scaling we expect to observe on average for all future events, and we include random effects to account for any event-specific peculiarities within the historical events we analyse. We will never be able to perfectly uncover the parameters of the underlying process and so we will always have parametric uncertainty. The effects of this uncertainty (for all model parameters) lead to confidence intervals in the prediction of the future mean ground-motions. The dashed lines in this figure represent that propagated parametric uncertainty.

For the present project, the GMM TI Team considered all the above contributions and gave particular focus to those attributes that are likely to be most hazard significant on the basis of preliminary hazard calculations for the target site.

The overall model for epistemic uncertainty in the mean is comprised of four components:

- Model-to-model variability, σ_{M2M}^2
- Conditional parametric variance associated with near-source saturation, σ_{CSAT}^2
- Additional epistemic uncertainty, σ_{ADD}^2
- Reduction factor for correlation of epistemic uncertainty, ζ_{COR}

These four components interact to define the standard deviation of the mean logarithmic spectral acceleration as defined in Equation 9-46.

9-46

$$\sigma_{\mu_{\ln Sa}} = \zeta_{COR}\sqrt{\sigma_{M2M}^2 + \sigma_{CSAT}^2 + \sigma_{ADD}^2}$$

Each of the components of Equation 9-46 are defined in Sections 9.2.5.2 through 9.2.5.5. Stafford (2022) demonstrated how multiple contributors to epistemic uncertainty could be represented within a three-branch meta-model. That approach requires the specification of correlations between different elements of epistemic uncertainty. The GMM TI Team decided to adopt this approach and it is described in Section 9.2.6.5.

9.2.6.2 Model-to-model variability

The variance arising from model-to-model differences among the seven individual model predictions is defined as the weighted variance in Equation 9-47. The relevant weights for use in this equation were previously provided in Table 9-11.

$$\sigma_{M2M}^2 = \sum_j^7 w_j \times \left(\ln Sa_j - \mu_{\ln Sa}\right)^2$$

This model-to-model variance will change with rupture scenario. Multi-GMPE approaches to logic-tree construction have been criticised, *e.g.*, Bommer and Stafford (2020), for not having suitable control over levels of uncertainty and for allowing 'pinching' to occur. There may be some concerns that this could also occur for the present model. This is countered by two distinct effects. Firstly, the use of the additional epistemic uncertainty σ_{ADD}, described in Section 9.2.6.4, ensures that complete pinching can never occur. Secondly, the FAS-based models associated with the inversions of Edwards only vary due to differences in stress parameter scaling, while the path scaling is effectively the same in all models, meaning that relative model positions are preserved with distance for these models (Figure 9-39).

The level of σ_{M2M} naturally arises from the model-to-model differences among the adjusted GMPEs. Those individual models reflect differences in many model development characteristics, such as:

- the selection and processing of ground-motion data (between Edwards and the GMM TI Team),
- the parameterisation of stress parameter scaling,
- functional forms for geometric spreading,
- frequency dependence of anelastic attenuation,
- treatment of site response,
- components of the RVT framework (RMS duration and peak factor models), and
- differences in excitation duration models.

Collectively, these aspects primarily relate to panels (a) and (b) of Figure 9-40.

The weights assigned to the models also influences the level of model-to-model variability. Figure 9-41 shows the proposed model (equivalent to the results previously shown in Figure 9-37) along with an alternative model corresponding to equal (uniform) weighting over all seven models (in practice, this only influences the weights for the Edwards inversion models as the GMM TI Team models already had 1/7 weights applied to them). In general, the lowest levels of σ_{M2M} are around 0.2 natural logarithmic units, while a representative average value is on the order of 0.3 units. Note that these values are lowest in the near field where stress parameter differences are mainly driving the small model-to-model variations along with some degree of near-source duration scaling for the larger magnitudes. At large distances, and for the short periods in particular, the model-to-model differences are greatest due to anelastic attenuation parameters playing an increasingly dominant role. The differences in frequency-dependent or frequency-independent quality factor models are especially important at the large distances and short periods.

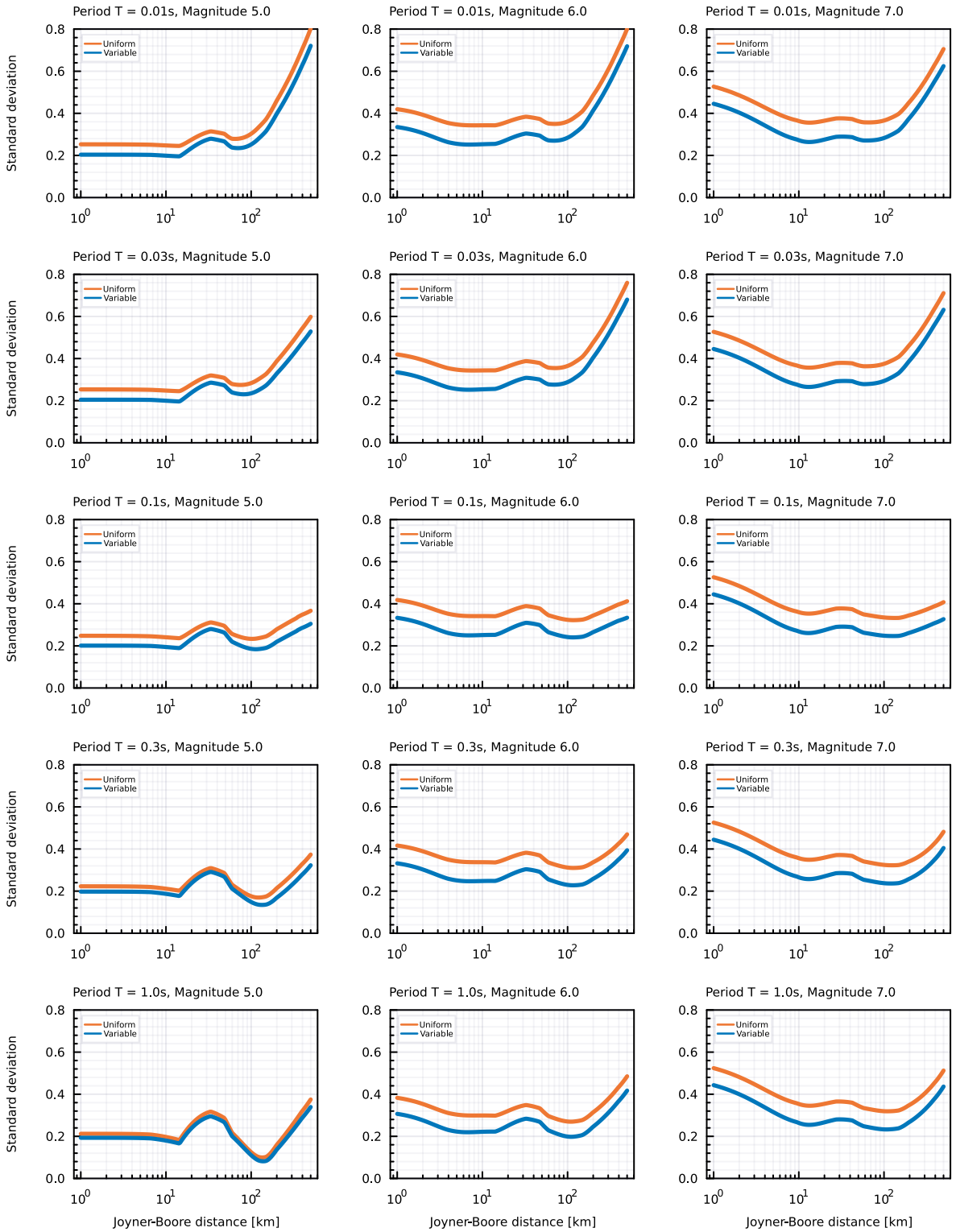

Figure 9-41. Model-to-model variability arising from the weighted variance of the seven individual ground-motion models. The orange lines show the extent of model-to-model variability when uniform weighting is applied to all seven models. The blue lines show the proposed model with the non-uniform weighting of Table 9-11. Rows correspond to different periods, as annotated in the upper left of the figure panels: 0.01, 0.03, 0.1, 0.3 and 1.0 seconds from top to bottom. Columns correspond to magnitudes, showing 5, 6, and 7 from left to right.

There is no 'correct' target level for this model-to-model variability. It is just one component of the overall model for epistemic uncertainty, and so does not need to be evaluated in isolation.

9.2.6.3 Parametric variance due to near-source saturation

Edwards and the GMM TI Team made assumptions about near-source saturation effects and those assumptions influence the implied near-source amplitudes (e.g., Boore, 2012; Yenier and Atkinson, 2015). As the data at short distances is extremely limited, it is hard to know which near-source saturation model is most appropriate for South Africa. For that reason, an investigation was carried out to understand how the seismic parameter sets and predicted ground-motion amplitudes would vary if alternative assumptions regarding the near-source saturation models had been made. The same exercise has recently been performed by Stafford (2022) using the New Zealand crustal ground-motion data, and that exercise was repeated here.

Taking the first of the GMM TI Team's four inversion models that made use of the Boore and Thompson (2015) near-source saturation model as the starting point, a new set of inversions was performed. These inversions used the same dataset and the same numerical methods and only changed the modelling of the near-source saturation. The models play a role in defining the equivalent point source distance that is used within the stochastic method. The equivalent point source distance is defined as:

9-48

$$R_{PS} = [R_{RUP}^{n} + h(\boldsymbol{M})^{n}]^{\frac{1}{n}}$$

where $h(\boldsymbol{M})$ is the saturation length provided by a near-source saturation model, and n is an exponent that determines how quickly the point-source distance R_{PS} transitions from $h(\boldsymbol{M})$, at very small values of the rupture distance R_{RUP}, towards the R_{RUP} value itself, as the distance increases or the magnitude decreases. Common values of the exponent are $n = 1$ and $n = 2$.

For the near-source saturation investigations, a total of five models were considered:

- Boore and Thompson (2015), with $n = 1$ and $n = 2$
- Stafford et al. (2022) inversion of CY14 (with $n = 1$)
- Yenier and Atkinson (2015), with $n = 1$ and $n = 2$

The saturation lengths for these models are shown in Figure 9-42, using both linear and logarithmic axes to highlight the similarities and differences among the models.

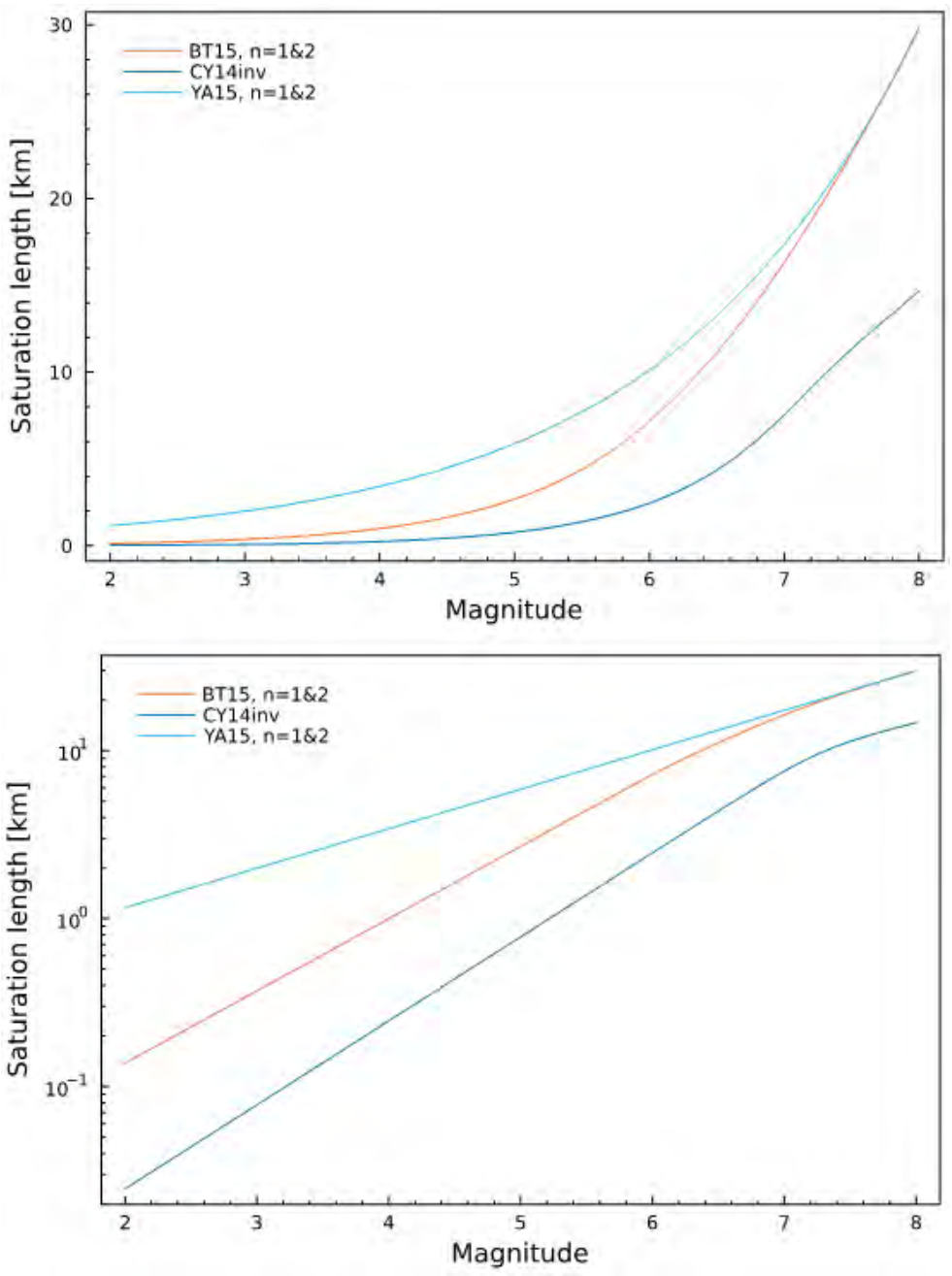

Figure 9-42. Near-source saturation lengths of the models considered within the saturation investigations. The top panel shows the lengths on a linear scale, while the bottom shows the lengths on a logarithmic scale. BT15 = Boore and Thompson (2015), YA15 = Yenier and Atkinson (2015) and CY14inv = Stafford et al. (2022).

Performing inversions with these different near-source saturation models leads to sets of seismic parameters that are all slightly different, but that behave similarly well in terms of matching the Inversion GMDB. Figure 9-43 shows forward RVT predictions using these saturation models and the associated seismic parameters. The reason why the models perform similarly against the Inversion GMDB can be appreciated by looking at the predictions for the smallest magnitude shown in Figure 9-43 (**M** 5). For these cases, the five different models quickly converge to essentially the same level of spectral acceleration as one moves away from the near-source and toward greater distances. When even smaller magnitudes are considered, this convergence occurs at even shorter distances. As the Inversion GMDB is

comprised primarily of smaller magnitudes at large distances, there is little difference in the performance of the near-source saturation models.

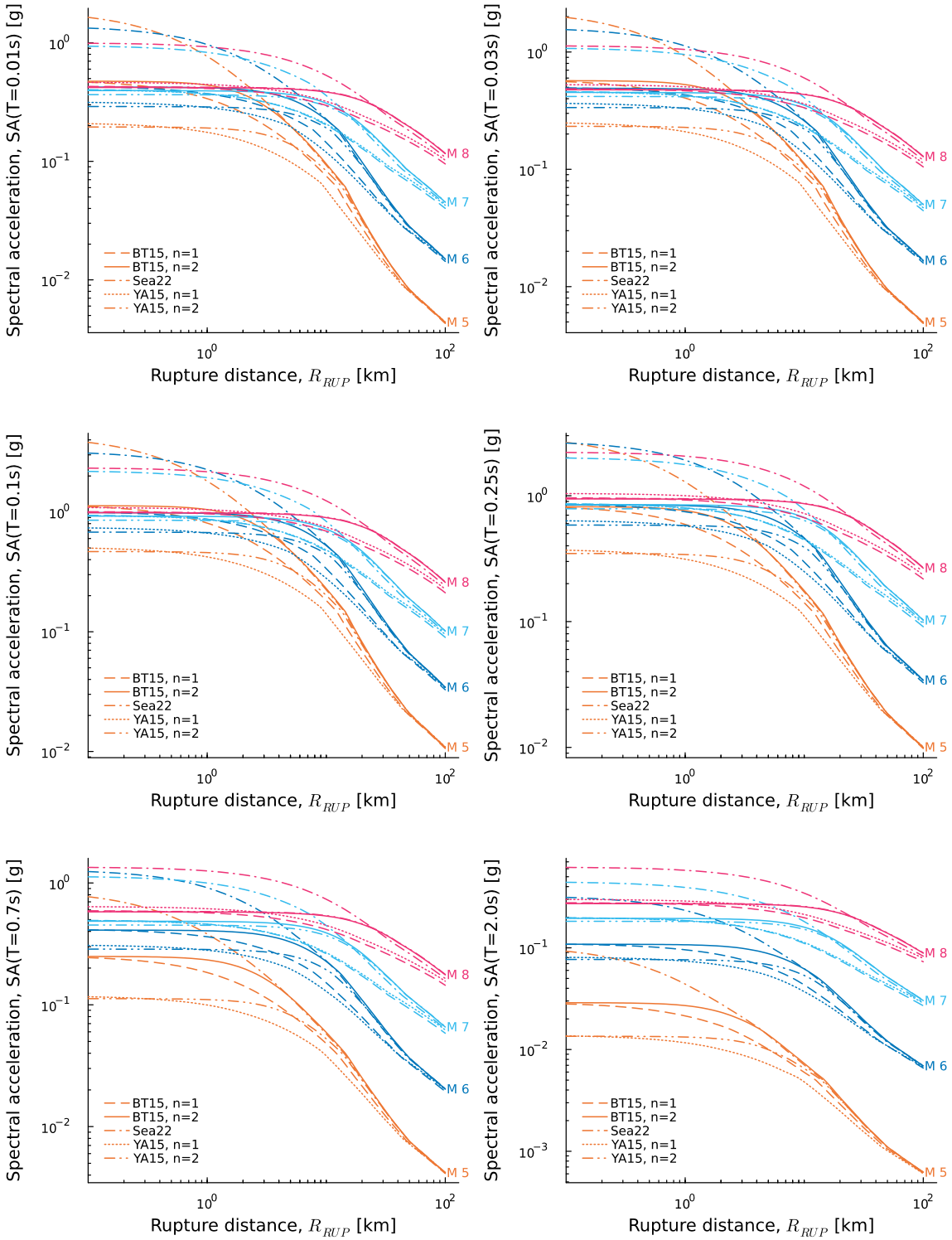

Figure 9-43. RVT-based predictions of response spectral ordinates against distance for a range of periods and magnitudes. Colours correspond to the magnitude values that are also annotated on the figure panels. The axes specify the period being predicted. BT15 = Boore and Thompson (2015), YA15 = Yenier and Atkinson (2015) and CY14inv = Stafford et al. (2022).

The implication is that any of these near-source saturation models will match the Inversion GMDB data well because these data are associated with rupture scenarios where the five different models are all essentially predicting the same levels of acceleration. At the same time, the implication of observing the spread of model predictions at very short distances is that one cannot use the Inversion GMDB to determine which of the five saturation models is most appropriate. For short-distance rupture scenarios, such as those that arise within the host seismic zone, the implications of selecting one saturation model over another are significant.

To address this element of epistemic uncertainty, the GMM TI Team decided to develop a model to represent the model-to-model variability that is associated with different near-source saturation models. The results of Figure 9-43 provide the basis for this model. At each period, including many that are not shown in the figure, the standard deviation of logarithmic spectral amplitudes is computed over magnitude-distance space. Figure 9-44 shows contour plots of this standard deviation for the periods shown in Figure 9-43. The patterns across periods are very similar. The largest variability occurs at short distances, and the variability tends towards zero as the distance increases. This behaviour is seen for all periods and magnitudes, but the greatest degree of variability that occurs at short distances is also clearly a function of magnitude, with the greatest variability seen for the smallest magnitudes, and very limited magnitude dependence seen for magnitudes above 7. These observations form the basis of the parametric model that is selected to represent these standard deviations over magnitude and distance.

At each period, the model chosen to represent the near-source saturation involves a function of magnitude and distance that is defined through Equations 9-49 and 9-50:

9-49

$$\sigma_{SAT}(\boldsymbol{M}, R_{RUP}; T) = \psi(\boldsymbol{M}; T) - \frac{\psi(\boldsymbol{M}; T)}{1 + \exp\left[-\frac{\ln R_{RUP} - \psi_3(T)}{\psi_4(T)}\right]}$$

and

9-50

$$\psi(\boldsymbol{M}; T) = \psi_1(T) + \psi_2(T)[\min(\boldsymbol{M}, 7) - 6]$$

Regression analyses were performed to obtain the parameters $\{\psi_1, \psi_2, \psi_3, \psi_4\}$ at each period. Figure 9-45 shows how these parameters vary with period, and the variation is very subtle. Therefore, a revised regression was performed using the functions in Equation 9-51 and 9-52 in which the parameters are period independent. The model for epistemic uncertainty associated with near-source saturation effects is therefore:

9-51

$$\sigma_{SAT}(\boldsymbol{M}, R_{RUP}) = \psi(\boldsymbol{M}) - \frac{\psi(\boldsymbol{M})}{1 + \exp\left[-\frac{\ln R_{RUP} - \psi_3}{\psi_4}\right]}$$

and

$$\psi(\boldsymbol{M}) = \psi_1 + \psi_2[\min(\boldsymbol{M}, 7) - 6]$$

The parameters of Equations 9-51 and 9-52 are defined as: $\psi_1 = 0.6543$, $\psi_2 = -0.17$, $\psi_3 = 1.246$ and $\psi_4 = 1.388$, and this final model is illustrated in Figure 9-46.

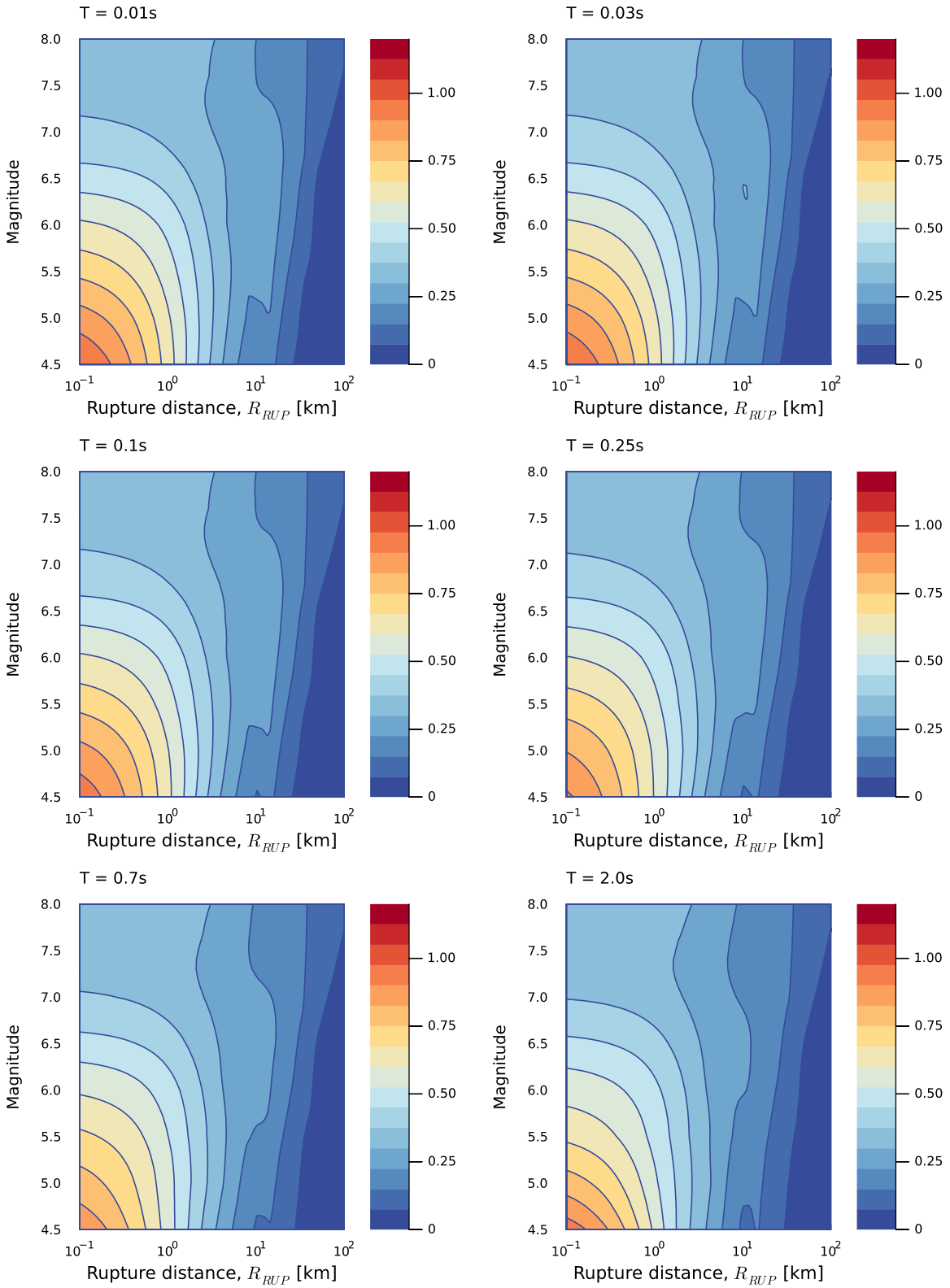

Figure 9-44. Standard deviation (in natural logarithmic units) of RVT predictions over the five considered saturation models as a function of magnitude and distance. Each panel corresponds to the period shown in the upper left of each panel and relate to the RVT predictions shown in Figure 9-43.

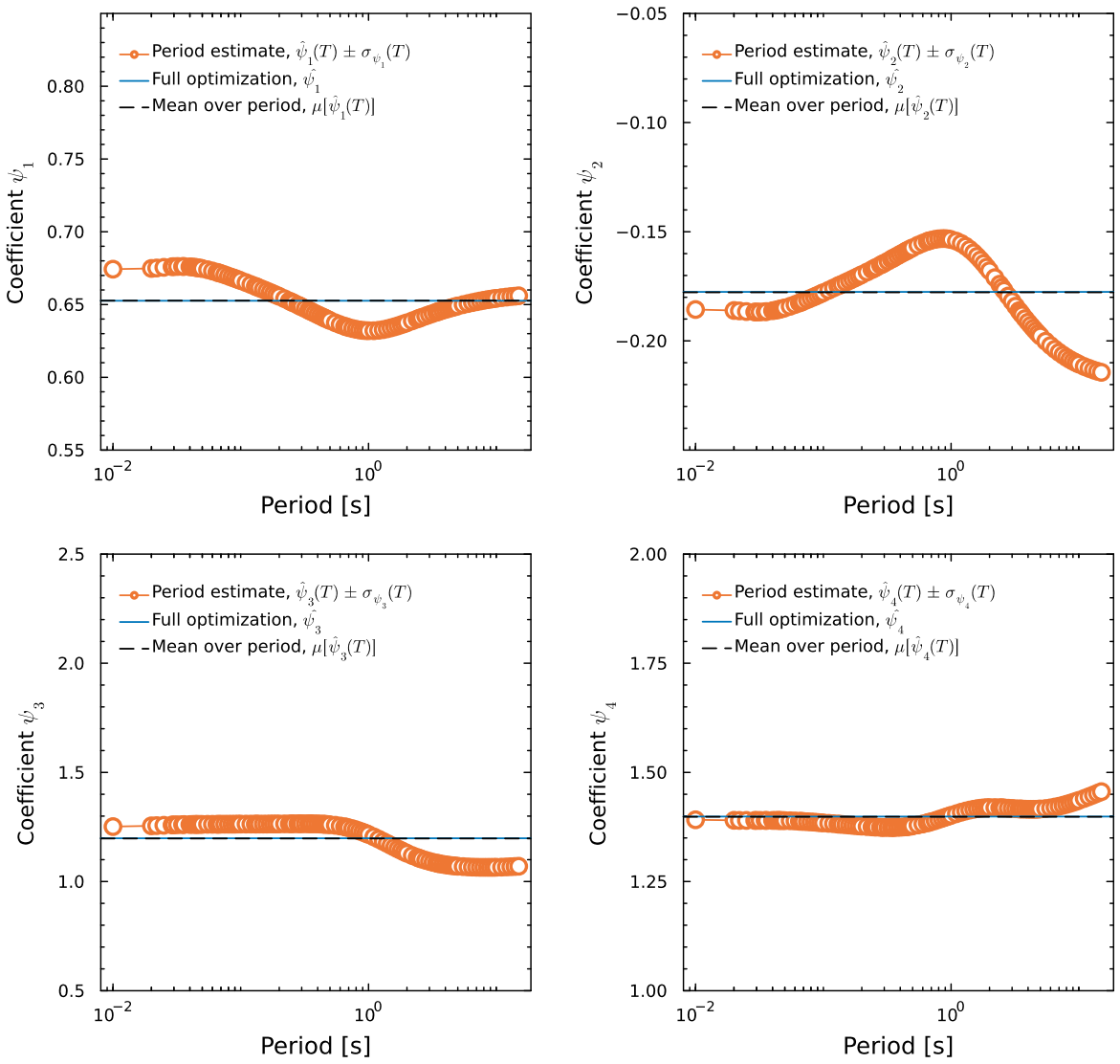

Figure 9-45. Period dependence of the parameters of Equations 9-49 and 9-50. Orange markers show the individual parameter estimates for each period and the shaded region shows the standard errors. The blue line and shaded regions show the estimates when a regression is performed over all periods. The dashed black line shows the mean of the period-dependent estimates and is essentially the same as the central blue line.

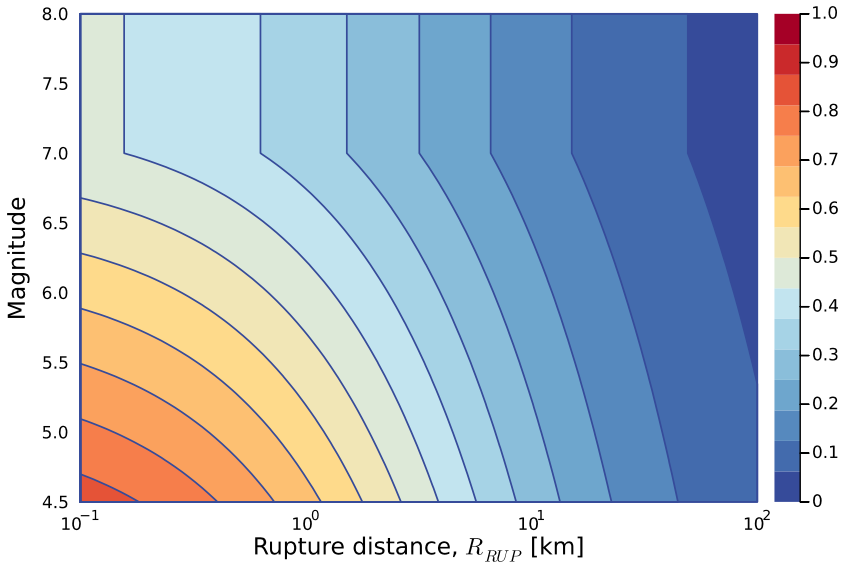

Figure 9-46. Magnitude-distance dependence of the variability of the near-source saturation model of Equations 9-51 and 9-52, σ_{SAT}.

In Equation 9-46, the variance contribution associated with near-source saturation effects was represented by σ_{CSAT} rather than σ_{SAT}. Equation 9-51 defines the unconditional uncertainty associated with near-source saturation effects, which is correlated with the model-to-model uncertainty since differences in data selection, model parameterisation, inversion approach, etc, are functions of how much empirical data is available to the analysts. If Edwards and the GMM TI Team were both presented with databases that contained far more recordings and covered the full range of rupture scenarios of interest, then the model-to-model differences in their results would decrease. At the same time, the uncertainty regarding which saturation model to use would also decrease. In addition, they would be able to isolate, or decouple, the uncertainty associated with near-source saturation from other sources of uncertainty that lead to model-to-model uncertainty. Therefore, the correlation between these components of epistemic uncertainty would decrease as the amount of data available increased (especially when that data includes coverage for near-source regions). Importantly, a key component of the model-to-model uncertainty, particularly for the models linked to Edwards' inversions, is the uncertainty associated with stress parameter. This stress parameter is directly linked to the assumptions made regarding the near-source saturation model: longer saturation gives lower stress parameters, and vice versa.

If we do not account for the correlation between the components of epistemic uncertainty then their contributions compound to give unrealistically high levels of uncertainty in the near-source region. We therefore need a framework that allows for consideration of the correlation. Deviations away from the mean logarithmic spectral amplitude for a given rupture scenario can be expressed as:

9-53

$$\mu^{*}_{\ln SA} = \mu_{\ln SA} + \delta_{M2M} + \delta_{SAT} + \delta_{ADD}$$

where $\mu^{*}_{\ln SA}$ is a possible level of the mean logarithmic amplitude, $\mu_{\ln SA}$ is the global mean amplitude, δ_{M2M} is a deviation linked to model-to-model variability, δ_{SAT} is a deviation linked to the choice of saturation model, and δ_{ADD} is a deviation linked to additional epistemic

uncertainty (discussed in the next section). This latter term is assumed independent of the other components, but δ_{M2M} and δ_{SAT} are assumed to be correlated.

There are three contributors to defining a particular level of $\mu^*_{\ln Sa}$, and these predictions are candidates for logic-tree branches. If the epistemic uncertainty is represented using just a three-node model, and a symmetrical distribution is assumed, one branch corresponds to $\mu^*_{\ln Sa} = \mu_{\ln Sa}$, and the upper and lower branches include specified deviations of the δ_{M2M}, δ_{SAT} and δ_{ADD} terms. When these terms involve correlations, one cannot simply move a standardised distance for each of these terms. Stafford (2022) proposed to define the model-to-model variability as being the primary deviation that will be most relevant for general rupture scenarios and to first specify a particular deviation for this term. The conditional deviation for the near-source saturation effects is then defined in terms of this primary deviation. The approach adopted by Stafford (2022) is equivalent to working with the conditional variability of saturation effects, σ_{CSAT}, rather than σ_{SAT}.

The conditional uncertainty due to saturation effects is defined by:

9-54

$$\sigma_{CSAT} = \sigma_{SAT}\sqrt{1 - \rho^2_{M2M,SAT}}$$

where $\rho_{M2M,SAT}$ is the assumed correlation between the saturation and model-to-model deviations. For this project, the GMM TI Team assumed a correlation value of $\rho_{M2M,SAT} = 0.7$. This value cannot be computed from data, it is simply a subjective estimate of the extent to which uncertainties in model-to-model variations and saturation are driven by the same underlying issues. The GMM TI Team chose this number based on the assumption that it should be higher than the value of 0.4 that Stafford (2022) adopted for New Zealand as the New Zealand study had significantly more data at close distances, and from hazard-relevant rupture scenarios, in comparison with the present project. In other words, the lack of data in South Africa is the primary reason why we have significant uncertainty in both the near-source saturation models and the level of empirical constraint. In New Zealand, there are more data that can help inform the near-source saturation and so the underlying sources of the uncertainty are less coupled. As the amount of data in the near-source region increased, we would expect these sources of uncertainty to become increasingly decoupled (one simply becomes pure empirical constraint, and the other becomes functional uncertainty in how to model the near-source saturation). Currently, in both regions being discussed, the lack of data means that we have all of the functional uncertainty associated with how to model near-source saturation, and insufficient data to judge the performance of alternative models).

9.2.6.4 Additional epistemic uncertainty

Figure 9-40 provided a conceptual representation of contributors to epistemic uncertainty. The model-to-model variability and near-source saturation effects are mostly focussed on the elements in panels (a) and (b) of that figure. There are additional contributions to epistemic uncertainty that have not yet been accounted for. The inclusion of the σ_{ADD} term in Equation 9-46 is used to provide an additional contribution to epistemic uncertainty that encapsulates elements not embedded within the other components.

In particular, the additional epistemic uncertainty is used to account for:

- **Seed GMPE representativeness**: uncertainty associated with how representative the seed GMPE is for the host site for those parameters that are unchanged by the adjustment process.
- **Data representativeness**: uncertainty associated with how representative the Inversion GMDB is for the target site (and rupture scenarios of relevance for hazard calculations).
- **Parametric uncertainty**: given an assumed functional parameterisation, how uncertain are the model parameters obtained? This relates to Figure 9-40c.
- **Underlying theory**: while Edwards and the GMM TI Team have different approaches to their inversions, they are both ultimately working with the same theoretical model for the Fourier amplitude spectrum. The extent to which their approaches captured the CBR of TDI.

Brief comments are made with respect to each of these items within the current section.

This section focuses on sources of epistemic uncertainty from the inversion and GMPE adjustment process, but the seed GMPE itself is not free of epistemic uncertainty. There is inherent epistemic uncertainty in the CY14 GMPE due to the scarcity of data, uncertainty in the long-period spectra due to the reduction in the dataset from usable frequency limit constraints, and uncertainy in the normal-faulting factors due to the limited number of normal faulting earthquakes in the CY14 dataset. These sources of epistemic uncertainty are incorporated in the GMM through the additional epistemic uncertainty term.

Edwards and the GMM TI Team both used the same initial database of ground-motion data, and they each then selected the records they thought most suitable for their needs from that database. That selection process was exclusively related to data quality and proximity issues, such as sufficient signal-to-noise ratio, and recordings being within a certain distance from a recording station. The analysts did not impose restrictions on these events being within a certain distance of the target site, nor did they give any greater weighting to recordings of rupture scenarios that are represented within the seismic source model. The analysts therefore implicitly assumed that all records within the database are equally representative of the motions that would be observed at the target site. This is an assumption, and some degree of epistemic uncertainty exists that relates to the unknown extent to which the compiled Inversion GMDB is truly representative of motions at the target site. This problem was previously highlighted through the presentation of the ray paths in Figure 9-8. That figure demonstrated that only a small percentage of the ray paths in the Inversion GMDB were sampling source locations and crustal properties of greatest relevance to the target site.

The appropriate level of this epistemic uncertainty cannot be computed. One can gain insight into the likely amplitude from considerations of regional variations in ground-motions seen within other regions.

Regarding the parametric uncertainty, the GMM TI Team formally considered this issue within the inversions and model development. The GMM TI Team inversion approach allows the covariance matrix of parameters to be computed in addition to marginal parametric uncertainties in the individual parameters. Examples of the correlation matrices for two inversions are shown in Figure 9-47. In the example on the left, the correlations are very

strong, and this partly results from fixing the stress parameter scaling. The example on the right corresponds to a scaled stress parameter and this allows correlations among the parameters to be lower.

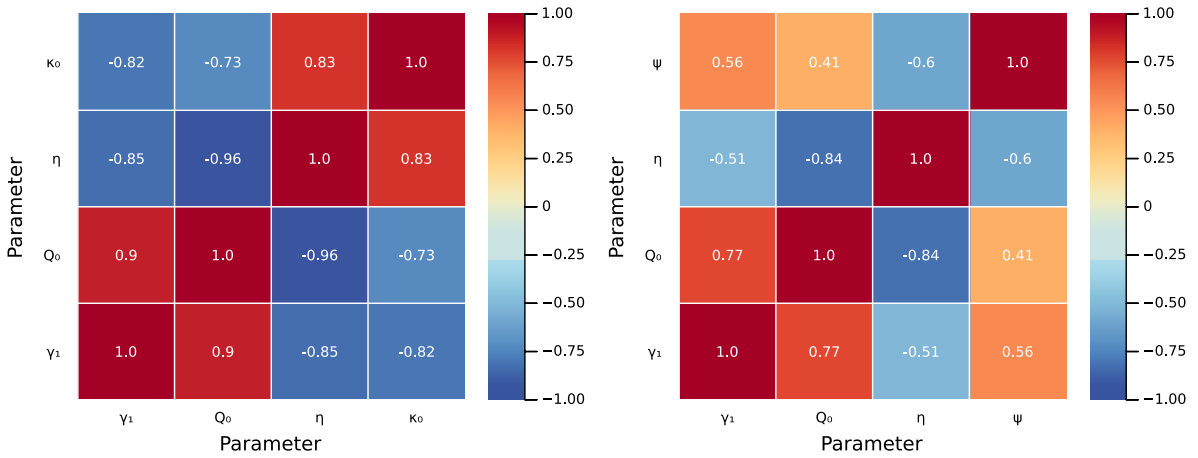

Figure 9-47. Correlation matrices for free seismic parameters used within the GMM TI Team inversion model 1 (left) and model 2 (right). Inversion model 1 has the stress parameter fixed to the Stafford et al. (2022) results from inverting CY14, and uses a free κ_0 value, while inversion model 2 scales the Stafford et al. (2022) stress parameter model and fixes $\kappa_0 = 0.039$ s.

The covariance matrices of the parameters can be sampled to generate suites of seismic parameters that are collectively consistent with the data used in the inversions. Figure 9-48 shows 1,000 samples of the covariance matrix associated with the correlation matrix on the left of Figure 9-47. Figure 9-48 shows the strong correlations that exist between the parameters, but also highlights that the marginal distributions are also relatively tight. Making forward predictions with these alternative seismic parameter sets gives insight regarding the extent of parametric uncertainty on logarithmic spectral ordinates. Figure 9-49 shows 1,000 predictions from RVT calculations using the sampled seismic parameter sets.

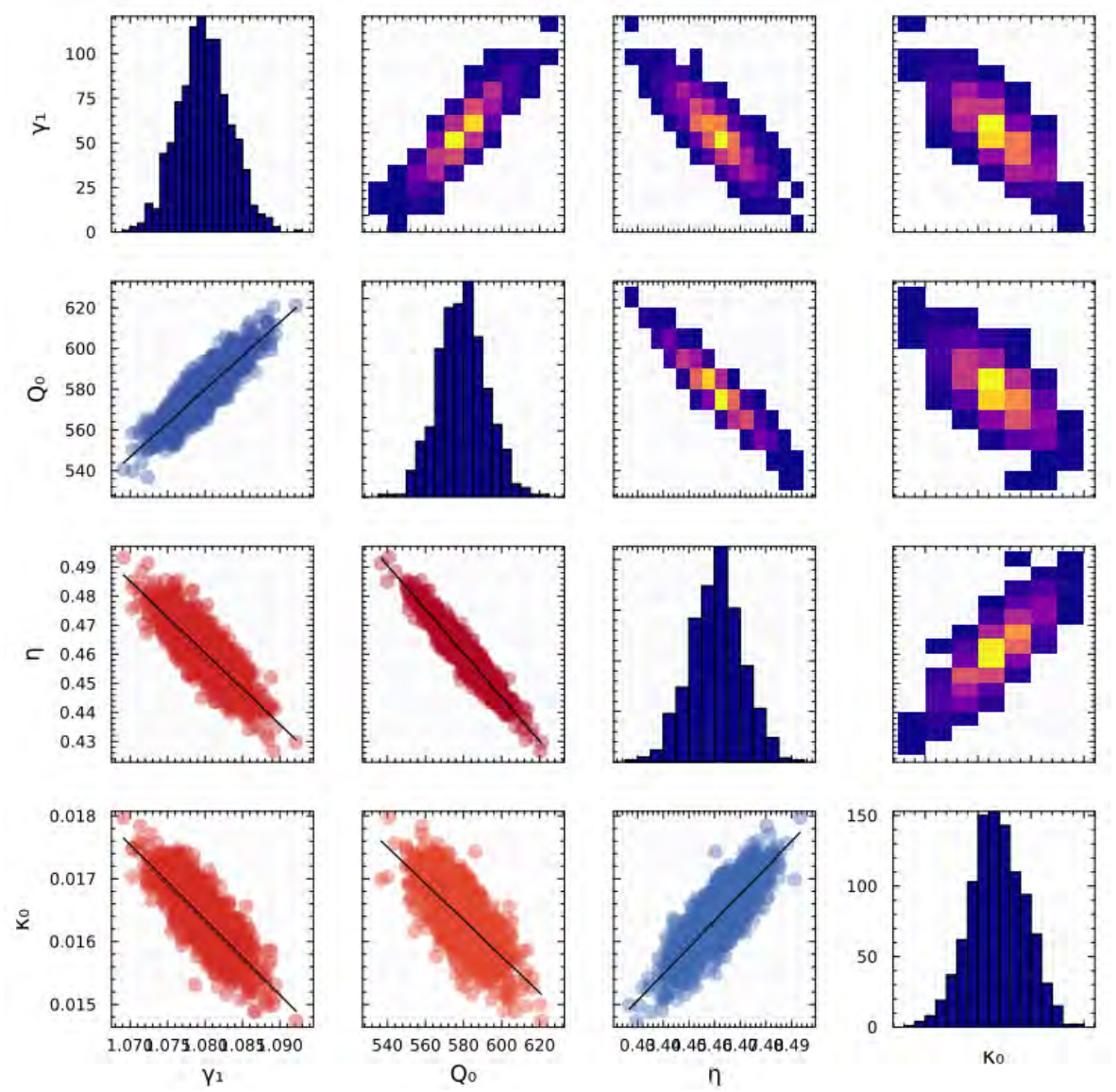

Figure 9-48. Samples of seismic parameters from the covariance matrix of the GMM TI Team inversions model 1. Diagonal panels show the marginal histograms, panels below the diagonal show scatterplots of the pairs of parameters, and panels above the diagonal show 2D histograms, with the higher number of samples corresponding to lighter colours.

While Figure 9-49 appears to show a series of three lines with one for each period and magnitude pair, there are actually 1000 lines plotted for each combination with each line corresponding to one of the samples shown in Figure 9-48. The effects of parametric uncertainty are therefore very small for this inversion model. It is important to note that this approach places 100% confidence in the theoretical model, meaning a theoretical model for the FAS is assumed to be valid and this model requires the specification of a small number of parameters and allows predictions for any combination of period, magnitude and distance. The model parameters are only calibrated using data from a very narrow range of magnitudes.

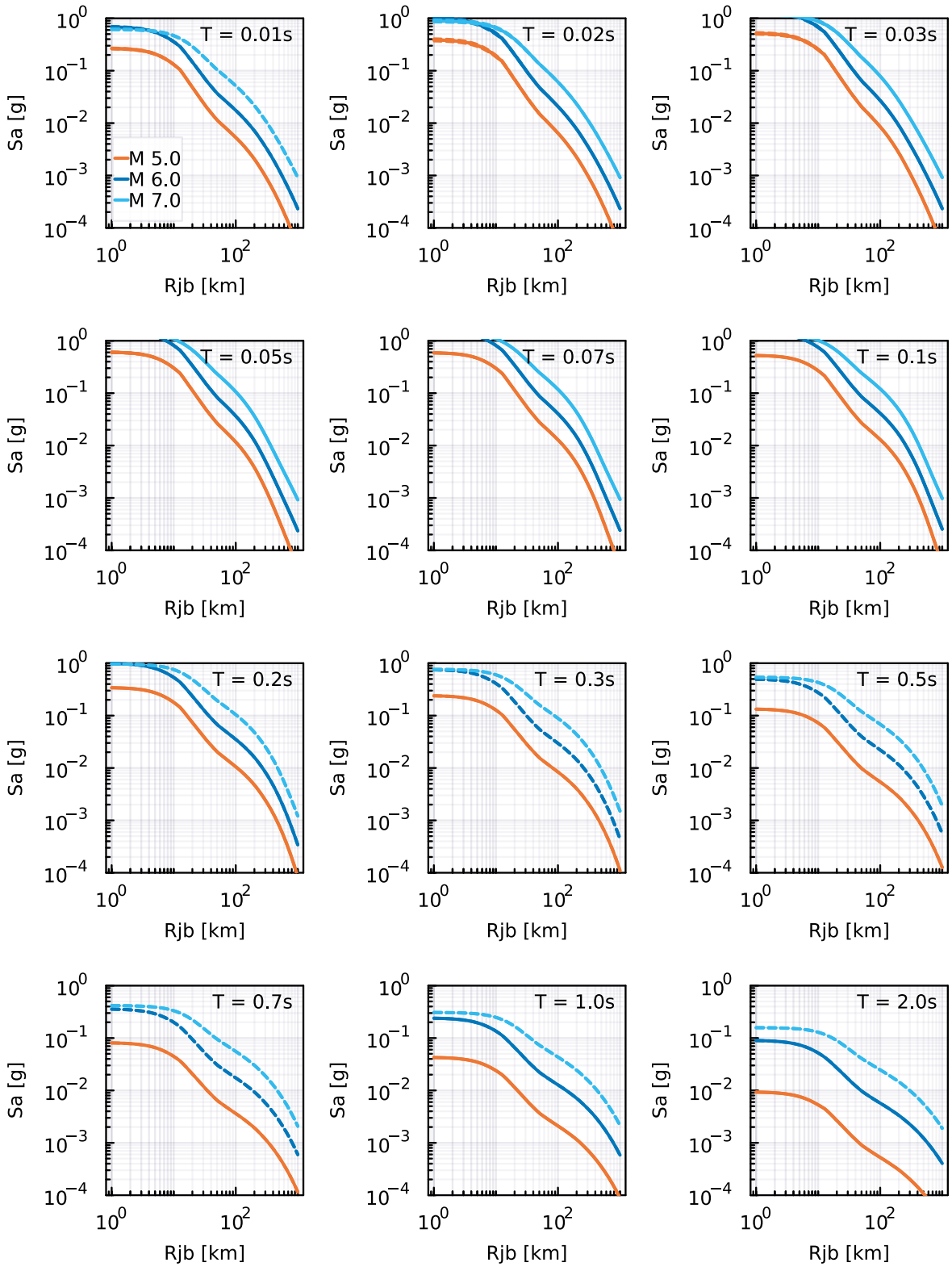

Figure 9-49. RVT predictions of response spectral ordinates against distance for a series of magnitudes and periods annotated in the panels. While the panels appear to show individual lines, there are 1,000 curves plotted for each magnitude and period combination – each curve corresponds to a sample shown in Figure 9-48.

Under this approach, if one had thousands of records all from earthquakes of magnitude 1 or below it can still imply that stress parameter values are well-constrained for events of magnitude above 7 because we assume we know the magnitude scaling of stress parameter perfectly. In reality, of course, this is not the case, so the true parametric uncertainty for larger magnitude scenarios is greater than what is shown here. That said, formal parametric uncertainty can be computed, while the true parametric uncertainty can only be estimated and must account for the extent to which we believe a given theory is valid. Parametric uncertainty is certainly greater than that implied by Figure 9-49, and the results of this figure only provide lower bound estimates.

The final contributor to additional epistemic uncertainty that was listed above is associated with the underlying theoretical models adopted. Edwards and the GMM TI Team both work with the same underlying theoretical model, despite using different inversion approaches. For example, both assume that the source spectrum is a single-corner omega-squared spectrum, both assume the same form of anelastic and κ_0 filters, etc. There are, of course, alternative source theories, and different models for attenuation, among other model components, that could have been selected. The selection of those different models would have required different seismic parameters to be estimated and would have led to different inversion results and resulting models. We cannot capture the body and range of TDI without allowing for the possibility that those alternative theories would have resulted in greater model-to-model variability than what is represented by the seven developed models.

The existence of the three contributors to epistemic uncertainty that have been discussed in this section is irrefutable, but they are also either impossible to truly quantify, or their quantification is not practically feasible within the scope of this project. In most other projects they are not explicitly considered, and it is not clear to what extent their effects have been consciously encapsulated in other model components. That said, the GMM TI Team also does not believe that these contributions collectively amount to large additional levels of epistemic uncertainty. For that reason the level of additional epistemic uncertainty was chosen to be $\sigma_{ADD} = 0.1$ natural logarithmic units, or roughly 10% uncertainty.

This additional epistemic uncertainty is a constant across all periods and rupture scenarios. A similar level of nominal uncertainty[5] of 0.1 natural logarithmic units was also used within a recent SSHAC Level 3 project for nuclear facilities in Spain. Furthermore, the within-model uncertainty (an estimate of parametric uncertainty) proposed by Al Atik and Youngs (2014) is 0.083 for most rupture scenarios relevant for the present project. That within-model parametric uncertainty is likely larger than the corresponding level of parametric uncertainty for the FAS-based inversion models of the present project due to the models considered by Al Atik and Youngs (2014) having far more degrees of freedom and heavier empirical, rather than theoretical, bases. Assuming that parametric uncertainty for the present project is no greater than the 0.083 obtained by Al Atik and Youngs (2014), and then adding uncertainty to account for data representativeness and limited exploration of alternative theoretical models, brings us to a level of around 0.1 natural logarithmic units.

[5] In the Spanish NPP project the nominal uncertainty was not conceived using the same reasoning as presented here, but played a similar role from a practical point-of-view.

9.2.6.5 Correlation of epistemic uncertainty

The final component of Equation 9-46 that remains to be defined is the correlation reduction factor ζ_{COR}. Figure 9-38 and Figure 9-39 both showed that, for any given rupture scenario, the seven individual ground-motion models have a ranking (in terms of predicted spectral amplitude), and that this ranking varies from scenario-to-scenario. That is, for some scenarios a particular model may predict the highest amplitudes, but for other a different model will predict the highest amplitude. The ranking changes with the scenario and if we computed a rank correlation coefficient between two different scenarios we would expect a correlation of less than 1.0. Obviously, in order for the ranking to change between two scenarios some models would need to cross each other between these scenarios. If we only look at the three models from the FAS-based inversions of Edwards, we see that the ranking does not change because these models effectively have the same path scaling and only differ due to stress parameter differences (there is only one degree of freedom, and that is the stress parameter which shifts all predictions 'up' or 'down' for all distances). If predictions had been made that also used the associated κ_0 parameters that Edwards coupled to his stress parameter values (see Table 9-5) then these models could also cross each other for certain rupture scenarios (or, at least, the ranking among the Edwards models could change from period-to-period) because of the trade-offs between stress parameter and kappa.

The same behaviour can be seen among other models that are ostensibly developed for the same region. That is, the ranking of the models change for different scenarios and this implies that the models will cross each other. For example, the NGA-West2 models or European models will cross each other as the rupture scenario varies continuously in terms of magnitude, distance and depth. Again, this change in rank, or crossing of models, means that the correlation between models is less than 1.0 (i.e., we only have a partial correlation between the model predictions).

Within a three-branch (or n-branch) meta-model (such as a scaled backbone model), the full hazard calculations are performed for a single branch at a time. This means that one hazard curve will correspond to a situation in which the predicted mean ground-motion is above average for every single rupture scenario, and another curve will have the opposite situation where predicted motions are below average for every single scenario. This implies perfect correlation of epistemic uncertainty, and is not consistent with what we know from functional and theoretical contributions to epistemic uncertainty. It is also not consistent with what we observe among the seven individual models derived for this project, i.e., because the models cross, the correlation is clearly imperfect. Empirical ground-motion modelling leads to the use of different functional forms that may cross one another while still having similar behaviour, on aggregate, over the databases they are calibrated to. Similarly, different theoretical models can lead to model predictions that cross one another (even when their parameters are perfectly calibrated). Note that in the SSHAC Level 3 Thyspunt study, the TI Team used three seed backbone models partly to address this issue (Bommer et al., 2015).

The GMM TI Team decided to adopt the solution to this problem proposed by Stafford and Bradley (2022). Their approach is based on asking the question of 'what is the effective epistemic standard deviation to be used within a backbone model in order to match hazard calculations that would be found from accounting for the correlation of epistemic uncertainty?' If the epistemic standard deviation in the mean spectral amplitude for an individual rupture

scenario, rup_i, is $\sigma_{bb,i}$, then the effective epistemic standard deviation to use within hazard calculations is $\sigma_{\mu_{\ln Sa}}(rup_i) = \zeta\sigma_{bb,i}$, where ζ is computed on a site-specific basis from:

9-55

$$\zeta^2 = \frac{\sum_{j=1}^{n_{rup}} \sum_{i=1}^{n_{rup}} w_i w_j \rho_{\mu_i,\mu_j}}{\sum_{j=1}^{n_{rup}} \sum_{i=1}^{n_{rup}} w_i w_j}$$

in which:

9-56

$$w_i = \frac{1}{\sigma_i}\phi\left(\frac{\mu_{bb,i} - im}{\sigma_i}\right)\lambda(rup_i)\sigma_{bb,i}$$

In Equation 9-55, the term ρ_{μ_i,μ_j} is the correlation of epistemic deviations away from the mean model between rupture scenario rup_i and rup_j. These epistemic deviations are conceptually equivalent to the sum of the δ_x terms in Equation 9-53. The overall mean logarithmic prediction, $\mu_{\ln Sa}$, is denoted by the μ_{bb} term in Equation 9-56, with the subscript i showing that this prediction relates to rupture scenario rup_i. The term im is the intensity measure associated with a given return period, and the $\lambda(rup_i)$ term is the rate of occurrence for scenario rup_i obtained from disaggregation of the hazard at this return period. The function ϕ is the standard normal probability density function and σ_i is the best estimate aleatory variability for a rupture scenario rup_i.

To evaluate ζ, one therefore needs to have disaggregation information, or approximate disaggregation information, to define the relative rates of occurrence of the different rupture scenarios. As this disaggregation information, as well as the value of im, will change with return period, the value of ζ will also change with return period. For the purpose of evaluating ζ values for the present application, the disaggregation information from the preliminary hazard calculations presented at Workshop 3 was used, and return periods of 10^4, 10^5, and 10^6 years were focussed on.

Figure 9-50 provides examples of the disaggregation distributions that were used to derive the model for ζ. These disaggregation distributions are not perfect replicas of the distributions that will arise from the final hazard model, as elements of both the SSM and GMM models have changed. They are reasonable approximations and give insight into where the main scenarios are concentrated, and how dispersed these contributions are in magnitude-distance space. In general, one can see that the distance range over which contributions occur is relatively limited, while contributions are non-trivial for a range of magnitudes.

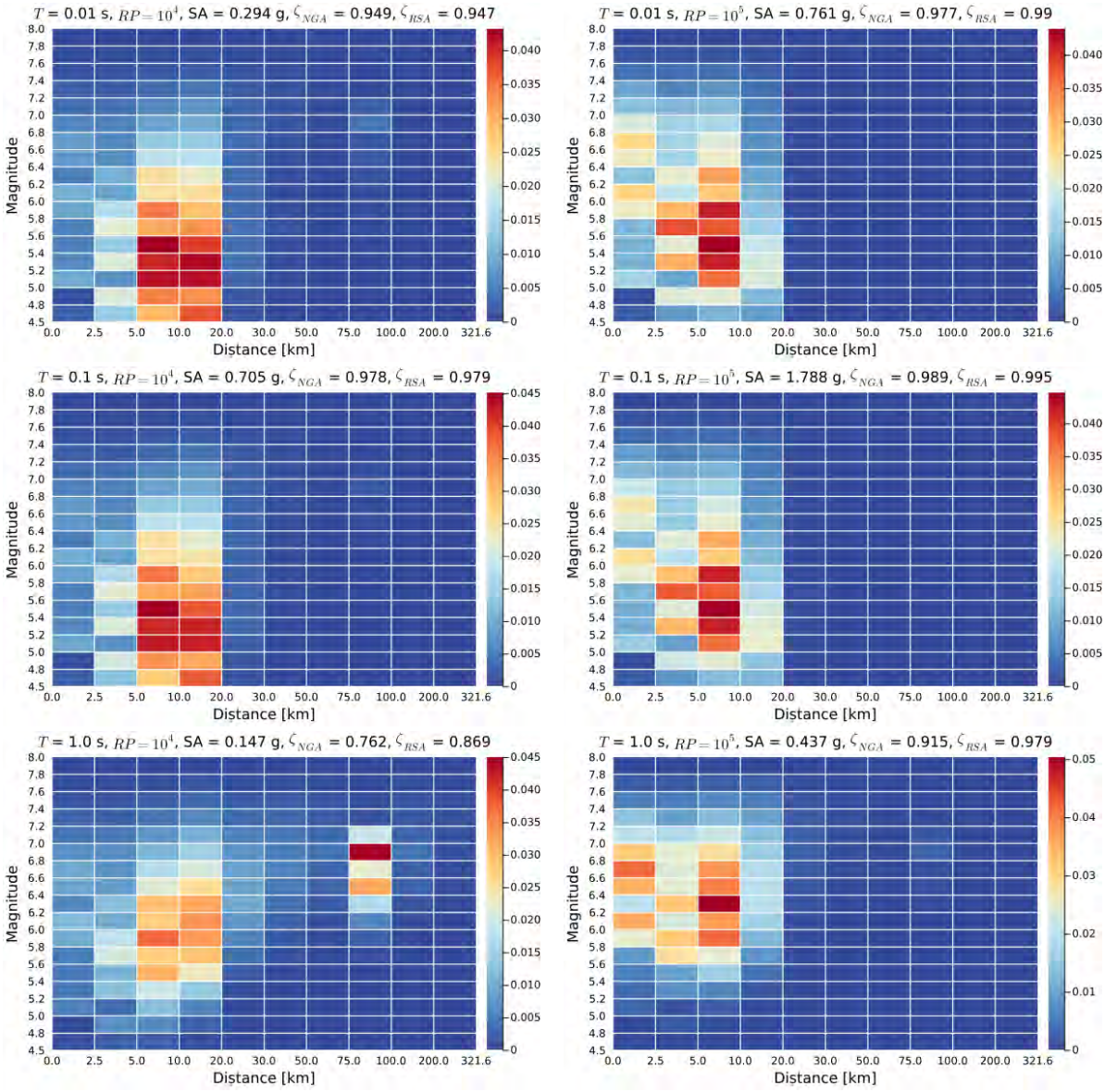

Figure 9-50. Example disaggregation distributions from the preliminary hazard calculations used to compute the epistemic correlation reduction factors. Colours of cells show fractional contribution to hazard for the given return period. Rows correspond to periods, with 0.01, 0.1 and 1.0 seconds shown from top to bottom. The left column corresponds to a return period of 10^4 years, while the right column is for a return period of 10^5 years.

Although the weights shown in Equation 9-56 depend upon the value of $\sigma_{bb,i}$, as these weights appear in both the numerator and denominator, their effect cancels out and no values need to be computed for these components. The reduction factors ζ do depend weakly upon the value of aleatory variability σ_i for each rupture scenario, but for convenience, and to be consistent with other approximate inputs, a representative constant value of 0.6 natural logarithmic units was adopted herein.

Figure 9-50 shows the intensity measure level, return period and oscillator period in the panel headers as well as the computed value of ζ (using the symbol in the figure) for two different cases. One term is denoted $\gamma\zeta_{NGA}$ while the other is $\gamma\zeta_{RSA}$. The first of these indicates that the epistemic correlations were computed using the scenario-to-scenario covariances of the NGA-West2 GMPEs. The second uses correlations computed from the seven adjusted GMPEs

developed for this project. To find these correlations, the logarithmic predictions of the NGA-West2 GMPEs, or the seven adjusted GMPEs, are made for all rupture scenarios represented by the hazard disaggregation distributions. These predictions are then used to compute correlations from scenario-to-scenario.

The NGA-West2 models were considered because they represent a good example of a situation where functional epistemic uncertainty drives the epistemic correlations. Each development team within that project selected functional forms that were mostly empirical in nature but were partially tied to some underlying theoretical expectations. These empirical models are also relatively well-supported by data over the magnitude-distance range spanning the disaggregation distributions. The way in which these models change rank with scenario is therefore representative of the typical epistemic correlations that would arise from a multi-GMPE approach to populating a logic-tree.

The South African GMPEs were also considered but were not exclusively used for reasons partly alluded to earlier. Both Edwards and the GMM TI Team adopt the same underlying theoretical FAS model, so model-to-model differences mainly reflect the role that different parameters play for certain rupture scenarios as well as how different model components are parameterised, e.g., the geometric spreading functions or the anelastic attenuation filters. In addition, the suite of models from Edwards has the same path scaling for each model and imposes artificially high correlation by only branching on the stress parameter. That is, the three models associated with Edwards' inversions are already like a scaled backbone model and will have near perfect correlation from scenario to scenario. To mitigate against this artificial inflation of the epistemic correlations, for the purpose of computing ζ, the four models related to the GMM TI Team's inversions along with just the central model from Edwards' inversions were used to compute correlations.

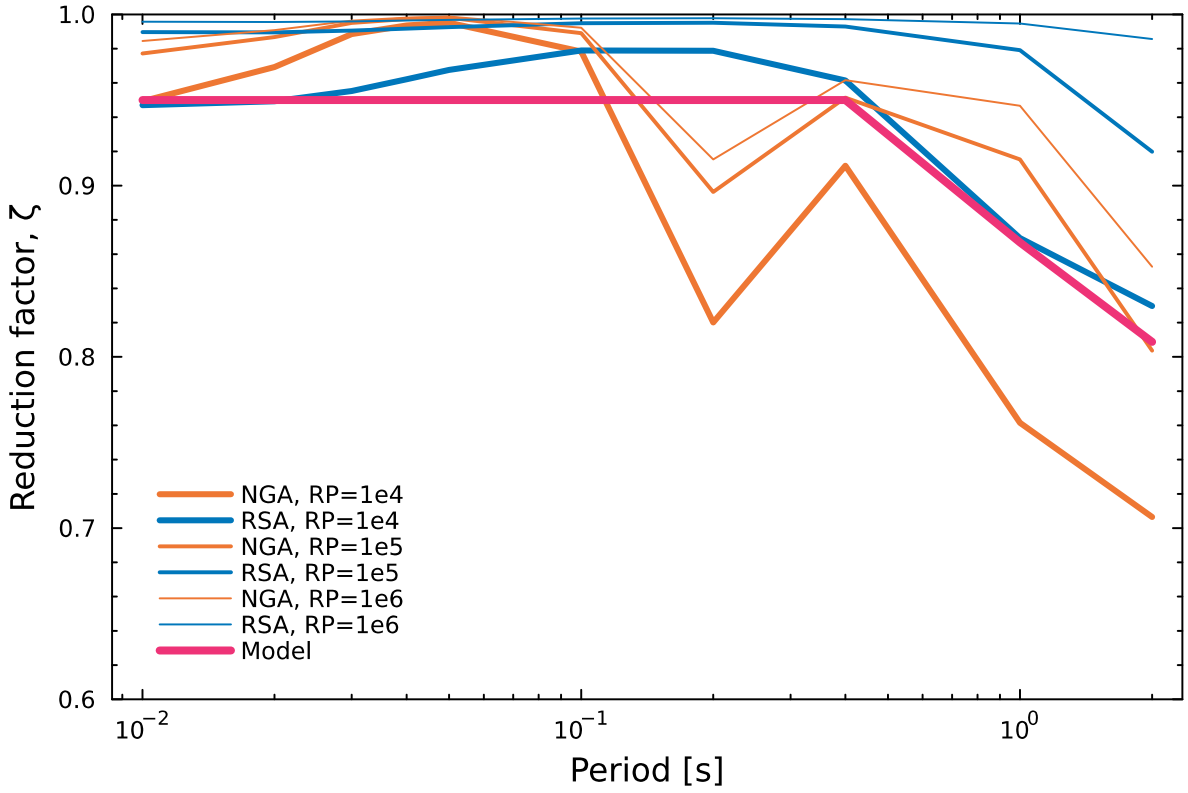

Figure 9-51. Variation of the epistemic reduction factor, ζ with period for three different return periods shown in the legend. The orange lines represent ζ factors computed from the NGA-West2 GMPEs, while the blue lines correspond to the factors obtained using the South African GMPEs. The proposed model is shown with the heavy pink line.

The proposed model is not found from a statistical analysis of these results but is subjectively chosen by the GMM TI Team to be consistent with the NGA-West 2 and South Africa levels at the shortest period where both results agree, and to stay constant at this level out to a period of 0.4 seconds. From that point, the reduction factor decreases. Holding the reduction factor constant over the short period range leads to an underestimation of the computed reduction factors for periods just below 0.1 seconds but is otherwise broadly representative of the factors computed for both the NGA-West2 and South Africa GMPEs. Note that far greater weight is given to the results for the return period of 10^4 than any other return period. The higher reduction factors for these longer return periods simply reflect the fact that disaggregation distributions are more concentrated at short distances for these longer return periods.

The proposed model is specified mathematically in Equation 9-57.

9-57

$$\zeta_{COR} = \begin{cases} 0.95 & T \leq 0.4 \\ 0.95 \exp\left[-0.1 \ln\left(\frac{T}{0.4}\right)\right] & \text{otherwise} \end{cases}$$

9.2.6.6 Overall model of epistemic uncertainty

Combining all the model elements discussed in this section leads to the overall model for epistemic uncertainty in the mean logarithmic spectral amplitudes. Figure 9-52, Figure 9-53, and Figure 9-54 show the variation of the variance components over magnitude-distance space for periods of 0.01, 0.1 and 1.0 seconds, respectively. The lower right panel in each figure shows the overall epistemic uncertainty $\sigma_{\mu_{\ln SA}}$ and includes the reduction factor ζ_{COR}.

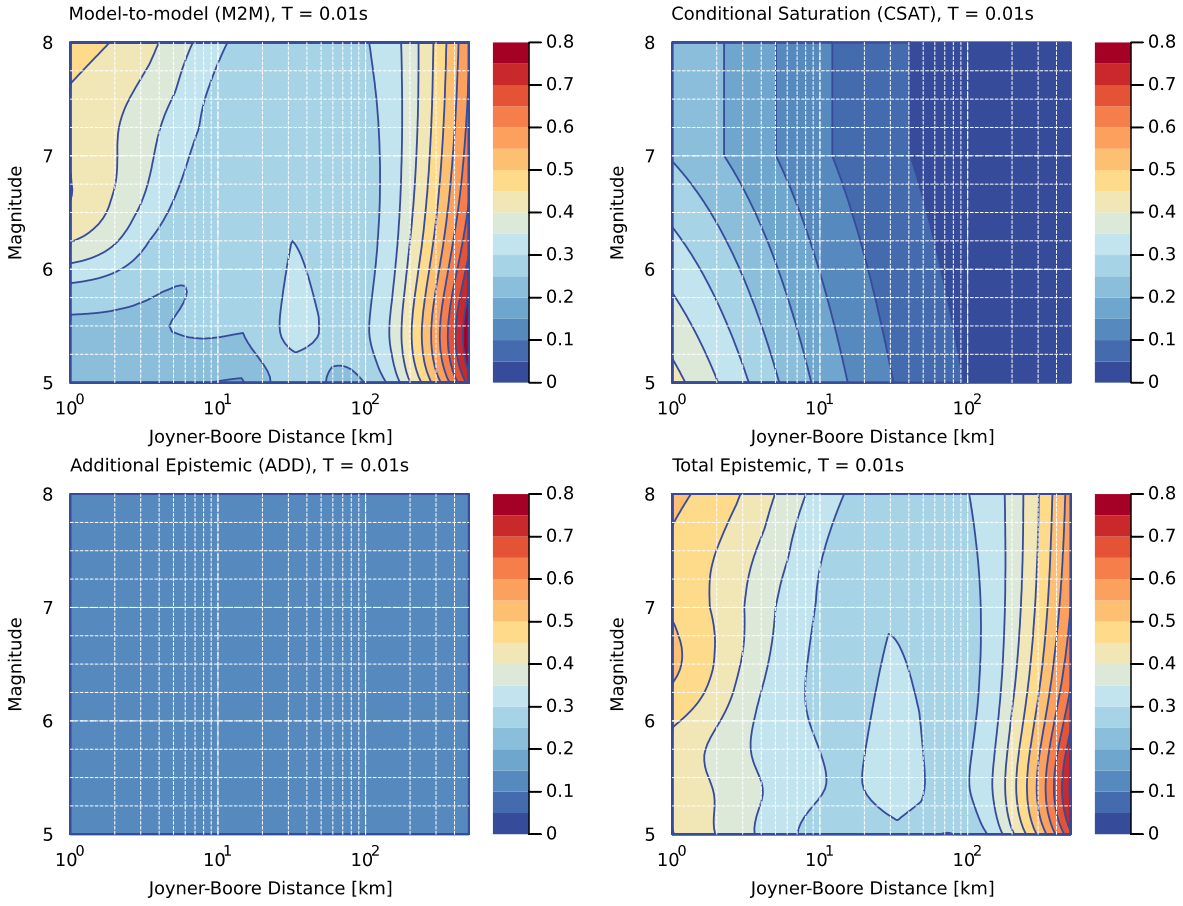

Figure 9-52. Components of Equation 9-46 plotted over magnitude-distance space for a period of 0.01 seconds. The title of each panel describes what is being plotted. The upper left panel shows model-to-model uncertainty, the upper right panel shows the conditional near-source saturation uncertainty, the lower left shows the additional epistemic uncertainty, and the lower right shows the total epistemic uncertainty.

The three example figures that are provided here (Figure 9-52 to Figure 9-54) are representative of periods that cover the range of interest for the present project. Note that for all figures, the conditional saturation and additional epistemic contributions are the same as these components are period independent. Thus, only the upper left and lower right panels change from figure to figure. As the ζ_{COR} is also period dependent, the values in the lower right panel in the final figure (Figure 9-54) are reduced more than the same panels in the earlier figures (Figure 9-52 and Figure 9-53).

Inspection of these figures shows that total levels of epistemic uncertainty have values of around 0.3 natural logarithmic units at their lowest points, although some small regions dip below this level, and tend to higher levels for shorter distances where near-source saturation effects contribute more as well as greater model-to-model uncertainty (mainly associated with

the finite distance metrics used within duration models). Also, for short periods, as the distances increase, we see increased epistemic uncertainty that reflects the differences in anelastic attenuation and large-distance geometric spreading rates. Note that the distances for which the epistemic uncertainty is plotted go beyond the greatest distance considered by Edwards (of 300 km). The path adjustments factors that were developed from all FAS parameter sets were developed out to distances of 700 km.

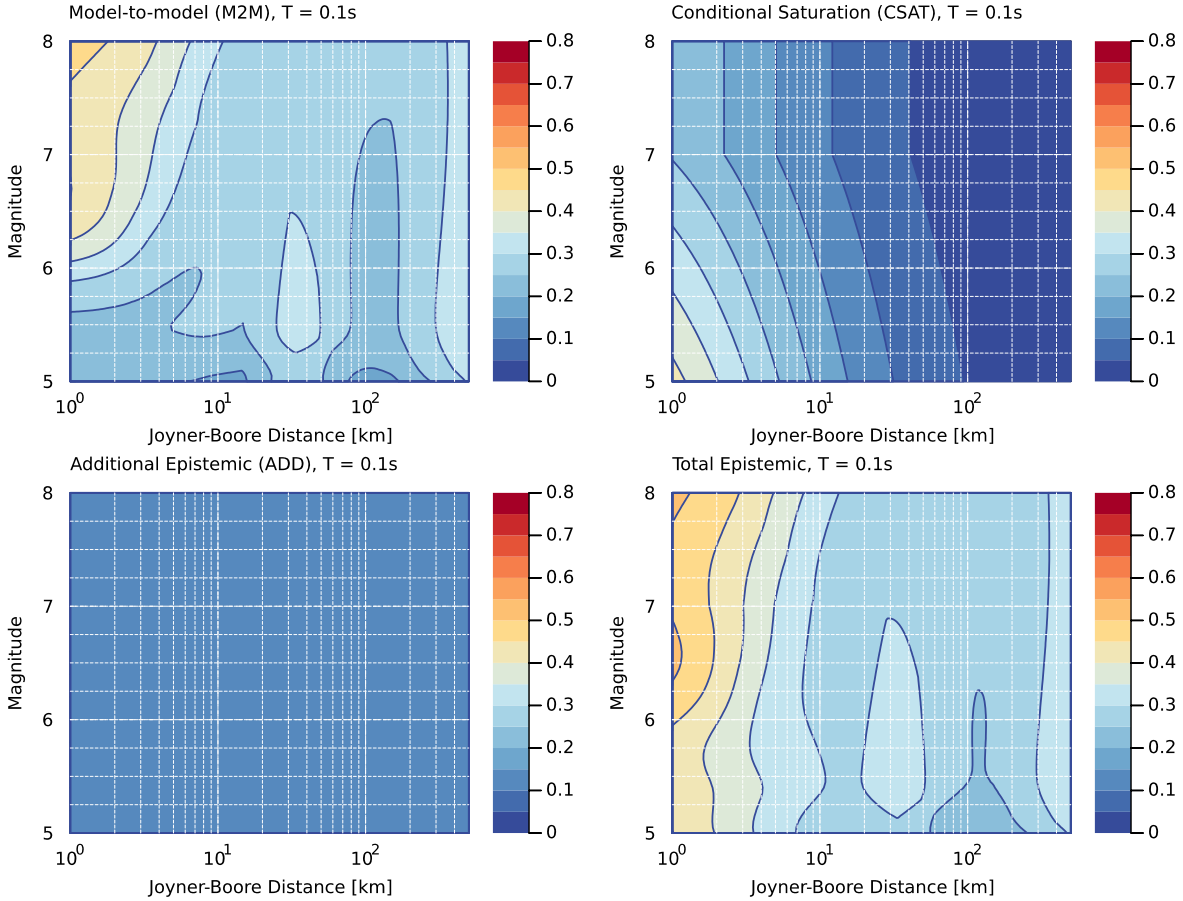

Figure 9-53. Components of Equation 9-46 plotted over magnitude-distance space for a period of 0.1 seconds. The title of each panel describes what is being plotted. The upper left panel shows model-to-model uncertainty, the upper right panel shows the conditional near-source saturation uncertainty, the lower left shows the additional epistemic uncertainty, and the lower right shows the total epistemic uncertainty.

The overall levels of epistemic uncertainty shown in the lower right panels cannot be directly compared with levels of epistemic uncertainty adopted for other projects that used backbone models as the results here include the epistemic reduction factor. For short periods the relevant reduction factors are not strong and so the levels of uncertainty shown here are representative for comparative purposes.

The representative values of at least 0.3 natural logarithmic units arise from the distinct components described throughout this section. The level of 0.3 units was not targeted from the outset. This level is comparable to levels of uncertainty that have been specified, or that have arisen, in other similar SSHAC projects. Note that the model presented herein explicitly accounts for contributions that are not usually (or not explicitly) considered within these other projects. Direct numerical comparisons are not strictly meaningful from project to project,

particularly given that the epistemic reduction factors depend upon the site-specific disaggregation information and the relative contributions of different rupture scenarios to the hazard. In addition, it is not possible to define what a 'correct' level of epistemic uncertainty should be – this requires quantifying the extent to which we do not know something. The approximate levels that arise from the process described here are comparable to levels found in other projects, and the GMM TI Team believes that it appropriately captures the body and range of TDI.

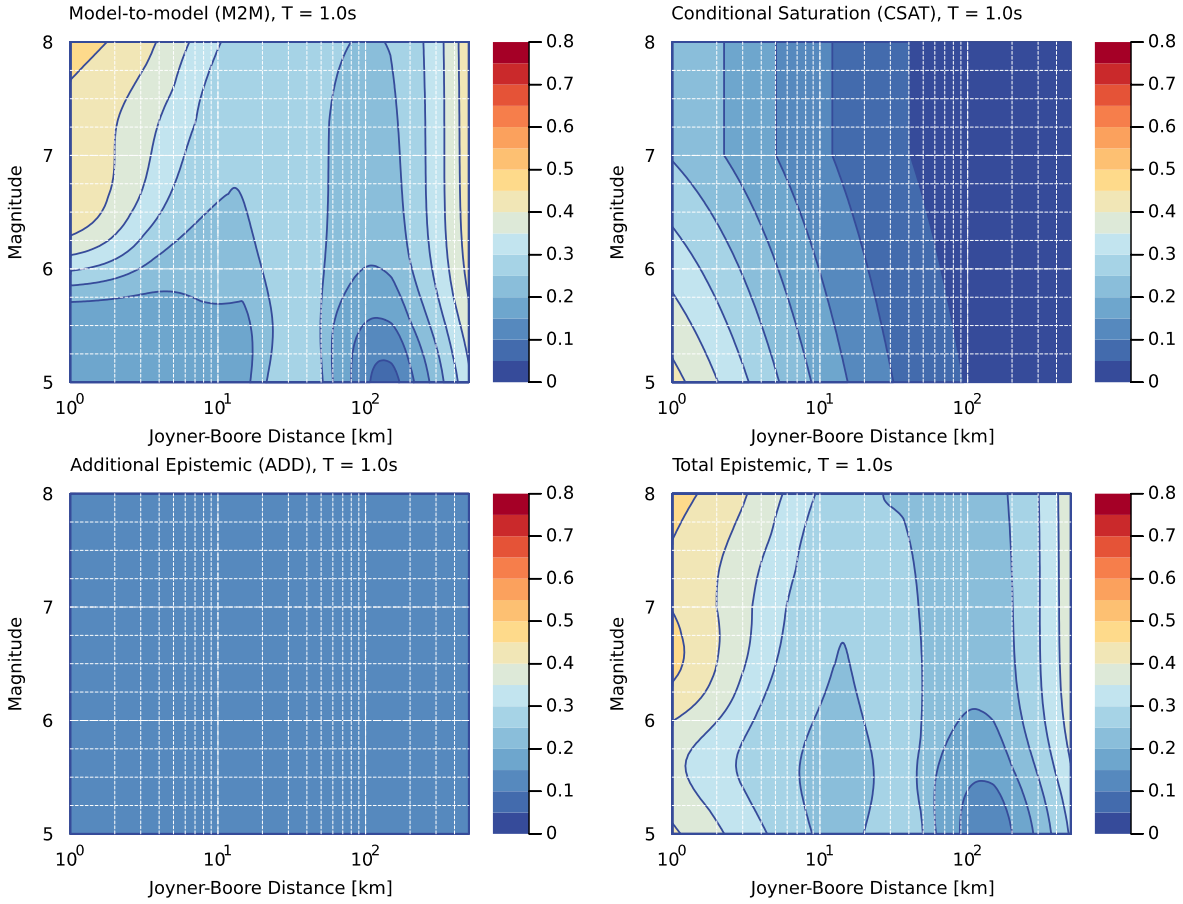

Figure 9-54. Components of Equation 9-46 plotted over magnitude-distance space for a period of 1.0 seconds. The title of each panel describes what is being plotted. The upper left panel shows model-to-model uncertainty, the upper right panel shows the conditional near-source saturation uncertainty, the lower left shows the additional epistemic uncertainty, and the lower right shows the total epistemic uncertainty.

9.2.6.7 Logic-tree definition for reference rock model

The epistemic uncertainty in the mean logarithmic ground-motion levels is assumed to be described by a normal distribution, centred on the mean $\mu_{\ln SA}$ from Equation 9-45, and with standard deviation $\sigma_{\mu_{\ln SA}}$ from Equation 9-46. The assumption of normality is based upon the central limit theorem and the recognition that the logarithmic mean arises through an additive process. That is, the mean is a linear combination of the individual models, and the epistemic uncertainty contributions are also represented as a linear sum of contributions. Such an additive process will asymptotically converge to a normal distribution according to the central limit theorem. Branches and weights for the logic-tree node associated with this epistemic

uncertainty are then specified using a three-point discrete representation of this continuous distribution (Keefer and Bodily, 1983).

Keefer and Bodily (1983) provide many three-point approximations for continuous random variables. Two of these are often-used within seismic hazard applications: the extended Pearson-Tukey and the extended Swanson-Megill approximations. Both of these methods provide very similar performance in terms of approximating the mean and variance of a random variable, especially a symmetric variable like a normally-distributed variable. The extended Pearson-Tukey approximation combines the 5th, 50th and 95th quantiles of the variable along with weights of 0.185, 0.63 and 0.185. The extended Swanson-Megill approximation combines the 10th, 50th and 90th quantiles of the variable with weights of 0.3, 0.4, and 0.3, respectively. For convenience, analysts sometimes simplify the extended Pearson-Tukey approximation further by making the weights 0.2, 0.6 and 0.2, leading to a slight overestimation of the variance.

Here, the extended Swanson-Megill approximation is used as the weights are already in a convenient compact form of 0.3, 0.4, and 0.3 and the GMM TI Team avoids any ambiguity regarding the values for the weights. These weights are tied to the 10th, 50th and 90th quantiles of a normal distribution, thus the central branch is simply the mean logarithmic prediction $\mu_{\ln SA}$, while the upper and lower branches are defined as: $\mu_{\ln SA} \pm 1.28\sigma_{\mu_{\ln SA}}$. The value of 1.28 comes from:

9-58

$$\Phi^{-1}(0.9) = 1.28155$$

where Φ is the cumulative distribution function of the standard normal distribution.

Finally, Figure 9-55 visually depicts the overall logic-tree node, branches and weights for the median reference rock model. The weighted mean of the seven inversion-based models are combined into a single model for the mean logarithmic spectral acceleration in Equation 9-45 and the various contributions to epistemic uncertainty are combined within Equation 9-46, thus the final logic-tree representation becomes very simple.

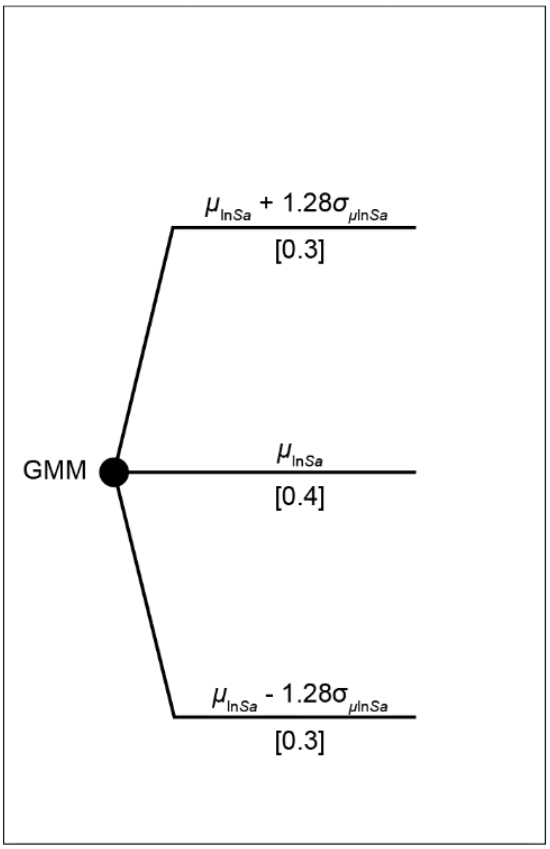

Figure 9-55. Reference rock logic-tree. Mean logarithmic spectral acceleration levels, $\mu_{ln\,SA}$, are defined through Equation 9-45, and the epistemic standard deviations, $\sigma_{\mu_{ln\,SA}}$, are defined through Equation 9-46

9.3 SIGMA MODEL

The aleatory variability describes the expected deviation from the mean ground-motion that can occur at a given site. To estimate this variability, we generally rely on the ergodic assumption, which states that variability in space (between different locations) can be used as a substitute for variability over time (Anderson and Brune, 1999). Using this assumption, global datasets are considered applicable for estimating the variability of the ground-motion at a given site.

Recent decades have seen a large increase in the number of ground-motion recordings that are available for use and numerous projects have made significant efforts to collect the recordings that are available. This has allowed for repeatable site effects at some stations to be determined and removed from the aleatory variability. This allows us to develop models for aleatory variability for single stations, referred to as “single-station sigma” (Atkinson 2006). The GMM TI Team decided to use single-station sigma since it is appropriate for sites where the site response model includes the epistemic uncertainty in the repeatable site effects.

This model is built from the individual components of single-station within-event variability and between-event variability that are then combined into a single-station sigma model. An overview of partially non-ergodic single-station sigma is given in Section 9.3.1. The evaluation and integration of within-event single-station variability and between-event variability are given in Section 9.3.2 and 9.3.3. The full sigma logic tree and a discussion of the distribution of sigma is given in Section 9.3.4.

9.3.1 Background of partially non-ergodic sigma

When repeatable site effects at a site can be modelled through a site adjustment to the median ground-motion prediction, aleatory variability reduces to a value referred to as single-station sigma (Atkinson 2006). The requirements for the use of single-station sigma on a project include: the characterisation of the median and epistemic uncertainty in the site-specific ground-motion adjustments, and accounting for the epistemic uncertainty in the single-station sigma. When these two conditions are met, the use of single-station sigma is not only allowed but required to capture the body and range of TDI. When total sigma is used under these conditions, the epistemic uncertainty in the site-specific ground-motion adjustments is double counted, once as aleatory variability in the total sigma and once as epistemic uncertainty in the site-specific ground-motion adjustments. This leads to overestimation of total variability.

Within the framework of single-station sigma, as defined by Al Atik et al. (2010), the total ergodic standard deviation of ground-motion is written as:

9-59

$$\sigma = \sqrt{\phi^2 + \tau^2}$$

where σ is the total ergodic variability, ϕ is the within-event ergodic variability, and τ is the between-event ergodic variability. The within-event variability can be separated into a site-to-site variability and a single-station variability as follows:

9-60

$$\phi = \sqrt{\phi_{S2S}^2 + \phi_{SS}^2}$$

where ϕ_{S2S} is the within-event site-to-site variability and ϕ_{SS} is the within-event single-station variability. The partially non-ergodic single-station sigma (σ_{SS}) can then be written as:

9-61

$$\sigma_{SS} = \sqrt{\phi_{SS}^2 + \tau^2}$$

In order to fully define the partially non-ergodic single-station sigma, we must define ϕ_{SS} and τ.

9.3.2 Single-station within-event variability

At Workshop 2, Linda Al Atik presented a number of ϕ_{SS} models (Al Atik, 2022). The Hanford and Thyspunt SSHAC projects both used the Hanford model, which was superceded by the SWUS and Al Atik (2015) models. The SWUS model was project specific and thus not appropriate for use on the current project. The Al Atik (2015) model and an update of this model applied to σ_{SS} in the INL SSHAC project were both presented as viable proponent models.

The Al Atik (2015) model is based on residuals of the NGA-West2 database of worldwide earthquakes. Using the within-event residuals of the NGA-West2 GMPEs, ϕ_{SS} was calculated using a mixed-effects regression with the station terms as the random effect for stations with a minimum of three recordings. The dependence of ϕ_{SS} on both magnitude and distance were examined and a global magnitude dependent ϕ_{SS} model developed for the average of the four NGA-West 2 GMPEs. The model is compared to the individual NGA-West2 GMPE results in Figure 9-56.

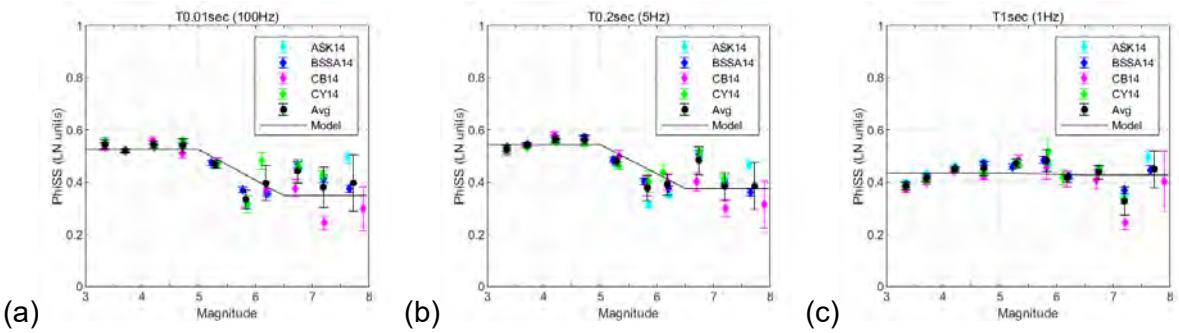

Figure 9-56. Comparison of Al Atik (2015) ϕ_{SS} model with individual ϕ_{SS} values from the NGA-West2 GMPEs for frequencies of (a) 100 Hz, (b) 5 Hz and (c) 1Hz.

This model has been evaluated for both the Western U.S. (WUS) (INL, 2023) sites and as part of the NGA-East project (Al Atik, 2015). The GMM TI Team explored the option of using the residuals from the inversions performed by Edwards and the GMM TI Team to make an adjustment to the Al Atik (2015) model in a similar manner to the NGA-East process. The

GMM TI Team determined that the data was not sufficiently numerous nor from large enough magnitude earthquakes to warrant a deviation.

The GMM TI Team decided to adopt the Al Atik (2015) model as it is the latest model available, developed from a large set of data, and there is insufficient data in the Inversion GMDB to warrant any changes. The functional form for the ϕ_{ss} model is as follows:

9-62

$$\phi_{ss} = \begin{cases} a \; for \; \boldsymbol{M} \leq 5.0 \\ a + (\boldsymbol{M} - 5.0) * \dfrac{(b-a)}{1.5} for \; \boldsymbol{M} \leq 6.5 \\ b \; for \; \boldsymbol{M} > 6.5 \end{cases}$$

where *a* and *b* are coefficients given in Table 9-12. The distribution of ϕ_{ss} is represented using one of the distributions from Keefer and Bodily (1983), the extended Pearson-Tukey approximation, which combines the 5th, 50th and 95th quantiles of the variable along with weights of 0.2, 0.6 and 0.2. The logic-tree for ϕ_{ss} is shown in Figure 9-57. The high and low *a* and *b* values to be used in this distribution are given in Table 9-12.

Table 9-12. Coefficients for the global ϕ_{ss} model (originally Table 5.11 in Al Atik, 2015).

Period (sec)	Frequency (Hz)	Central		High		Low	
		a	***b***	***a***	***b***	***a***	***b***
0.01	100	0.5423	0.3439	0.6553	0.4446	0.4367	0.2525
0.02	50	0.5410	0.3438	0.6537	0.4452	0.4357	0.2518
0.03	33	0.5397	0.3437	0.6521	0.4459	0.4347	0.2510
0.04	25	0.5382	0.3436	0.6503	0.4466	0.4334	0.2503
0.05	20	0.5371	0.3435	0.6489	0.4473	0.4326	0.2496
0.1	10	0.5308	0.3431	0.6412	0.4505	0.4277	0.2461
0.2	5	0.5189	0.3585	0.6266	0.4673	0.4182	0.2600
0.4	2.5	0.4973	0.4004	0.6002	0.5057	0.4010	0.3037
1	1	0.4475	0.4201	0.5403	0.5217	0.3607	0.3263
2	0.5	0.3984	0.3986	0.4836	0.4818	0.3189	0.3208

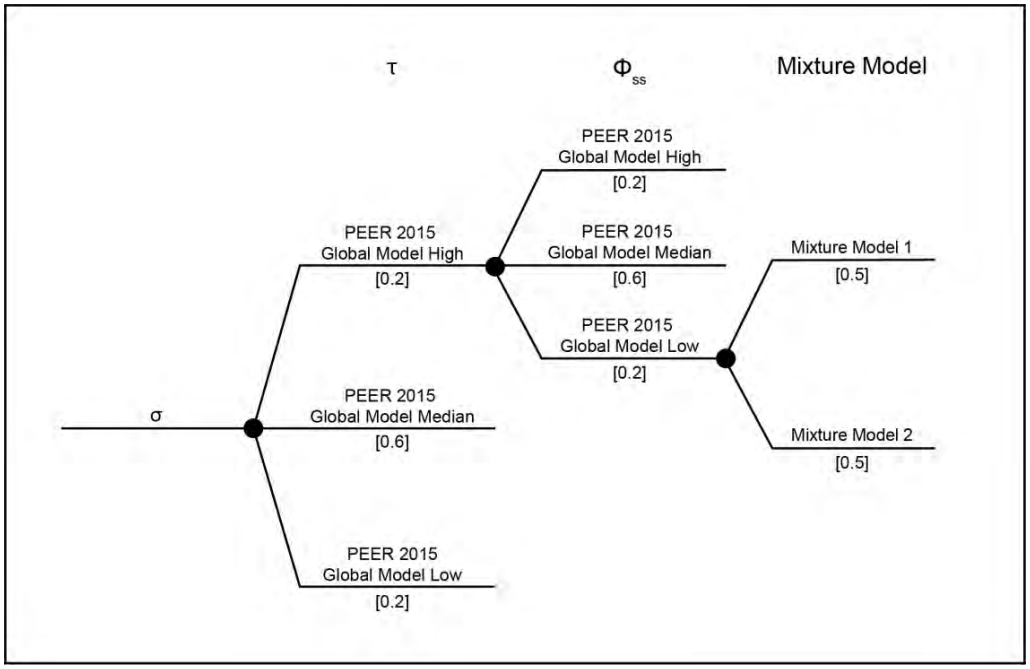

Figure 9-57. Partially non-ergodic single-station sigma logic tree.

9.3.3 Between-event variability

At Workshop 2, Linda Al Atik presented a number of τ models (Al Atik, 2022). The Hanford and SWUS SSHAC project models have been superceded by the Al Atik (2015) model. The Al Atik (2015) model and an update applied to σ_{SS} and used on the INL SSHAC project were both presented as viable proponent models.

The evaluations described in the previous section similarly apply to the τ models. The GMM TI Team decided to adopt the Al Atik (2015) model as there is not sufficient data to reject the hypothesis that earthquakes in South Africa exhibit similar variability to worldwide datasets. Additionally, it is developed from a large set of data and has been utilised on other SSHAC projects. The functional form for the τ model is as follows:

9-63

$$\tau = \begin{cases} \tau_1 \; for \; \boldsymbol{M} \leq 4.5 \\ \tau_1 + (\tau_2 - \tau_1) * \dfrac{(M - 4.5)}{0.5} for \; \boldsymbol{M} \leq 5.0 \\ \tau_2 + (\tau_3 - \tau_2) * \dfrac{(M - 5.0)}{0.5} for \; \boldsymbol{M} \; \leq 5.5 \\ \tau_3 + (\tau_4 - \tau_3) * \dfrac{(M - 5.5)}{1.0} for \; \boldsymbol{M} \leq 6.5 \\ \tau_4 \; for \; \boldsymbol{M} > 6.5 \end{cases}$$

where τ_1 through τ_4 are coefficients given in Table 9-13. The distribution of τ is represented using one of the distributions from Keefer and Bodily (1983), the extended Pearson-Tukey approximation, which combines the 5th, 50th and 95th quantiles of the variable along with weights of 0.2, 0.6 and 0.2. The logic-tree for τ is shown in Figure 9-58. The high and low τ_1 through τ_4 coefficients to be used in this distribution are given in Table 9-13.

Table 9-13. Coefficients for the global τ model (originally Table 5.11 in Al Atik, 2015).

	τ_1	τ_2	τ_3	τ_4
Central	0.4436	0.4169	0.3736	0.3415
Low	0.3280	0.2928	0.2439	0.2343
High	0.5706	0.5551	0.5214	0.4618

9.3.4 Logic-tree for sigma model

At Workshop 2, Linda Al Atik presented a model for σ_{SS} that is composed of adjusted weights on the logic-tree branches (Al Atik, 2022). This model was developed as part of the INL SSHAC project (INL, 2023) and was presented to the GMM TI Team prior to publication of the final report. The model accounts for the spatial correlation of within-event residuals at a given station, where an increase of ϕ_{ss} on the order of 10% and a reduction in τ of 0-7% has been shown as in Figure 9-59.

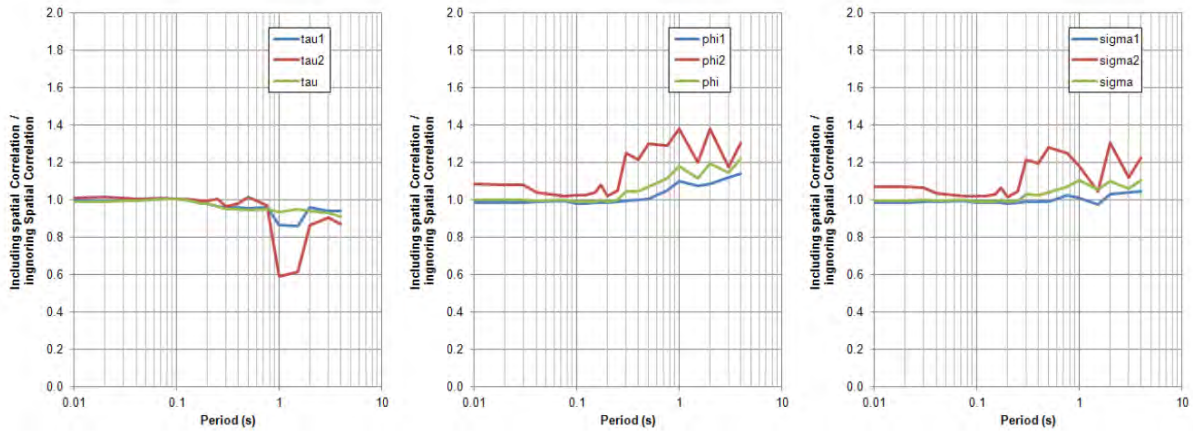

Figure 9-58. Impact of spatial correlation on ϕ_{ss}, τ, and σ_{SS}. Tau1, phi1, and sigma1 are for magnitude less than or equal to 5.0. Tau2, phi2, and sigma2 are for magnitude greater than or equal to 7.25. Tau, phi and sigma are for a homoscedastic model. From Geopentech (2015).

While the GMM TI Team agrees that the INL sigma-station sigma model applies a method to try to account for spatial correlation, there are several other factors that may influence σ_{SS} that it does not account for and which may shift the distribution of σ_{SS}sigma back to the original model. For example, apparent spatial correlations can arise from magnitude uncertainties and uncertainties in shear-wave velocity estimates (that are not accounted for in the above analyses), and there are strong trade-offs between the spatial correlations and the event terms that regression algorithms find extremely challenging to decouple. These trade-offs can mean that lower estimates of between-event variability are obtained for certain spatial correlation lengths, and this reduction in tau is offset by an increase in phi. In addition, spatial correlation models that are used in these sorts of regressions are isotropic, have a variable performance with lag distance (i.e., their predictive performance varies strongly with inter-station spacing), and the regression frameworks ignore station-specific nugget effects that have important impacts upon the estimated correlation lengths and variance components.

Additionally, The INL report was not yet complete when the evaluation of single-station sigma was evaluated. It was the opinion of the GMM TI Team that the INL single-station sigma model was not yet mature enough to adopt for the present study as there may be additional factors that were not considered, and the full description of the model was unavailable. The GMM TI Team decided to use the original Al Atik (2015) model given that additional research may push the INL model back to the original form. This logic-tree is shown in Figure 9-59.

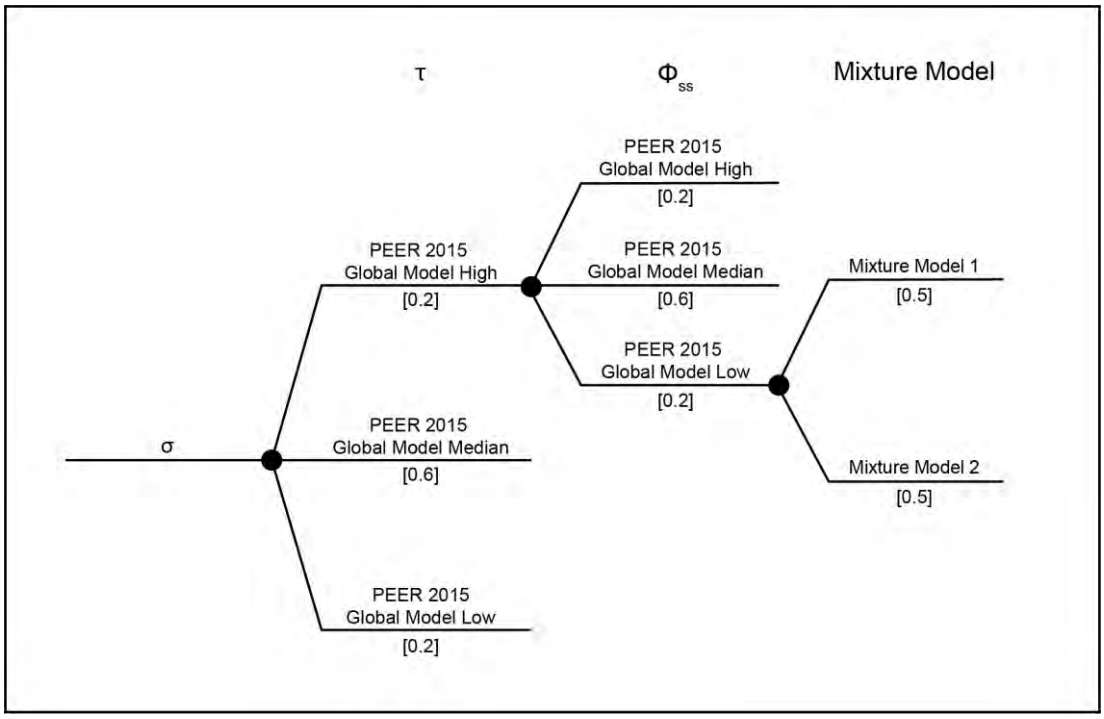

Figure 9-59. Aleatory Variability Logic-Tree

It has long been observed that ground-motion residuals from GMPEs do not match a log-normal distribution at the tails, as shown in Figure 9-60 (Coppersmith et al., 2014). As part of the SSHAC Level 3 Hanford Sitewide PSHA and the Southwestern United States studies, analyses of between-event residuals of the Abrahamson et al. (2014) and Chiou and Youngs (2014) GMPEs were performed and a deviation from the assumed normal distribution found at the upper and lower epsilon values. This deviation was not observed for within-event residuals. The deviation from the assumed normal distribution for within-event residuals can be modelled using two normal distributions and is referred to as the mixture-model (PNNL 2014, Geopentech, 2015). To account for this, the GMM TI Team decided to apply the mixture-model. A mixture model of two equally weighted normal distributions was adopted similar to PNNL (2014), Geopentech (2015), and many other SSHAC projects. These two normal distributions use 0.8 and 1.2ϕ_{ss}.

9-64

$$P(Z > z) = 0.5\left\{1 - \Phi\frac{(z-\mu)}{\sigma_{mix1}}\right\} + 0.5\left\{1 - \Phi\frac{(z-\mu)}{\sigma_{mix2}}\right\}$$

where, σ_{mix1} and σ_{mix2} are the standard deviations obtained by using 0.8 and 1.2ϕ_{ss} with the interevent standard deviation, τ.

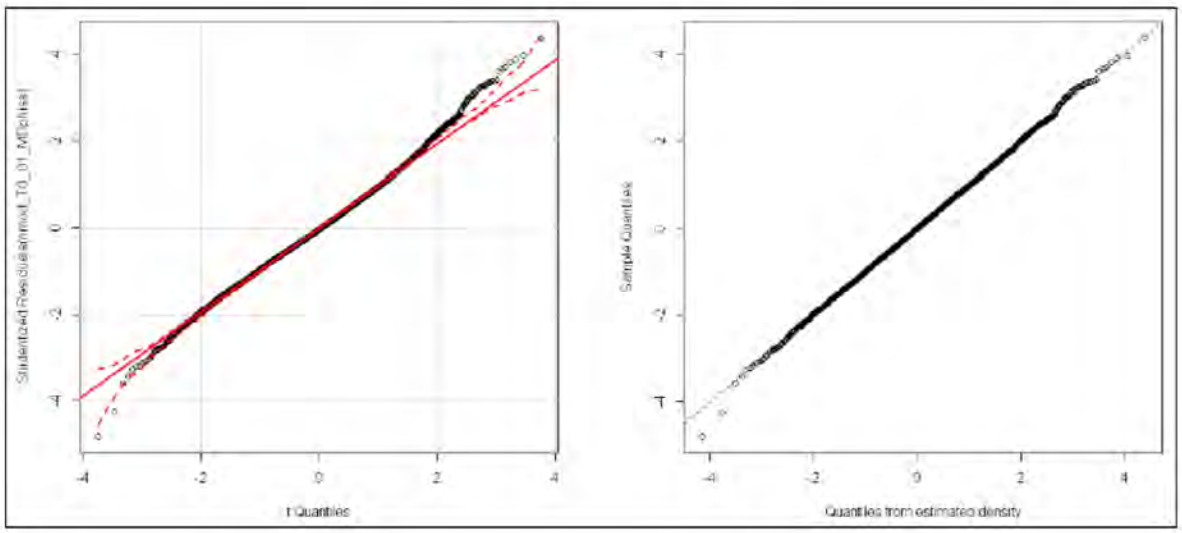

Figure 9-60. Fit to (a) normal and (b) mixture model distributions of the Abrahamson et al. (2014) event- and site-corrected residuals. The mixture model in (b) uses two distributions with sigma ratios of 1.2 and 0.8 with 50% weight to each distribution. From Coppersmith et al. (2014).

9.4 SITE AMPLIFICATION MODEL

9.4.1 Background of one-step site response

This section describes the host-to-target site adjustments for the Duynefontyn site. As described in Section 9.1.5, the GMM TI Team decided to adopt the one-step site response approach recommended by Rodriguez-Marek et al. (2021) and Williams and Abrahamson (2021). In this approach, the site amplification model is developed by performing site response analyses for both the target site profile and the host site profile. The site response analyses used to develop the SAF require the following, each of which is considered in a logic-tree:

- Selection of the numerical approach that will be utilised to compute site amplification.
- Site-specific shear-wave velocity profiles that extend to a depth that merges with the V_S profile of the reference condition associated with the host backbone model of CY14
- Site-specific κ_0 values to constrain the small-strain damping profile.
- Nonlinear modulus reduction and damping (MRD) curves for the site-specific subsurface conditions.

The GMM TI Team constructed a logic-tree with assigned weights to each viable combination of these inputs to the site response calculations, as shown in Figure 9-61, Figure 9-62, and Figure 9-63. We provide the justification for the organisation of this logic-tree and the individual weights in the subsequent sections.

Preliminary evaluations of the geologic conditions and associated V_S profiles at the Duynefontyn site (for both the new build and the Koeberg sites) indicated that the site response should not be significantly nonlinear. This assessment was based on the excavation of overlying sand layers to the top of rock strata prior to construction of the existing KNPS (and assuming a similar course of action for the Duynefontyn site) and the large shear-wave velocities measured at the site for the rock materials. Thus, the GMM TI Team decided to perform the site response analyses using the equivalent-linear (EQL) approach. EQL analyses were performed using pystrata (Kottke, 2022), a Python-based version of the well-known Strata software (Kottke and Rathje, 2008).

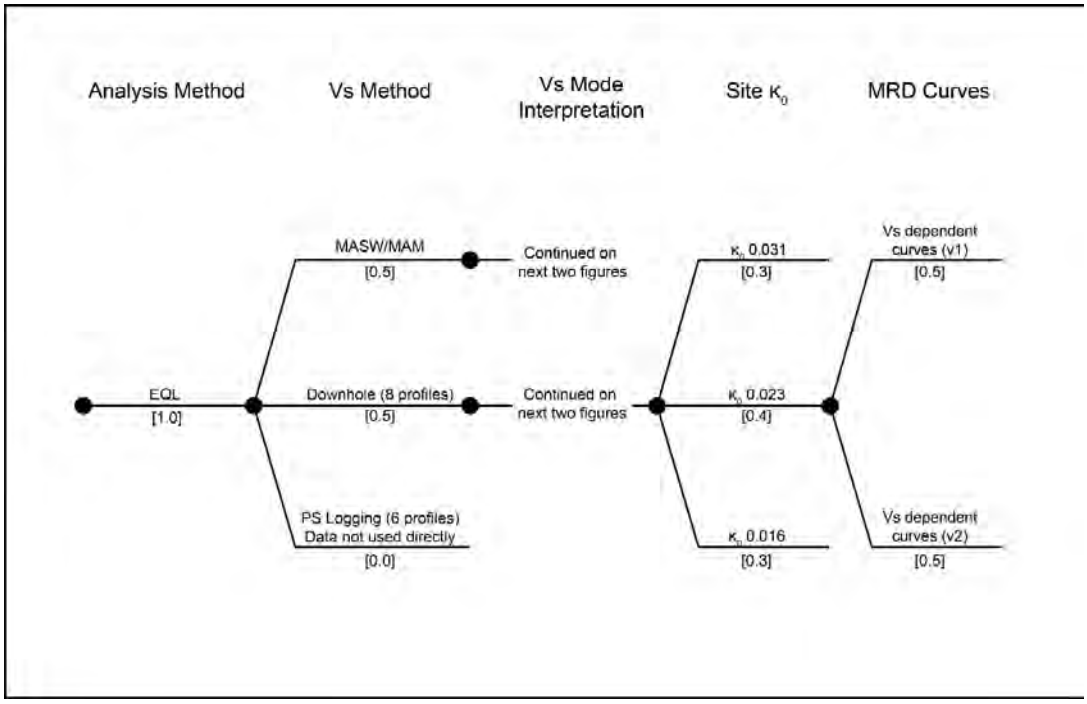

Figure 9-61. Logic-tree for site response model at the Duynefontyn site.

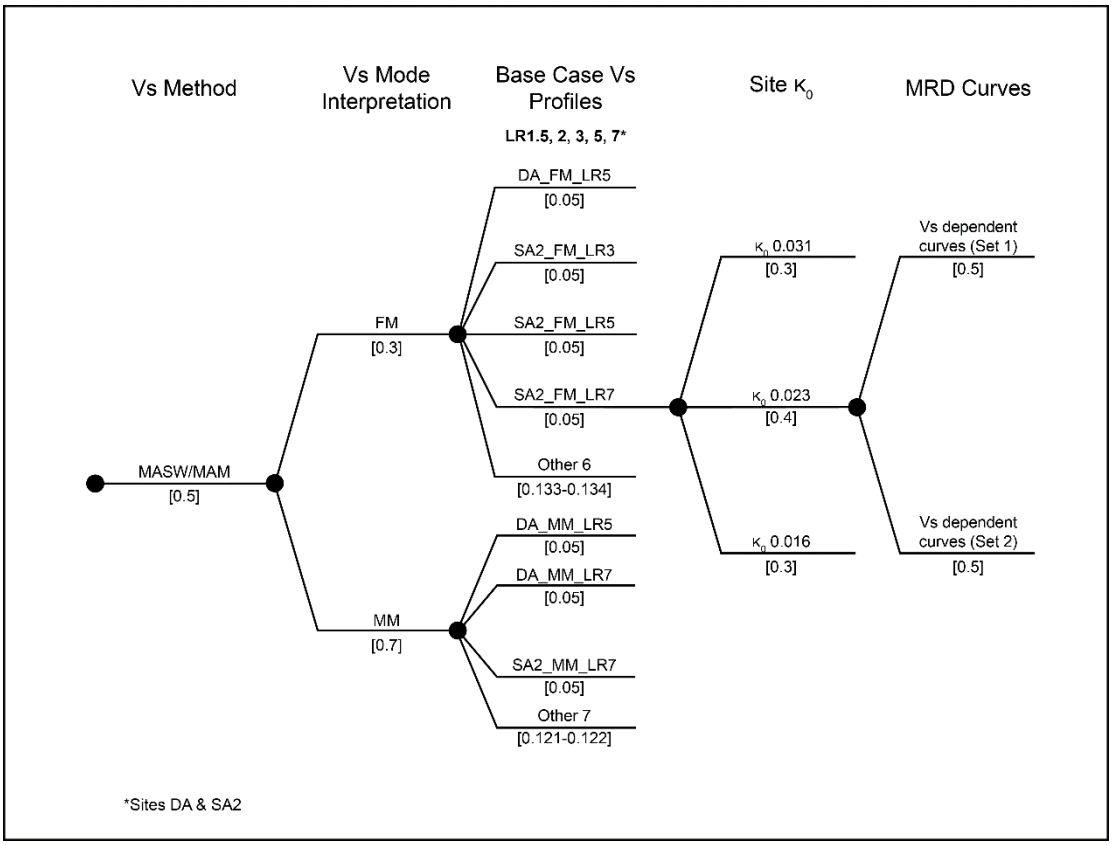

Figure 9-62. Logic-tree for multichannel analysis of surface waves (MASW) and microtremor array measurement (MAM) V_S profiles.

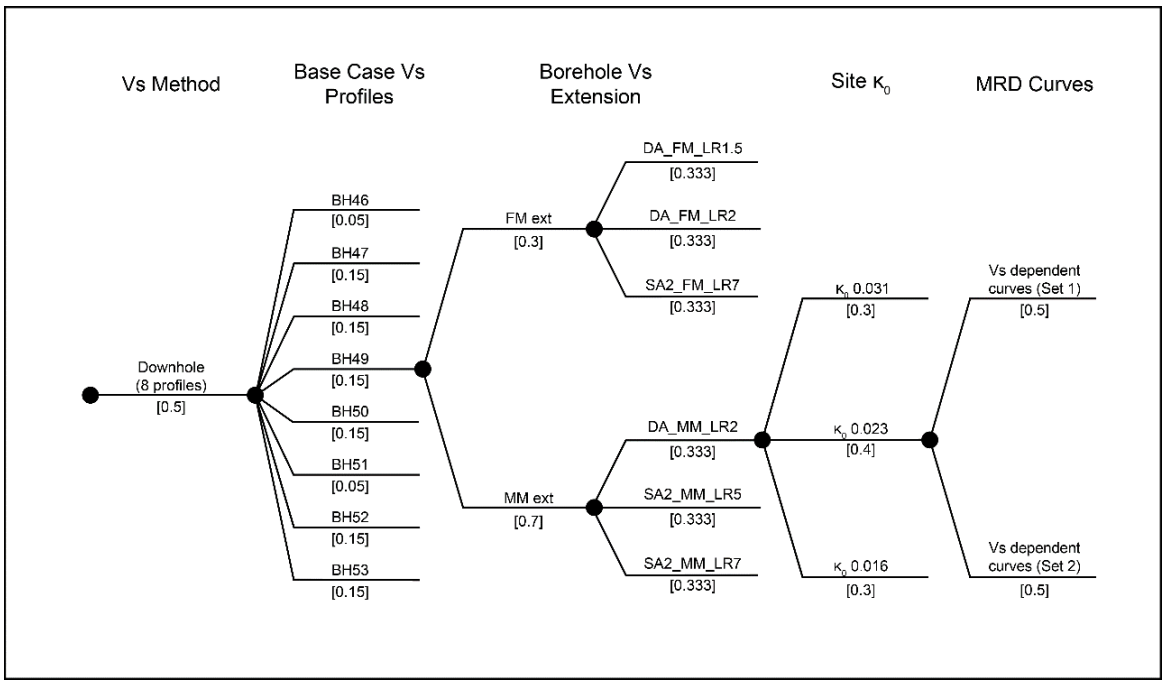

Figure 9-63. Logic-tree for the downhole V_S profiles.

9.4.2 Development of site profiles

The site-specific V_S characteristics are a fundamental input to the site response analysis. Estimates of V_S can come from a variety of sources, each with advantages and limitations. As discussed in Chapter 4, several phases of geotechnical and geophysical site investigations were performed across the Duynefontyn site. A summary of these methodologies is provided in this section, and the locations of these investigations are shown in Figure 9-64. Additional information about the site investigation can be found in Section 4.5.

Cox et al. (2024) performed combined multichannel analysis of surface waves (MASW) and microtremor array measurement (MAM) at two locations (DA and SA2). and produced V_S profiles down to depths of approximately 1500 m below the ground surface. SRK Consulting (Du Plessis, 2021) performed downhole (DH) seismic testing in eight boreholes (labelled BH46-BH53). These boreholes generally extended approximately 80 m below the ground surface (i.e. from the top of existing sand layer) and up to 50 m below the base of the sand (i.e. top of rock).

Wireline Workshop performed V_S profiling in six boreholes via PS-suspension logging down to a depth of approximately 90-100 m (below the top of rock) at the DA and SA2 locations, with shallower PS logging (approximately 50 m below the top of rock) performed at other locations across the site (ST1-ST4). Cox et al. (2024) interpreted the raw data from these measurements to obtain estimates of V_S at discrete points within the depths tested.

Figure 9-64. Locations of SRK boreholes (BH), MASW/MAM surface arrays (DA, SA2), and CGS boreholes (DA, SA2, ST).

V_S profiles derived from the MASW/MAM data for the two locations were introduced in Chapter 4.5 and are compared with each other in Figure 9-65. Dispersion data at both DA and SA2 locations were inverted using five layering ratios (LR) of between 1.5 and 7.0 and both a fundamental mode (FM) and multi-mode (MM) interpretation. The LR controls the number of layers, such that larger values of LR result in fewer layers. As shown in Figure 9-65a, V_S values are in the range of 3700-4000 m/s at depths between 200 m and 750 m. In contrast, the MM approach shown in Figure 9-65b yields maximum V_S values nearing 3,300 m/s at depths between 800-1,000 m. As shown in Figure 9-65c and Figure 9-65d, the FM and MM profiles have similar overall trends for the two testing locations (i.e., DA and SA2). The large V_S values from the FM interpretation of the MASW/MAM data were discussed at length by the GMM and SSM TI Teams.

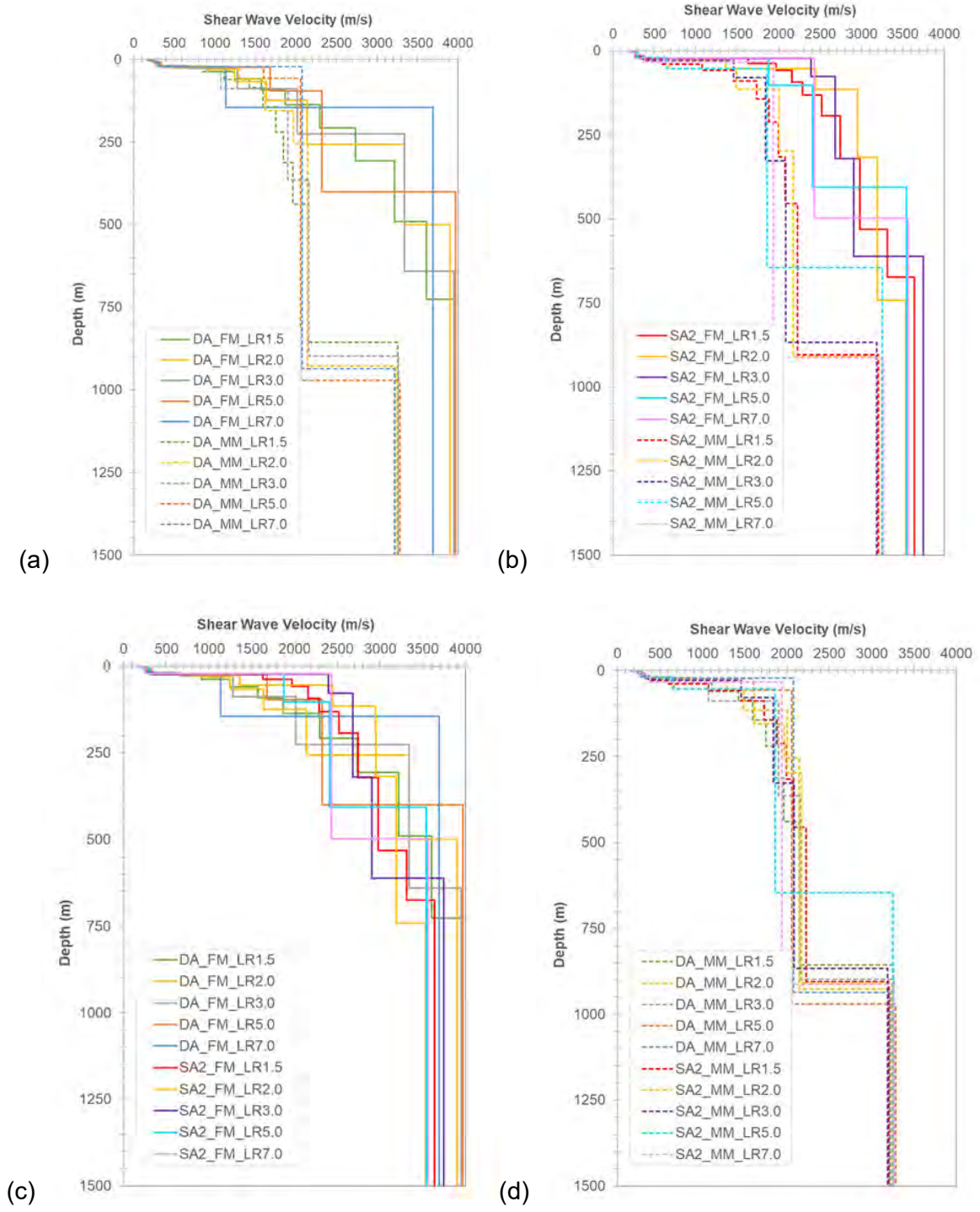

Figure 9-65. V_S profiles from MASW/MAM testing: (a) Fundamental mode (FM) and multi-mode (MM) interpretations at DA site, (b) FM and MM interpretations at SA2 site, (c) comparisons of FM interpretations at the two sites, (d) comparisons of MM interpretations at the DA and SA2 sites.

Figure 9-66 shows the V_S profiles from the DH testing and compares them with those from the MASW/MAM testing. Note that the DH profiles only extend to a depth of approximately 80 m, while the MASW/MAM profiles extend to 1500 m. As discussed in Chapter 4, these DH V_S profiles are based on revised interpretations of the travel time measurements by Cox (2023b) as opposed to the two alternative interpretations from SRK (which the TI Team considered to be either too coarse or too fine in terms of layer thickness). Nearly all the DH profiles have a

reversal in the V_S profile (i.e. an increase in V_S followed by a decrease) between about 45 and 75 m depth. The range of V_S values at the base of the DH profiles roughly aligns with the range of V_S values at the same depth from the MASW/MAM profiles for the DA location but are slightly on the lower end of the range of V_S values at the same depth from the MASW/MAM profiles for the SA2 location.

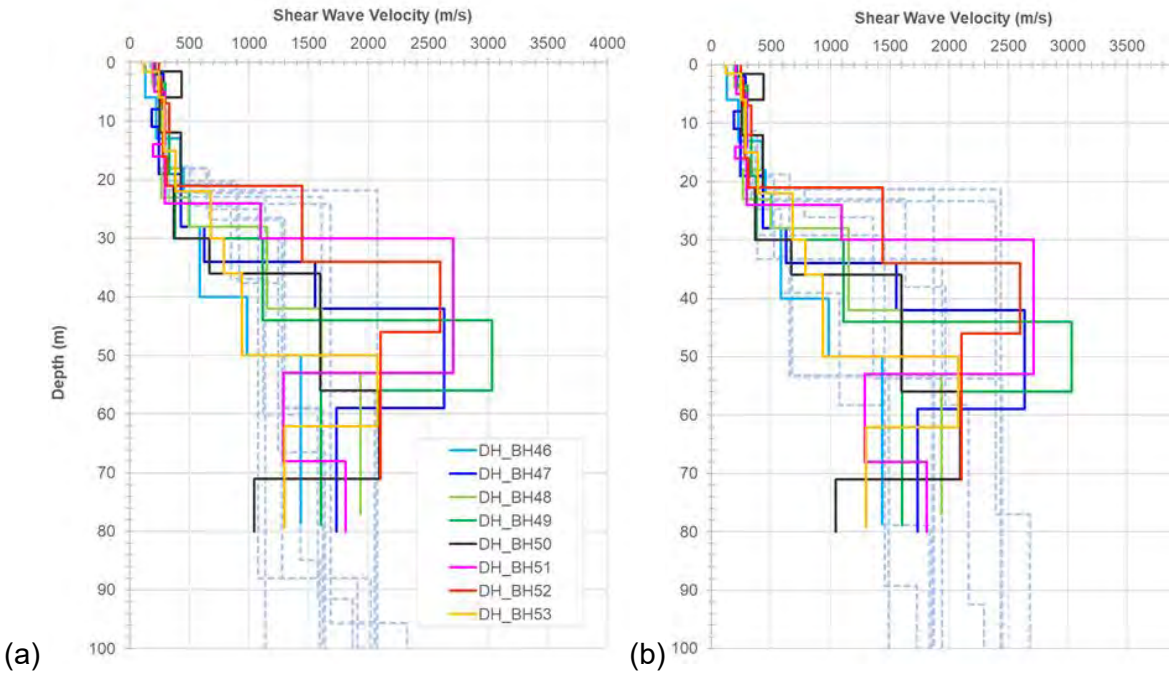

Figure 9-66. Comparison of SRK downhole shear-wave velocities and MASW/MAM profiles in dashed lines as (a) DA site and (b) SA2 site.

As discussed in Section 4.5, the V_S values obtained from the PS logging as interpreted by Matamela and Cox (2024) were of varying quality (Cox, 2022b) due to poor waveforms and unclear shear-wave arrivals. Only V_S values with Code 1 (high confidence), Code 2 medium confidence) and Code 3 (low confidence/ambiguous picks) were considered. Although the Code 1 V_S values are reliable, there are relatively few of these in each borehole. The paucity of high confidence V_S values makes it difficult to develop full V_S values from the PS measurements, and thus the GMM TI Team decided only to use the PS logging V_S values (Codes 1-3) to compare with the higher quality DH and MASW/MAM V_S profiles.

Figure 9-67 groups the V_S values from PS logging by test location (DA, SA2, ST1-ST4) and compares these values with the DH and MASW/MAM V_S profiles. There is general consistency between the PS logging data and the DH and MASW/MAM V_S profiles in the top 20 m, but the PS logging data tends to be larger at depths below about approximately 20-25 m. The deeper V_S from PS logging is predominantly Code 3 data where two V_S values were reported because the analysts could not confidently identify a single wave arrival. Thus, these data are less reliable.

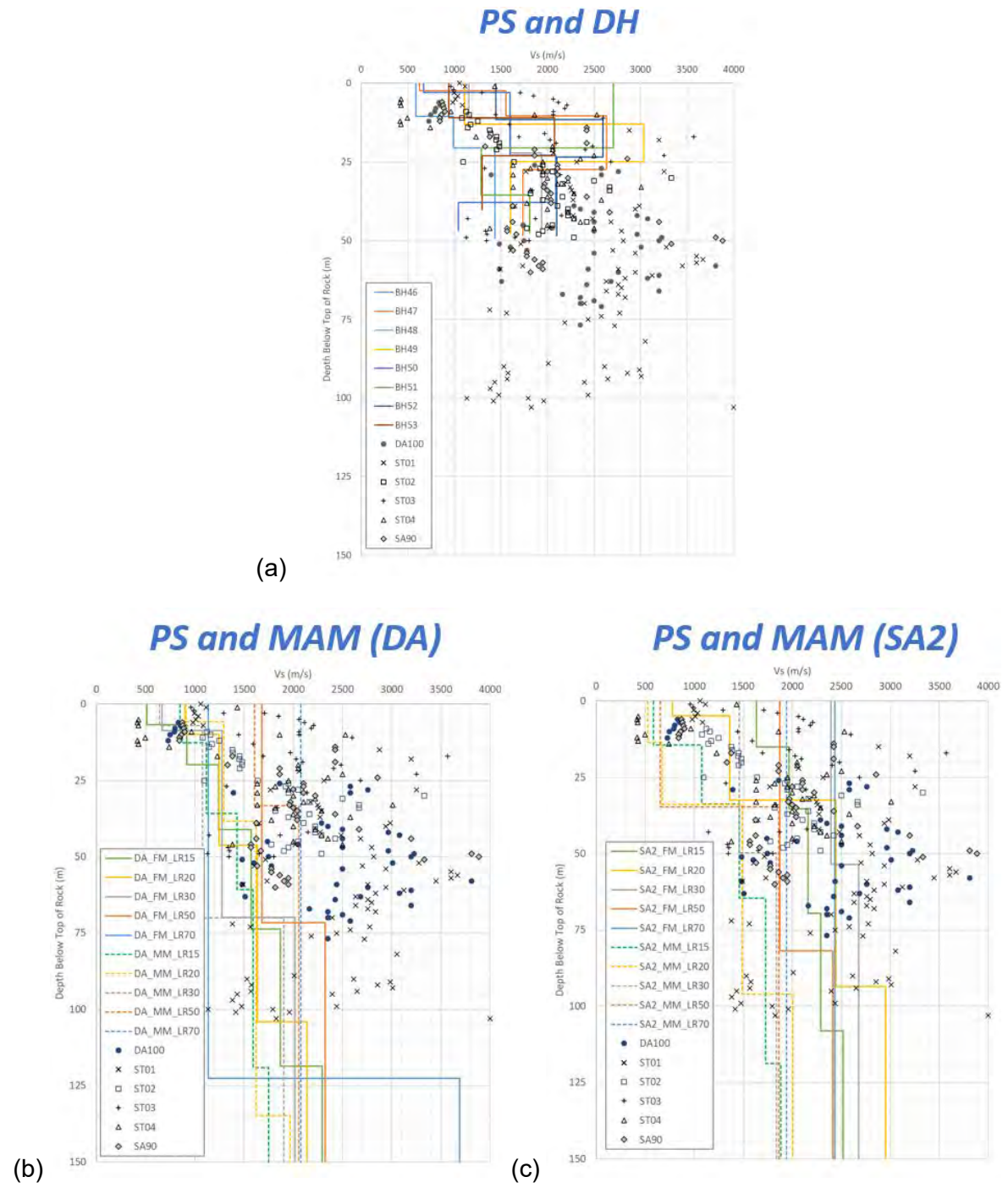

Figure 9-67. V_S estimates obtained from PS logging compared with (a) DH and MASW/MAM profiles from (b) DA site and (c) SA2 site.

The MASW/MAM and DH methods of V_S measurement are considered viable and complementary techniques, with MASW/MAM providing a more global measurement (i.e. averaged over space) and DH providing a more local, point measurement. The quality of the collected data for each technique was deemed high based on the clarity of the dispersion data for MASW/MAM and based on the clarity of the shear-wave arrivals on the downhole records. The quality of the PS logging data was deemed very low due to the difficulty in identifying shear-wave arrivals in the waveforms.

The GMM TI Team considered both the MASW/MAM and the DH methodologies to be equally viable approaches and assigned them equal weights of 0.5 (Figure 9-61). The PS logging results were not used directly to develop V_S base case profiles for the site response analyses because of the lower quality of these measurements, and thus were given a weight of zero (Figure 9-61). The base case V_S profiles were developed separately from the MASW/MAM and DH profiles, as discussed in the following sections.

9.4.2.1 V_S profile development using MASW/MAM data

As discussed in Chapter 4.5, obtaining V_S profiles from the MASW/MAM dispersion measurements requires an inversion process that yields non-unique solutions. Depending on the assumptions made in the inversion process (e.g., mode interpretation, layer thicknesses), the range of the inverted V_S profiles can vary significantly.

Although most MASW/MAM inversions assume a FM when matching the dispersion data, an abrupt increase in V_S at depth can cause a mode jump to a higher mode to be present in the data. The effect of higher modes can be considered using a MM interpretation. The difference between an FM and MM interpretation is predominantly epistemic uncertainty, and the preference of one interpretation over another is guided by additional information (e.g., understanding what causes mode jumps), as we discuss subsequently.

To capture additional epistemic uncertainty in the inversion process, Cox et al. (2024) considered a range of layering ratios (LRs) which tuned the average layer thickness in a V_S profile to be thinner or thicker. For example, a higher LR will typically lead to fewer, thicker layers compared to lower LRs (see LR = 7.0 vs other LRs in Figure 9-68 as an example).

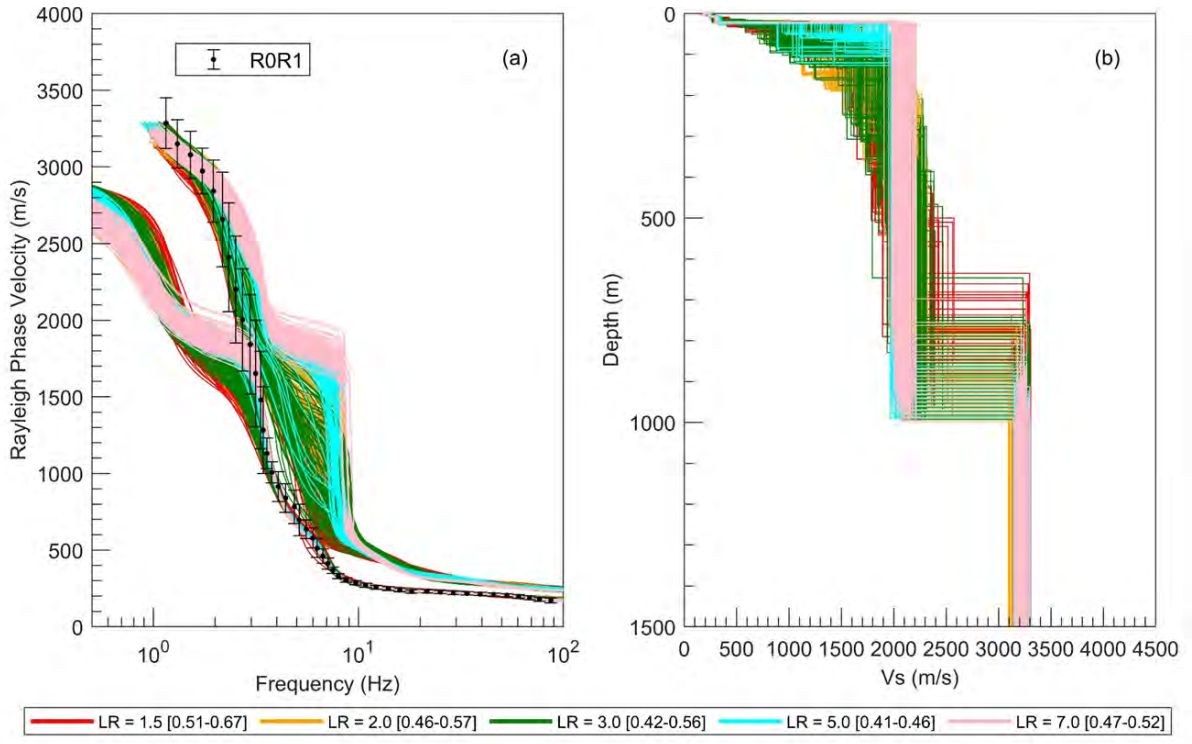

Figure 9-68. Top 100 V_S profiles with lowest misfit values based on dispersion data obtained at the DA location using five LRs and MM interpretation. Misfit ranges are shown in square brackets in the legend.

As discussed in Chapter 4.5.1, Cox et al. (2023a) developed V_S profiles using both FM and MM inversions. For the FM inversion, the dispersion data at low frequencies could not be fit unless the V_S in the rock was allowed to be greater than 4,000 m/s, particularly at the DA site. These velocities are unlikely for relatively shallow depths (~< 500 m). The MM inversions used the fundamental mode and first higher mode to fit the dispersion data. For these inversions, the maximum values of V_S in the MM profiles were successfully restricted to ~3,300 m/s or less while still fitting the dispersion data well.

Based on Cox et al. (2023a), the FM interpretations are considered less likely than the MM profiles because:

- The dispersion data at low frequencies could not be fit well unless V_S in the rock was allowed to be greater than 4,000 m/s (particularly at the DA site). These velocities are unlikely for relatively shallow depths (~< 500 m).
- It is common for very strong impedance contrasts to yield mode jumps and/or superposed modes that can be hard to distinguish at low frequencies. Given the sand and rock interface at the Duynefontyn site, this phenomenon is likely.

The GMM TI Team agreed with these assessments, and they were the basis for the weights assigned to the MM profiles (0.7) and FM profiles (0.3), as shown in Figure 9-62.

Cox et al. (2023a) developed V_S profiles using five LRs (1.5, 2.0, 3.0, 5.0, and 7.0) and using both FM and MM interpretations for both the DA and SA2 locations. Without systematic differences in the V_S profiles at the two sites (Figure 964), the GMM TI Team considered data from the SA2 and DA sites equally valid in the site response analysis. Any differences represent epistemic uncertainty associated with defining a baseline V_S profile at a spatially variable site. Thus, the profiles from SA2 and DA were considered together when defining the base case profiles, yielding a total of 20 MASW/MAM base case V_S profiles (Figure 9-65).

The proposed plan for construction of the new build at the Duynefontyn site includes removal of the surficial sand down to the top of the shallowest rock layer. The V_S profiles based on MASW/MAM measurements included the surficial sand, and thus required removal of V_S values associated with the sand layers prior to using these V_S profiles in site response analyses. To objectively simplify this process, the GMM TI Team assumed that V_S values less than 500 m/s represented sand. The justification of this approach is discussed in Section 4.5.1. The modified V_S profiles after removing the sand are shown in Figure 9-69.

The V_S profiles from the various LRs generally are considered equally likely and thus the TI Team assigned them equal weighting, except for seven profiles. The GMM TI Team decided to down weight these profiles to 0.05 because they included a large V_S at the top of rock (Figure 9-69), which was considered contrary to the expected gradual increase in V_S at the top of rock due to weathering of the rock. The large V_S at the top of rock is considered less likely and thus the following profiles received a weight of 0.05 in the logic-tree:

- DA_FM_LR5
- SA2_FM_LR3
- SA2_FM_LR5
- SA2_FM_LR7
- DA_MM_LR5

- DA_MM_LR7
- SA2_MM_LR7

The other base case V_S profiles were assigned equal weights, such that the total weights add up to 1.0, as shown in Figure 9-62.

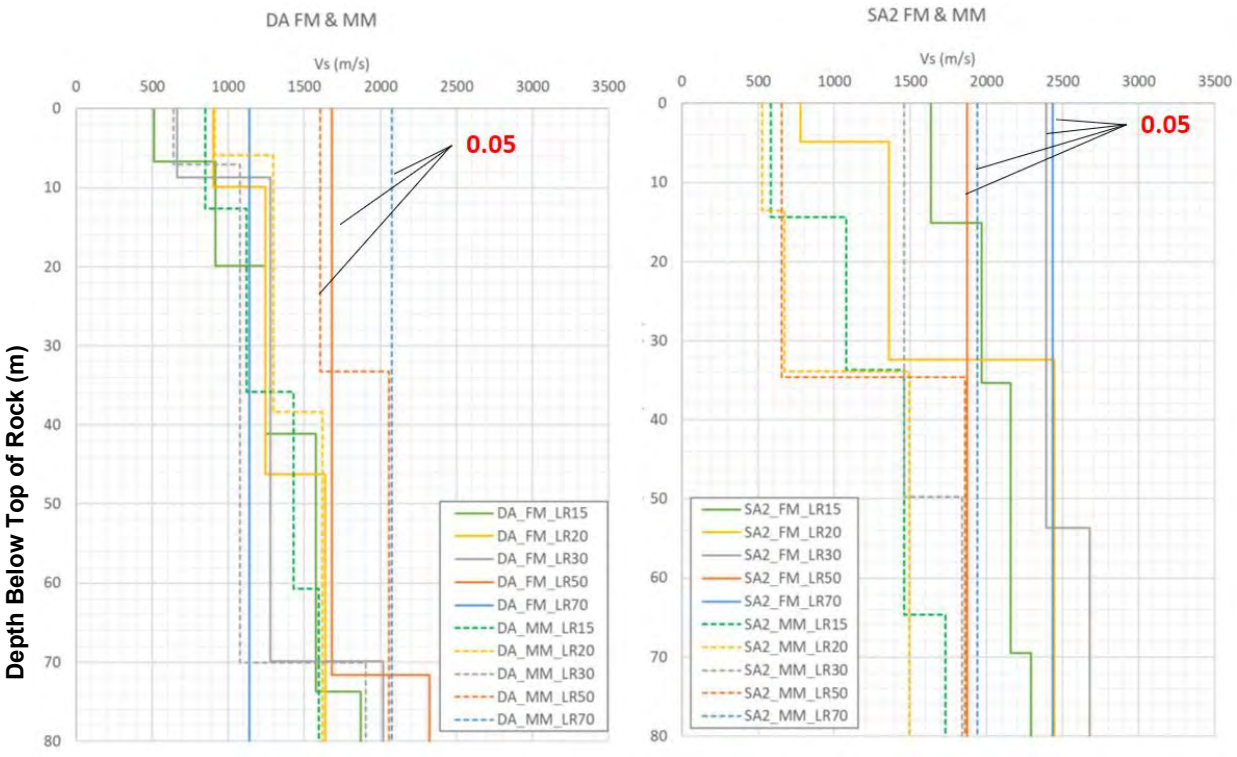

Figure 9-69. Top 80 m of base case MASW/MAM V_S profiles with sand removed for (a) DA site with FM and MM interpretations, and (b) SA2 site with FM and MM interpretations. Profiles with reduced weight (0.05) identified.

To capture aleatory variability in each MASW/MAM base case profile, the GMM TI team decided to use the top 60 V_S profiles from Cox's inversions for each of the 20 base case profiles. In this case, "top 60" refers to the sixty profiles with the lowest misfit from Cox's analyses. No additional randomisation was performed, because variation in layer thickness is already represented in the 60 profiles and the standard deviation of the V_S values in the 60 profiles (Figure 9-70) was already sufficiently high (Stewart et al., 2014).

Typically, it is recommended that randomized V_S profiles should be checked for consistency with the surface-wave dispersion curves (e.g., Teague et al., 2018). In the case of the Duynefontyn site, the dispersion curves inherently include the presence of the surficial sand layers that will be removed prior to the construction of facilities at Duynefontyn. Therefore, the dispersion curves of the V_S profiles developed without surficial sand could not be compared with the measured dispersion curves that included surficial sand.

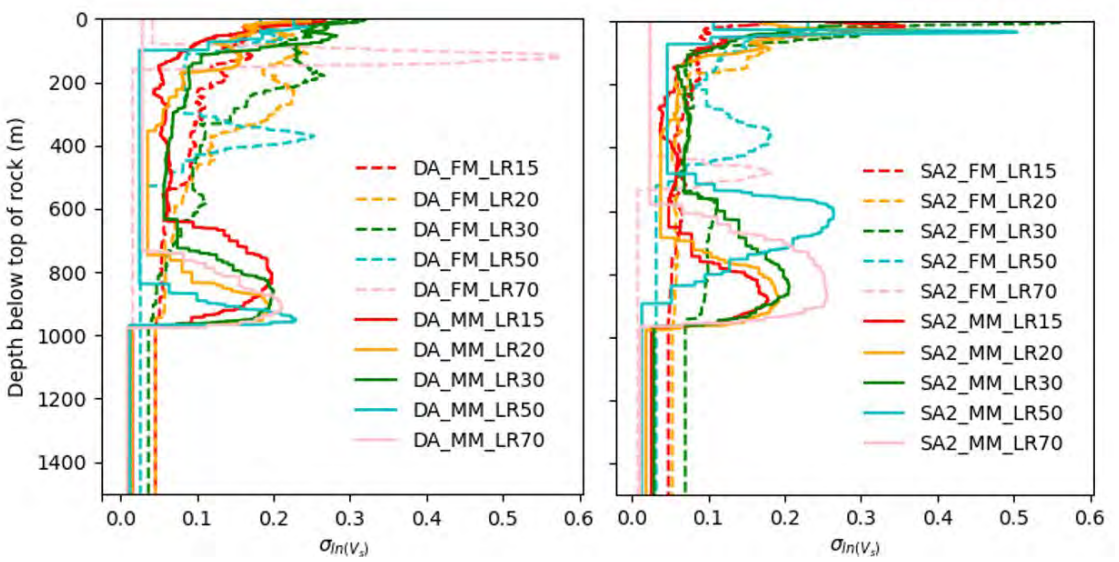

Figure 9-70. Standard deviations of ln(V_S) for the top 60 V_S profiles in each of the 20 base case MASW/MAM profiles excluding surficial sand layer for (a) DA site and (b) SA2 site.

As shown in previous figures (Figure 9-67 and Figure 9-70), the MASW/MAM profiles extend only to 1,500 m depth. To facilitate the one-step approach to estimate SAF, each V_S profile was extended to the maximum depth of the host profile ("AAA21", Al Atik and Abrahamson, 2021), which is approximately 6,000 m deep. A comparison of the MASW/MAM profiles and the AAA21 profile is shown in Figure 9-71. Given the high V_S values at the base of the MASW/MAM profiles, the GMM TI team decided that it was unnecessary to increase the V_S values with increasing depth unless the maximum V_S value of the MASW/MAM profile was less than the maximum V_S value of the AAA21 profile (i.e. 3,300 m/s). In essence, the GMM TI Team assumed that the V_S of the bottom layer in the MASW/MAM profile remains constant with depth until it intersects the AAA21 profile, at which point the extended MASW/MAM profile would follow the AAA21 profile. If the V_S of the bottom layer in the MASW/MAM profile was higher than the maximum V_S of the AAA21 profile, then the V_S of the MASW/MAM profile remained constant down to the full depth of approximately 6,000 m.

To verify that there were no undesirable effects from using a maximum V_S in the site-specific V_S profile that is larger than the maximum V_S of the host profile (AAA21), the GMM TI Team performed sensitivity analyses. In these analyses, the surface response spectrum computed using the inverted V_S profile with the maximum V_S exceeding the maximum V_S of the host profile (i.e. 3,300 m/s) were compared with the surface response spectrum computed using a modified V_S profile in which the V_S of the deepest layer was set equal to 3,300 m/s. The results of the sensitivity analyses showed that the surface response was not significantly affected by allowing the maximum V_S of the profile to exceed 3,300 m/s. The average difference for MM profiles was within 2% for frequencies less than 1 Hz and nearly 0% for frequencies above 1 Hz, and the average difference for FM profiles was within 7% for frequencies less than 1 Hz and within 2% for frequencies above 1 Hz. The DA FM profiles led to the largest differences, because the maximum V_S values for these profiles were generally higher than the maximum V_S values of the other profiles. Thus, the GMM TI Team agreed not to force the V_S of the deepest layer to match the V_S of the deepest layer of the host profile. This decision only affected the FM profiles, because the MM profiles were restricted to 3,300 m/s maximum during the inversion process.

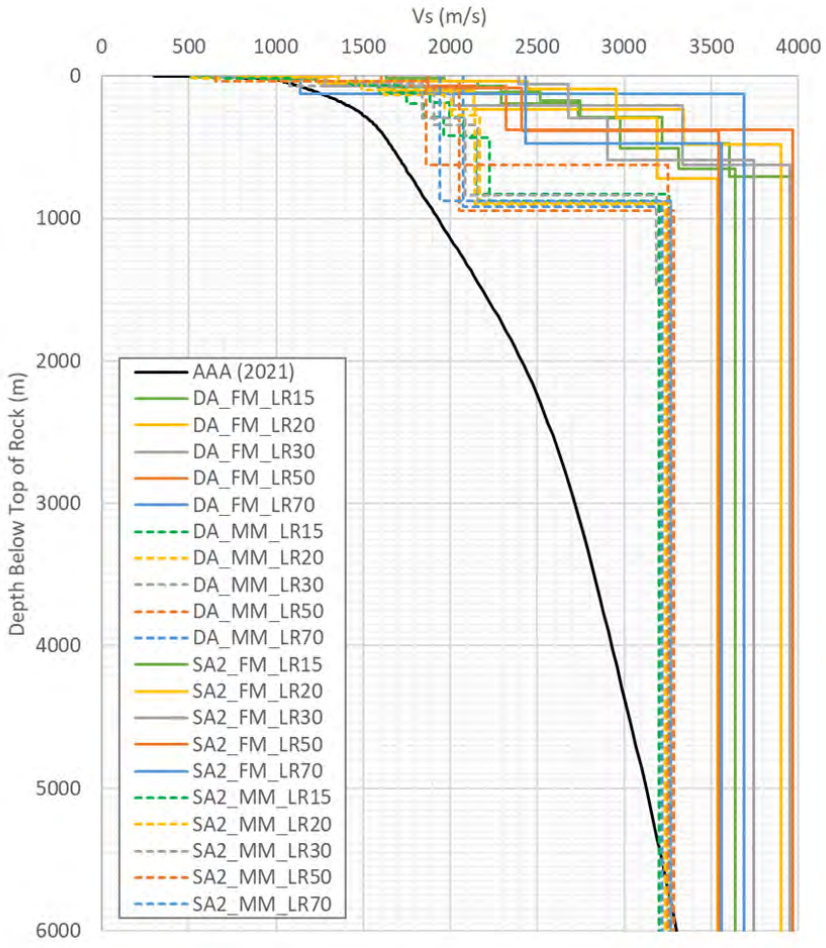

Figure 9-71. Comparison of MASW/MAM V_S profiles vs the host V_S profile (AAA21)

9.4.2.2 V_S profile development using downhole data

SRK performed DH testing in eight boreholes across the site (labelled BH46-BH53). These boreholes generally extended approximately 80 m below the ground surface (i.e. top of existing sand layer) and up to 50 m below the base of the sand (e.g., top of rock). The eight DH profiles represent both spatial variability across the site and heterogeneity in the V_S of the soil and rock at the site. In some past SSHAC studies, GMM TI Teams have decided to either statistically combine the V_S profiles to develop a reduced number of representative base case V_S profiles (e.g., lower-bound, upper-bound, and best estimate) or to use all available V_S profiles to develop base case V_S profiles. In either case, appropriate weights should be assigned to adequately represent the CBR of TDI of the potential V_S profiles. This contributes to developing an adequate estimate in the epistemic uncertainty in the SAFs from site response analyses.

As discussed in Chapter 4.5.2, the V_S profiles based on DH measurements included the surficial sand, and the V_S values that represented the sand layers were removed using the descriptions in the boring logs to identify the top of the rock. These depths were typically about 30 m. The modified V_S profiles after removing the sand are shown in Figure 9-72. Different approaches were used to remove the sand from the MAM/MASW and DH V_S profiles. Both approaches generally removed the same thickness of sand (i.e. about 30 m), but the elevation of the top of rock at each measurement location was not necessarily the same. Given the

significant distance between measurement locations, as shown in Figure 9-64, and the unknown location of specific facilities at the Duynefontyn site, the GMM TI Team deemed it acceptable to utilize the top of rock to define the top of the V_S profiles.

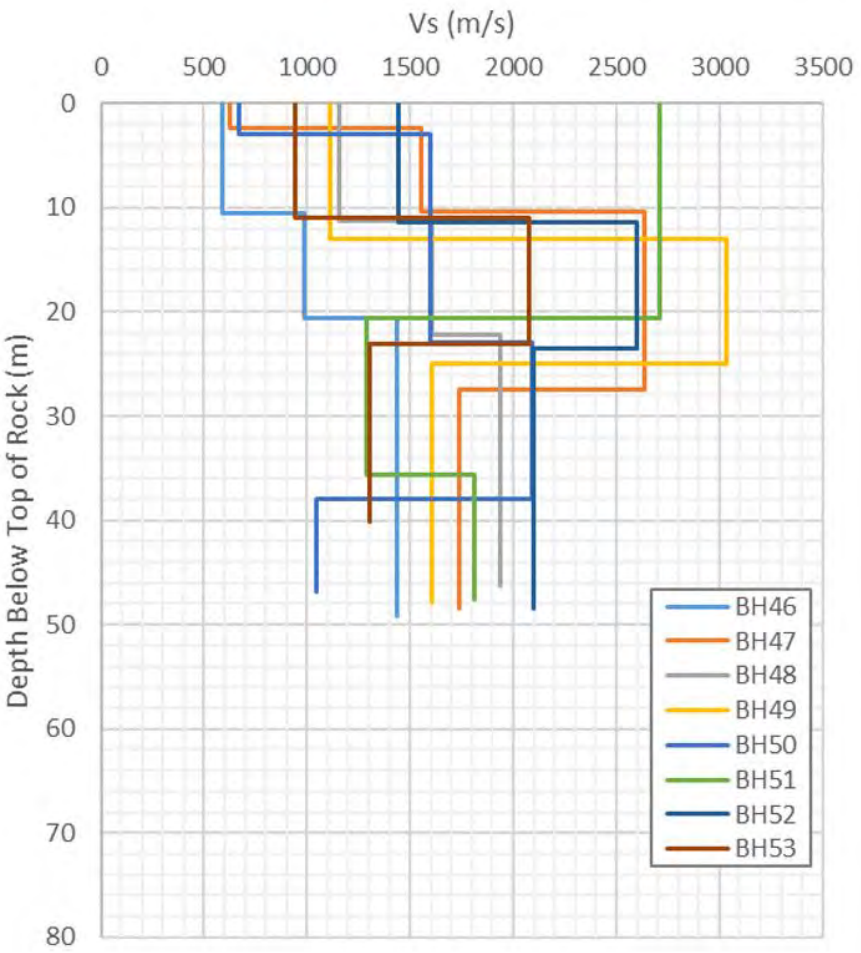

Figure 9-72. Base case DH V_S profiles with sand removed.

The GMM TI Team decided to use all eight DH profiles to create base case V_S profiles representing the DH V_S method, rather than developing a reduced number of representative base case V_S profiles. This decision was made because including all eight profiles in the site response analyses compared to using fewer did not unduly increase the computational burden, and because reducing the V_S profiles to a median and two profiles that are shifted up or down by one standard deviation can lead to smoothed results in SAF space that are undesirable (Ulmer et al., 2021).

DH profiles BH46 and BH51 received lower weights of 0.05, as compared to the weights of 0.15 for the other DH profiles. The reasons for these two DH profiles receiving lower weights are:

- BH46: the geology in this borehole was significantly different from the other boreholes and it is not as characteristic of the site as a whole. The rock encountered in the borehole was mostly shale with some siltstone and sandstone, whereas most of the other boreholes contained predominantly sandstone mixed with some shale and siltstone.

- BH51: The V_S value at the top of rock in this profile was unusually high (V_S = 2,700 m/s). We would expect a more gradual increase in V_S due to weathering in the top of the rock. This larger V_S value may be a consequence of misalignments in the boring log descriptions and V_S measurements.

After removing the surficial sand, the DH V_S profiles typically reached a maximum depth of nearly 50 m. As with the MASW/MAM profiles, each of the base case DH V_S profiles need to extend to a depth of 6,000 m to be consistent with the AAA21 host profile. The velocity at the bottom of the DH profiles cannot simply be extended to 6,000 m because they are so shallow. In these cases, the GMM TI Team decided that the MASW/MAM profiles should inform the V_S values between 50 m and 1500 m depth. Incorporating all possible combinations of the 20 MASW/MAM base case V_S profiles and the eight DH profiles was considered unnecessary. Instead, the GMM TI Team decided to use six different MASW/MAM profiles (three from FM inversions and three from MM inversions) to extend the DH profiles from 50 m to 1500 m depth, and these MASW/MAM profiles were selected to represent the range of site amplification associated with the full set of MASW/MAM profiles. The six selected extension profiles are:

- DA_FM_LR1.5
- DA_FM_LR2.0
- SA2_FM_LR7.0
- DA_MM_LR2.0
- SA2_MM_LR5.0
- SA2_MM_LR7.0

Figure 9-73 provides a comparison of the six V_S profiles used as extensions and the other MASW/MAM V_S profiles. The extension V_S profiles span the range of observed V_S. An example of the extension for one of the DH profiles (BH47) and one of the six selected extensions (DA_FM_LR2.0) is shown in Figure 9-74.

Each of the extensions was assigned an equal weight of 0.333 (Figure 9-63) but to maintain alignment with the previous assignment of weights based on MASW/MAM mode interpretation, the GMM TI Team assigned a weight of 0.7 to the MM V_S extensions and 0.3 to the FM V_S extensions (Figure 9-63). With those weights, each of the three alternative extensions for each mode interpretation received equal weights (i.e. 0.7 x 0.333 for MM extensions or 0.3 x 0.333 for FM extensions).

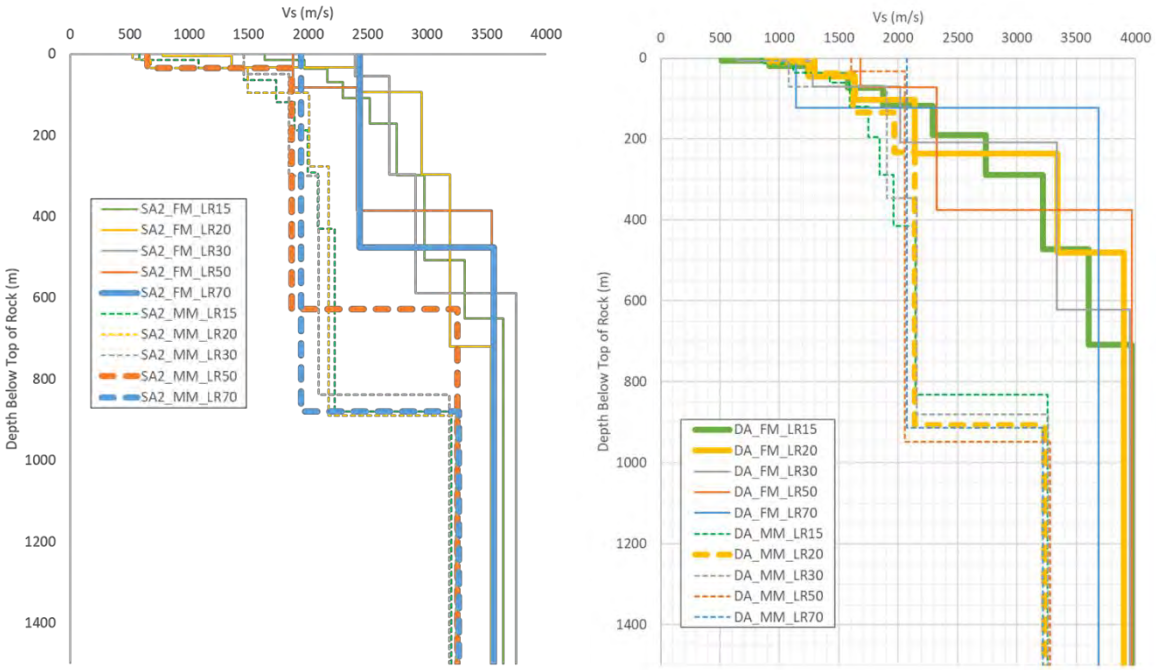

Figure 9-73. Six selected MASW/MAM profiles used to extend DH profiles are shown in bold lines and are shown with other MASW/MAM V_S profiles for the (a) SA2 site and (b) DA site.

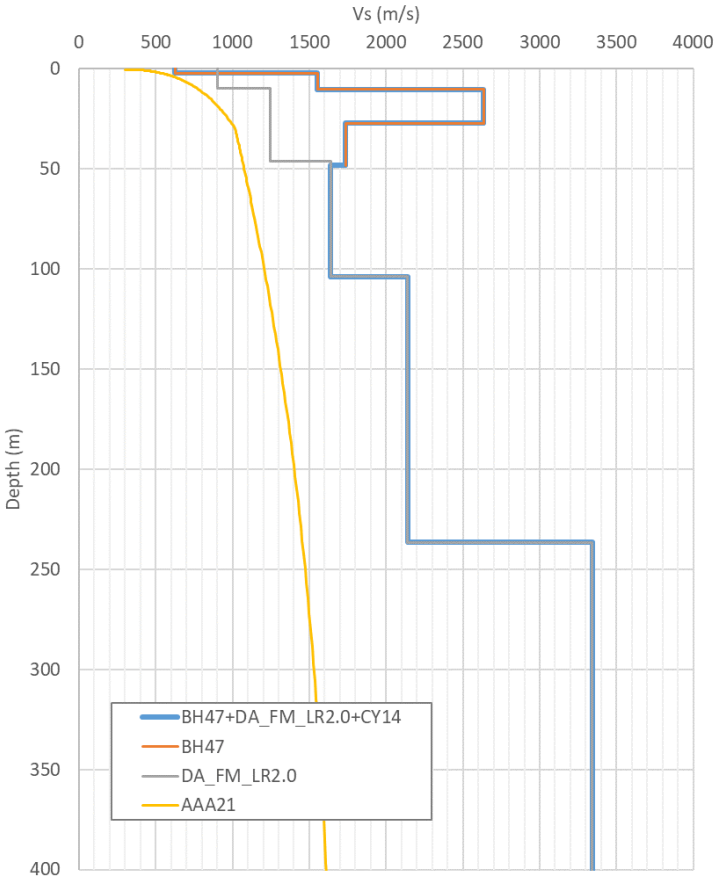

Figure 9-74. Example extension for a given DH profile (BH47) and a given MASW/MAM extension (DA_FM_LR2.0).

To capture aleatory variability for each DH base case profile, the GMM TI Team decided to randomize the V_S values within the 50 m depth below top of rock for each of the 48 base case profiles (i.e. eight DH boreholes x six MASW/MAM extension profiles). The GMM TI Team generated randomised V_S profiles using a Toro-stye approach (Toro, 1995), as illustrated in Figure 9-75. We first assume an interlayer correlation (ρ_{IL}) of 0.8 (Rathje et al. 2010) and assume that the standard deviation of the V_S values (σ_{lnVs}) for the DH profiles is equal to the σ_{lnVs} in the 0-50 m range of the corresponding MASW/MAM extension profile (Figure 9-75). Then using the Z score (Z_i, Figure 9-75) at 50 m depth, the V_S of each layer in the overlying DH profile is computed using the assumed ρ_{IL}, σ_{lnVs}, and random variable (ε_i). The resulting V_S profiles in the top 50 m for DH profile BH46 are illustrated in Figure 9-75. No additional randomisation was performed, because variation in layer thickness is already represented in the eight DH boreholes and the 60 top profiles.

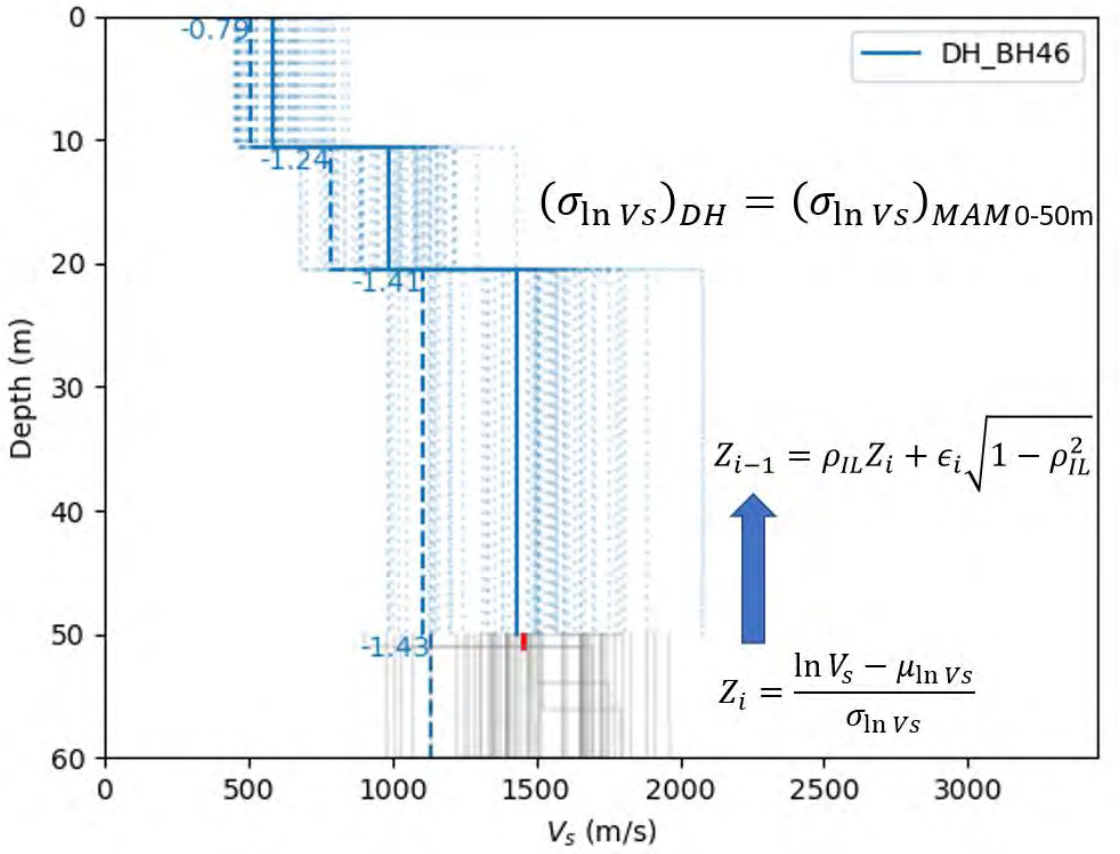

Figure 9-75. Illustration of the randomisation process for DH V_S profiles. Thin dashed blue lines represent randomised DH profiles and thick dashed blue line represents a single randomisation (blue numbers represent individual Z_i values). Gray lines represent the top 60 V_S profiles from Cox et al. (2024) inversions for one of the 6 selected MASW/MAM extensions.

9.4.3 Evaluation of κ_0

The high-frequency decay parameter at the site (κ_0) controls the roll-off of the FAS at high frequencies. It was defined by Anderson and Hough (1984) using the equation $e^{-\pi\kappa f}$, where κ is a combination of κ_0 and a regional, anelastic attenuation component [κ(distance)]. An important part of the site response is defining κ_0 at the site, as it has been interpreted to represent the small-strain damping at the site and it controls the high-frequencies components

of motion, which are generally significant for response of sensitive components at nuclear power plants. Higher κ_0 values correspond to higher small-strain damping, which in turn corresponds with lower values of FAS at high frequencies.

9.4.3.1 Available datasets

Five sources of data were available for evaluating κ_0: the Inversion GMDB, the κ GMDB, the Colenso GMDB, the Temporary Array GMDB, and the Duynefontyn station GMDB. Additional information about these databases can be found in Section 7.3.

The Inversion GMDB was developed for use in the ground-motion inversions and captured a subset of earthquakes with magnitude greater than 2.5 located across South Africa. The κ GMDB was developed to assist in κ evaluations and captured small-magnitude earthquakes close to the site. Both of these databases include recordings from stations in the SANSN (see Sections 7.3.2 and 7.3.3). The GMM TI Team decided to give κ values from these databases a weight of zero as there was data available from ground motion stations at much closer distances and that have more similar site conditions to Duynefontyn.

The Colenso GMDB includes recordings from stations that are closer than the Inversion GMDB and κ GMDB, but on different geologic units from the Duynefontyn site (see Section 7.3.4). The GMM TI Team decided to give κ values from this database a weight of zero as the recordings are from stations on different geologic units than the Duynefontyn site and there was data available on the same geologic unit.

Thus, two datasets were available to the GMM TI Team that included nearby recordings on the same geologic unit as the site: the Temporary Array GMDB from Quiros and Sloane (2023), and the Duynefontyn GMDB (see Sections 7.3.5 and 7.3.6).

The Temporary Array was deployed from 24 July 2021 to 27 October 2021 and included 19 seismic stations from the University of Cape Town instrument pool. These stations recorded one earthquake during their deployment on 4 August 2021. The earthquake was located at latitude -33.675, longitude 18.308 and a depth of 7 km. No magnitude was estimated by Quiros and Sloane (2023) for the event beyond identifying it as small. Given the seismicity in the region, the magnitude of the recorded earthquake was likely below 2. The 19 stations were deployed predominantly on the greywacke geologic unit or greywacke overlain by alluvium. The stations that are not on greywacke were given a weight of zero by the GMM TI Team as there was sufficient data available on the greywacke for the κ_0 evaluation. The GMM TI Team decided to give the Temporary Array GMDB a weight of 0.3 as the station sites were on the same geologic unit as the site, but not directly located at the Duynefontyn site.

The Duynefontyn stations were installed by the CGS between February and April of 2023. The data from these stations were provided to the GMM TI Team on June 26, 2023, thus the GMM TI Team did not evaluate data from earthquakes that occurred after this date. During this time period the station recorded 12 earthquakes. The Duynefontyn stations are located within the perimeter of the Duynefontyn site, thus the GMM TI Team decided to give the Duynefontyn GMDB a weight of 0.7 based on the preference for data at the Duynefontyn site.

The Duynefontyn station consists of two down-hole arrays installed at boreholes SA1 and DA1. Both arrays have seismometers installed at the surface, a depth of 30 m and a depth of

90 m. All seismometers are recording three components with the HH components preferred over the HN components as the HH components are weak motion sensors that are better calibrated to recording small magnitude events. The signal-to-noise ratios for the recordings that are from events greater than 80 km from the site are too low for usable information on κ_0 to be interpreted from the recordings. This leaves a single earthquake on 5 May 2023 with of M 1.7 and 68 km from the station. This recording was determined by the GMM TI Team to be of sufficient quality for a κ_0 evaluation to be performed based on the signal-to-noise ratio.

For the 5 May 2023 event, data from eight of the horizontal components were provided to the GMM TI Team by the CGS. The time histories and Fourier spectra for these recordings are shown in Figure 9-76 through Figure 9-83.

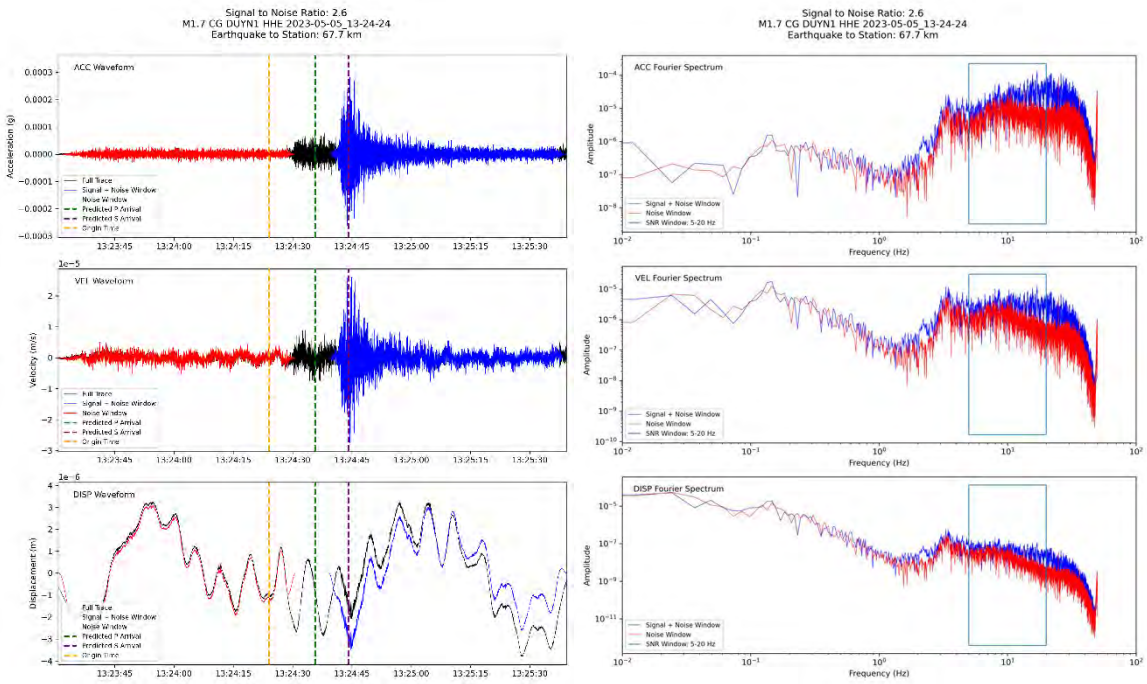

Figure 9-76. Time histories and Fourier spectra of the East-West component of Duynefontyn station located at DA1 at the surface for the M 1.7 earthquake on 5 May 2023.

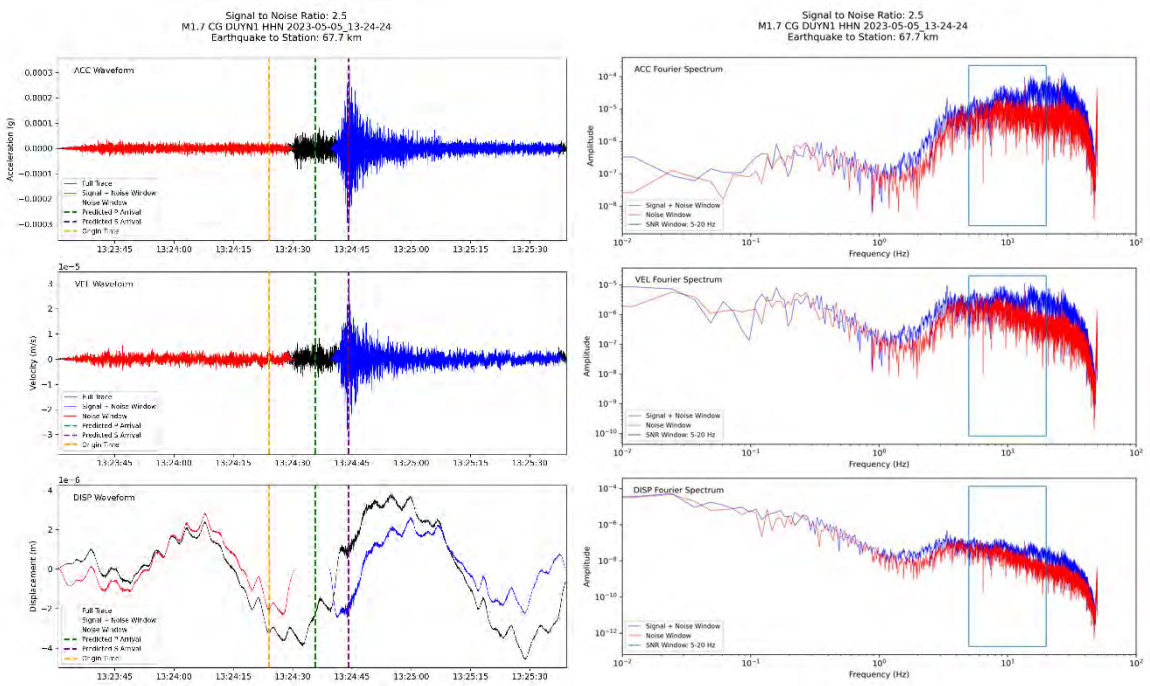

Figure 9-77. Time histories and Fourier spectra of the North-South component of Duynefontyn station located at DA1 at the surface for the M 1.7 earthquake on 5 May 2023.

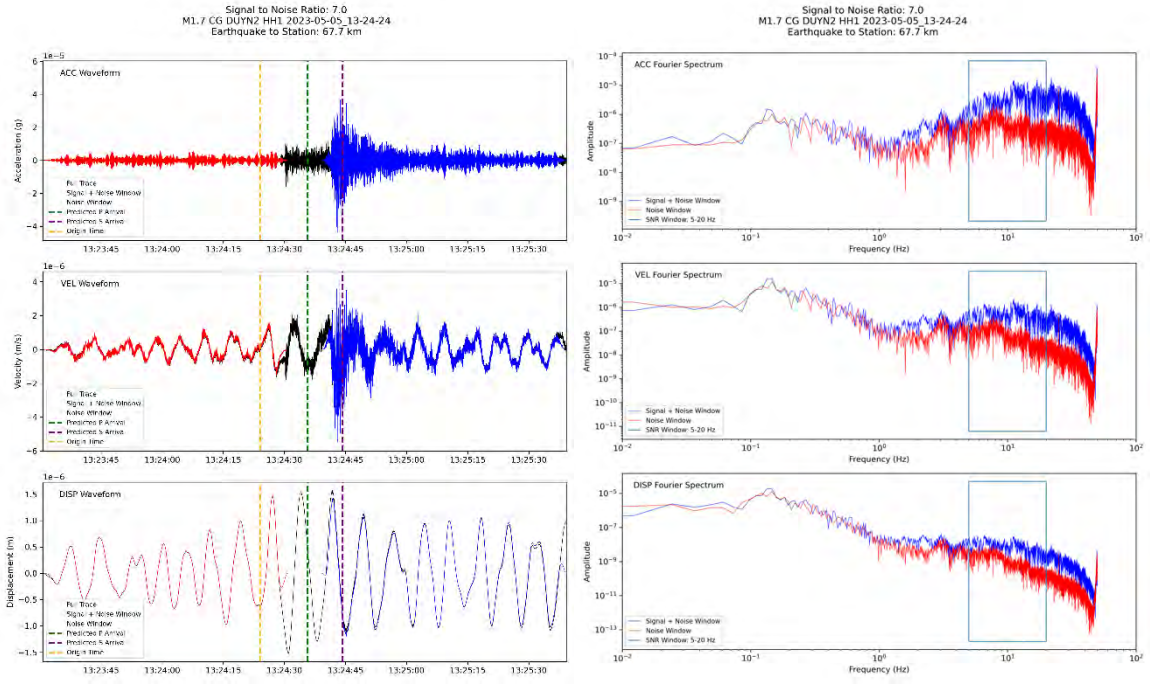

Figure 9-78. Time histories and Fourier spectra of the first component of Duynefontyn station located at DA1 at a depth of 30 m for the M 1.7 earthquake on 5 May 2023.

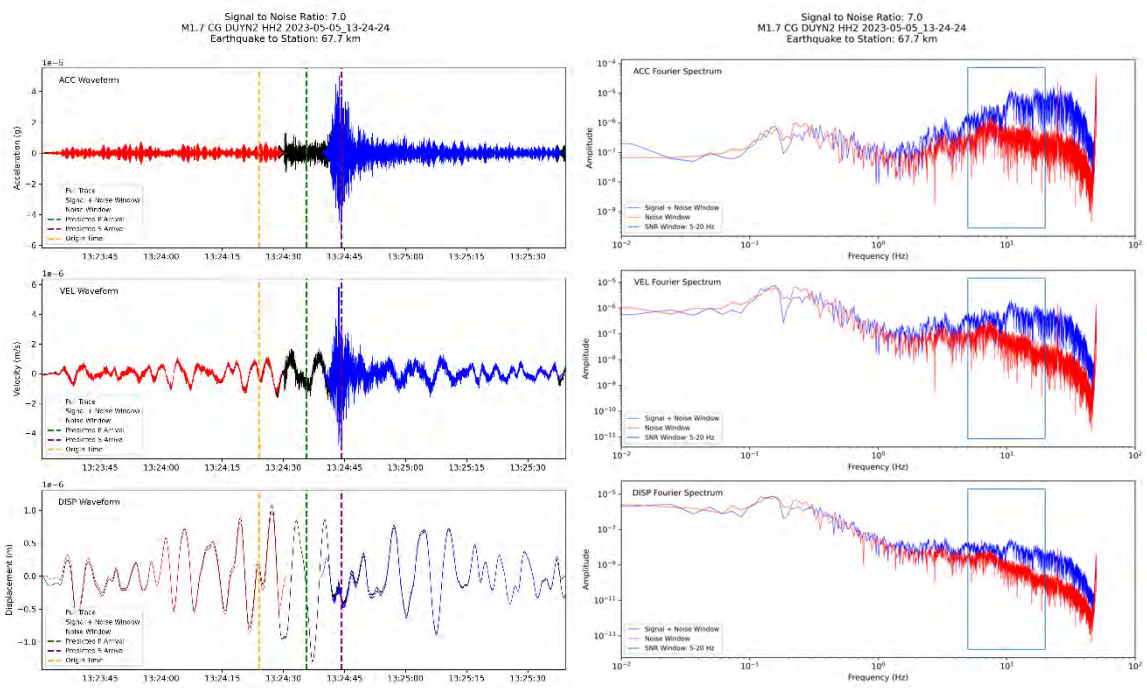

Figure 9-79. Time histories and Fourier spectra of the second component of Duynefontyn station located at DA1 at a depth of 30 m for the M 1.7 earthquake on 5 May 2023.

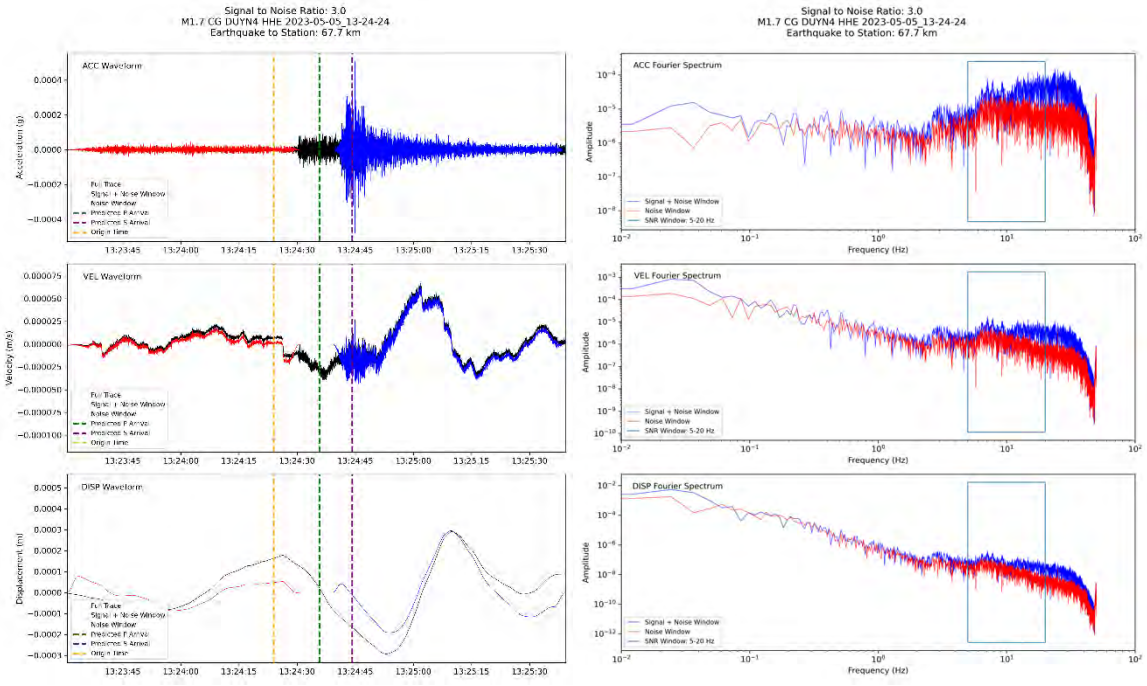

Figure 9-80. Time histories and Fourier spectra of the East-West component of Duynefontyn station located at SA1 at the surface for the M 1.7 earthquake on 5 May 2023.

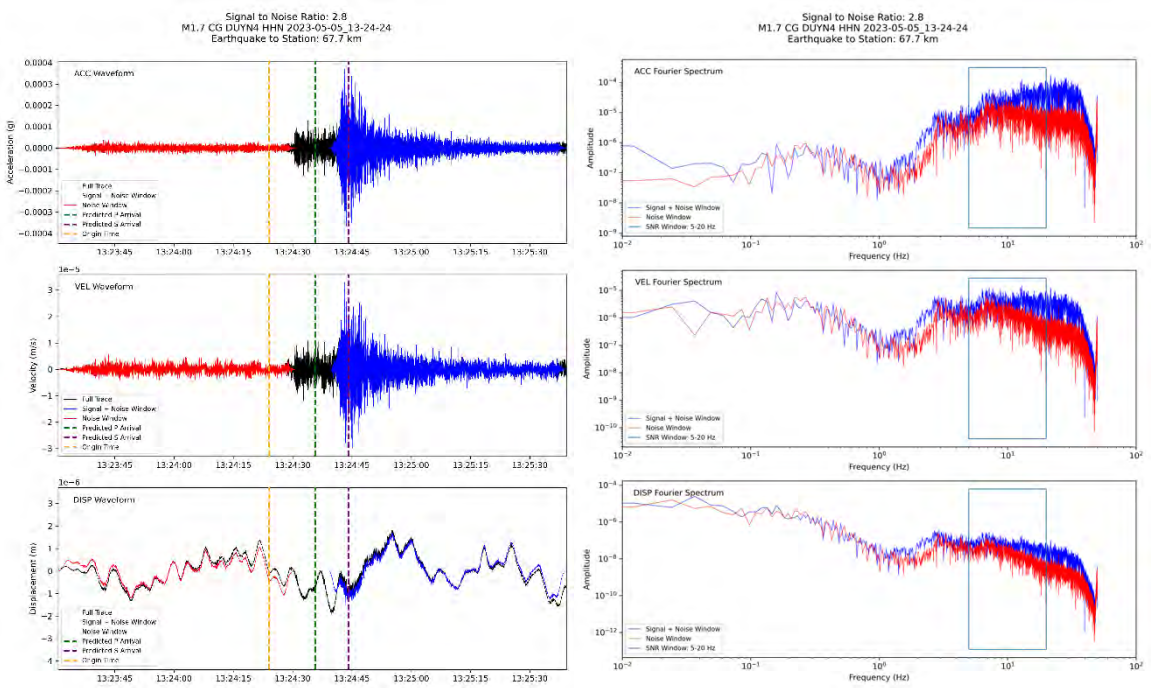

Figure 9-81. Time histories and Fourier spectra of the North-South component of Duynefontyn station located at SA1 at the surface for the M 1.7 earthquake on 5 May 2023.

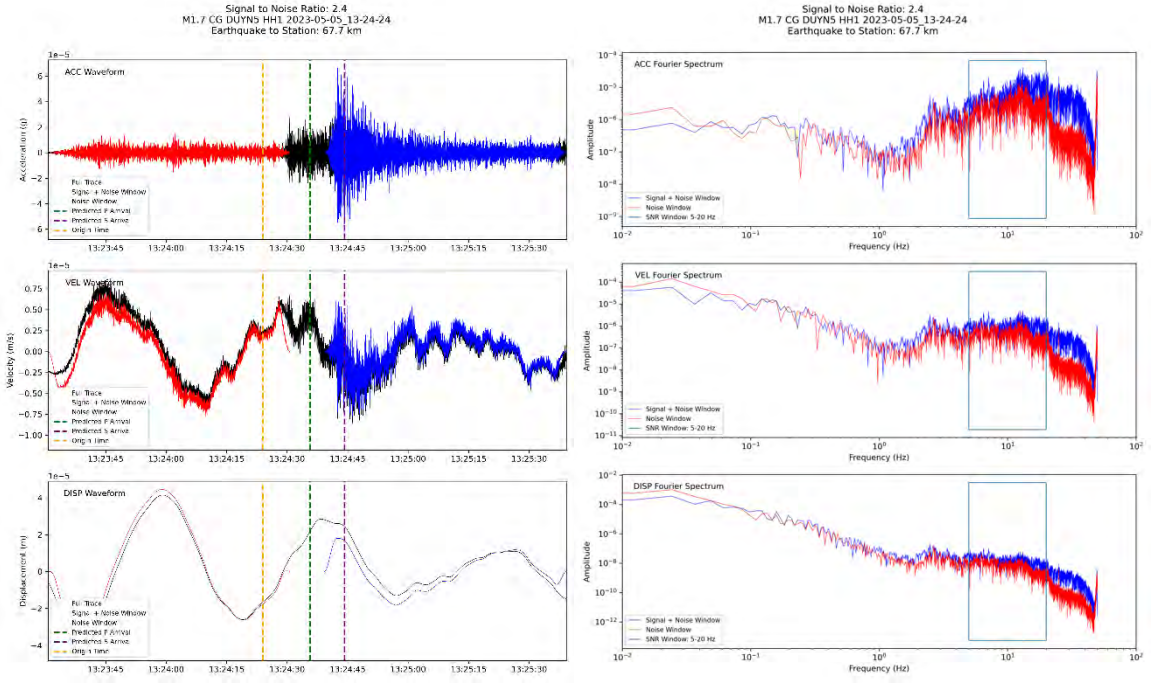

Figure 9-82. Time histories and Fourier spectra of the first component of Duynefontyn station located at SA1 at a depth of 30 m for the M 1.7 earthquake on 5 May 2023.

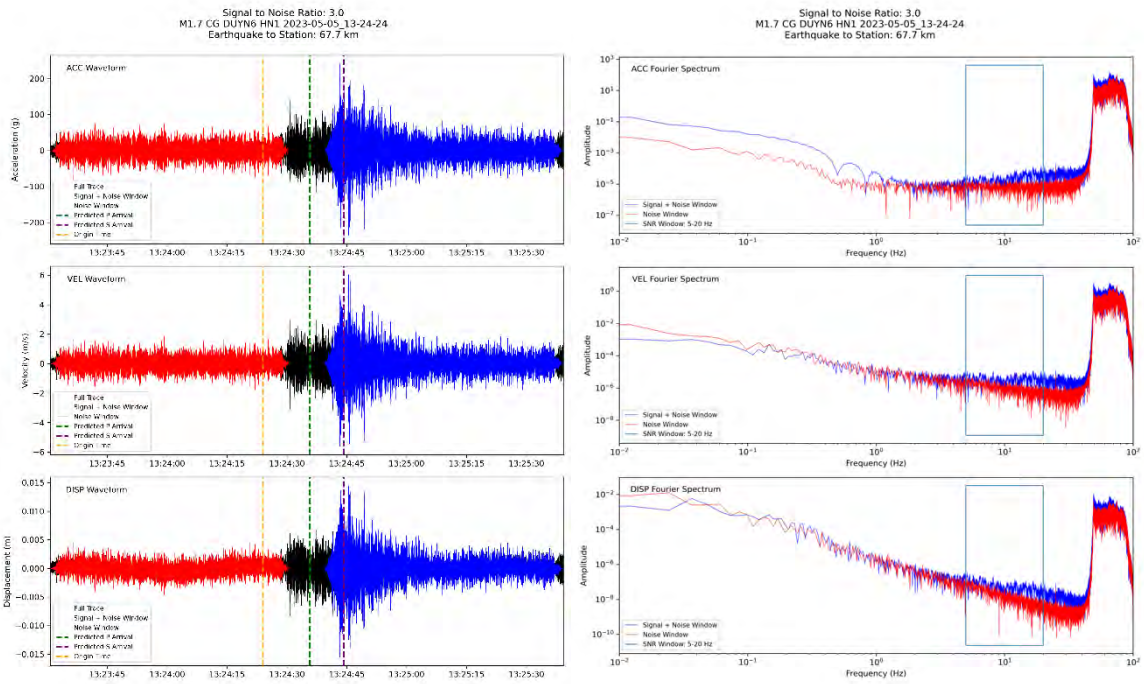

Figure 9-83. Time histories and Fourier spectra of the first component (HN) of Duynefontyn station located at DA1 at a depth of 90 m for the M 1.7 earthquake on 5 May 2023.

9.4.3.2 κ calculation methodology

Three resource experts presented alternative κ calculation methodologies at Workshop 2. Norm Abrahamson presented his proposed methodology based on Tamp1.5 (Abrahamson, 2022). This methodology requires stable estimates of PGA to implement. Of the two sources of data that the GMM TI Team elected to use for estimating κ_0, the Temporary Array GMDB did not include PGA estimates for this use and the Duynefontyn GMDB included PGAs for only one very small magnitude earthquake. The GMM TI Team assigned this methodology a weight of zero as the majority of the data did not include PGA estimates and thus this methodology could not be used.

Ben Edwards presented a potential methodology based on noise estimates and Olga Ktenidou presented methodologies based on Fourier amplitude spectra from the acceleration and displacement time series. These methodologies are discussed in the following subsections.

9.4.3.2.1 κ from Noise

The presentation from Ben Edwards included summaries of the work by Butcher et al. (2020) and Dikmen et al. (2016) who investigated the use of noise and coda waves as a means of obtaining κ_0. Their work was based on the assumption that the white noise Fourier spectrum is flat, and thus the high-frequency decay in the spectra can be attributed to κ. Prof. Edwards presented results wherein he used noise spectra at a site to calculate κ and compared it to published predictions and showed a generally good fit.

The white noise spectrum at the Duynefontyn site is unknown, thus the GMM TI Team engaged a specialty contractor to investigate whether this methodology could be applied at the site. Quiros and Sloane (2023) used their Temporary Array Data to compare κ calculated

from the single earthquake recorded (computed using the displacement spectrum) and κ calculated from the Fourier amplitude spectra of a noise window (both velocity and displacement time histories of the noise were considered). The κ values from these methods are presented in Table 9-14. Quiros and Sloane did not remove site effects from their FAS before calculating κ as V_S profiles were not yet available at the sites.

Table 9-14. κ values from earthquake and noise spectra (Quiros and Sloane, 2023).

	Earthquake κ (s)		**Noise Displacement κ (s)**		**Noise Velocity κ (s)**	
Station	East-West	North-South	East-West	North-South	East-West	North-South
ACF	0.0146	0.02	0.0367	0.0208	0.0152	0.0118
ACG	0.0218	0.026			0.0236	0.0243
ACH	0.0284	0.0117				
ACK			0.0529	0.0505		
ACL	0.0101	0.0262				
ACM	0.0185	0.0146	0.023	0.0206		
ACN	0.0234	0.0239	0.0322	0.0317		
ACR	0.029	0.0326	0.0341	0.0324	0.0187	0.0192
ACS			0.0307	0.0194		
ACT						0.0113
ACX	0.0115	0.0212	0.0406	0.0427		
AD0			0.0298	0.0248		
AD1	0.0307	0.0193	0.0402	0.0241	0.0105	0.0116
AD2	0.0243	0.0146	0.0478	0.0396		
AD5	0.0128					
AD7	0.0139	0.0192	0.0536	0.0565	0.0098	0.0143
AD7	0.015	0.0254				

To determine if the κ values from noise can be used to estimate κ from earthquakes, the two are plotted against one another in Figure 9-84. As shown in the figure, the values of κ from noise (either from displacement or velocity) do not match those from the earthquake recordings, thus these methods cannot be demonstrated to be good predictors of κ_0 based on this dataset. The GMM TI Team decided not to use κ calculated from noise spectra to determine κ_0 because the methodology could not be validated.

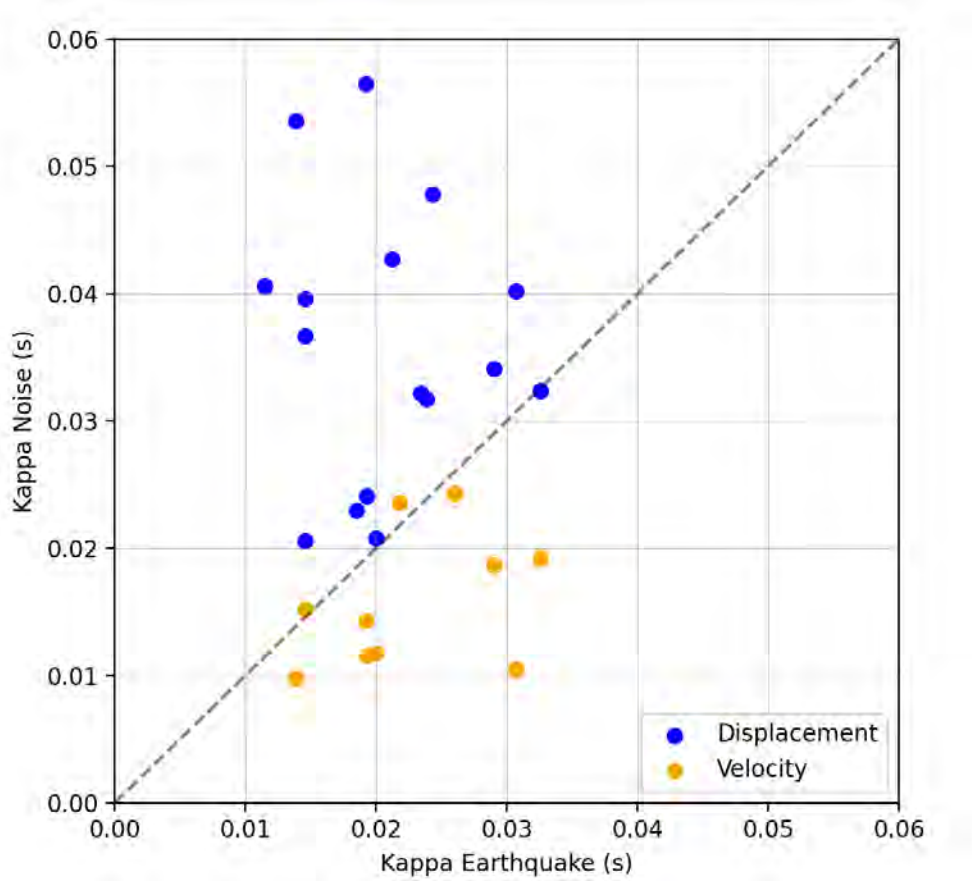

Figure 9-84. κ values calculated from Fourier noise spectra from displacement (blue) and velocity (orange) time histories plotted versus κ values calculated from a single small magnitude earthquake (Quiros and Sloane, 2023).

9.4.3.2.2 κ from acceleration and displacement Fourier amplitude spectra

At Workshop 2, Olga Ktenidou presented the GMM TI Team with a summary of methods for estimating κ_0 and provided a proponent position on which methodologies are appropriate for the current study (Figure 9-85; Ktenidou, 2022). The most robust approaches to measure κ_0 involve the analysis of ground-motion recordings at or near the site of interest. For ground motions from events larger than about **M** 3.0, κ_0 is evaluated from the decay of the acceleration FAS at frequencies above the corner frequency (generally above 15 Hz for events of this size). Values derived from this approach are classified κ_{AS} because they are derived from the acceleration spectrum (AS). For ground-motions from events smaller than about **M** 2.0, κ_0 is evaluated from the decay of the displacement FAS at frequencies below the corner frequency (generally above 30 Hz for these smaller events). Values derived from this approach are classified κ_{DS} because they are derived from the displacement spectrum (DS). For both approaches, the effects of regional attenuation must be considered to derive κ_0 from the κ measurements. The NGA-East project compared κ_0 values from κ_{AS} and κ_{DS} and noticed differences between the two sets (Ktenidou et al. 2021). This was attributed to site-specific amplification in the records that was not accounted for in the κ_0 evaluation. Site response was removed from the FAS, as explained subsequently in this section, and the GMM TI Team considers this step to produce consistent κ estimates on theoretical grounds, though the similarity cannot be demonstrated from direct data analysis. Typically, the κ values are plotted

versus distance from the source and a linear relationship is fit to the data to extrapolate back to the zero-distance κ (κ_0).

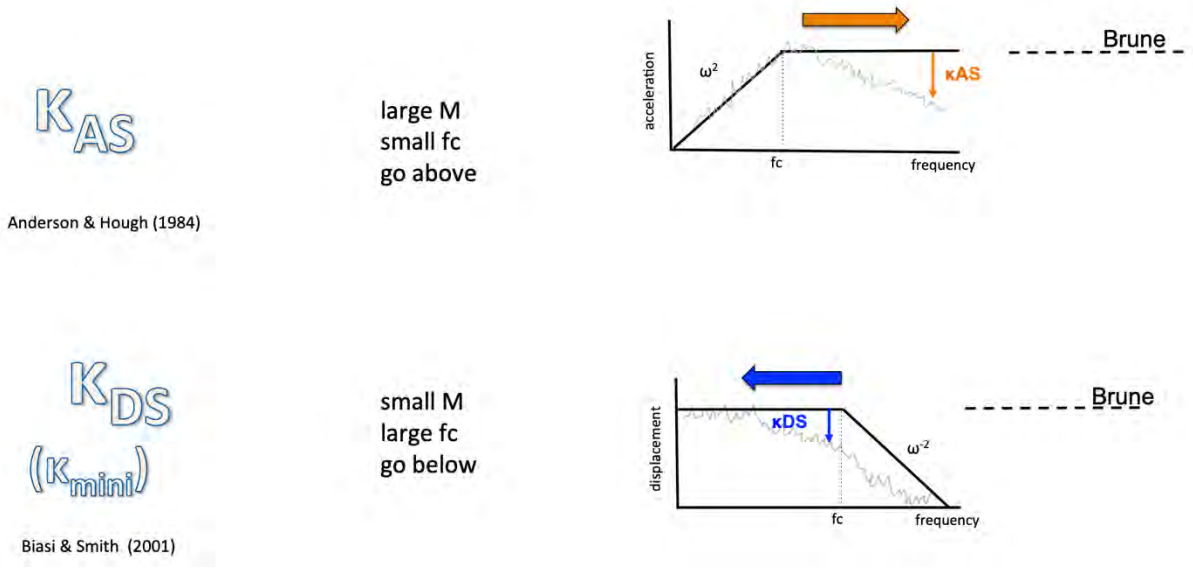

Figure 9-85. Methodologies for calculating κ_0 from the acceleration spectrum (κ_{AS}) and the displacement spectrum (κ_{DS}) From Ktenidou 2022.

The data to be used for evaluating κ on this project are from very small earthquakes. For earthquakes of that size, Ktenidou recommended using κ_{DS}. Ktenidou also recommended that the site response transfer function be removed from the Fourier spectrum before κ values are calculated. The GMM TI Team decided to adopt this methodology as it is most appropriate for small magnitudes.

κ_{DS} values from the Temporary Array data were provided by Quiros and Sloane (2023). It is worth noting that Quiros and Sloane (2023) did not remove site effects prior to calculation of κ_{DS}. κ_{DS} values from the Duynefontyn GMDB were calculated by the GMM TI Team. The first step was the removal of the site response transfer function. To accomplish this, the GMM TI Team chose a single representative site profile and calculated a transfer function consistent with the depth of the recording station. This was then removed from the displacement Fourier spectra.

The GMM TI Team calculated κ for a range of frequencies and evaluated the impact of local peaks, spectral shape, filtering and corner frequency on the κ values. The corner frequency of the **M** 1.5 earthquake recorded by the Duynefontyn stations appears from visual examination to be between 20 and 30 Hz. The impact of the filtering was examined by looking at alternative filtering bands with poles at 25 Hz, 30 Hz and 40 Hz. These alternatives did not have significant impact on κ. The flat part of the displacement Fourier spectrum appears to end around 5 Hz.

The GMM TI Team decided to use two frequency ranges for estimating κ. The first range of 5-20 Hz was selected as the broadest applicable range, noting that this is likely between the flat part of the displacement Fourier spectrum and the corner frequency and/or low-pass filter frequency. A second frequency range of 7-15 Hz was used to account for the uncertainty in the frequencies where the flat part of the spectrum ends (the corner frequency) and the

potential impact of the filtering. The Fourier spectra were also smoothed using a simple moving average. The resulting κ values are given in Table 9-15. The κ values from the station at SA1 at a depth of 90 m were given a weight of zero by the GMM TI Team because the numbers were unstable and from a different recording type (HN).

Table 9-15. κ values from the Duynefontyn stations.

Location	Depth	Comp.	SNR (5-20 Hz)	5-20 Hz κ (s)			7-15 Hz κ (s)		
				Original	TF Removed	Smoothed	Original	TF Removed	Smoothed
DA1	0 m	E-W	2.6	0.0225	0.0234	0.0418	0.0291	0.0345	0.0000
DA1	0 m	N-S	2.5	0.0237	0.0247	0.0420	0.0303	0.0357	0.0000
DA1	30 m	1	7	0.0367	0.0382	0.0319	0.0285	0.0301	0.0000
DA1	30 m	2	7	0.0214	0.0228	0.0368	0.0081	0.0097	0.0000
SA1	0 m	E-W	3	0.0261	0.0271	0.0412	0.0277	0.0331	0.0000
SA1	0 m	N-S	2.8	0.0231	0.0241	0.0232	0.0192	0.0247	0.0000
SA1	30 m	1	2.4	0.0281	0.0295	0.0093	0.0098	0.0114	0.0000
SA1	90 m	1 (HN)	3	0.0024	0.0038	0.0261	-0.0389	-0.0372	0.0000

The anelastic attenuation in South Africa is very low and is not expected to have a significant impact on κ_0. This is demonstrated by the consistency in κ estimates between the Temporary Array GMDB and the Duynefontyn GMDB. The single datapoint from the Duynefontyn GMDB also does not allow for the removal of path effects on κ_0. The GMM TI Team decided to treat the κ values as κ_0 for these reasons.

9.4.3.3 κ logic-tree

The GMM TI Team created a logic-tree for the κ_0 values from the Temporary Array GMDB and the Duynefontyn GMDB to display the mean and epistemic uncertainty on κ_0. The GMM TI Team has a strong preference for the Duynefontyn station data over the Temporary Array data because it reflects measurements at the project site with multiple depths and two locations, robust site-specific site corrections, plus multiple frequency bands and smoothing approaches. Within the Duynefontyn GMDB the GMM TI Team has a strong preference for the κ_0 values from smoothed Fourier spectra and is impartial to the choice of frequency band. The GMM TI Team constructed the logic-tree in Figure 9-86 based on these considerations.

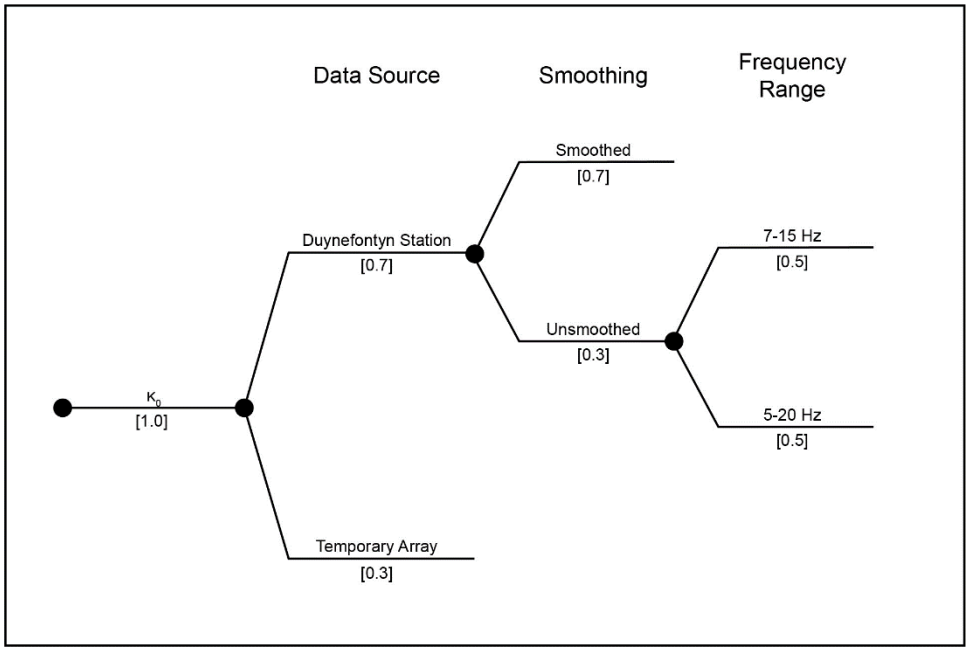

Figure 9-86. κ_0 logic-tree.

From the κ_0 logic-tree a mean and sigma can be derived by examining the cumulative density function in Figure 9-87. From the figure, the mean κ_0 value is 0.023 s and the standard deviation is 0.006 s. This distribution is incorporated into the site response logic-tree by using the mean and sigma to develop three branches as shown in Figure 9-61.

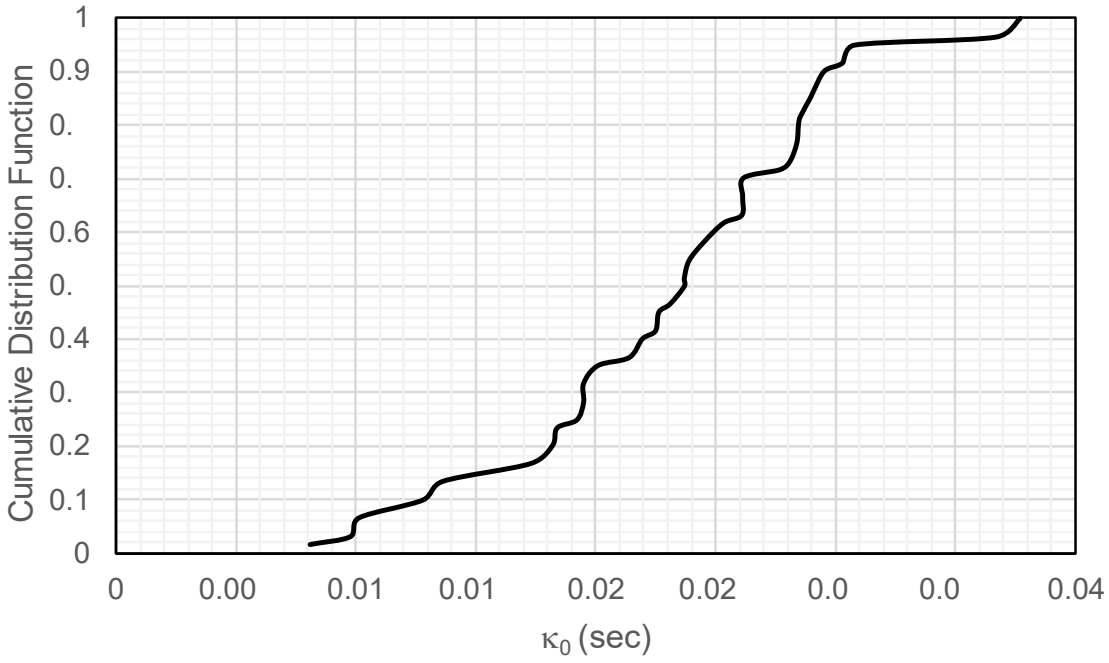

Figure 9-87. κ_0 CDF from logic-tree.

9.4.4 Nonlinear soil properties

Modulus reduction and damping (MRD) curves are used in EQL site response analyses to approximate nonlinear material properties. A modulus reduction curve describes the variations of the normalised shear modulus (G/G_{max}, where G_{max} is the small-strain shear modulus and G is the secant shear modulus) as a function of shear strain. A damping curve describes the material damping (D) as a function of shear strain. Damping is partitioned into two components representing small-strain damping (D_{min}) and nonlinear hysteretic damping (D_{hys}). D_{min} is assigned based on the site κ_0 and D_{hys} is derived from nonlinear MRD models. The input motions used in the site response analyses were defined with κ_0 equal to zero, thus κ_0 is assumed to be fully associated with D_{min} as (Hough and Anderson 1988):

9-65

$$\kappa_0 = \int \frac{2D_{min}}{V_s} dz$$

where *z* is the depth below the top of the subsurface model (i.e. the top of rock after removing the surficial sand layer).

Nonlinear properties of rock materials are difficult to measure directly in the laboratory due to fractures from the coring process and the large shear stresses required to induced nonlinearity. Additionally, to the GMM TI Team's knowledge, no lab in South Africa has the appropriate resonant column, torsional shear, or cyclic triaxial equipment to measure these properties. Thus, the GMM TI Team relied on a range of existing MRD curves for rock instead of site-specific curves.

The materials at the site can be characterised as soft to very hard rock. Due to the stiffness of the site, strains induced in the subsurface will be limited and the impact of nonlinear soil properties should be minimal. A search for published MRD curves for rock materials in the literature yielded only a few results, as plotted in Figure 9-88. These included EPRI rock curves (EPRI 1993), curves for weathered and unweathered shale from Oakridge, Tennessee (Stokoe et al., 2003), curves for different tuff units from Yucca Mountain, Nevada (Jeon, 2008; Choi, 2008), and curves for Bandelier tuff from Los Alamos National Laboratory, New Mexico (Choi, 2008). It is not clear where the EPRI rock curves originated, thus their applicability to the site and their potential limitations are difficult to assess. The weathered shale curves are more nonlinear than soil (i.e. G/G_{max} less than 0.5 for strains larger than about 0.01%), and thus were not considered realistic for our predominantly rock site. The MRD curves for the unweathered shale from Stokoe's work were similar to the MRD curves for volcanic tuff rocks. Although none of the curves in Figure 9-88 represent the rock types at Duynefontyn (i.e. predominantly sandstone), the unweathered shale curve in Figure 9-88 was used as a reference for comparison for the curves used for the site response analyses.

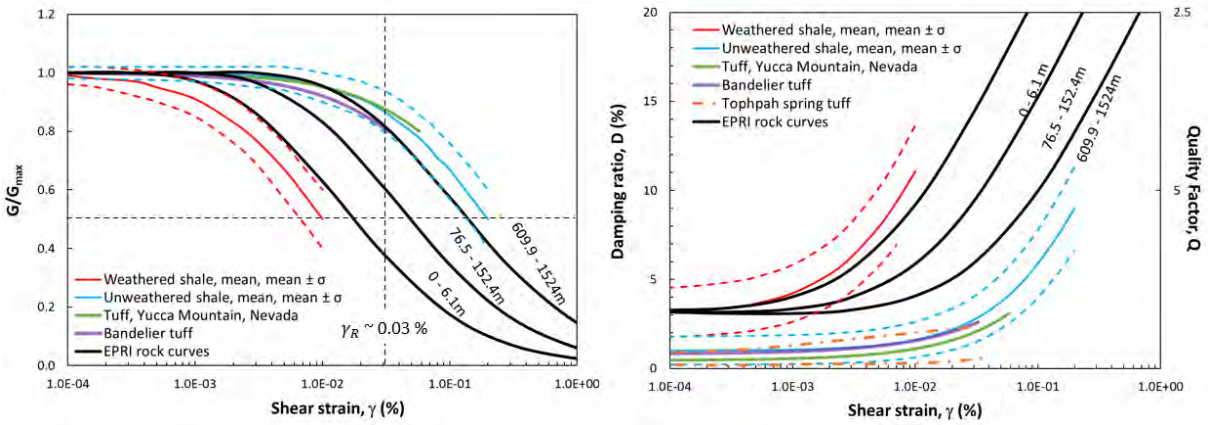

Figure 9-88. Summary of available rock MRD curves from the literature.

Set 1 of the MRD curves represent curves derived for the Taiwan SSHAC project (NCREE, 2021) for rock materials. The curves are shown in Figure 9-89, with the damping curves in this figure only representing the hysteretic component (i.e. the small-strain D_{min} was subtracted from the D value at each strain level). These curves are V_S-dependent for V_S > 1,000 m/s and were derived by Ken Stokoe using his judgment and experience in testing linear and nonlinear properties of soil and rock materials. These curves show more linear behaviour (i.e. larger G/G_{max}) with less damping as the V_S of the material increases, and the curves are not defined past 0.2%. For materials with V_S < 1,000 m/s, the GMM TI Team decided to incorporate Stokoe's unweathered shale curves.

The Set 1 G/G_{max} curves are at the upper bound of the available rock curves (Figure 9-89) and the Set 1 D curves are at the lower bound of the available curves. Because the Set 1 MRD curves represent a more linear response relative to the available data, a second set of MRD curves were developed. Set 2 of the MRD curves are also V_S-dependent but represent an alternative to the stiffer Set 1 curves (Figure 9-90). The Set 2 curves are centred on the unweathered shale curves for V_S = 1500-2000 m/s, and the curves for other V_S values were developed by shifting the reference strain (i.e. the strain level at which G/G_{max} = 0.5) down for smaller V_S and up for larger V_S. These curves maintain the trend of more linear behaviour and less damping with increasing V_S, but overall the Set 2 curves are more nonlinear than Set 1. The Set 2 curves are plotted over a wider range of strains than Set 1 because they are derived from an extension of the hyperbolic model. The Set 2 curves are still more linear than those for soil (reference strain for soil ~ 0.03%), and thus represent an intermediate level of nonlinearity that is consistent with the fact that the site consists of rock materials.

For both sets of MRD curves, the values at strains greater than about 0.2% are uncertain because limited data exist at those strain levels for stiff rock materials. We expect that the induced strains will mostly stay below 0.2% due to the large V_S at the site. The induced strains for our analyses are discussed in Section 9.4.4.

The logic-tree for MRD curves includes two branches that represent two different sets of MRD curves (Set 1 and Set 2) that are assigned based on the V_S of the material. The GMM TI Team evaluated that Set 1 or Set 2 are equally likely because they both fall within the range of available data (Figure 9-88), and thus decided to assign equal weights of 0.5 to both branches in the logic-tree (Figure 9-61).

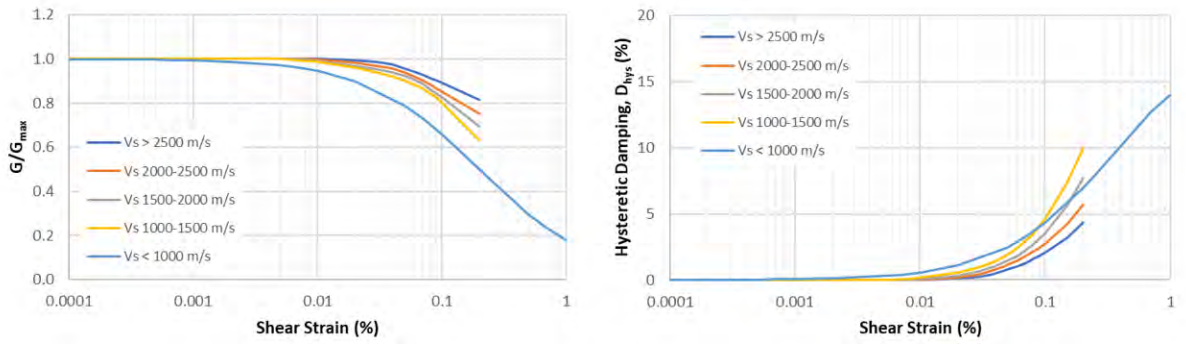

Figure 9-89. Nonlinear V_S-dependent MRD curves (Set 1) derived from work by K. Stokoe using judgment for rock materials for the Taiwan SSHAC project (NCREE 2021).

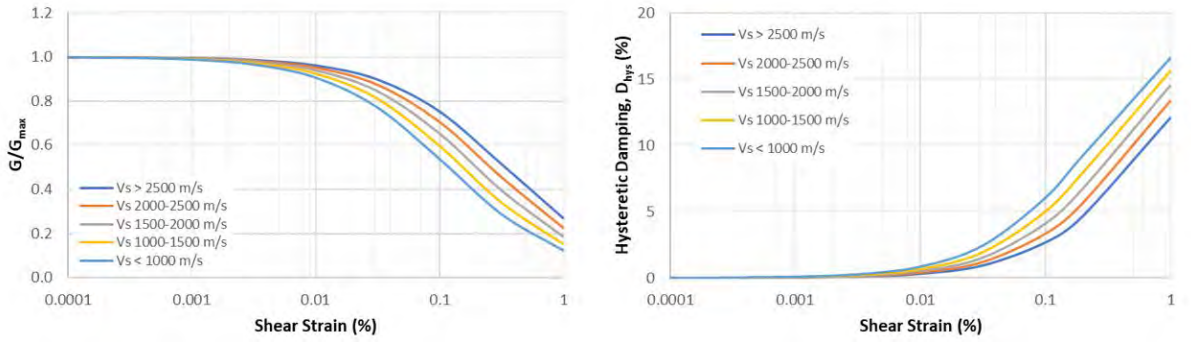

Figure 9-90. Nonlinear V_S-dependent MRD curves (Set 2).

9.4.5 Model error

Two approaches are available to incorporate model error in the SAFs and they were presented at Workshop 2 (Rathje, 2022). Alternative 1 is to add model error as an additional uncertainty component such that it is combined with the epistemic uncertainty associated with the material characterisation (i.e. parametric uncertainty in the V_S profile and MRD curves). This alternative assumes that the model error is uncorrelated from all other sources of epistemic uncertainty, and thus the variances are summed to represent the total epistemic uncertainty in the SAF. Alternative 2 is to use model error as the minimum epistemic uncertainty in the SAF. This assumes that the model error cannot be separated from the parametric uncertainties in site response and is only considered when the parametric uncertainty is too small. Alternative 2 has been applied in several recent projects (Thyspunt NSP, Hanford PSHA, Spain SL3, Idaho National Laboratory).

In past SSHAC projects, the model error for 1D site response analysis has been adopted either as a constant period-independent value (e.g., 0.20) or as a period-dependent value assigned by past studies (e.g., Stewart and Afshari, 2021), such as those shown in Figure 9-91. These different period-dependent estimates for model error are based on different datasets of ground-motion recordings and different assumptions about the uncertainty in the V_S profiles at the recording stations.

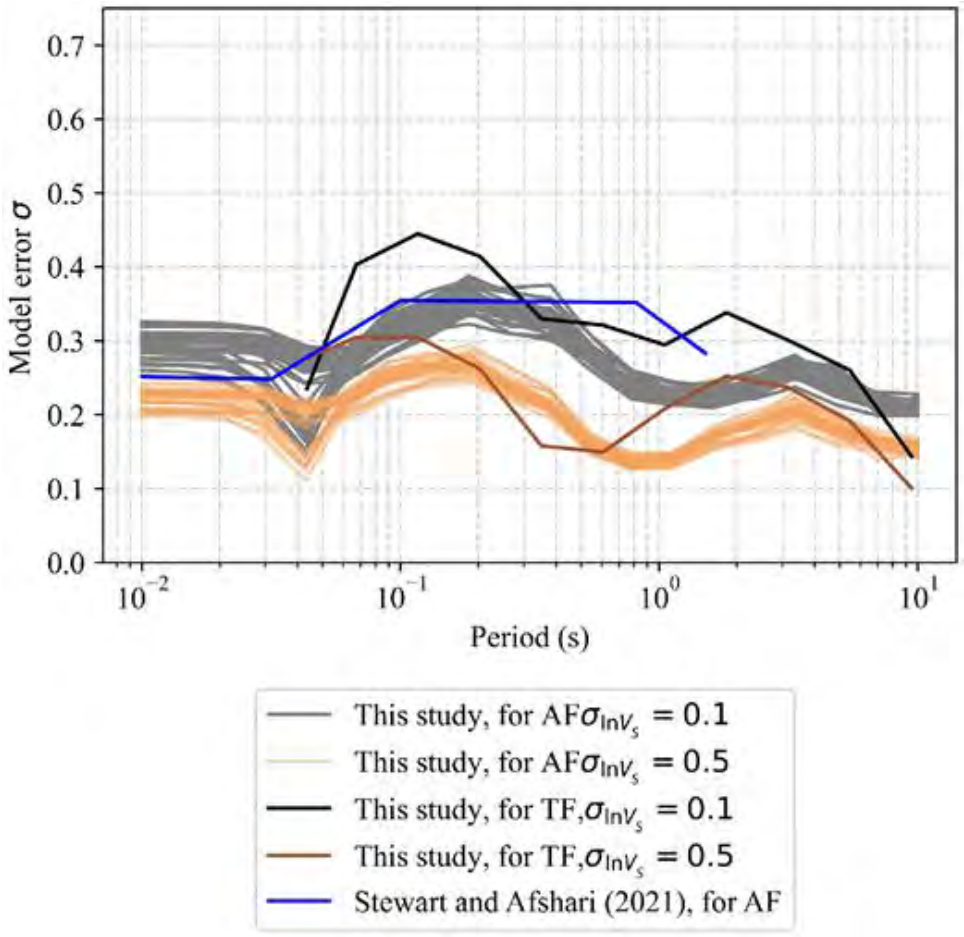

Figure 9-91. Different estimates for model error for one-dimensional site response (Bahrampouri and Rodriguez-Marek, 2023). TF in legend is transfer function.

The plateau in the model error in Figure 9-91 from work by Stewart and Afshari (2021) extends to a period of 0.8s, which represents the average site period for the sites analysed to develop their recommendations. Stewart and Afshari (2021) indicate that in practice, this period can be replaced with the first mode period of the site being analysed, provided that the site period is in the range of those considered by Stewart and Afshari (2021); this range of site periods is 0.2 to 1.4 s. The average site period of the Duynefontyn site is less than 0.1 s, which is outside of this range. Thus, the GMM TI Team decided for the current project to adopt a period-independent model error of 0.25, which is intermediate among those shown in Figure 9-91.

The TI team assigned equal weights of 0.5 to Alternative 1 and Alternative 2 for incorporating the model error, because both alternatives are considered equally valid and represent reasonable methods to incorporate model error. Figure 9-92 demonstrates the model error of 0.25 using both alternatives for representative results at the project site. Alternative 1 increases the spread in the SAF values at all frequencies, whereas Alternative 2 increases the spread of SAF values only at frequencies where the epistemic uncertainty in SAF due to the logic-tree alone is less than the model error (in this case, 0.25). For the representative data shown in Figure 9-92, this typically occurs for oscillator frequencies less than about 4 Hz.

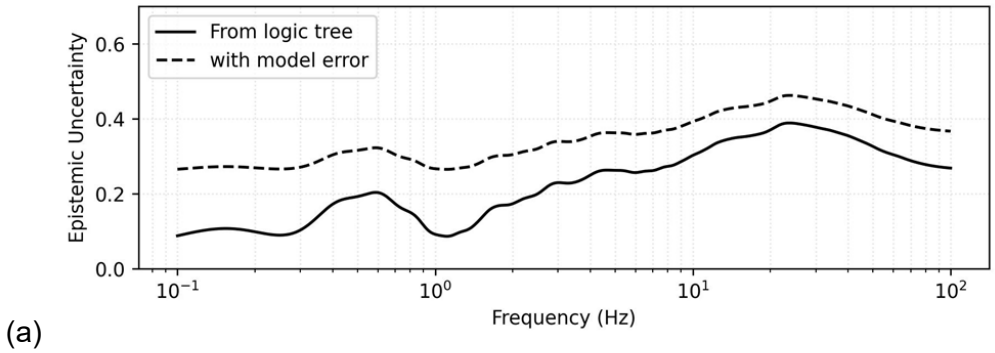

(a)

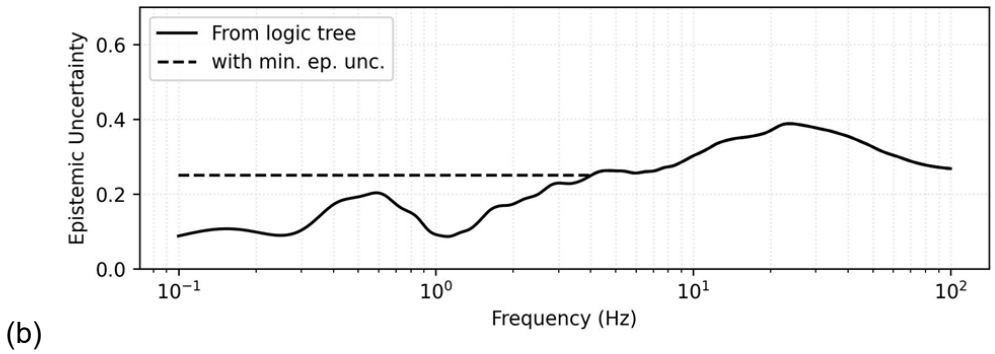

(b)

Figure 9-92. Epistemic uncertainty in SAF values resulting from (a) Alternative 1 and (b) Alternative 2 to incorporate model error. For M 6.5, intensity level scaled to PGA = 0.4g.

9.4.6 2D Site Response

In a 1D equivalent linear site response analysis, one of the underlying assumptions is that the shear waves are vertically propagating through horizontally layered strata with horizonal impedance boundaries. When those assumptions are not true due to more complex conditions (e.g., steeply dipping impedance boundaries), then multi-dimensional analyses may be required (e.g., USNRC 2007, Regulatory Guide 1.208).

Photos of the excavation at the Koeberg NPP at the Duynefontyn site (Figure 9-93) show the presence of steeply dipping rock layers across the site. The likelihood of such features also being present at the proposed new build at the Duynefontyn site was supported by evidence provided by the SSM TI team. For example, patterns of dipping beds visible in bathymetry data off the coast of the Koeberg NPP, photos of outcrops in the region where high V_S layers have been identified (Figure 9-94), and the SSM TI Team's understanding of the geologic setting. The SSM TI Team also indicated that these features could include turbidites with highly variable V_S cycling between relatively higher and lower values. In response to these observations, the GMM TI Team discussed the possibility of 2D site effects being noticeably different than the 1D site response analysis that is used to compute the SAF.

Figure 9-93. Photo of excavation to top of rock at the Koeberg NPP (Eskom, 1977)

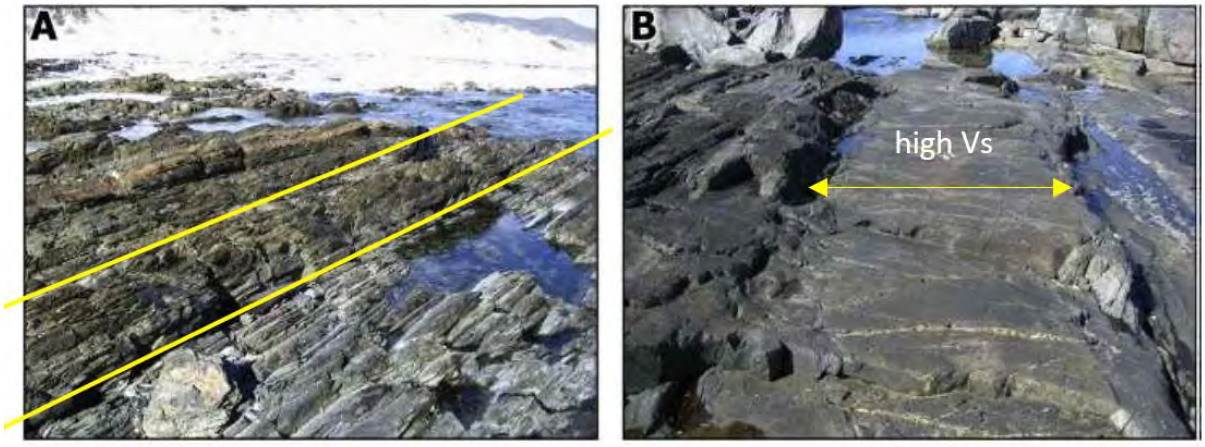

Figure 9-94. Annotated photos of rock outcrops in the region a few kilometres south of the Duynefontyn site (modified from McHutchon et al. 2020)

To investigate the potential effects of steeply dipping planes and variable V_S values within the turbidite formations, the GMM TI Team requested that the CGS engage specialty contractors Prof. Brendon Bradley and Dr Chris De La Torre (University of Canterbury, New Zealand) to perform 2D site response analyses (De la Torre and Bradley, 2023). The GMM TI Team worked with the SSM TI Team to produce a conceptual 2D cross-section (Figure 9-95) for the site based on preliminary data and several bounding scenarios to test the sensitivity of the surface motions to the 2D effects. De La Torre and Bradley used the conceptual 2D cross-section to perform 2D site response analyses varying the lower (V_S1) and higher (V_S2) V_S values, the width and depth of the model, and the input rock motion acceleration time series (Section 9.4.7). The results of their analyses are shown in Figure 9-96 in terms of the ratio of the 2D to 1D spectral accelerations (SA) at different spectral periods (T). These results showed that if the V_S1 and V_S2 values within the turbidites were significantly different (e.g., 500 vs 1,500 m/s or 500 vs 2,500 m/s), then the 2D SA values were markedly different

compared to the 1D SA. If the V_S1 and V_S2 values were more similar (e.g., 1,000 vs 2,000 m/s or 1,500 vs 2,500 m/s), the 2D SA were nearly the same as the 1D SA. In addition, when the average V_S of the V_S1 and V_S2 values was larger with the same absolute difference (e.g., 1,500 vs 2,500 m/s compared with 1,000 vs 2,000 m/s), then the 2D SA were even more similar to the 1D SA.

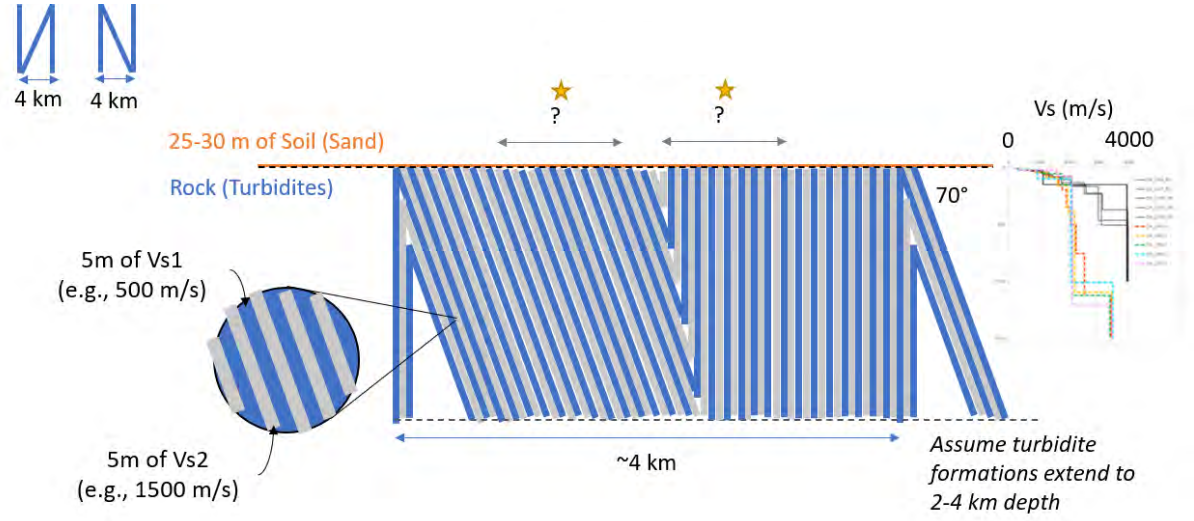

Figure 9-95. Conceptual 2D cross section used for the 2D site response analyses (WM3).

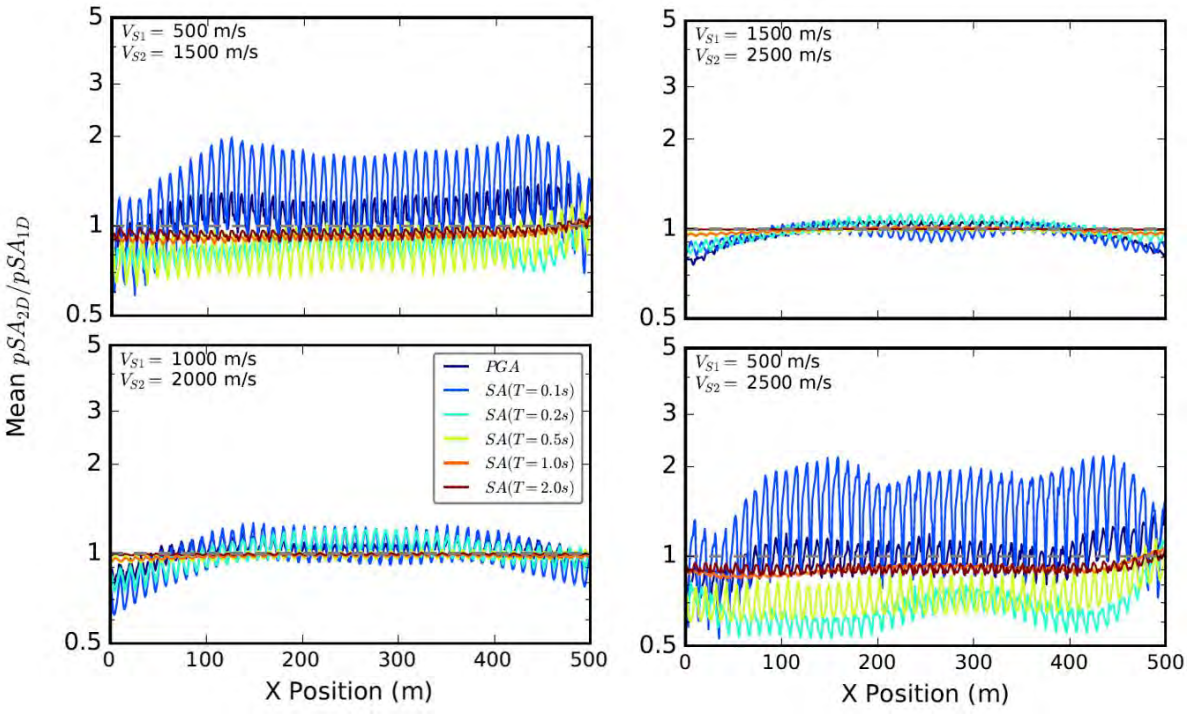

Figure 9-96. Ratios of pseudo-spectral acceleration at the ground surface from 2D analyses (pSA2D) to pseudo-spectral acceleration from 1D site response analyses (pSA1D) vs horizontal position along the conceptual 2D cross-section for four different scenarios of low and high V_S values (a-d) and for six oscillator periods (T = 0.01 to 2.0 s).

After reviewing the results from the study performed by De La Torre and Bradley, the GMM TI Team requested acoustic velocity measurements of samples from outcrop rock in the region where samples of the turbidites could be obtained and tested to estimate the variation in low/high V_S values within these formations. The CGS staff collected samples from accessible outcrops in the region south of the Duynefontyn site, tested the samples, and provided a summary report to the GMM TI Team (Maré, 2022). The median V_S measured in the top of the turbidites was 3,149 m/s (standard deviation = 549 m/s) and the median in the base of the turbidites was 3,891 m/s (standard deviation = 362 m/s), which indicates that the variation of V_S across the turbidites is not significant.

The GMM TI Team considered the results of the 2D site response analyses and the acoustic velocity analyses of rock samples to decide whether an alternative branch in the logic-tree to account for 2D effects was warranted. The acoustic velocity analyses suggested that the difference between low and high V_S values in the turbidites was approximately 750 m/s, which was less than the difference between the V_S1 and V_S2 values tested within the 2D site response analyses. In addition, the absolute values of V_S from the acoustic velocity analyses were higher than those evaluated in the 2D site response analyses. Given that the 2D SA were almost indistinguishable from 1D SA when the difference between the low and high V_S values was 1,000 m/s and the maximum V_S was 2,500 m/s, the GMM TI team concluded that there was no need to include an additional logic-tree branch to incorporate 2D vs 1D aggravation factors. This decision was based on the low/high V_S values from the acoustic testing of turbidite samples being higher and more similar to each other than we had modelled previously in the 2D site response analyses.

9.4.7 Input motions

An important component of the one-step approach is to define an input base motion that approximately generates the reference GMM at the surface (e.g., left-hand side of Figure 9-97) for the reference site host profile. As discussed in Section 9.2.1.1, the reference GMPE is CY14. The Stafford et al. (2022) optimal seismic parameter model for CY14 is tuned to produce CY14 at the ground surface and site amplification associated with the AAA21 V_S profile for CY14 and V_{S30} = 760 m/s computed by the quarter wavelength approach and a κ_0 = 0.039 s. In our study, we use pyStrata (Kottke, 2022) to compute site amplification to allow for automation of the hundreds of thousands of site response analyses and to account for the nonlinear site response using the equivalent-linear approach. It is important to confirm that the full resonance amplification modelled by pyStrata combined with the Stafford et al. (2022) seismic parameters (without site amplification) produces surface response spectra consistent with CY14. It is not required that the full resonance site amplification exactly reproduce the quarter wavelength site amplification or the reference GMM at the surface of the host profile because the SAF is defined using the surface spectral acceleration from the full resonance site amplification before it is applied to the reference GMM.

For this evaluation, the GMM TI Team performed site response analyses with the input motion defined by the Stafford et al. (2022) seismic parameters with crustal site amplification A(f) = 1.0 and κ_0 = 0.00 s. This FAS is propagated through the AAA21 profile and the surface response spectrum is computed using RVT in pyStrata. A depth-independent minimum damping (D_{min}) of 0.8% was used to achieve the AAA21 target κ_0 = 0.039 s consistent with AAA21. Density was estimated as a function of V_S consistent with the equation that AAA21

used. Both the site transfer function and the surface spectral acceleration were compared with those presented in Stafford et al. (2022). An exact match with CY14 is not required because we use the computed surface response spectrum at the top of the reference profile (Sa^*_{ref} in Figure 9-97) as the denominator in the SAF computation, rather than the response spectrum from CY14 directly.

The surface response spectra for M 6 and a distance of 20 km are compared in Figure 9-98 for Stafford et al. (2022) using QWL site amplification and pyStrata using full resonance site amplification. The spectral shapes are very similar, but pyStrata predicts slightly larger values due to the larger amplitudes of the site transfer function. Interestingly, the pyStrata surface response spectrum in Figure 9-99 better matches the CY14 spectrum than the Stafford et al. (2022) QWL prediction, particularly at frequencies greater than 3 Hz. This result highlights the fact that even the QWL site amplification approximation does not match CY14 perfectly. Thus, the match in Figure 9-99 was deemed reasonable by the GMM TI Team and provided a sufficiently defensible basis to proceed with using pyStrata full resonance site amplification with the Stafford et al. (2022) seismic parameters for the site response analyses in this project. The uncertainty associated with this decision is incorporated within the overall epistemic uncertainty of the GMM. Note that we observed similar comparisons for other combinations of magnitude and distance.

After confirming that pyStrata could adequately suit the needs of the project, a set of input motions that span a range of magnitudes and intensities, as defined by the computed Sa^*_{ref} at the surface of the AAA21 reference profile, was defined. These input motions were defined for three magnitudes (**M** 5.5, **M** 6.5, and **M** 7.5) at a distance of 20 km and scaled to seven reference PGA values (0.05, 0.1, 0.2, 0.4, 0.8, 1.6, and 3.2 g). The resulting reference motions are summarised in Figure 9-100. These spectra indicate that earthquake magnitude influences the spectral shape at low frequencies, with larger **M** events containing more low-frequency energy. Each of these motions has an associated Sa_{input} at the base of the AAA21 profile (Figure 9-97) that is used as input into the site response V_S profiles defined by the logic-tree.

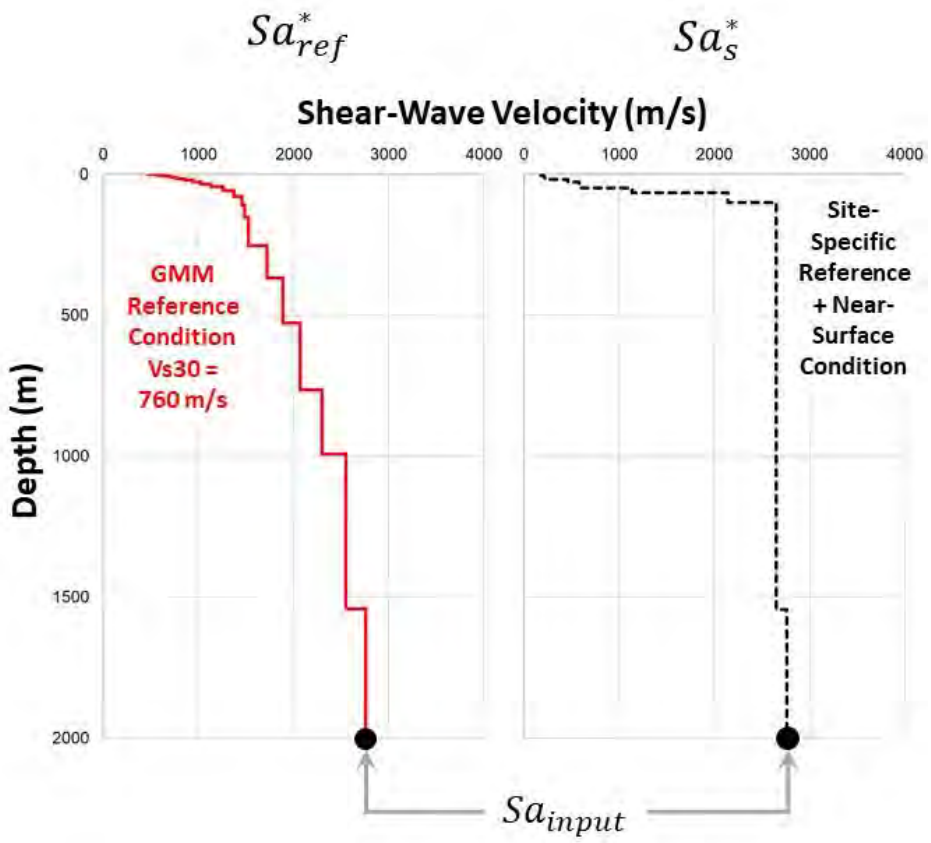

Figure 9-97. Schematic of input motion specification for the one-step approach (Rodriguez-Marek et al. 2021).

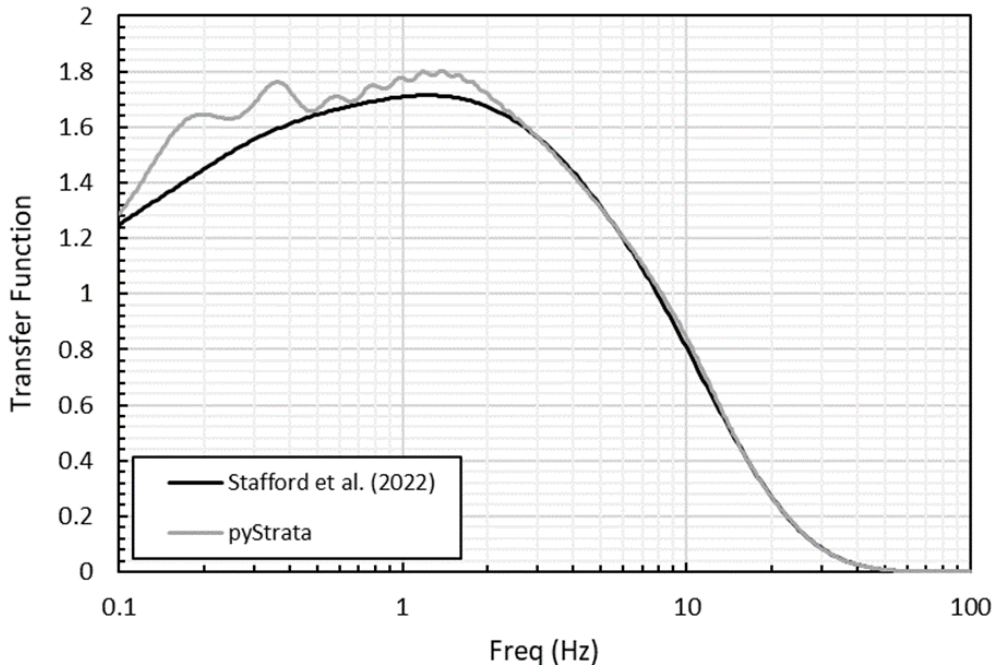

Figure 9-98. Comparison of quarter wavelength transfer function from Stafford et al. (2022) and full resonance transfer function from pyStrata for the AAA21 shear-wave velocity profile.

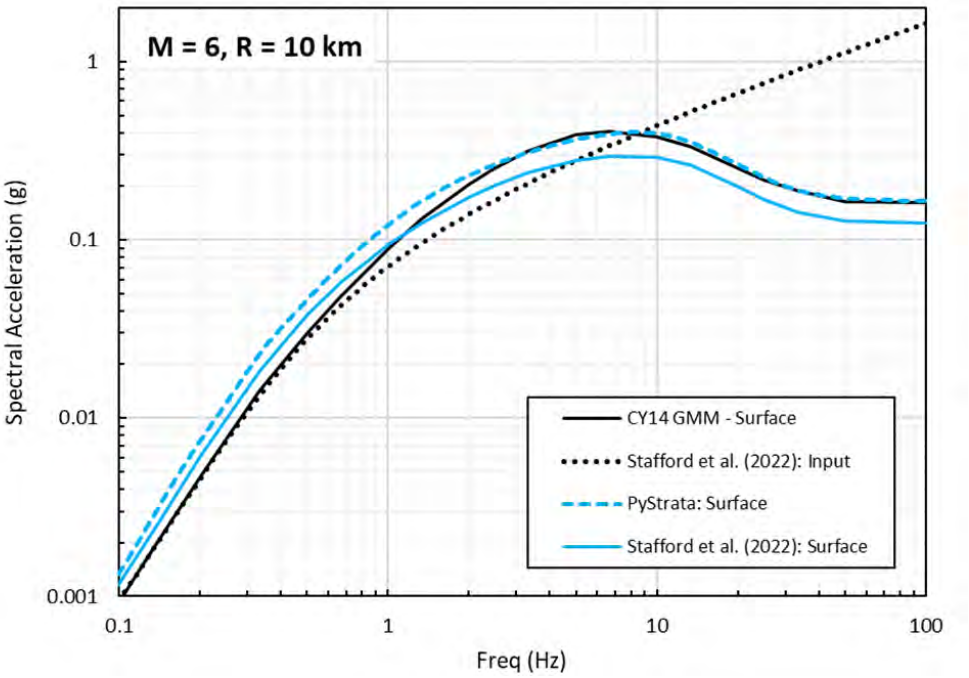

Figure 9-99. Surface response spectrum for the host reference condition (Sa^{*}_{ref}) computed by pyStrata using Stafford et al. (2022) input motion and AAA21 reference condition (V_S profile and κ_0). For comparison, also shown are surface response spectra from Stafford et al. (2022) representation of CY14 GMM and directly from the CY14 GMM.

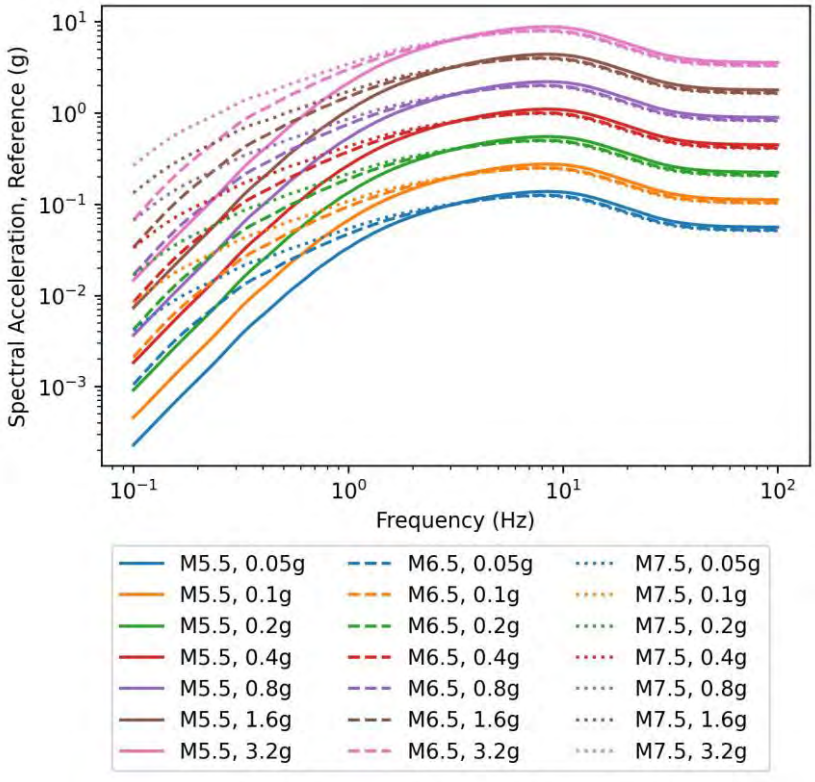

Figure 9-100. Reference motions (Sa^{*}_{ref}) at the top of the AAA21 reference profile representing input motions for site response analyses.

9.4.8 Site amplification factors

As described in Section 9.4.7, the GMM TI Team performed site response analyses for 60 randomised profiles for each of the end-branches of the site response logic-tree (Figure 9-61). EQL analyses were performed using pystrata (Kottke, 2022), a Python-based version of the well-known Strata software (Kottke and Rathje, 2008). As described in Section 9.4.7, input motions were developed using RVT and scaled to match seven intensity levels for the reference condition (PGA = 0.05, 0.1, 0.2, 0.4, 0.8, 1.6, and 3.2 g) at three magnitudes (**M** 5.5, **M** 6.5, **M** 7.5). Thus, 60 randomisations for 408 terminal branches, three magnitudes, and seven intensity levels yields 514,080 site response analyses. The following discussion summarizes the general trends in SAF from these analyses and the sensitivities of SAF values to individual components of the site response logic-tree.

9.4.8.1 Sensitivities of SAF vs frequency based on logic-tree branches

Different components of the logic-tree are explored to look at the sensitivity of the SAF. For the assessments below, the SAF vs frequency for all 408 terminal branches are shown for the **M** 6.5, PGA = 0.4 g input motion. Figure 9-101 shows SAF vs frequency for all 408 terminal branches, the weighted average SAF across those same branches, and the weighted average standard deviation of ln(SAF) (i.e. the aleatory variability, σ_{lnSAF}). Each subsequent figure shows the sensitivity in SAF for the different parameter values associated with each segment of the logic-tree.

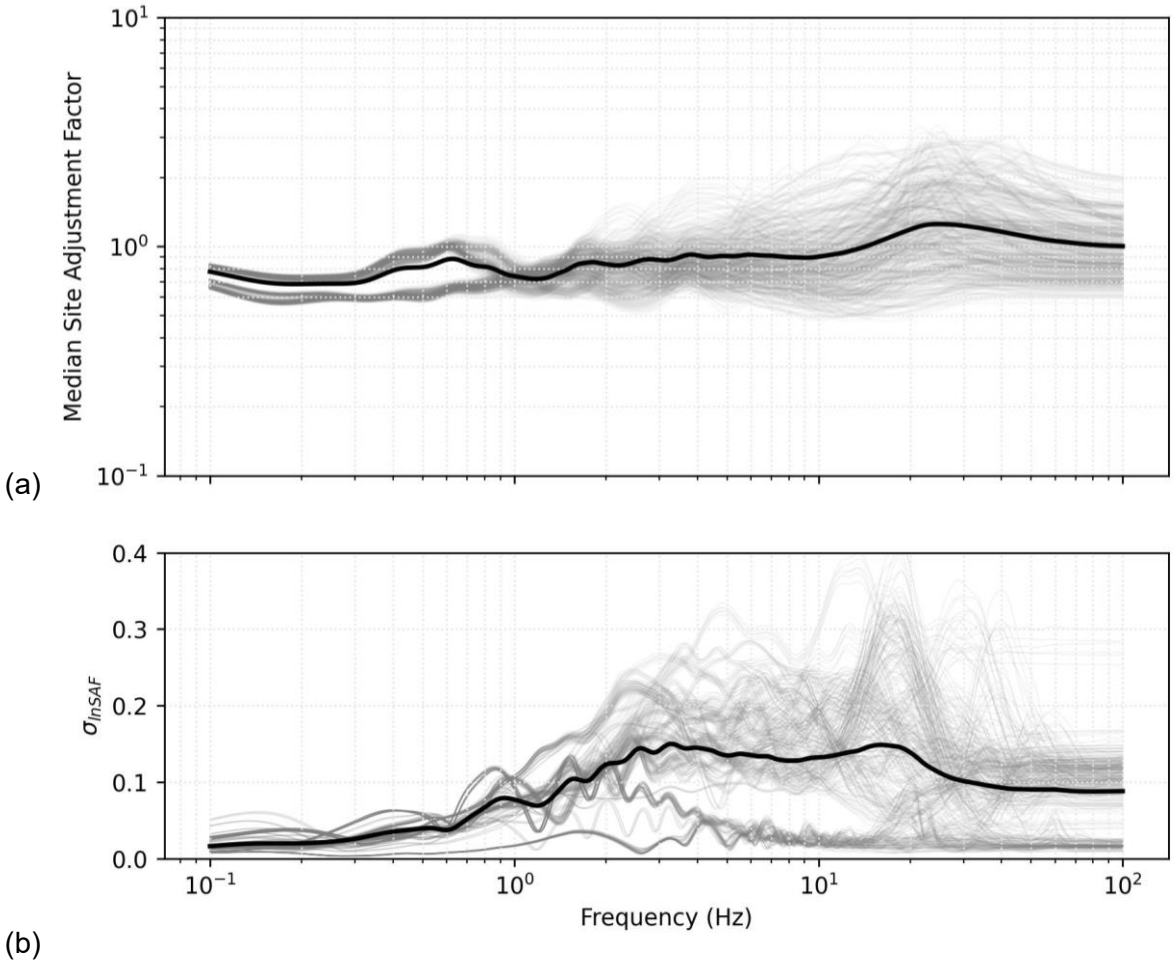

Figure 9-101. a) SAF and b) σ_{lnSAF} vs frequency for M 6.5 and PGA = 0.4 g intensity input motion. Thin grey lines represent median SAFs for each of the 408 terminal branches of the logic-tree, bold lines represent weighted average SAFs and σ_{lnSAF}.

As shown in the site response logic-tree (Figure 9-61) and discussed in Sections 9.4.2.1 and 9.4.2.2, the V_S profiles used in the site response analyses are divided into categories representing V_S method (i.e. MASW/MAM vs downhole) and V_S mode (i.e. FM vs MM). Figure 9-102 shows the SAF vs frequency for all 408 terminal branches using the **M** 6.5, PGA = 0.4 g input motion. The bold, coloured lines represent the median SAF values across terminal branches for a given combination of V_S method and V_S mode. In general, for frequencies above 1 Hz, the median SAF for the four combinations shown here are relatively similar. Differences between these groups occur for frequencies less than 1 Hz because of the different V_S profiles from the different mode interpretations from MASW/MAM. The SAF values are larger for the profiles associated with the MM mode interpretation (i.e. MASW/MAM MM and downhole profiles with MASW/MAM MM extensions) than for the profiles associated with FM interpretation (i.e. MASW/MAM FM and downhole profiles with MASW/MAM FM extensions). The larger SAF are caused by the smaller V_S values that extend deeper in the MM profiles, which leads to more low-frequency amplification.

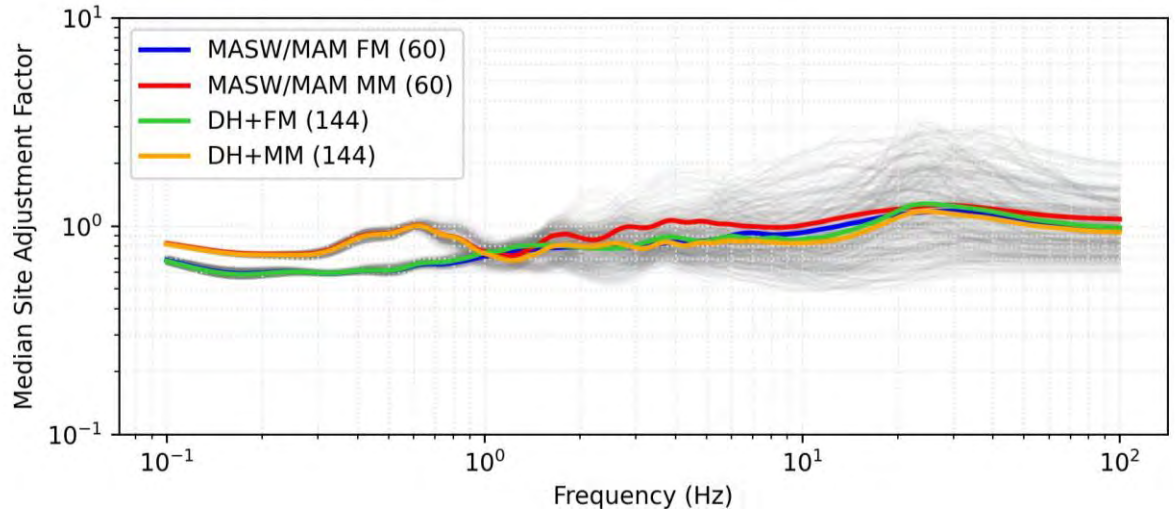

Figure 9-102. SAF vs frequency for M 6.5 and PGA = 0.4 g intensity input motion. Thin grey lines represent median SAF for each of the 408 terminal branches of the logic-tree, bold coloured lines represent median SAF for all terminal branches corresponding to nodes of the V_S method and V_S mode levels of the logic-tree. Numbers in parentheses represent the number of terminal branches represented in that group.

As shown in the site response logic-tree (Figure 9-61 and Figure 9-62) and discussed in Section 9.4.1, the V_S profiles used in the site response analyses are divided into categories representing the layering ratio (LR) used to interpret the dispersion data to create V_S profiles (i.e. LR 1.5-7.0). Figure 9-103 shows again the SAF values, with the bold, coloured lines representing the median SAF across the terminal branches for a given LR. For frequencies below 1 Hz, the median SAF for the five LR are essentially indistinguishable due to the fact that the low-frequency epistemic uncertainty is controlled by the MASW/MAM mode interpretation (Figure 9-102). The difference between the SAF from the different LR profiles is more apparent for frequencies above 1 Hz, where the SAF values generally decrease as LR increases. For example, V_S profiles with LR = 1.5 have the largest SAF whereas V_S profiles with LR = 7.0 have the smallest SAF. The profiles with the smaller LR tend to have more V_S layers that result in profiles with thinner layers with smaller V_S near the surface (e.g., Figure 9-69), and these profiles generate more high-frequency amplification.

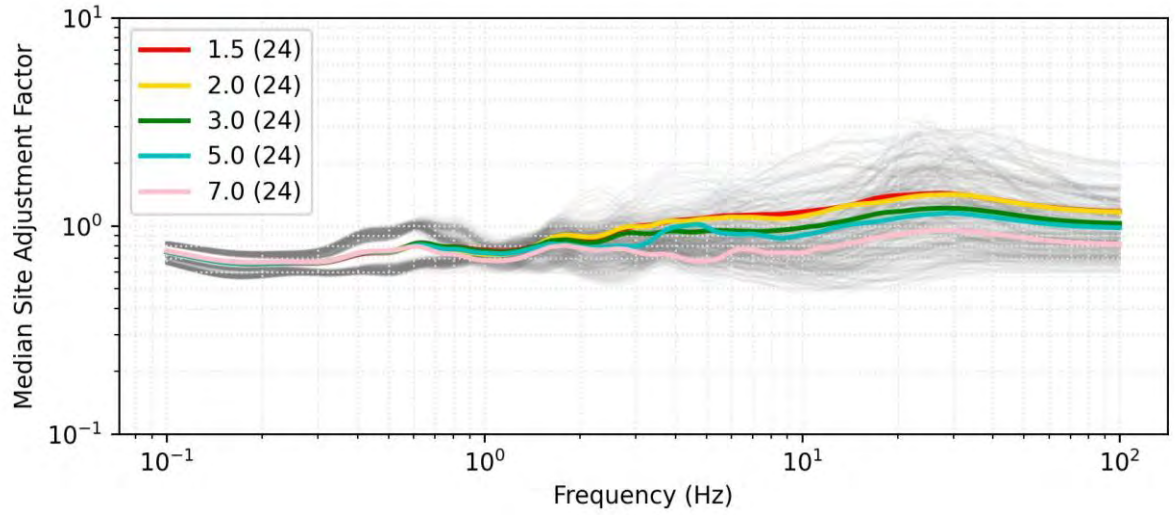

Figure 9-103. SAF vs frequency for M6.5 and PGA = 0.4 g intensity input motion. Thin grey lines represent median SAF for each of the 408 terminal branches of the logic-tree, bold coloured lines represent median SAF for all terminal branches corresponding to nodes of the LR level of the logic-tree. Numbers in parentheses represent the number of terminal branches represented in that group.

As shown in the site response logic-tree (Figure 9-61 and Figure 9-63) and discussed in Section 9.4.2.2, the downhole V_S profiles are given individual weights based on the borehole number (i.e. BH46-BH53). Figure 9-104 shows the median SAF values across terminal branches for a given DH V_S profile. In general, for frequencies below 1 Hz, the median SAF trends for the different DH profiles are indistinguishable, because the SAF values at low frequency are controlled by the mode interpretations for the MASW/MAM extensions. The effect of the DH profile is more apparent for frequencies above 1 Hz, where the SAF values vary widely depending on the selected DH profile. These higher frequencies are controlled by the near-surface V_S of the DH profiles, which only extend to 50 m (Figure 9-72). As discussed in Section 9.4.2.2, DH V_S profiles BH 46 and BH 51 received reduced weights due to the assessment that the V_S characteristics of these profiles were not representative of the site as a whole. These two DH V_S profiles also yield the most noticeably different SAF values compared to the general trend of the other DH V_S profiles. The SAF for BH 46 are larger at high frequencies due to the smaller velocities in this profile, and the SAF for BH 51 are smaller at high frequencies due the larger velocities in this profile.

As shown in the site response logic-tree (Figure 9-61 and Figure 9-86) and discussed in Section 9.4.3, the three branches representing site κ_0 are given individual weights. Figure 9-105 shows the median SAF values across terminal branches for a given κ_0 value. For frequencies below 1 Hz, the median SAF for the three κ_0 values are indistinguishable because κ_0 predominantly affects high oscillator frequencies. Thus, the difference between these κ_0 values is more apparent for frequencies above 1 Hz, where the SAF values increase as κ_0 decreases.

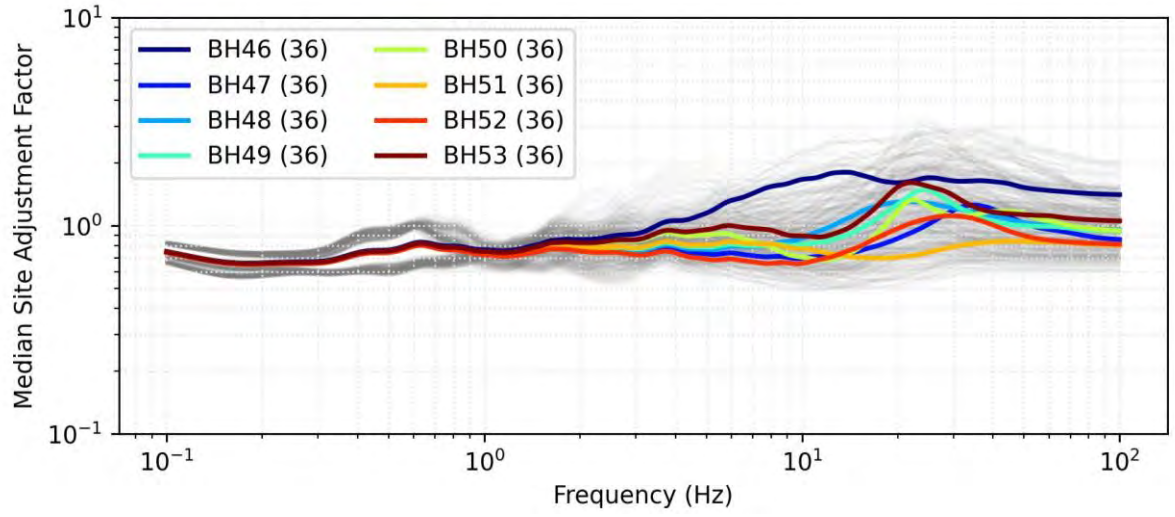

Figure 9-104. SAF vs frequency for M 6.5 and PGA = 0.4 g intensity input motion. Thin grey lines represent median SAF for each of the 408 terminal branches of the logic-tree, bold coloured lines represent median SAF for all terminal branches corresponding to nodes of the DH level (i.e. borehole numbers BH46-BH53) of the logic-tree. Numbers in parentheses represent the number of terminal branches represented in that group.

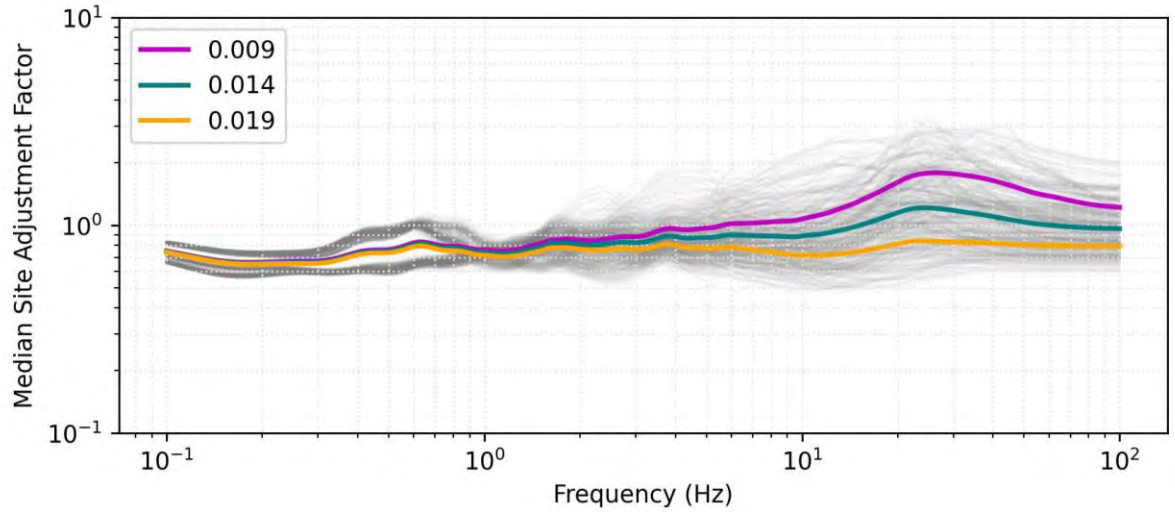

Figure 9-105. SAF vs frequency for M 6.5 and PGA = 0.4 g intensity input motion. Thin grey lines represent median SAF for each of the 408 terminal branches of the logic-tree, bold coloured lines represent median SAF for all terminal branches corresponding to nodes of the κ_0 level of the logic-tree.

As shown in the site response logic-tree (Figure 9-61) and discussed in Section 9.4.4, the two branches representing MRD curves (i.e. Set 1 and Set 2) are given equal weight. Figure 9-106 shows the SAF values, with the bold, coloured lines representing the median SAF values across terminal branches for a given set of MRD curves. For frequencies below 1 Hz, the median SAF for the two MRD curves are indistinguishable. The difference between these groups is more apparent for frequencies above 1 Hz, where the SAF values are larger for Set 1 than Set 2. As discussed in Section 9.4.4, the two sets of MRD curves represent a stiffer condition (Set 1) and a softer condition (Set 2). Additionally, for the softer Set 2 condition (Figure 9-90), the damping increases more rapidly at the moderate strain levels (~0.01%). As a result, the softer Set 2 MRD curves generate more damping for a given input motion, which results in smaller high-frequency SAF for the Set 1 MRD, as illustrated in Figure 9-106.

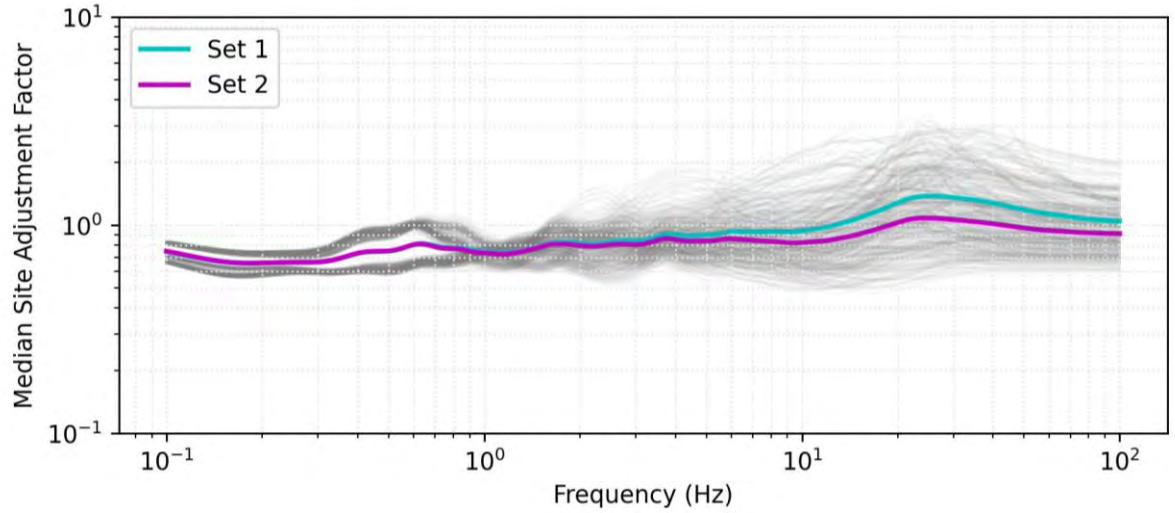

Figure 9-106. SAF vs frequency for M 6.5 and PGA = 0.4 g intensity input motion. Thin grey lines represent median SAFs for each of the 408 terminal branches of the logic-tree, bold coloured lines represent median SAFs for all terminal branches corresponding to nodes of the MRD level of the logic-tree.

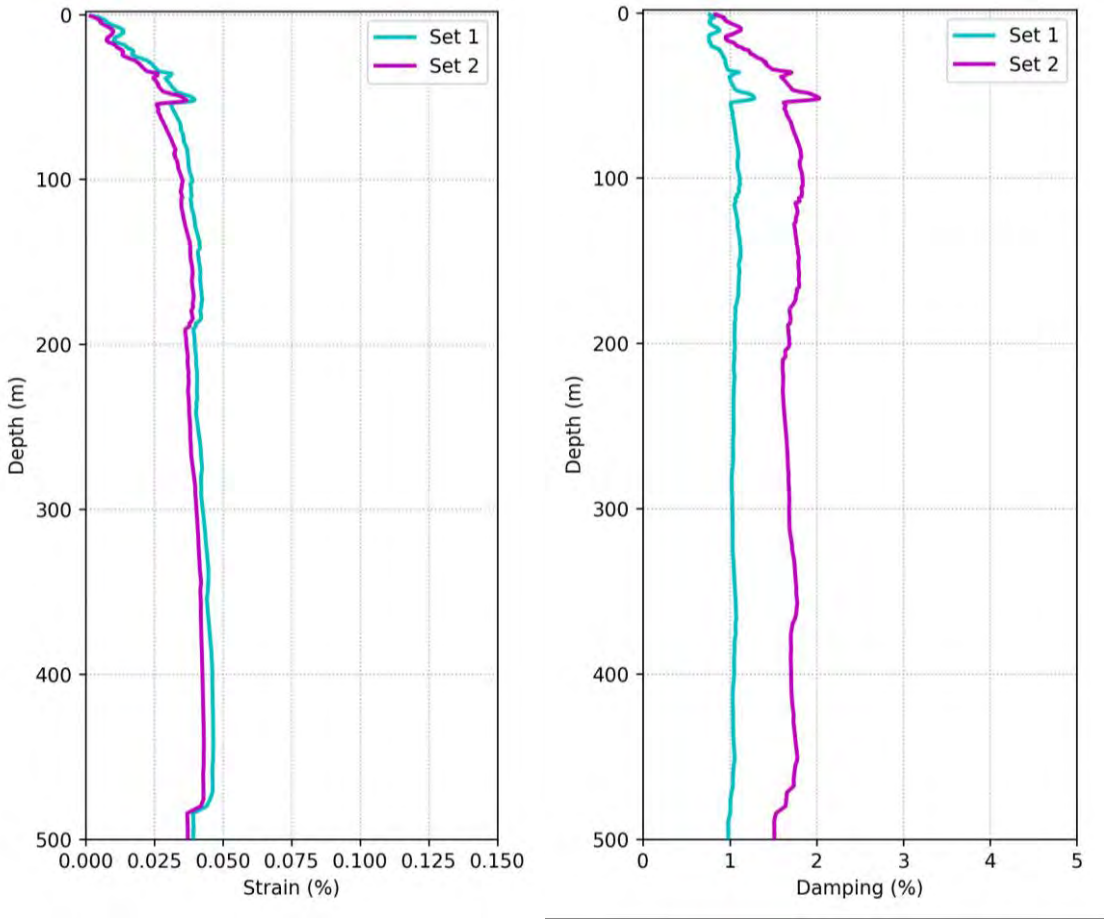

Figure 9-107. Median a) strain and b) damping profiles for M 6.5, 3.2 g input motion, showing the difference between the two MRD curves used in the site response analyses: Set 1 and Set 2.

9.4.8.2 Sensitivities of SAF based on magnitude and intensity effects

In this section, we illustrate the effects of earthquake magnitude (**M** 5.5-7.5) and reference ground-motion intensity (PGA = 0.05 – 3.2 g) on the median SAFs across all 408 terminal branches of the logic-tree. For the input motions utilised, earthquake magnitude influences the spectral shape at lower frequencies (Figure 9-100).

Figure 9-108 shows the influence of earthquake magnitude on the weighted median SAF for two intensity levels: PGA = 0.4 g and PGA = 3.2 g. For the input intensity of PGA=0.4 g (Figure 9-108a), the effect of magnitude is almost indiscernible, regardless of the oscillator frequency. For the input intensity of PGA=3.2 g (Figure 9-108b), the effect of magnitude is more pronounced with smaller SAF at oscillator frequencies above 1 Hz for larger **M**. The effect of earthquake magnitude on the induced strains and damping is shown in Figure 9-109 for each input intensity. For each intensity, the larger **M** events induced more strain and more damping, with the effect being more pronounced at larger intensities. These larger levels of induced strain and damping, which lead to less high-frequency amplification, are a result of the more significant low-frequency content of the larger magnitude events.

Figure 9-110 shows the influence of input intensity on the weighted median SAF for the **M** 6.5 input motion. Input motion intensity has little influence on the median SAFs for frequencies less than 1 Hz, but for higher frequencies the three highest intensity levels (PGA = 0.8, 1.6, and 3.2 g) have noticeable smaller median SAFs. The four smallest intensity levels (PGA = 0.05, 0.1, 0.2, and 0.4 g) are essentially indistinguishable from each other. The sensitivity of SAF values to intensity is due to the increased strain and damping at higher intensity levels, as illustrated in Figure 9-109. The strain levels induced by the different input motion intensities vary by orders of magnitude. It is only for the three largest intensity levels that the strains are large enough for the damping to change enough to affect the SAF.

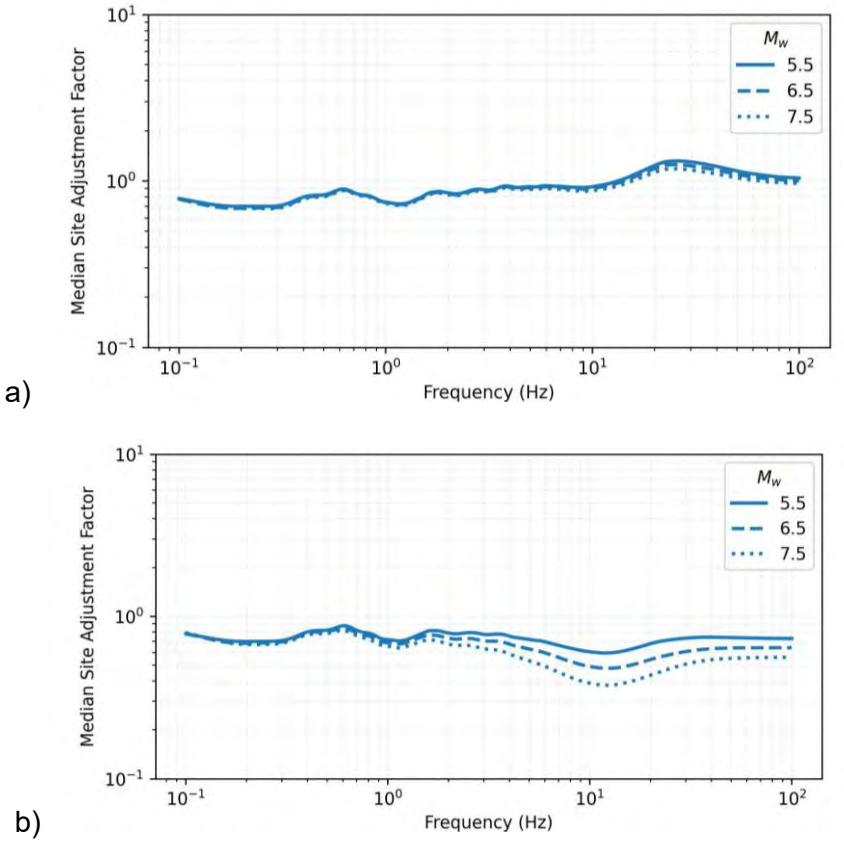

Figure 9-108. Weighted median SAF vs oscillator frequency for three magnitudes (5.5, 6.5 and 7.5) and two intensities: a) 0.4 g and b) 3.2 g.

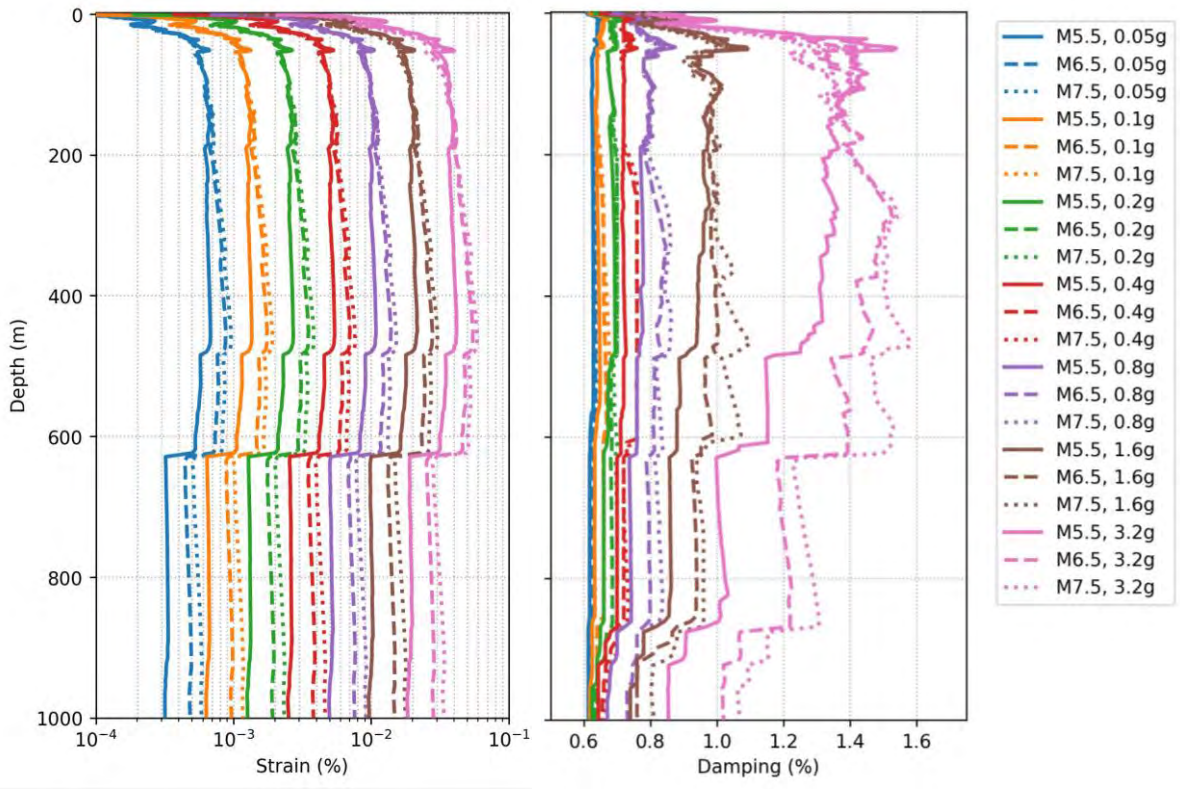

Figure 9-109. Median a) strain and b) damping profiles for three magnitudes (M 5.5, 6.5 and 7.5) and seven intensities (0.05-3.2 g). Only the upper 1000 m is shown.

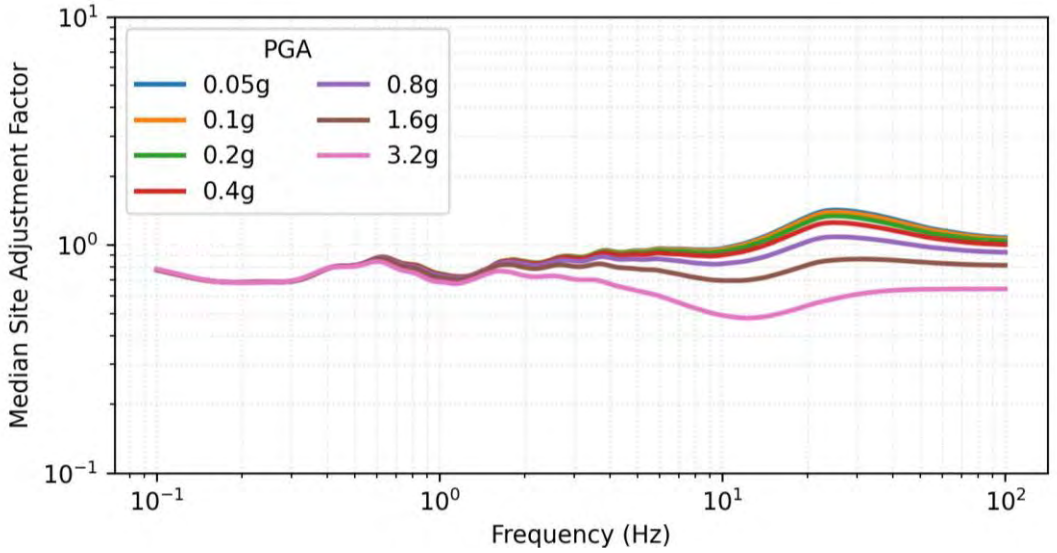

Figure 9-110. SAFs vs oscillator frequency for seven intensity levels (0.05-3.2 g) and M 6.5.

9.4.8.3 Percent contribution to total variance

We now show the individual percent contributions to the total variance associated with the epistemic uncertainty in ln(SAF) for each of the levels in the logic-tree associated with parametric uncertainty. The purpose of this discussion is to identify which aspects of the logic-tree contribute the most to the overall epistemic uncertainty and to see how these contributions change depending on oscillator frequency and intensity of the input motion. Figure 9-111 summarizes the percent contribution to the total variance across four oscillator frequencies and four intensity levels. For each frequency and intensity level, the total epistemic uncertainty (σ_{ep}) is also indicated in the legend. The additional epistemic uncertainty associated with model error is addressed separately.

First, we focus on the 0.5 Hz oscillator frequency. Regardless of the intensity of the input motion (0.1-1.6 g), the two components of the logic-tree that contribute the most to the total variance are the V_S mode and the V_S extension for the DH V_S profiles. Because the DH V_S extensions include three FM and three MM profiles, the variance contribution at low frequencies associated with the DH essentially represents the V_S mode of the DH extensions. The strong effect of V_S mode was observed in the almost bi-modal grouping of the SAF values at 0.5 Hz for the MM and FM groups (Figure 9-102). Other components of the logic-tree contribute essentially no variance at 0.5 Hz.

The variance for 2.5 Hz is distributed across several components of the logic-tree, with the LR component contributing nearly half of the total variance, regardless of the intensity of the input motion. The V_S extension and V_S method each contribute about 10-20% to the total variance. Similar to the 0.5 Hz oscillator frequency, these contributions do not vary noticeably with input intensity.

Next, we focus on the 10 Hz oscillator. At lower intensity input motions (e.g., 0.1g and 0.4g), the total variance is almost equally distributed between V_S method, LR#, BH#, and κ_0, with little to no contributions from V_S mode, the V_S extension for the DH V_S profiles, and the MRD curves. At higher intensity input motions (e.g., 0.8 g and 1.6 g), the influence of MRD curves is more pronounced and becomes the dominant contributor to variance at the 1.6 g intensity

level. The contribution of the MRD curves become more pronounced at larger intensities because the effects of larger strains and increased damping influence the SAF at 10 Hz.

Finally, the total variance in SAF values for the 33 Hz oscillator is mostly driven by κ_0 and the MRD curves, with the contribution of each of these components varying with the intensity of the input motion. At lower intensity levels (e.g., 0.1 g and 0.4 g), the κ_0 branch contributes over 60% of the total variance, whereas at higher intensity levels (e.g., 0.8 g and 1.6 g), the MRD curves become increasingly influential until the MRD branch contribute over 50% of the total variance for the 1.6 g intensity level. Again, the increased contribution of the MRD curves at larger intensity is due to the effect of larger induced strains and damping that influence higher frequencies.

In summary, each of the components of the logic-tree contributes some measurable amount of total variance (i.e. no component of the logic-tree is completely irrelevant), and the percent contribution to the total variance changes depending on oscillator frequency and intensity of the input motion.

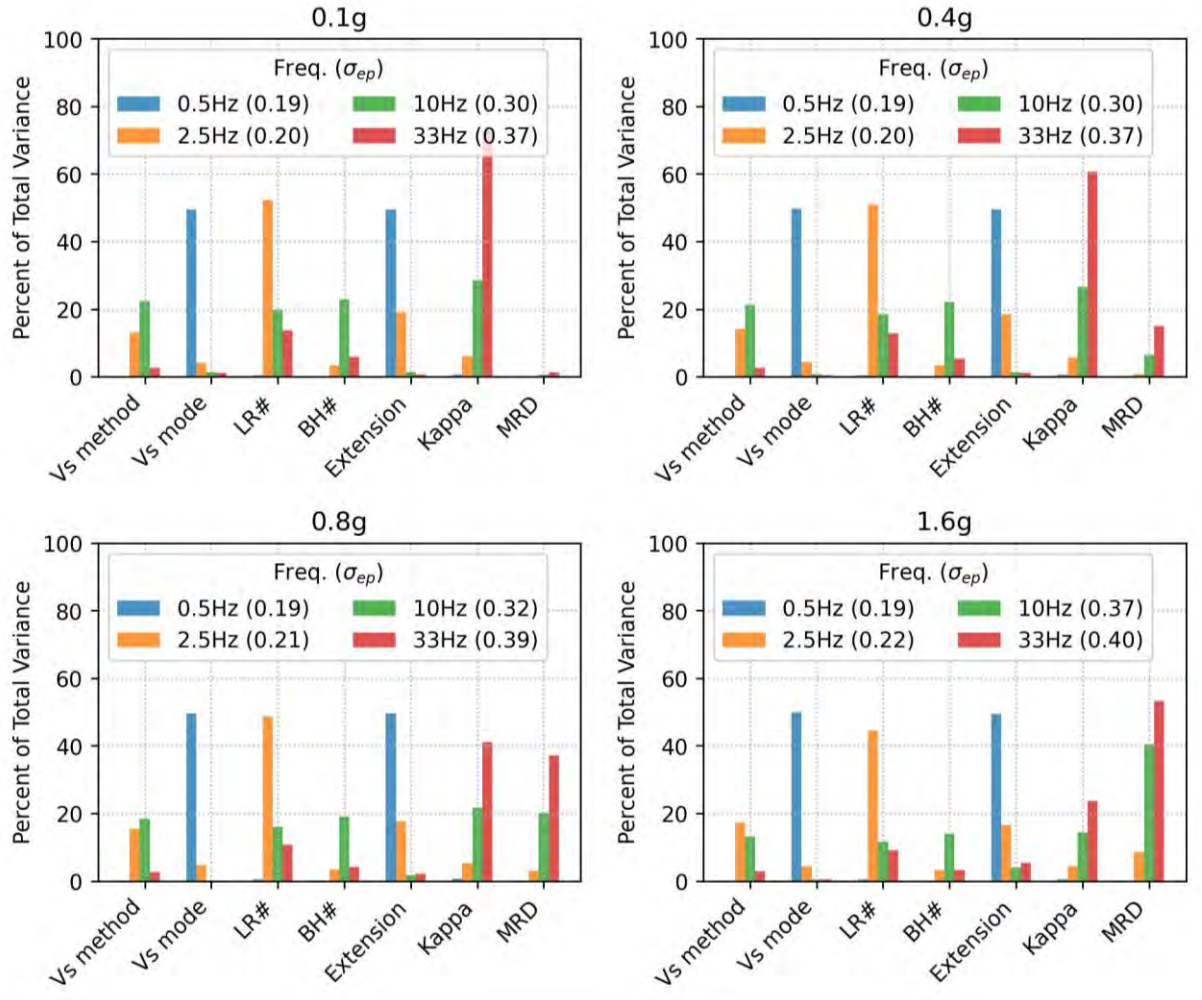

Figure 9-111. Percent contributions to total variance for M6.5 separated into seven levels of the logic-tree, four oscillator frequencies (0.5, 2.5, 10, and 33 Hz), and four intensity levels: a) 0.1 g, b) 0.4 g, c) 0.8 g, and d) 1.6 g. Values in parentheses in the legends represent total epistemic uncertainty in the ln(SAF) values.

9.4.9 Final site amplification model

The following sections outline the steps to develop the final site amplification model: 1) resampling the SAF values from the full site response logic-tree, 2) quantifying the epistemic uncertainty in ln(SAF) (σ_{ep}) and incorporating additional uncertainty due to model error, and 3) defining the models for SAF and aleatory variability in the SAF (σ_{lnSAF}) as a function of reference intensity.

9.4.9.1 Resampling SAF from full logic-tree

As has been done in past SSHAC projects (e.g., Idaho National Laboratory) and recommended by Rodriguez-Marek et al. (2021), the GMM TI Team decided to reduce the number of branches from the full site response logic-tree (i.e. 408 branches) for use in the hazard calculations by resampling (or down-sampling). Resampling is typically done to allow for increased complexity in the site response logic-tree (Section 9.4.1) to more fully capture the CBR of TDI in terms of SAF without unduly penalising the hazard calculations by making them too computationally intensive. Previous SSHAC projects have used a 7-point discrete approximation from Miller and Rice (1983) for resampling, which provides discrete approximations for any continuous probability distributions using Gaussian Quadrature. This 7-point discrete distribution has been shown to provide a reasonable approximation to the hazard results using the full distribution of median SAF (Rodriguez-Marek et al., 2021).

When considering the 7-point discrete distribution from Miller and Rice (1983), the GMM TI Team decided that the bi-modal distribution of SAFs at frequencies less than 1 Hz would not be well represented using an odd-numbered discrete distribution in which the branch with the highest weight would fall between the two groups of SAF values where there are no data (e.g., Figure 9-102). Thus, the GMM TI Team decided to use a 6-point distribution.

The process to resample the SAFs into a 6-point discrete distribution for each magnitude-intensity-frequency combination is:

1. Sort the SAF values in ascending order
2. Compute the weighted empirical cumulative distribution function (CDF)
3. Obtain corresponding SAF values from the weighted empirical CDF using the discrete CDF values from Miller and Rice (1983)
4. Record the discrete values of SAF, which represent the resampled branches, and assign the corresponding weights from Miller and Rice (1983).

This process is illustrated in Figure 9-112 for the **M** 6.5, 0.4 g input motion and Table 9-16 provides the corresponding CDF values and weights recommended by Miller and Rice (1983) for a 6-point distribution.

The resampled SAF branches for the **M** 6.5, 0.4 g input motion are plotted against frequency in Figure 9-113. At frequencies less than 1.0 Hz, the resampled SAF capture well the bimodal distribution of the SAF data. At higher frequencies, the resampled SAF are distributed more widely and capture well the more evenly distributed SAF data. Also shown in Figure 9-113 is the epistemic uncertainty (σ_{ep}) across all 408 logic-tree branches for each frequency. The epistemic uncertainty varies considerably with frequency, with values as small as 0.1 at low frequencies and as large as 0.4 at higher frequencies.

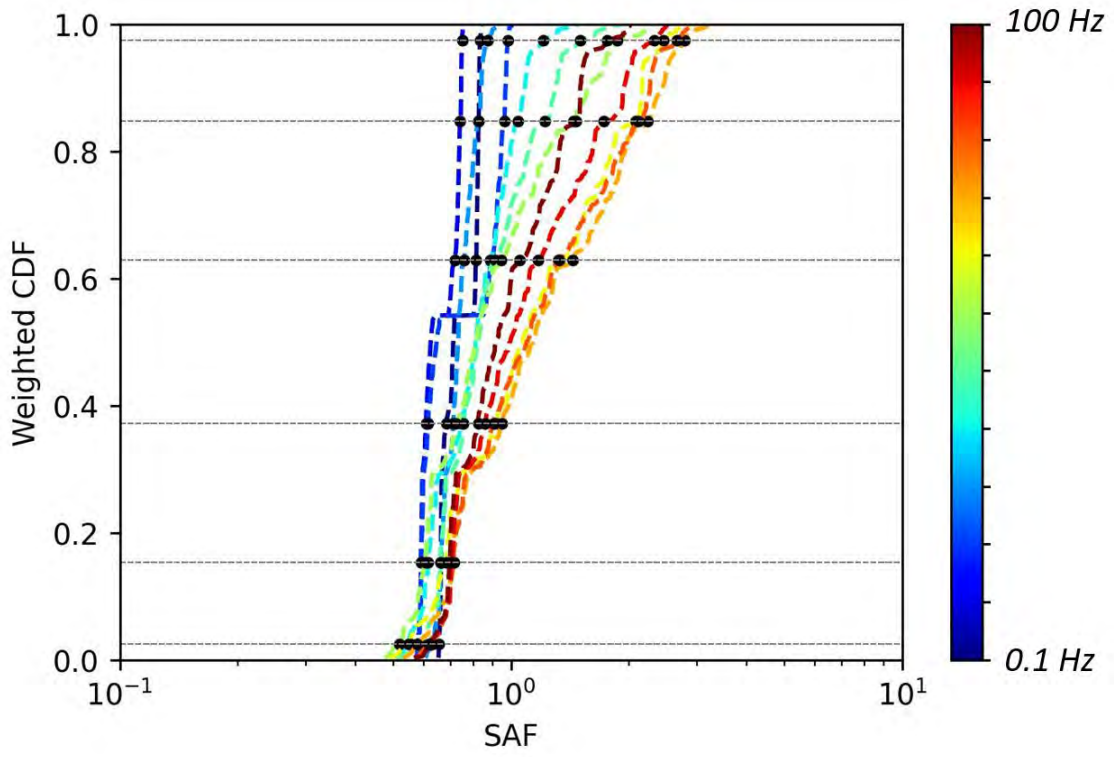

Figure 9-112. Weighted CDFs of SAF for oscillator frequencies between 0.1 and 100 Hz and the M6.5, 0.4g input motion. Horizontal dashed lines represent the CDF values associated with a 6-point distribution from Miller and Rice (1983).

Table 9-16. CDF values and weights recommended by Miller and Rice (1983) for a 6-point distribution.

Branch	CDF	Weight
SAF1	0.025219	0.072713
SAF2	0.152820	0.178624
SAF3	0.371852	0.248663
SAF4	0.628148	0.248663
SAF5	0.847180	0.178624
SAF6	0.974781	0.072713

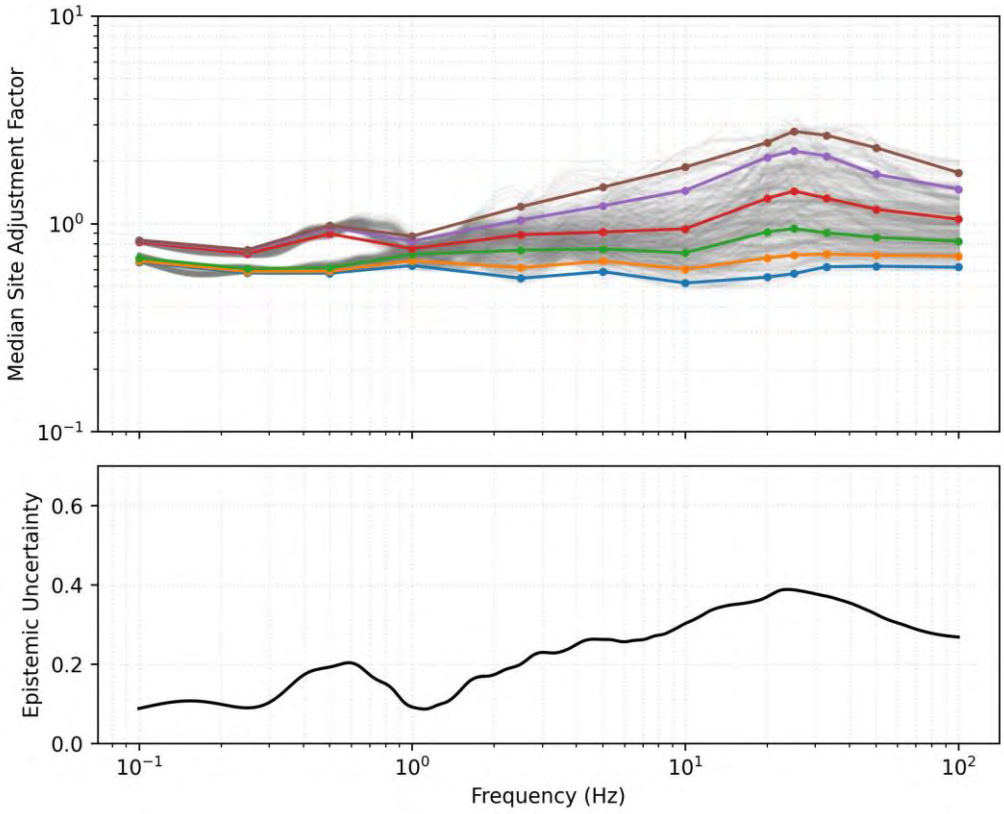

Figure 9-113. SAF values for each terminal branch of the logic-tree using the M 6.5, 0.4 g input motion (thin grey lines), resampled SAF values (bold coloured lines) using a 6-point distribution, and the weighted epistemic uncertainty from the logic-tree (σ_{ep}) plotted against frequency.

9.4.9.2 Epistemic uncertainty and incorporating model error

The weighted average epistemic uncertainty in the ln(SAF), represented by σ_{ep}, is the uncertainty due to the 408 logic-tree branches after incorporating the weights from the logic-tree. Epistemic uncertainty varies with frequency (as shown in the previous section) and can vary with magnitude and intensity of the input motion. Figure 9-114 shows the influence of intensity and magnitude on the σ_{ep} values. The σ_{ep} values for the four smallest intensities are essentially the same and do not vary with magnitude, while the epistemic uncertainty increases for most oscillator frequencies as intensity increases for the three highest intensities (0.8, 1.6, and 3.2 g). At higher frequencies there is some reduction in σ_{ep} at the largest intensity for **M** 7.5, which is likely due to the larger induced strains and damping for this case that reduce the effect for some of the components of the logic-tree. Magnitude only has a noticeable effect on the epistemic uncertainty at the largest intensities, with σ_{ep} increasing as magnitude increases for some oscillator frequencies (e.g., 3-11 Hz) and decreasing for other frequencies (e.g., 20-100 Hz).

The GMM TI Team reviewed the level of epistemic uncertainty due to the logic-tree alone and found that the range of σ_{ep} (0.1-0.48 in log units) was reasonable considering the level of uncertainty represented in other projects (i.e. INL: σ_{ep} typically was between 0.1 and 0.6 depending on frequency, magnitude, and intensity). Thus, the site response logic-tree was considered to adequately capture an appropriate range of SAF values. This epistemic uncertainty is further modified to account for model error, as discussed below.

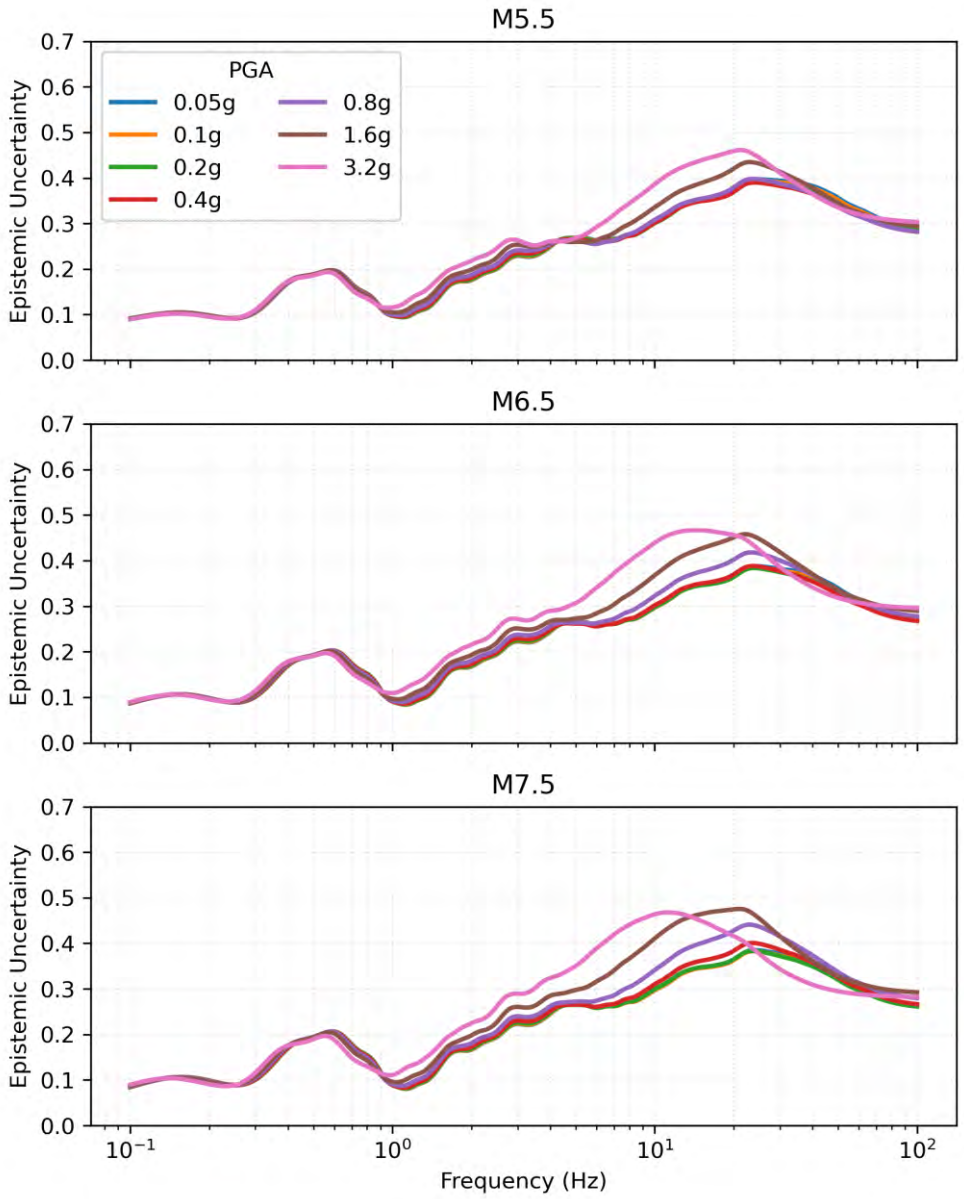

Figure 9-114. Epistemic uncertainty (σ_{ep}) vs frequency for three magnitudes (5.5, 6.5 and 7.5) and seven intensities (0.05-3.2g).

The GMM TI Team selected two approaches to incorporating model error in the SAF from site response analyses (Section 9.4.5). For Alternative 1, model error (σ_{ME}) is added as an additional uncertainty component such that it is combined with the epistemic uncertainty associated with the logic-tree ($\sigma_{ep,LT}$). This alternative assumes that the model error is uncorrelated from all other sources of epistemic uncertainty, and thus the variances are summed to represent the total epistemic uncertainty in the SAF ($\sigma_{ep,\,total}$) using:

9-66

$$\sigma_{ep,\,total} = \sqrt{\sigma_{ep,LT}^2 + \sigma_{ME}^2}$$

For Alternative 2, model error is used as the minimum epistemic uncertainty in the SAF. This assumes that the model error cannot be separated from the parametric uncertainties in site

response and is only considered when the parametric uncertainty is too small. Alternative 2 has been applied in several recent projects (Thyspunt NSP, Hanford PSHA, Spain SL3, Idaho National Lab). Thus, for Alternative 2, $\sigma_{ep,\,total}$ is taken as σ_{ME} if $\sigma_{ep,LT}$ is less than σ_{ME}

The GMM TI Team ultimately adopted a constant period-independent value of 0.25 to represent model error and gave equal weights (0.5) to Alternatives 1 and 2 to incorporate the model error (Section 9.4.5). Figure 9-115 and Figure 9-116 show the expanded, resampled SAF branches using Alternative 1 and Alternative 2, respectively, for the **M** 6.5, 0.4 g input motion. Alternative 1 increases the spread in the SAF values at all frequencies, whereas Alternative 2 increases the spread of SAF values only at frequencies where the epistemic uncertainty in SAF due to the logic-tree alone is less than the model error (0.25). For the analyses performed, this typically occurs at oscillator frequencies less than about 4 Hz.

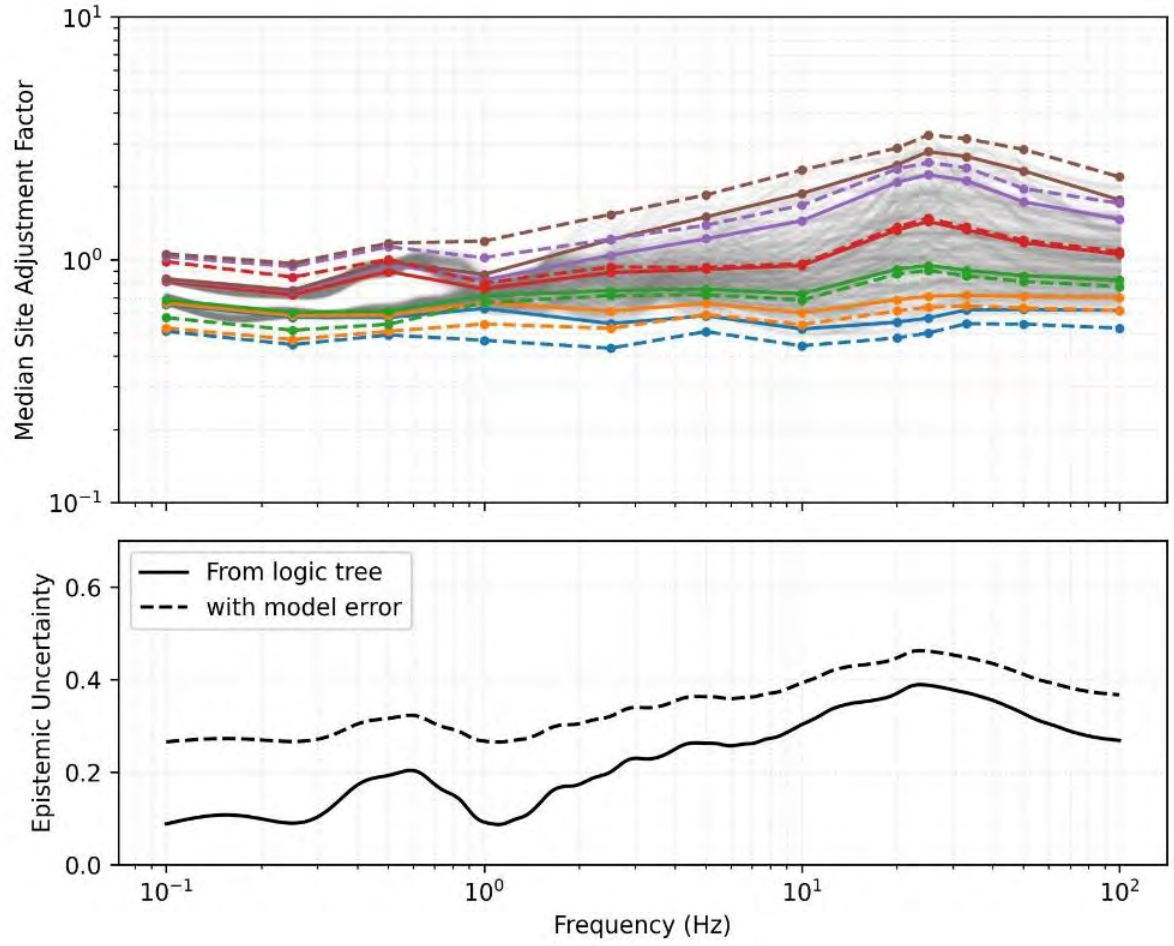

Figure 9-115. SAF values for each terminal branch of the logic-tree using the M 6.5, 0.4 g input motion (thin grey lines), resampled SAF values (bold, solid, coloured lines) using a 6-point distribution, expanded distribution using Alternative 1 to incorporate model error (bold, dashed, coloured lines), and the weighted epistemic uncertainty per the logic-tree alone (bold, solid, black line) and including model error (bold, dashed, black line) plotted against frequency.

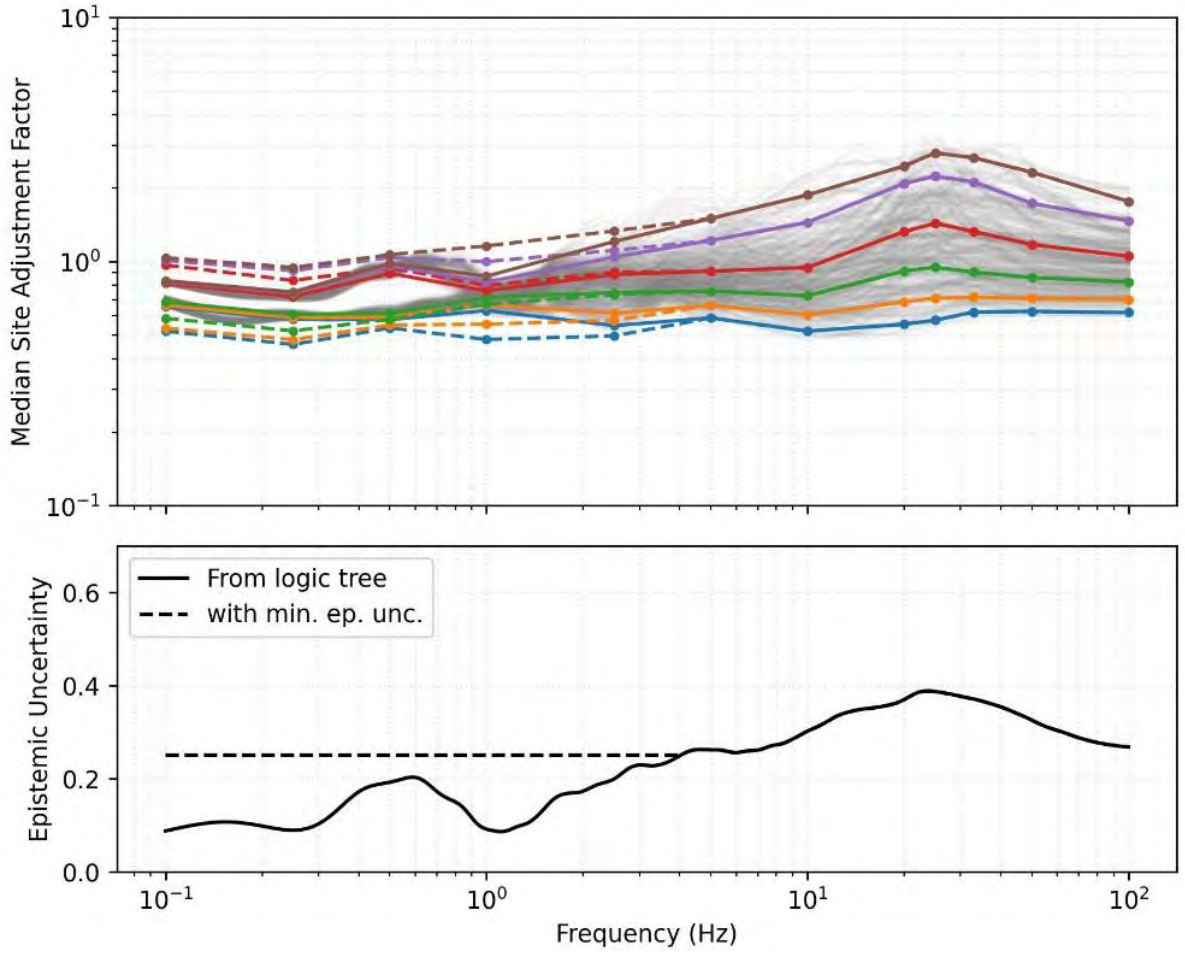

Figure 9-116. SAF values for each terminal branch of the logic-tree using the M 6.5, 0.4 g input motion (thin grey lines), resampled SAF values (bold, solid, coloured lines) using a 6-point distribution, expanded distribution using Alternative 2 to incorporate model error (bold, dashed, coloured lines), and the weighted epistemic uncertainty per the logic-tree alone (bold, solid, black line) and including model error (bold, dashed, black line) plotted against frequency.

9.4.9.3 Final models for site amplification and aleatory variability

Figure 9-117 and Figure 9-118 show the final SAF values plotted as a function of the reference spectral acceleration and earthquake magnitude after applying model error using Alternatives 1 and 2, respectively. These plots represent the final site amplification models incorporated into the hazard calculations. This includes 12 final branches of SAF values (i.e. six re-sampled branches and two alternatives to incorporate model error) and their associated weights (i.e. Table 9-16 for the six branches and 0.5 each for Alternatives 1 and 2) for each combination of magnitude, intensity, and oscillator frequency. This was provided to the hazard analyst team in the form of tables.

The SAF remain relatively constant with increasing reference intensity for lower frequencies (i.e. less than 2.5 Hz) and show a reduction with increasing intensity for higher frequencies. This nonlinearity is most pronounced for frequencies between 10 and 25 Hz. Additionally, the nonlinearity is strongest for the **M** 7.5 scenario.

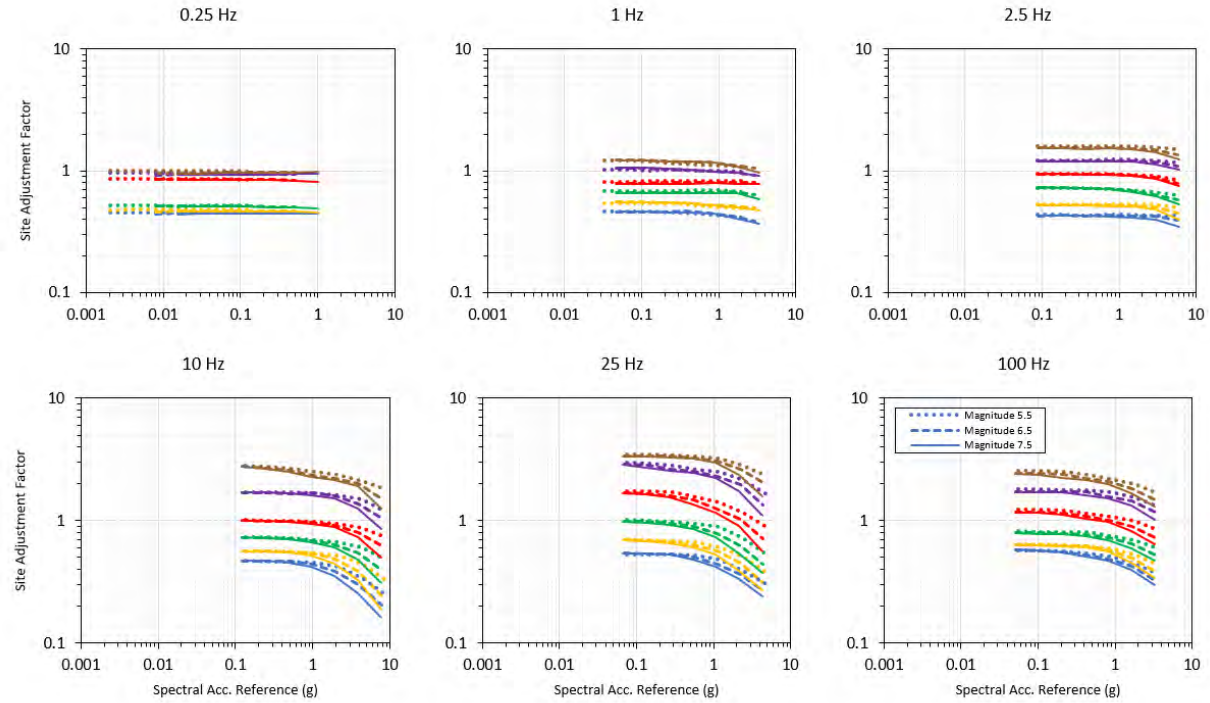

Figure 9-117. Resampled SAF values using a 6-point distribution and expanded using Alternative 1 to incorporate model error plotted against the reference spectral acceleration.

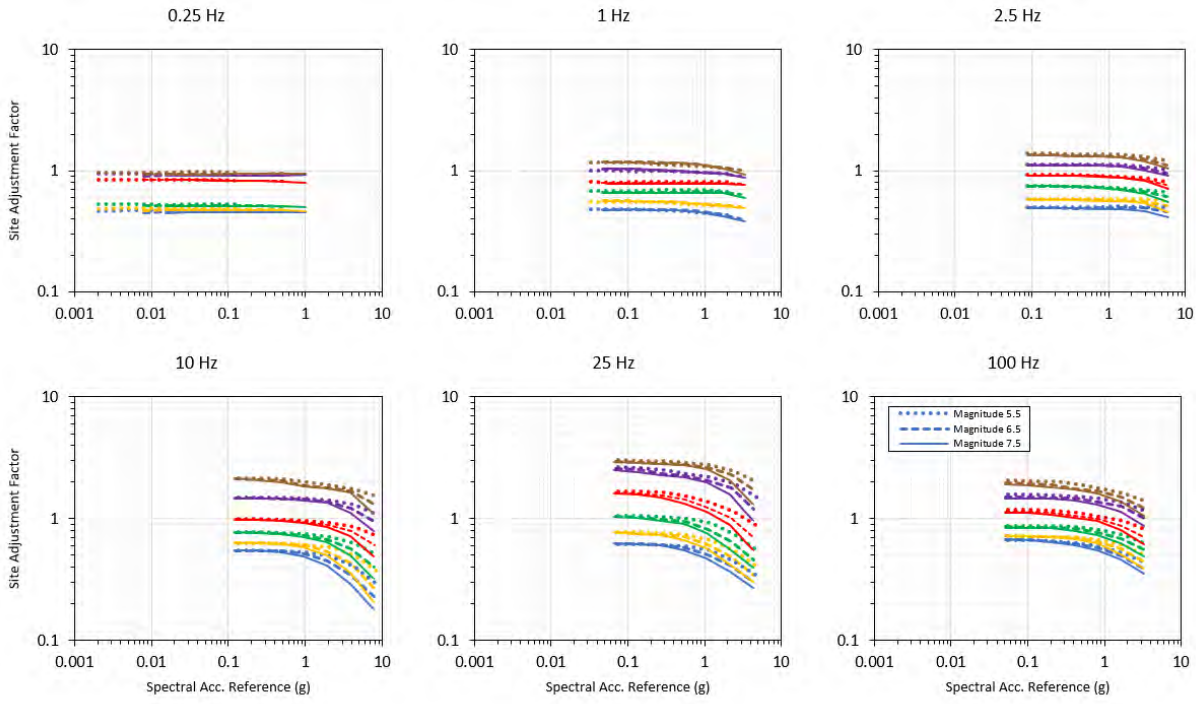

Figure 9-118. Resampled SAF values using a 6-point distribution and expanded using Alternative 2 to incorporate model error plotted against the reference spectral acceleration.

In addition to providing the final 12 branches of SAF values, the final SAF model includes an estimate of the aleatory variability, σ_{lnSAF} to include in the hazard calculations. In accordance with the recommendations of Rodriguez-Marek et al. (2021), the GMM TI Team assumed that the low intensity (i.e. linear elastic) σ_{lnSAF} is captured by the single-station sigma, σ_{ss}, and therefore only the non-linear σ_{lnSAF} is necessary to incorporate into the hazard calculations. This is summarized by the following equation:

9-67

$$\sigma_{lnSAF,\,NL} = \sqrt{\sigma_{lnSAF}^2 - \sigma_{lnSAF,lin}^2}$$

where $\sigma_{lnSAF,\,lin}$ and $\sigma_{lnSAF,\,NL}$ are the linear and nonlinear components, respectively, of the total aleatory variability, σ_{lnSAF}. The distinction between the linear and nonlinear components is typically made based on judgment after plotting σ_{lnSAF} against the reference spectral acceleration (Sa_{ref}) for each oscillator frequency of interest. For each frequency, a threshold value of Sa_{ref} is identified below which σ_{lnSAF} is a constant and this σ_{lnSAF} is taken as $\sigma_{lnSAF,lin}$. Above the Sa_{ref} threshold, each σ_{lnSAF} is converted to $\sigma_{lnSAF,NL}$ using Equation 967. Figure 9-119 shows that there is almost no variation in σ_{lnSAF} as Sa_{ref} increases, regardless of the oscillator frequency. This is likely due to the limited nonlinearity of the site because of high V_S values throughout the profile. Therefore, the TI Team concluded that there was no nonlinear component of aleatory variability to include in the hazard calculations (i.e. $\sigma_{lnSAF,NL}$ = 0).

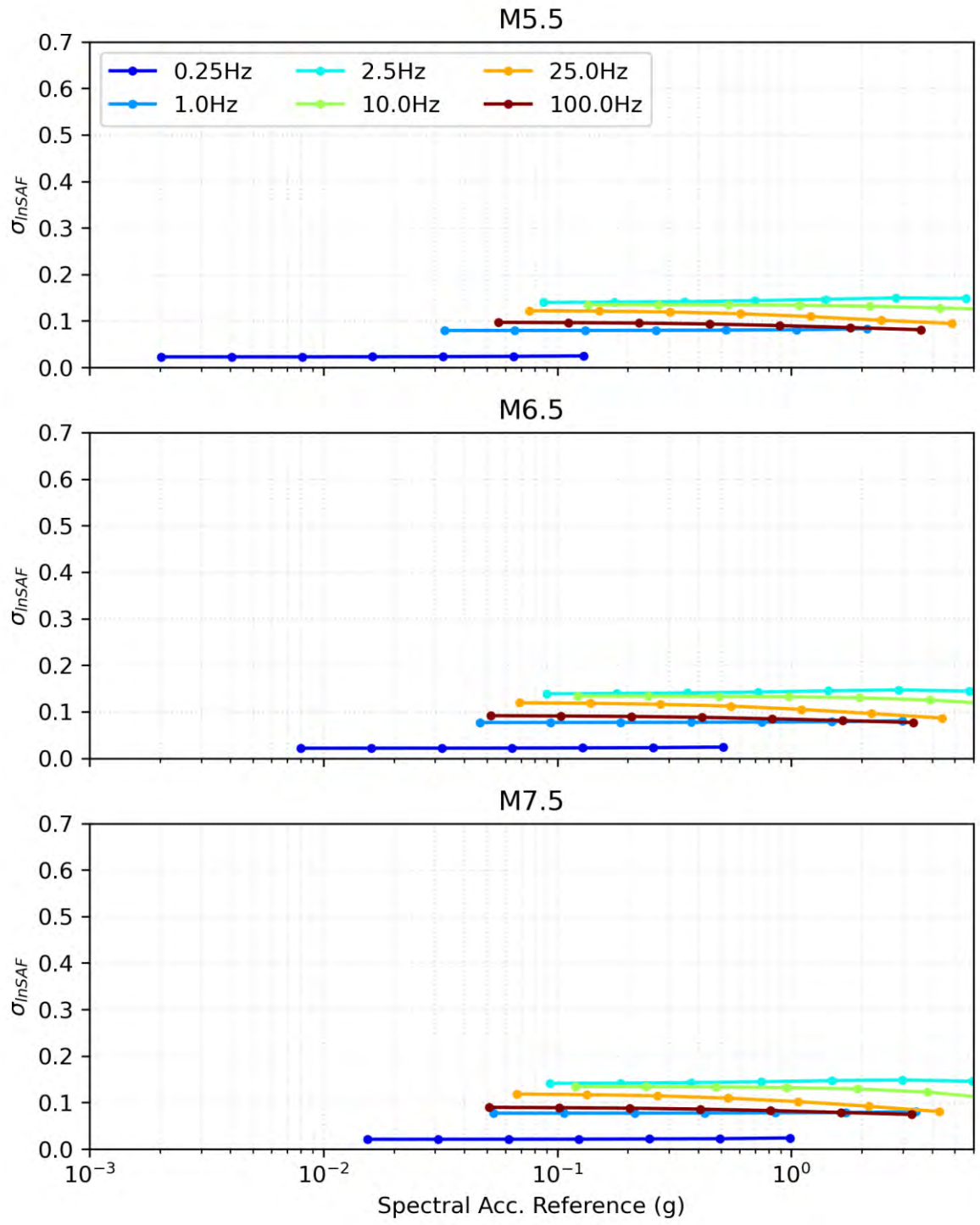

Figure 9-119. Aleatory variability of SAF ($\sigma_{\ln(SAF)}$) for M 6.5 input motions and seven intensity levels plotted against spectral acceleration of the reference conditions (Sa_{ref}).

9.5 REFERENCES

Abrahamson, N.A. (2022). Uses of Intensity Data to Constrain GMMs. Workshop 2, SSHAC EL2 Duynefontyn Nuclear Power Plant.

Abrahamson, N.A. and Silva, W.J. (2008). Summary of the Abrahamson & Silva NGA Ground Motion Relations. Earthquake Spectra 24(1). 67-97.

Abrahamson, N.A. and Silva. W.J. (1997). Empirical Response Spectral Attenuation Relations for Shallow Crustal Earthquakes. Seismological Research Letters 68. 94-127.

Abrahamson, N.A.; Silva, W.J. and Kamai, R. (2014). Summary of the ASK14 Ground Motion Relation for Active Crustal Regions. Earthquake Spectra 30(3). 1025-1055.

Aki, K. (1967). Scaling Law of Seismic Spectrum. Journal of Geophysical Research 72(4). 1217-1231.

Al Atik, L. (2015). NGA-East: Ground Motion Standard Deviation Models for Central and Eastern North America. PEER Report 2015/09. Pacific Earthquake Engineering Research Center, University of California, Berkeley, California, USA.

Al Atik, L. and Youngs, R.R. (2014). Epistemic Uncertainty for NGA-West2 Models. Earthquake Spectra 30(3). 1301-1318.

Al Atik, L. and Abrahamson, N.A. (2021). A Methodology for the Development of 1D Reference VS Profiles Compatible with Ground-Motion Prediction Equations: Application to NGA-West2 GMPEs. Bulletin of the Seismological Society of America 111(4). 1765-1783.

Anderson, J.G. and Brune, J.N. (1999). Probabilistic Seismic Hazard Analysis without the Ergodic Assumption. Seismological Research Letters 70. 19-28.

Anderson, J.G. and Hough, S.E. (1984). A Model for the Shape of the Fourier Amplitude Spectrum of Acceleration at High Frequencies. Bulletin of the Seismological Society of America 74. 1969-1993.

Atkinson, G.M. (2008). Ground-Motion Prediction Equations for Eastern North America from a Referenced Empirical Approach: Implications for Epistemic Uncertainty. Bulletin of the Seismological Society of America 98(3). 1304-1318.

Atkinson, G.M. (2006). Single-Station Sigma. Bulletin of the Seismological Society of America 96(2). 446-455.

Atkinson, G.M.; Bommer, J.J.; Abrahamson, N.A. (2014). Alternative Approaches to Modeling Epistemic Uncertainty in Ground Motions in Probabilistic Seismic-Hazard Analysis. Seismological Research Letters 85(6) 1141-1144.

Bahrampouri, M. and Rodriguez-Marek, A. (2023). One-Dimensional Site Response Analysis: Model Error Estimation. Bulletin of the Seismological Society of America 113(1.). 401-416.

Baker, J.W.; Bradley, B.A. and Stafford, P.J. (2021). Seismic Hazard and Risk Analysis. Cambridge University Press.

Bommer, J.J. (2022). Earthquake Hazard and Risk Analysis for Natural and Induced Seismicity: Towards Objective Assessments in the Face of Uncertainty. Bulletin of Earthquake Engineering 20. 2825-3069.

Bommer, J.J.; Douglas, J.; Scherbaum, F.; Cotton, F.; Bungum, H. and Fäh, D. (2010). On the Selection of Ground-Motion Prediction Equations for Seismic Hazard Analysis. Seismological Research Letters 81(5). 794-801.

Bommer, J.J.; Coppersmith, K.J.; Coppersmith, R.T.; Hanson, K.L.; Mangongolo, A.; Neveling, J.; Rathje, E.M.; Rodriguez-Marek, A.; Scherbaum, F.; Shelembe, R.; Stafford, P.J. and Strasser, F.O. (2015). A SSHAC Level 3 Probabilistic Seismic Hazard Analysis for a New-Build Nuclear Site in South Africa. Earthquake Spectra 31(2). 661-698.

Bommer, J.J. and Stafford, P.J. (2020). Selecting Ground-Motion Models for Site-Specific PSHA: Adaptability Versus Applicability. Bulletin of the Seismological Society of America 110(6). 2801-2815.

Boore, D.M. (2003). Simulation of Ground Motion Using the Stochastic Method. Pure and Applied Geophysics 160. 635-676.

Boore, D.M. (2012). Updated Determination of Stress Parameters for Nine Well-Recorded Earthquakes in Eastern North America. Seismological Research Letters 83(1). 190-199.

Boore, D.M.; Stewart, J.P.; Seyhan, E. and Atkinson G.M. (2014). -NGA-West2 Equations for Predicting PGA, PGV, and 5% Damped PSA for Shallow Crustal Earthquakes. Earthquake Spectra 30(3). 1057-1085.

Boore, D.M. and Thompson, E.M. (2014). Path Durations for Use in the Stochastic-Method Simulation of Ground Motions. Bulletin of the Seismological Society of America 104(5). 2541-2552.

Boore, D.M. and Thompson, E.M. (2015). Revisions to Some Parameters Used in Stochastic-Method Simulations of Ground Motions. Bulletin of the Seismological Society of America 105(2A). 1029-1041.

Boore, D.M.; Stewart, J.P.; Seyhan, E. and Atkinson, G.M. (2014). NGA-West2 Equations for Predicting PGA, PGV and 5% Damped PSA for Shallow Crustal Earthquakes. Earthquake Spectra 30. 1057-1085.

Boore, D.M.; Youngs, R.R.; Kottke, A.R.; Bommer, J.J.; Darragh, R.; Silva, W.J.; Stafford, P.J.; Al Atik, L.; Rodriguez-Marek, A. and Kaklamanos, J. (2022). Construction of a Ground-Motion Logic-Tree through Host-to-Target Region Adjustments Applied to an Adaptable Ground-Motion Prediction Model. Bulletin of the Seismological Society of America 112(6). 3063-3080.

Bora, S.; Scherbaum, F.; Kuehn, N. and Stafford, P.J. (2016). On the Relationship between Fourier and Response Spectra: Implications for the Adjustment of Empirical Ground-Motion Prediction Equations (GMPEs). Bulletin of the Seismological Society of America 106(3). 1235-1253.

Brune, J.N. (1970). Tectonic Stress and the Spectra of Seismic Shear Waves from Earthquakes. Journal of Geophysical Research 75(26). 4997-5009.

Brune, J.N. (1971). Correction. Journal of Geophysical Research 76(20). 5002.

Butcher, A.; Luckett, R.; Kendall, M.J. and Baptie, B. (2020). Seismic Magnitudes, Corner Frequencies, and Microseismicity: Using Ambient Noise to Correct for High-Frequency Attenuation. Bulletin of the Seismological Society of America 110. 1260-1275.

Campbell, K.W. and Bozorgnia, Y. (2014). NGA-West2 ground motion model for the average horizontal components of PGA, PGV, and 5% damped linear acceleration response spectra. Earthquake Spectra 30(3). 1087-1115.

Campbell, K.W. (2003). Prediction of Strong Ground Motion Using the Hybrid Empirical Method and Its Use in the Development of Ground-Motion (Attenuation) Relations in Eastern North America. Bulletin of the Seismological Society of America 95(3). 1012-1033.

Cartwright, D.E. and Longuet-Higgins, M.S. (1956). The Statistical Distribution of the Maxima of a Random Function. Proceedings of the Royal Society of London 237. 212-232.

Chiou, B.S.J. and Youngs, R.R. (2008). An NGA Model for the Average Horizontal Component of Peak Ground Motion and Response Spectra. Earthquake Spectra 24(1). 173-215.

Chiou, B.S.J. and Youngs, R.R. (2014). Update of the Chiou and Youngs NGA Model for the Average Horizontal Component of Peak Ground Motion and Response Spectra. Earthquake Spectra 30(3), 1117-1153.

Choi, W. K. (2008). Dynamic Properties of Ash-Flow Tuffs. PhD Dissertation, The University of Texas at Austin.

Coppersmith, K.; Bommer, J.; Hanson, K.; Coppersmith, R.; Unruh, J.; Wolf, L.; Youngs, R.; Al Atik, L.; Rodriguez-Marek, A. and Toro, G. (2014). Hanford Sitewide Probabilistic Seismic Hazard Analysis. Report prepared for the US Department of Energy Under Contract DE-AC06076RL01830 and Energy Northwest, Pacific National Lab Report PNNL-23361.

Cotton, F.; Scherbaum, F.; Bommer, J.J. and Bungum, H. (2006). Criteria for Selecting and Adjusting Ground-Motion Models for Specific Target Applications: Applications to Central Europe and Rock Sites. Journal of Seismology 10(2). 137-156.

Cox, B. (2022a). What We Know So Far About VS and Its Uncertainty at the Duynefontyn Site. Workshop 2, SSHAC EL2 Duynefontyn Nuclear Power Plant.

Cox, B. (2022b). What We Know So Far About VS and Its Uncertainty at the Duynefontyn Site - Updated 4 August 2022. Presentation at GMM Working Meeting, SSHAC EL2 Duynefontyn Nuclear Power Plant.

Cox, B.R.; Abbas, A.; Mulabisana, T.; Jele, V.; Mantsha, R.; Sethobya, M.; Sobothonma, S. and Nxantsiya, Z. (2024). Deep Shear-Wave Velocity Profiling Using MASW and MAM Surface Wave Methods: Duynefontyn Project, South Africa. CGS Report 2023-0203 (Rev.0). Council for Geoscience, Pretoria, South Africa.

De la Torre, C.A. and Bradley, B.A. 2023. 2D Site Response at the Proposed Duynefontyn Nuclear Power Plant Site: The Influence of Steeply Inclined Interbedded Rock Layers. Bradley Seismics.

Der Kiureghian, A. (1980). Structural Response to Stationary Excitation. Journal of the Engineering Mechanics Division: ASCE 106(6). 1195-1213.

Dikmen, S.U.; Pinar, A. and Edincliler, A. (2016). Near-Surface Attenuation Using Traffic-Induced Seismic Noise at a Downhole Array. Journal of Seismology 20. 375–384.

Douglas, J. and Boore, D.M. (2011). High-Frequency Filtering of Strong-Motion Records. Bulletin of Earthquake Engineering 9(2). 395-409.

Edwards, B. (2022). Inversion of Ground Motion Data for Seismological Source-, Path- and site-effects, with Example Application to the Groningen Gas Field, Netherlands. Workshop 2, SSHAC EL2 Duynefontyn Nuclear Power Plant.

Edwards, B. (2023). Final Report on Inversion of Ground-Motion Data to Determine Target Source and Path Parameters for the Development of the Ground Motion Model for Duynefontyn, South Africa. Report ISEIS-CGS-001.0.

Electric Power Research Institute (EPRI) (1993). Guidelines for Determining Design Basis Ground Motion, Final Report. Electric Power Research Institute, Palo Alto, California, USA.

Fukushima, Y. (1996). Scaling Relations for Strong Ground Motion Prediction Models with M^2 Terms. Bulletin of the Seismological Society of America 86(2). 329-336.

GeoPentech (2015). Southwestern United States Ground Motion Characterisation SSHAC Level 3. Technical Report (Rev. 2).

Grünthal, G. and Wahlström, R. (2003). An M_w Based Earthquake Catalogue for Central, Northern and Northwestern Europe Using a Hierarchy of Magnitude Conversions. Journal of Seismology 7. 507-531.

Hough, S. E., and J. G. Anderson (1988). High-frequency spectra observed at Anza, California: Implications of Q structure, Bulletin of the Seismological Society of America 78, 692–707.

Jeon, S. Y. (2008). Dynamic and Cyclic Properties in Shear of Tuff Specimens from Yucca Mountain, Nevada. PhD Dissertation, The University of Texas at Austin.

Keefer, D.L. and Bodily, S.E. (1983). Three-Point Approximations for Continuous Random Variables. Management Science 29(5). 595-609.

Kottke, A.R. and Rathje E.M. (2008). Technical Manual for Strata. Report 2008-10. Pacific Earthquake Engineering Research Center, University of California, Berkeley, California, USA.

Gablonsky, J.M., and Kelley, C.TA locally-biased form of the DIRECT algorithm. Journal of Global Optimisation 21. 27-37.

Idriss, I.M. (2014). An NGA-West2 empirical model for estimating the horizontal spectral values generated by shallow crustal earthquakes. Earthquake Spectra 30(3). 1155-1177.

Johnson, S.G. (2007). The NLopt nonlinear-optimisation package. https://github.com/stevengj/nlopt

Kottke, A.R. (2022). pystrata. Github. https://github.com/arkottke/pystrata.

Kraft, D. (1994). Algorithm 733: TOMP--Fortran modules for optimal control calculations. ACM Transactions on Mathematical Software 20. 262-281.

Ktenidou, (2022). Considerations Relating to the Estimation of Kappa from Seismic Data. Workshop 2, SSHAC EL2 Duynefontyn Nuclear Power Plant.

Liu, L. and Pezeshk, S. (1999). An Improvement on the Estimation of Pseudoresponse Spectral Velocity Using RVT Method. Bulletin of the Seismological Society of America 89. 1384-1389.

Maré, L.P. (2022). Acoustic Velocity Analyses of Tygerberg Formation Sediments in Support of Probabilistic Seismic Hazard Analyses for Duynefontyn. CGS Report 2022-0151. Council for Geoscience, Pretoria, South Africa.

McHutchon, M.R.; de Beer, C.H.; van Zyl, F.W. and Cawthra, H.C. (2020). What the Marine Geology of Table Bay, South Africa Can Inform About the Western Saldania Belt, Geological Evolution and Sedimentary Dynamics of the Region. Journal of African Earth Sciences 162. 103699.

Miller, A.C. and T.R. Rice (1983). Discrete Approximations of Probability Distributions. Management Science 29(3). 352-362.

NCREE (2021). Development of GMRS and FIRS for Nuclear Power Plants in Taiwan. National Center for Research on Earthquake Engineering, Taipei, Taiwan.

Quiros, D. and Sloan, A. (2023). Estimation of Kappa Values in the Coastal Plain Between Cape Town and Saldanha Bay. CGS Report RFQ SAS060. Council for Geoscience, Pretoria, South Africa.

Rathje, E.M., Kottke, A.R. and Trent, W.L. 2010. The Influence of Input Motion and Site Property Uncertainties on Seismic Site Response Analyses. Journal of Geotechnical and Geoenvironmental Engineering, ASCE, 136(4), 607-619.

Rathje, E.M. (2022). Host-to-Target Site Response Methodologies. Workshop 2, SSHAC EL2 Duynefontyn Nuclear Power Plant.

Revels, J., Lubin, M. and Papamarkou, TForward-mode automatic differentiation in Julia. https://arxiv.org/abs/1607.07892

Rodriguez-Marek, A., Rathje, E., Ake, J., Munson, C., Stovall, S., Weaver, T., Ulmer, K., and Juckett, M. (2021). Documentation Report for SSHAC Level 2: Site Response. US Nuclear Regulatory Commission, RIL 2021-15.

Scasserra, G.; Stewart, J.P.; Bazzurro, P.; Lanzo, G. and Mollaioli, F. (2009). A Comparison of NGA Ground-Motion Prediction Equations to Italian Data. Bulletin of the Seismological Society of America 99(5). 2961-2978.

Stafford, P.JStochasticGroundMotionSimulation.jl. https://github.com/pstafford/StochasticGroundMotionSimulation.jl

Stafford, P.J. (2022). A Model for the Distribution of Response Spectral Ordinates from New Zealand Crustal Earthquakes Based Upon Adjustments to the Chiou and Youngs (2014) Response Spectral Model. GNS Science Report 2022/15.

Stafford, P.J. (2021). Risk Oriented Earthquake Hazard Assessment: Influence of Spatial Discretisation and Non-ergodic Ground-motion Models. Advances in Assessment and Modeling of Earthquake Loss. 169-187.

Stafford, P.J. (2015). Variability and Uncertainty in Empirical Ground-Motion Prediction for Probabilistic Hazard and Risk Analyses. In: Ansal, A. (Ed.). Perspectives on European Earthquake Engineering and Seismology 2. Springer Open. Chapter 4. 97-128.

Stafford, P.J. (2014). Crossed and Nested Mixed-Effects Approaches for Enhanced Model Development and Removal of the Ergodic Assumption in Empirical Ground-Motion Models. Bulletin of the Seismological Society of America 104(2). 702-719.

Stafford, P.J.; Strasser, F.O. and Bommer, J.J. (2008). An Evaluation of the Applicability of the NGA Models to Ground-Motion Prediction in the Euro-Mediterranean Region. Bulletin of Earthquake Engineering 6(2). 149-177.

Stafford, P.J.; Sgobba, S. and Marano, G.C. (2009). An Energy-Based Envelope Function for the Stochastic Simulation of Earthquake Accelerograms. Soil Dynamics and Earthquake Engineering 29(7). 1123-1133.

Stafford, P.J.; Rodriguez-Marek, A.; Edwards, B.; Kruiver, P.P. and Bommer, J.J. (2017). Scenario Dependence of Linear Site-Effect Factors for Short-Period Response Spectral Ordinates. Bulletin of the Seismological Society of America 107(6). 2859-2872.

Stafford, P.J.; Boore, D.M.; Youngs, R.R. and Bommer, J.J. (2022). Host-Region Parameters for an Adjustable Model for Crustal Earthquakes to Facilitate the Implementation of the Backbone Approach to Building Ground-Motion Logic-Trees in Probabilistic Seismic Hazard Analysis. Earthquake Spectra 38(2). 917-949.

Stafford, P.J. and Bradley, B.A. (2022). Correlation of Epistemic Uncertainty: Effective Standard Deviation to Use Within Backbone Models (Unpublished White Paper).

Stewart J, Afshari K, Hashash Y. Guidelines for performing hazard-consistent one-dimensional ground response analysis for ground motion prediction. Berkeley, California, Pacific Earthquake Engineering Research Center; 2014.

Stewart, J.P. and Afshari, K. (2021). Epistemic Uncertainty in Site Response as Derived from One-Dimensional Ground Response Analyses. Journal of Geotechnical and Geoenvironmental Engineering 147(1). 04020146.

Stokoe, I.I.; Kenneth, H.; Graves, J.C.; Graves, M.T.; Choi, W.K. and Menq, F.Y. (2003). Dynamic Laboratory Tests: Unweathered and Weathered Shale Proposed Site of Building 9720-82 Y-12 National Security Complex, Oak Ridge, Tennessee (No. Y1997—0056-0799-0011). Oak Ridge Y-12 Plant (Y-12). Oak Ridge, Tennessee, USA.

Teague, D.P.; Cox, B.R. and Rathje, E.R. (2018). Measured vs. Predicted Site Response at the Garner Valley Downhole Array Considering Shear Wave Velocity Uncertainty from Borehole and Surface Wave Methods. Soil Dynamics and Earthquake Engineering 113(10). 339-355.

Toro, G.R. (1995). Probabilistic Models of Site Velocity Profiles for Generic and Site-Specific Ground-Motion Amplification Studies. Technical Report 779574. For Brookhaven National Laboratory, Upton New York.

Ulmer, K.J.; Rodriguez-Marek, A. and Green, R.A. (2021). Accounting for Epistemic Uncertainty in Site Effects in Probabilistic Seismic Hazard Analysis. Bulletin of the Seismological Society of America 111(4). 2005-2020.

United States Nuclear Regulatory Commission (USNRC) (2001). Technical Basis for Revision of Regulatory Guidance on Design Ground Motions: Hazard- and Risk-Consistent Ground Motion Spectra Guidelines. NUREG/CR-6728. US Nuclear Regulatory Commission, Office of Nuclear Regulatory Research, Washington DC, USA.

United States Nuclear Regulatory Commission (USNRC) (2007). A Performance-Based Approach to Define the Site-Specific Earthquake Ground Motion. Regulatory Guide 1.208. US Nuclear Regulatory Commission, Washington DC, USA.

United States Nuclear Regulatory Commission (USNRC) (2018). Updated Implementation Guidelines for SSHAC Hazard Studies. NUREG-2213. US Nuclear Regulatory Commission, Office of Nuclear Regulatory Research, Washington DC, USA.

Vanmarcke, E.H. (1975). On the Distribution of the First-Passage Time for Normal Stationary Random Processes. Journal of Applied Mechanics 42(1). 215-220.

Wald, David and Allen, Trevor. (2007). Topographic Slope as a Proxy for Seismic Site Conditions and Amplification. Bulletin of the Seismological Society of America. 97. 1379-1395. 10.1785/0120060267.

Williams, T. and Abrahamson, N. (2021). Site-Response Analysis Using the Shear-Wave Velocity Profile Correction Approach. Bulletin of the Seismological Society of America 111(4). 1989-2004.

Yenier, E. and Atkinson, G.M. (2015). An Equivalent Point-Source Model for Stochastic Simulation of Earthquake Ground Motions in California. Bulletin of the Seismological Society of America 105(3). 1435-1455.

CHAPTER 10: HAZARD RESULTS

10. HAZARD RESULTS

10.1 INTRODUCTION

This chapter presents the seismic hazard results for the new build site at Duynefontyn and the Koeberg Nuclear Power Station (KNPS) in accordance with the requirements specified in Chapter 1. Section 10.2 provides an overview of the methods used to perform the hazard calculations for both the LTO license for KNPS and the new build site at Duynefontyn, including a summary of the verification performed to check the implementation of the seismic hazard model. The subsequent sections present the hazard calculation results in various formats, starting with the overall mean and fractile hazard curves in Sections 10.3.1.1 and 10.4.1.1 (for the new build site at Duynefontyn and KNPS respectively). Next, Sections 10.3.1.2 and 10.4.1.2 present the contributions of individual seismic sources to the total mean hazard and the contribution of different magnitude-distance scenarios. Sections 10.3.1.4 and 10.4.1.4 present the uniform hazard response spectra (UHRS) ranging from 0.5 Hz to 100 Hz for the new build site at Duynefontyn and KNPS, respectively. Sections 10.3.1.5 and 10.4.1.5 present the design response spectra (DRS) for each site (per ASCE/SEI 43-19). Finally, Sections 0 and 10.4.2 present the hazard sensitivities performed for both the SSM and GMM.

10.2 HAZARD ANALYSIS METHODOLOGY

This section presents the methodology for the PSHA, including details regarding the specific software used, the configuration of individual runs and an overview of the verification methods used to validate the implementation of the hazard model. The PSHA for this study generally follows the approach first developed by Cornell (1968) with the inclusion of parameters for randomisation and the consideration of epistemic uncertainty.

10.2.1 Probabilistic Seismic Hazard Calculation

A Poisson process is used to compute how often a specified level of ground-motion will be exceeded at a site. The PSHA computes the annual number of events that produce a ground-motion parameter (Z), that exceeds a specified level (*z*). This number of events per year (ν) is also called the "annual frequency of exceedance", the inverse of which is called the "return period". See Section 1.2.2 for a more complete description of PSHA.

The calculation of ν considers the rate of earthquakes of magnitudes 5 or greater, the rupture dimension of the earthquakes, the distance of the site relative to the earthquake, and the attenuation of the ground-motion from the earthquake rupture to the site. The annual rate of exceedance of *z*, from a source, *i*, for a given earthquake that occurred on the source, *i*, is given by the equation:

10-1

$$\nu_i(Z > z) = N_i(E_i)P(Z > z|E_i)$$

where, E_i is the given earthquake from source *i*, with a known magnitude and distance and $N_i(E_i)$ is the annual rate of the given earthquake per year from source *i.*

The PSHA calculations are performed using the computer program HAZ45.3 developed by Dr Norman Abrahamson (Abrahamson, 2017) and models added by Slate Geotechnical Consultants. This program was validated as part of the Pacific Earthquake Engineering Research (PEER) centre PSHA Code Verification Project (Hale et al., 2018).

The logic tree components of the SSM and GMM are summarised in the Hazard Input Document (HID), which is the vehicle for transmitting the quantitative model to the hazard analysts for preliminary and final PSHA calculations. The HID is presented in Appendix D of this report. The hazard calculations, including adjustments made by Slate Geotechnical Consultants to the software, were validated and verified through the process outlined in the Verification and Validation Plan (VVP) (Wooddell and Watson-Lamprey, 2022) and the results of this Verification and Validation (V&V) are presented in the V&V report (Largent et al., In Prep.).

10.2.2 Virtual Rupture Generator

The ruptures used for the host zone (Saldania, SDZ) were generated using the Slate virtual rupture generator (VRG). The VRG is a Python-based code which generates virtual ruptures based on zone-specific parameter distributions provided by the SSM TI Team through the HID (Appendix D). The VRG was fully verified and validated through the VRG V&V Report (Largent

et al., 2024). For SDZ, these virtual ruptures were used to calculate the distances used in the GMM: rupture distance (R_{rup}) and Joyner-Boore distance (R_{jb}), the shortest distance from any point on the rupture to the site and the closest distance to the surface projection, respectively. There are three primary stages that the VRG goes through: (1) determining the overall quantity and magnitude range of the ruptures, (2) determining the epicentre location for each rupture, and (3) determining the geometry for each rupture plane. Additional information about the inputs to these stages can be found in Sections 1.3 and 8.2. This process is also depicted in Figure 10-1.

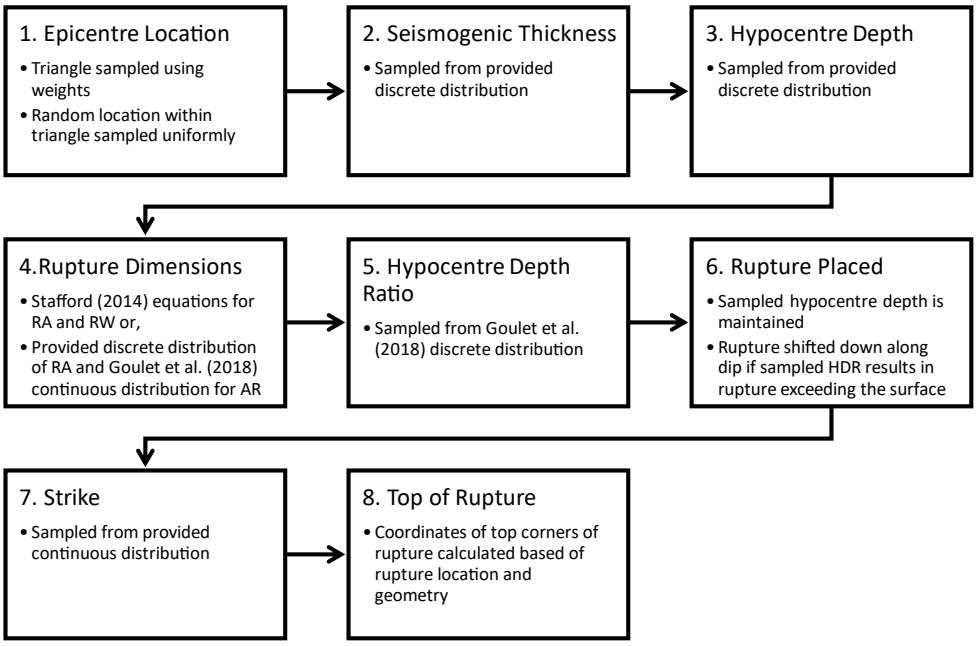

Figure 10-1. Flow chart depicting the stages of the virtual rupture generator.

For each run of the VRG, the first parameters specified are the minimum and maximum magnitudes, the magnitude step/bin size, and the number of ruptures per bin. The VRG establishes the magnitude bins, beginning at the minimum magnitude and working up (one bin size at a time) until the maximum magnitude is reached or exceeded. Each bin is identified by the middle value (e.g., the ruptures in a bin ranging from **M** 5.6 to 5.7 all have **M** 5.65). If the upper value of the highest bin would exceed the specified maximum magnitude, the bin is instead truncated, with the rupture magnitude set to the midpoint of the new truncated bin. Once the number of bins and the magnitudes of the ruptures within them have been determined, an overall list of ruptures is generated for the run by adding the specified quantity of ruptures per bin, starting with the lowest bin, and working upward.

The next two stages, determining epicentre location and rupture geometry, are performed individually for each rupture as the code iterates through the overall list of ruptures. Specifically, the second stage is determining epicentre location, which is not affected by rupture magnitude. Prior to any epicentre locations being sampled, each zone is geometrically triangulated, with the exact method of triangulation depending on the spatial smoothing method (uniform, adaptive kernel, or 100 km kernel gridding).

For uniform smoothing, the zone is triangulated using an ear-clipping approach where a triangle is created using the boundary vertex with the smallest interior angle and the two neighbouring vertices, that vertex is then removed, and the process is repeated iteratively until only three vertices remain and the entire source zone has been triangulated. An example of this type of triangulation is presented in Figure 10-2a. In this case, the weight of each triangle is calculated by normalising the area of that triangle to the total area of the source zone.

With the gridded sources (100 km kernel or adaptive kernel), a repeating pattern of eight right triangles are generated centred around every other grid point in both latitude and longitude. Triangles are only generated where the entire triangle would fall within the source zone, resulting in some neglected space near the zone boundary. So long as the grid is fine relative to the scale of the source zone, this space does not significantly impact results for this site. An example of this type of triangulation is presented in Figure 10-2b. For this case, the weight of the triangle is assigned using the gridded kernel values of the three vertices.

Once a set of weighted triangles has been produced, either through the uniform or gridded process, the triangle containing the epicentre of each rupture is selected randomly, with the probability proportional to the triangles' weighting values. The location of the epicentre within that triangle is then selected randomly using the sampling method described in Osada et al. (2002), which uniformly samples points within a triangle based on the coordinates of its vertices.

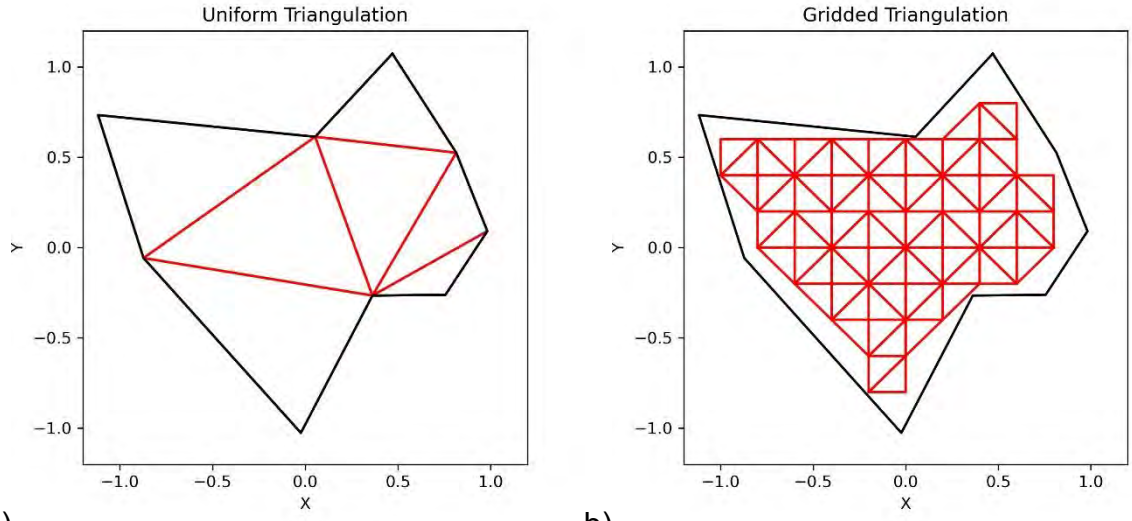

Figure 10-2. Depictions of the triangulation for a) uniform seismicity and b) gridded seismicity.

Once the location of the epicentre has been determined, the third stage of the VRG is to determine the geometry of the rupture plane itself. This involves either importing multiple parameters of the rupture plane as distributions or calculating them within the VRG. The methods for selecting and/or estimating each parameter for the SDZ zone are listed in Table 10-1.

Table 10-1. Virtual Rupture Generator rupture plane parameter.

Parameter	Method
Seismogenic Thickness	Discrete Distribution
Hypocentre Depth	Discrete Distribution
Dip	Discrete Distribution
Rupture Area	Calculated/Discrete Distribution
Aspect Ratio/Rupture Width	Continuous Distribution/Calculated
Hypocentral Depth Ratio	Discrete Distribution
Strike	Continuous Distribution
Along-Strike	Centre of Rupture

The first parameters sampled are the seismogenic thickness (H_{seismo}) and the dip of the rupture plane. Depending on the H_{seismo} value sampled, the hypocentre depth is then sampled from a corresponding distribution. The dimensions of the rupture can then be calculated/sampled depending on the method specified for the run.

The HID specified two methods for determining rupture dimensions. The first method uses the relationships developed by Stafford (2014) to calculate rupture area and rupture width. The relationships are based on the rupture magnitude and provided coefficients which are specific to fault type. The maximum width of the rupture (RW_{max}) is limited by what will fit within the sample seismogenic thickness as shown in Equation 10-2.

10-2

$$RW_{max} = \frac{H_{seismo}}{\sin(\delta)}$$

where, RW_{max} is the maximum rupture width and δ is the sampled dip. The rupture length is then calculated as the ratio of the area and width.

The second method samples magnitude-specific rupture areas (weighted average of multiple methods) presented in the HID, and the aspect ratio is sampled from the fault-type and magnitude dependent distributions described in Section 8.2.6. This aspect ratio is used until the rupture width exceeds the limit described above for the Stafford (2014) method, at which point the rupture plane is expanded laterally along strike to achieve the sampled area.

The desired hypocentral depth ratio for all ruptures is sampled from the appropriate fault-type-specific, as described in Section 8.2.6. The VRG first places the rupture plane relative to the sampled hypocentre depth to achieve the sampled value. If doing so results in a rupture plane that exceeds the ground surface, the plane is shifted downward along the dip until the top of the plane is at the ground surface.

The last sampled parameter is the strike of the rupture plane. This is sampled from the appropriate fault-type dependent, continuous distributions specified in the HID.

Finally, once the location and dimensions of each rupture plane have been determined, the coordinates of the top two corners of the rupture plane are calculated to determine R_{rup} and R_{jb}, which are inputs in the hazard analysis for SDZ.

As part of the interface between the SSM TI Team and the HAT, the probability density functions (PDFs) and cumulative distribution functions (CDFs) of the VRG distances for SDZ were provided to the SSM TI Team. Figure 10-3 shows the PDFs and CDFs for one branch of the host zone. This figure compares the point source distribution (orange) with the VRG distribution (blue), overall showing the VRG brings seismicity closer to the site as it mimics ruptures. Figure 10-3 shows the differences between the two alternative branches for rupture dimension scaling shown in Figure 8-17.

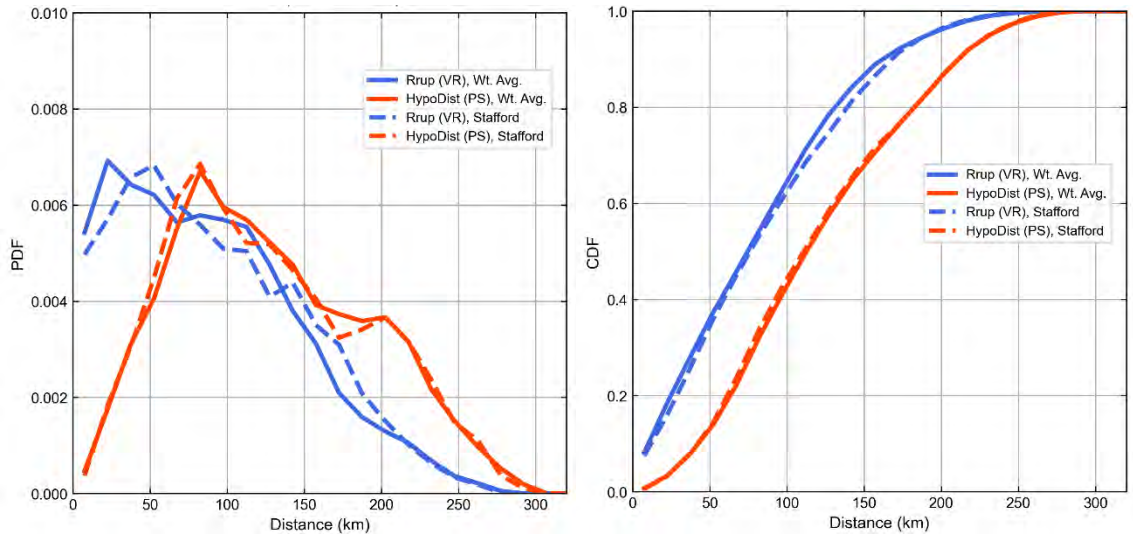

Figure 10-3. Probability density function (left) and cumulative density function (right) for the two alterative branches for rupture dimension scaling shown in Figure 8-17.

10.2.3 Ground-motion model implementation

The GMM TI Team utilised a backbone approach following the guidance provided by Bommer and Stafford (2020). This is described in Section 9.2 of this report and was used to estimate the median (mean in log-space) spectral acceleration value for reference rock conditions (shear wave velocity in the upper 30 meters, V_{S30}, of 760 m/s), as well as the uncertainty about the median. The HAT started with the Chiou and Youngs (2014) GMPE (CY14), and applied the modifications provided by the GMM TI Team. The Haz45.3 implementation was then validated by comparing to the GMM TI Team's implementation in the Julia code (Stafford, 2023).

The aleatory variability model by Al Atik (2015) was used for both single station within-event variability (ϕ_{SS}) and between-event variability (τ). Each model has a central, high, and low branch (representing median, 95th, and 5th percentile), thus this results in a total of nine aleatory variability models. This aleatory variability model was then used in a mixture model of two equally weighted normal distributions similar to previous SSHAC projects (PNNL, 2014; Geopentech, 2015). Details regarding the aleatory variability model can be found in Section 9.3.

Additional epistemic uncertainty was also included in the hazard calculations, designated as $\sigma_{\mu ln,Sa}$. Three branches were included that varied the epistemic uncertainty through: (1) model-to-model differences from the seven individual models, (2) uncertainty due to near-source saturation, and (3) additional uncertainty. This is described in Section 9.2.5.

10.2.4 Site amplification

Approach 4 from NUREG/CR-6728 (USNRC, 2001), where site response is included in the hazard calculation, was used and as such the total hazard results include the site amplification. The amplification factors implemented into the hazard calculation are discussed in Section 9.4 and summarised in the HID in Appendix D. For each amplification model (12 in total), the amplification factors were selected based on frequency, moment magnitude, and response spectral value for reference rock conditions (V_{S30} of 760 m/s) computed using the unadjusted CY14 GMPE, designated as SA_{CY}. The amplification factors were then linearly interpolated within the hazard code with frequency and SA_{CY} in log-space and moment magnitude in linear-space. The interpolated amplification factor was then applied to the site-specific reference rock response spectral value (from the adjusted CY14 model) in log-space. This was repeated for each frequency, amplification factor model, and site-specific reference rock spectral value computed in the hazard code. The amplification model is described in Section 9.4.9.

10.2.5 Hazard runs

The hazard analyses were performed for ten oscillator frequencies: 100 (PGA[1]), 50, 33, 25, 20, 10, 5, 2.5, 1, and 0.5 Hz and extend from annual frequencies of exceedance (AFEs) of 10^{-2} to 10^{-8}. Each hazard analysis was performed for 16 targeted ground-motion levels, which are consistent for all periods: 0.00001, 0.0025, 0.005, 0.01, 0.025, 0.05, 0.1, 0.2, 0.3, 0.35, 0.45, 0.7, 1, 2, 3, and 12g, with the exception of frequencies of 5, 10, 20, and 25 Hz where an additional analysis at 18g was performed in order to determine the 10^{-8} UHRS. Linear interpolation in log-space was used to obtain the acceleration values at required AFEs. The hazard calculations were then repeated to compute the total mean hazard value at each of the target oscillator periods for AFEs of 10^{-4}, 10^{-5}, and 10^{-6} to obtain the disaggregation at each AFE.

To capture the three epistemic branches for the GMM developed for reference rock conditions, the nine aleatory variability models implemented, and the 12 site adjustment factors (SAFs), a total of 324 input models were used in the hazard analysis. A summary of the 27 models used in the hazard input file at each oscillator frequency for each site amplification model is presented in Table 10-2. The full model list (324 models) used in the hazard input file, with a description of each is presented in Appendix F.

The two sites presented below are adjacent to one another, thus the underlying site properties, source characterisation and path variables are similar. As such, the hazard results are similar. Hazard results for both sites are presented within this report for completeness.

[1] The TI Team assumed that PGA is equal to 100 Hz, which is based on traditional assessments.

Table 10-2. Hazard input GMMs.

Calculation ID	Epistemic Uncertainty Branch	Aleatory Variability Branch	Weight (without SAF)
550101 - 550112	Lower	1 (low φ_{ss}, low τ)	0.0102675
550201 - 550212	Lower	2 (mid φ_{ss}, low τ)	0.034965
550301 - 550312	Lower	3 (high φ_{ss}, low τ)	0.0102675
550401 - 550412	Lower	4 (low φ_{ss}, mid τ)	0.034965
550501 - 550512	Lower	5 (mid φ_{ss}, mid τ)	0.11907
550601 - 550612	Lower	6 (high φ_{ss}, mid τ)	0.034965
550701 - 550712	Lower	7 (low φ_{ss}, high τ)	0.0102675
550801 - 550812	Lower	8 (mid φ_{ss}, high τ)	0.034965
550901 - 550912	Lower	9 (high φ_{ss}, high) τ)	0.0102675
560101 - 560112	Middle	1 (low φ_{ss}, low τ)	0.01369
560201 - 560212	Middle	2 (mid φ_{ss}, low τ)	0.04662
560301 - 560312	Middle	3 (high φ_{ss}, low τ)	0.01369
560401 - 560412	Middle	4 (low φ_{ss}, mid τ)	0.04662
560501 - 560512	Middle	5 (mid φ_{ss}, mid τ)	0.15876
560601 - 560612	Middle	6 (high φ_{ss}, mid τ)	0.04662
560701 - 560712	Middle	7 (low φ_{ss}, high τ)	0.01369
560801 - 560812	Middle	8 (mid φ_{ss}, high τ)	0.04662
560901 - 560912	Middle	9 (high φ_{ss}, high) τ)	0.01369
570101 - 570112	Upper	1 (low φ_{ss}, low τ)	0.0102675
570201 - 570212	Upper	2 (mid φ_{ss}, low τ)	0.034965
570301 - 570312	Upper	3 (high φ_{ss}, low τ)	0.0102675
570401 - 570412	Upper	4 (low φ_{ss}, mid τ)	0.034965
570501 - 570512	Upper	5 (mid φ_{ss}, mid τ)	0.11907
570601 - 570612	Upper	6 (high φ_{ss}, mid τ)	0.034965
570701 - 570712	Upper	7 (low φ_{ss}, high τ)	0.0102675
570801 - 570812	Upper	8 (mid φ_{ss}, high τ)	0.034965
570901 - 570912	Upper	9 (high φ_{ss}, high τ)	0.0102675

10.2.6 Hazard verification

According to the VVP, the parameters included in the HID (Appendix D) are required to be verified and validated. Specifically for the hazard calculations, the two code components (Haz45.3 and the VRG) were verified and validated. First, the updates to Haz45.3 (the GMM and site amplification implementation) were validated using a minimum of two calculation methods. For instance, the implementation of the backbone GMM (described in Section 9.2) were calculated both in Haz45.3 and in the Julia code provided by Peter Stafford. The second code component, the VRG, was compared to another rupture generator that has been used on previous SSHAC projects (Largent et al., 2024). Further information regarding the verification process can be found in the V&V Report (Largent et al., In Prep.).

10.3 NEW BUILD SITE AT DUYENFONTYN SEISMIC HAZARD RESULTS

The following section provides the hazard results for the new build site at Duynefontyn. These results are presented in different forms as outlined in Section 10.1. The total mean seismic hazard curves and source contribution curves are presented for all ten oscillator frequencies. Three fractile hazard curves are presented at 100, 10, and 1 Hz for the host zone. The disaggregation results for magnitude-distance are presented at AFEs of 10^{-4}, 10^{-5}, and 10^{-6}, followed by the UHRS at AFEs from 10^{-3} to 10^{-8} and the DRS. Finally, sensitivity analyses are presented for the 100, 10, and 1 Hz for multiple parameters in the overarching model. Hazard curves associated with each sensitivity analysis for the remaining seven frequencies are presented in Appendix G.

10.3.1 Seismic hazard curves

Figure 10-4 depicts the total mean hazard curves for each of the ten oscillator frequencies. The grey dashed lines show the three AFE values used in the disaggregation.

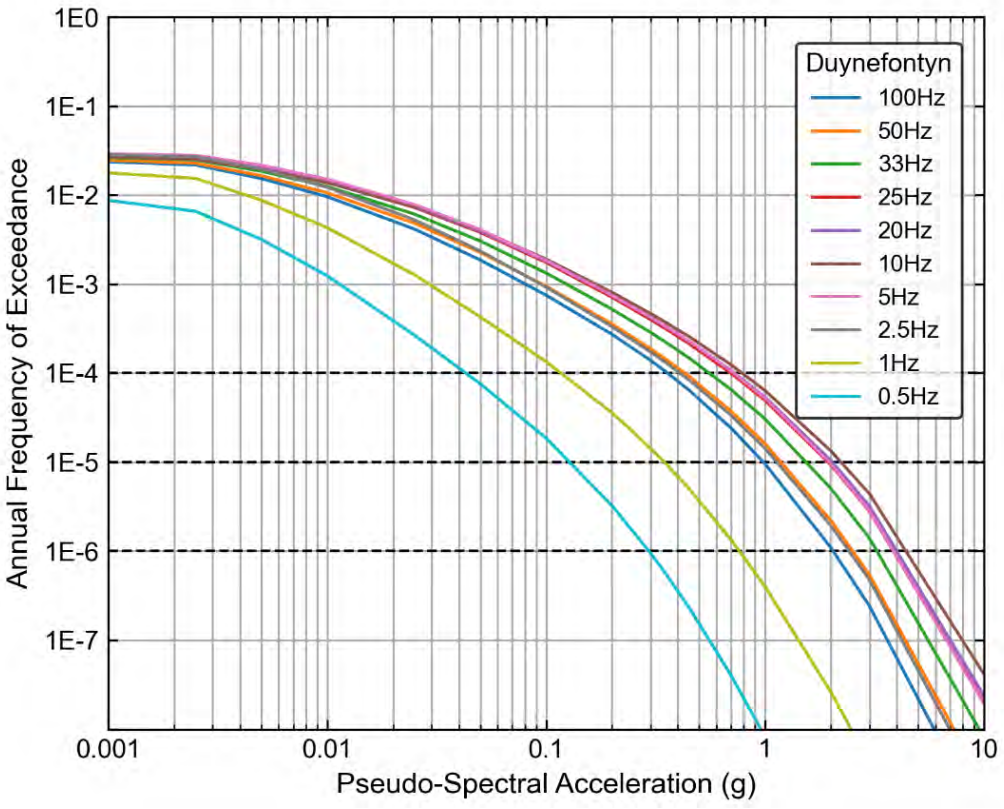

Figure 10-4. Total mean hazard results for the new build site at Duynefontyn.

10.3.1.1 Fractiles

Figure 10-5 to Figure 10-7 depict the fractile results for the new build site at Duynefontyn for 100, 10, and 1 Hz, respectively. The black line in each figure represents the median, the red line the mean, the dashed lines represent the 5th and 95th percentiles, and the dotted lines represent the 15th and 85th percentiles. The pseudo-spectral acceleration values associated with each are presented in Table 10-3 for an AFE of 10^{-4}, which demonstrates the uncertainty in the pseudo-spectral acceleration values computed for the new build site at Duynefontyn.

As is typical, the mean hazard curves approach higher fractiles as the AFEs increase. At both 100 Hz (Figure 10-5) and 10 Hz (Figure 10-6) the total mean hazard crosses the 85th percentile hazard curve at higher AFE values because there is larger epistemic uncertainty in the tails of the distribution at these frequencies. The slope of the mean hazard curve is a combination of the epistemic uncertainty and the aleatory variability, whereas the slope of the median is largely representative of the aleatory variability.

Table 10-3. Pseudo-spectral acceleration values for the presented fractiles for the new build site at Duynefontyn for an AFE of 10^{-4}

Frequency (Hz)	5th	15th	Median	Mean	85th	95th
100	0.110	0.147	0.269	0.359	0.496	0.709
10	0.229	0.312	0.555	0.784	1.082	1.607
1	0.044	0.057	0.096	0.117	0.159	0.214

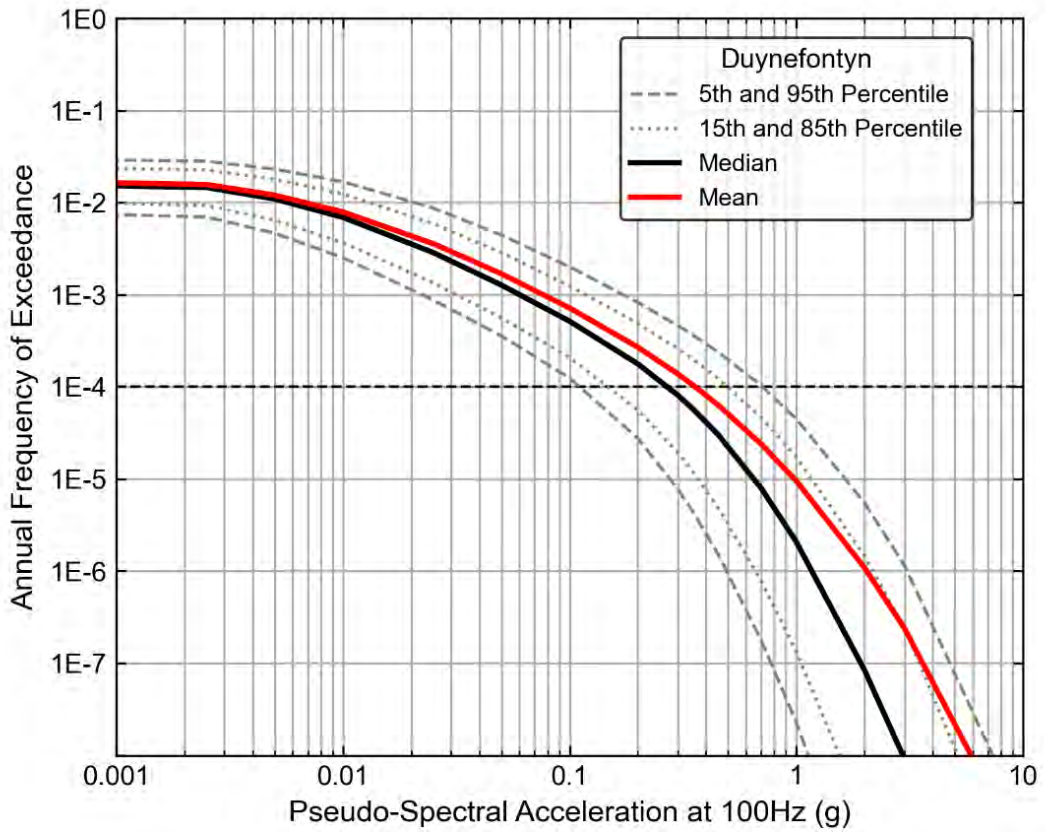

Figure 10-5. Fractile hazard curves for the host zone at 100 Hz for the new build site at Duynefontyn.

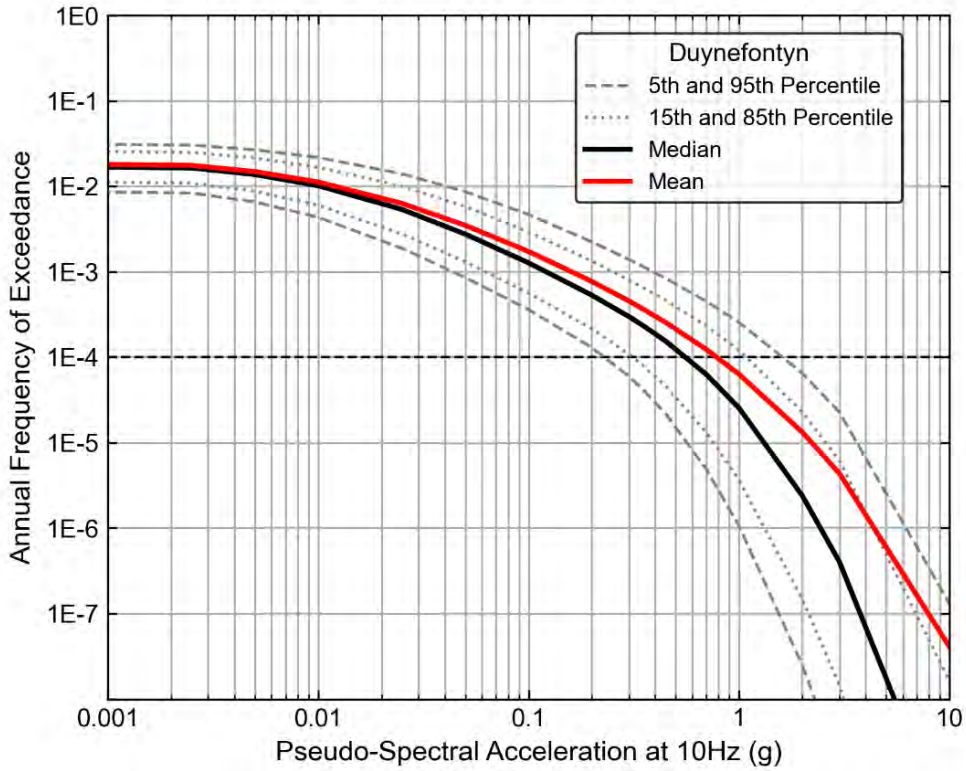

Figure 10-6. Fractile hazard curves for the host zone at 10 Hz for the new build site at Duynefontyn.

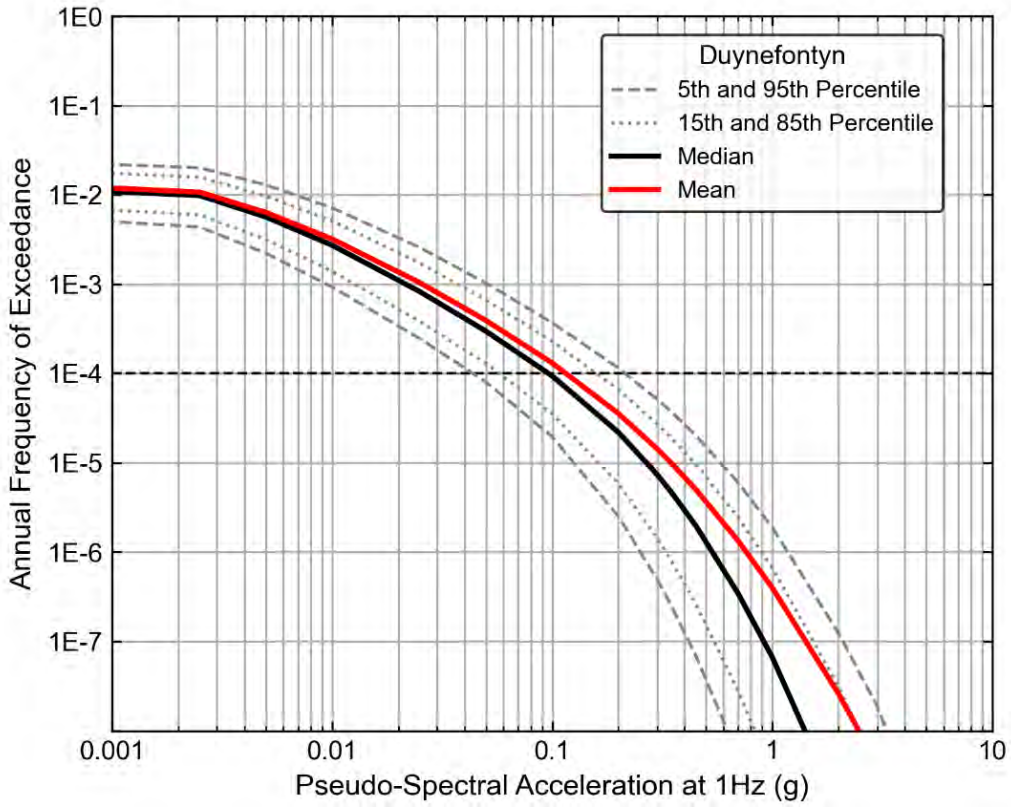

Figure 10-7. Fractile hazard curves for the host zone for 1 Hz at the new build site at Duynefontyn.

10.3.1.2 Contributions by seismic source

The following section presents the hazard contribution from each seismic source at the new build site at Duynefontyn for the ten oscillator frequencies. The new build site at Duynefontyn is within the SDZ and approximately 50 km from the Groenhof Fault Source. Figure 10-8 to Figure 10-17 show the total mean hazard (black line), the Saldania Zone (SDZ, host zone, red), Olifants River Zone (ORZ, yellow), Agulhas Zone (AGZ, green), Orange Basin Zone (OBZ, blue), Combined Outer Zone (COZ, orange), and the Groenhof Fault Source (GFS, purple). For the new build site at Duynefontyn, the largest contributing source is the SDZ followed by GFS for all oscillator frequencies.

As evident in these figures, the total hazard is dominated by the contribution from the SDZ at AFEs less than 10^{-2}. This is not surprising because the activity rate in the SDZ is higher than the other source zones and the earthquakes in this zone are closest to the site. For example, Figure 8-15 shows the highest concentration of earthquakes occur in the SDZ based on the adaptive kernel model for spatial smoothing. The small contribution of the Groenhof Fault Source reflects the minimal slip rate (mean slip rate of 0.01 mm/yr).

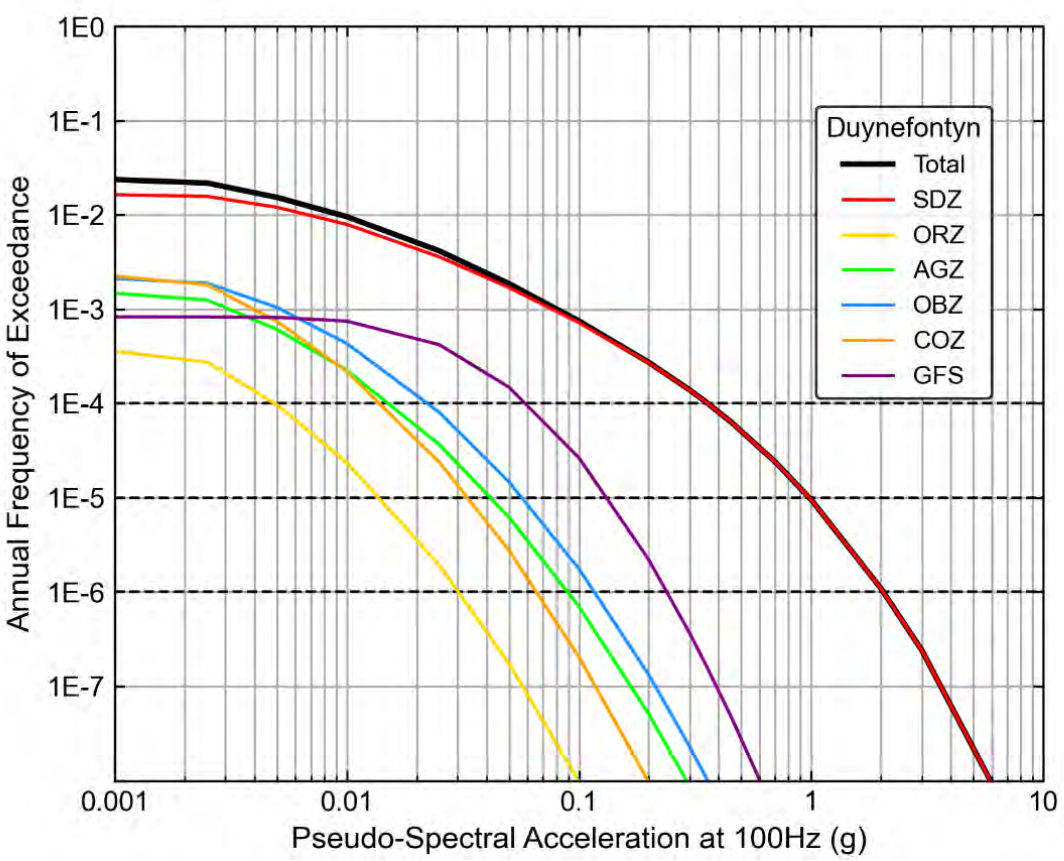

Figure 10-8. Source contribution hazard curves for 100 Hz at the new build site at Duynefontyn.

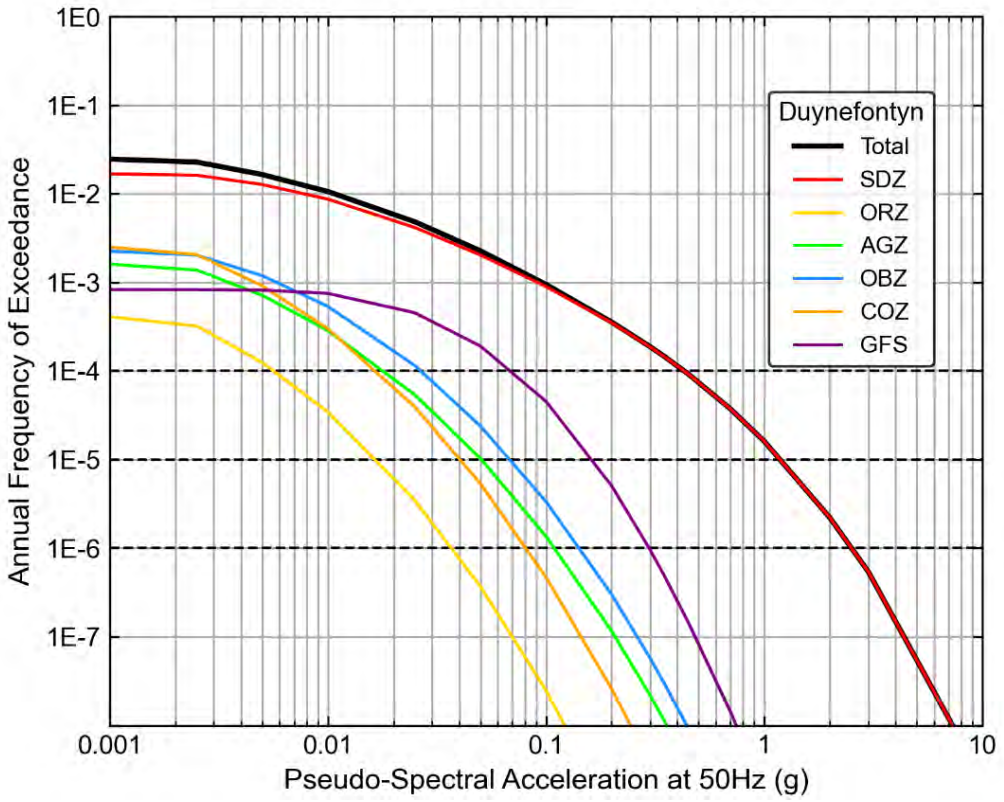

Figure 10-9. Source contribution hazard curves for 50 Hz at the new build site at Duynefontyn.

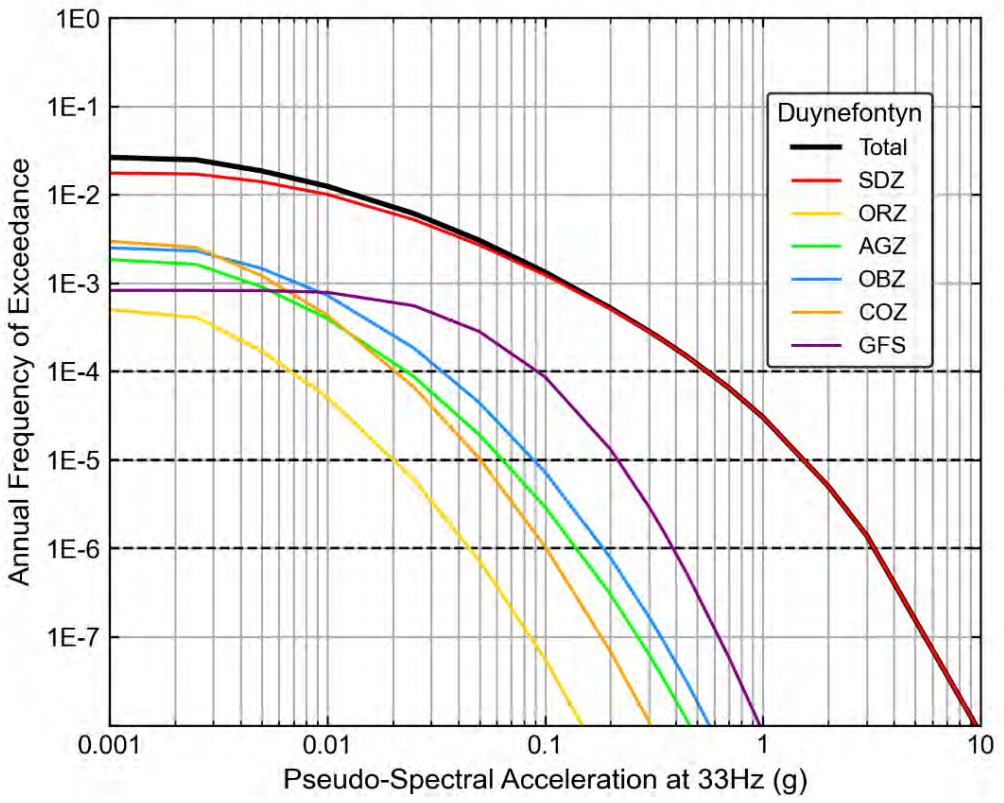

Figure 10-10. Source contribution hazard curves for 33 Hz at the new build site at Duynefontyn.

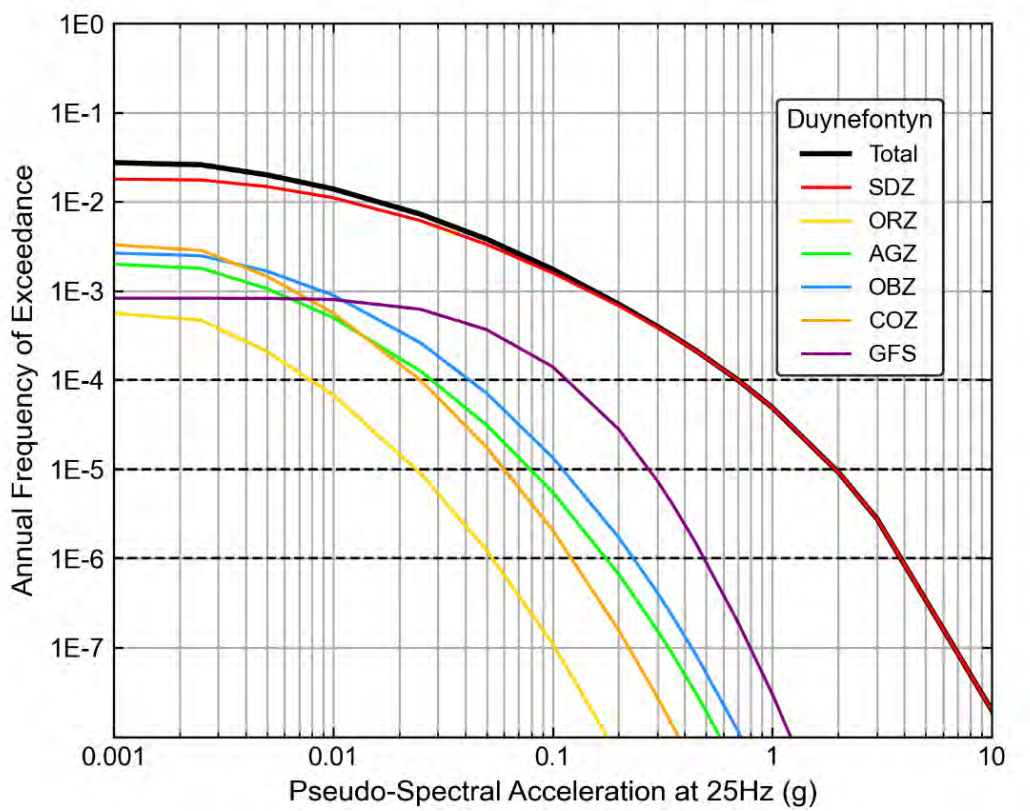

Figure 10-11. Source contribution hazard curves for 25 Hz at the new build site at Duynefontyn.

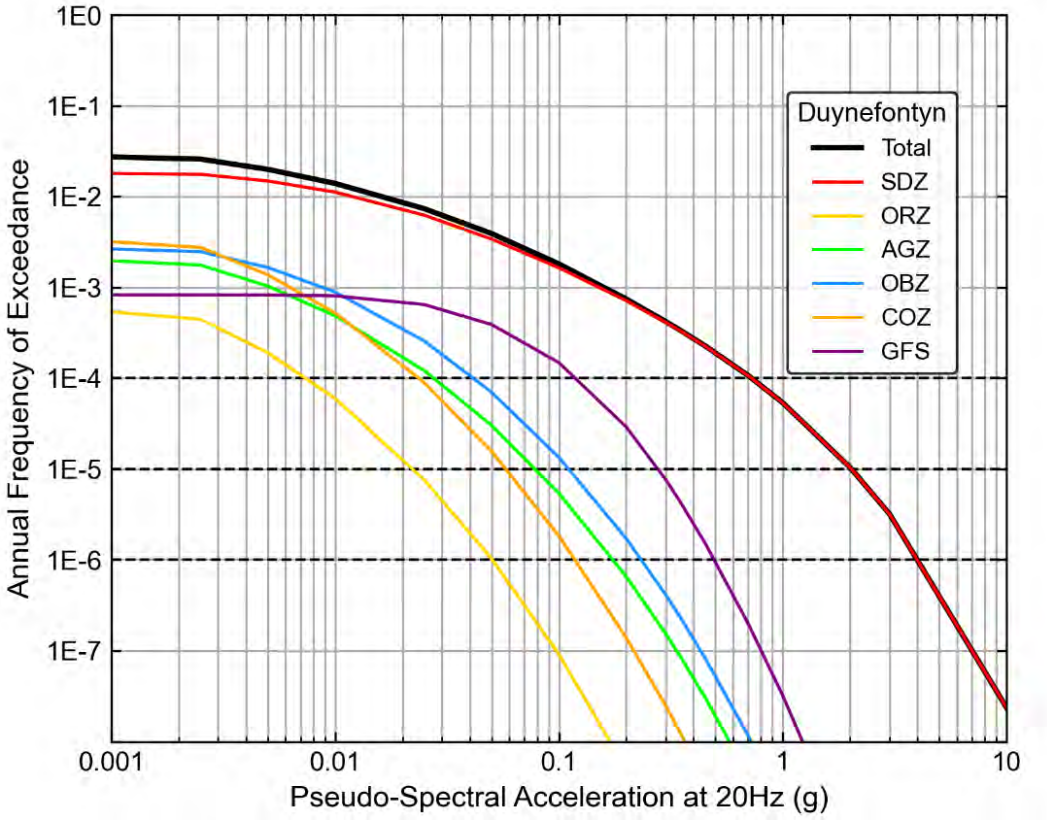

Figure 10-12. Source contribution hazard curves for 20 Hz at the new build site at Duynefontyn.

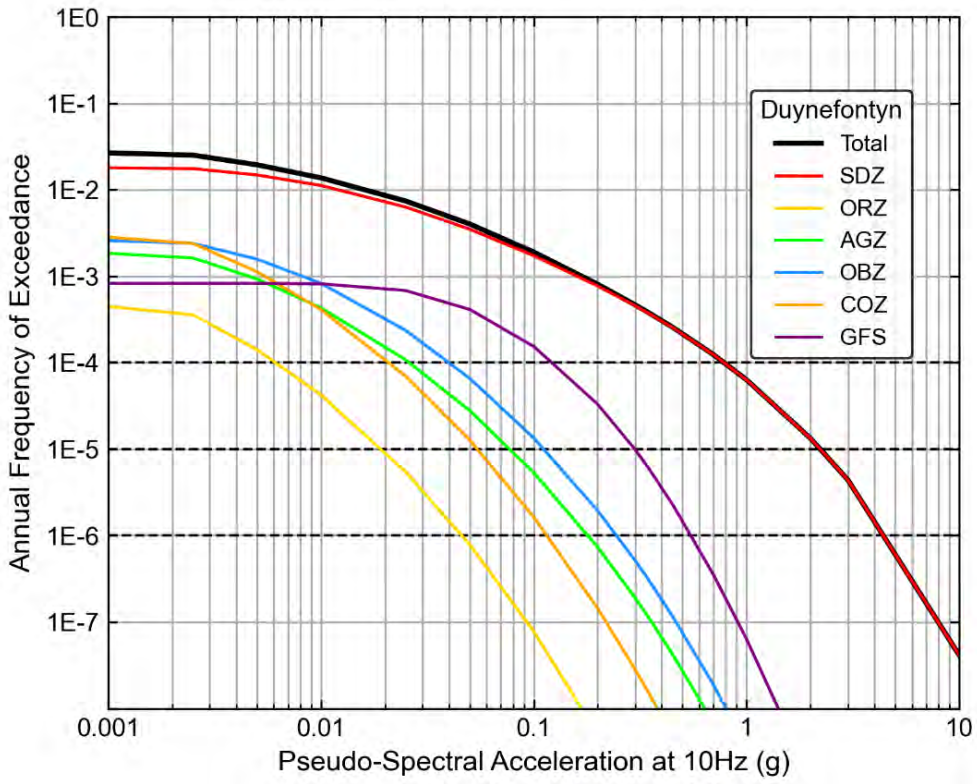

Figure 10-13. Source contribution hazard curves for 10 Hz at the new build site at Duynefontyn.

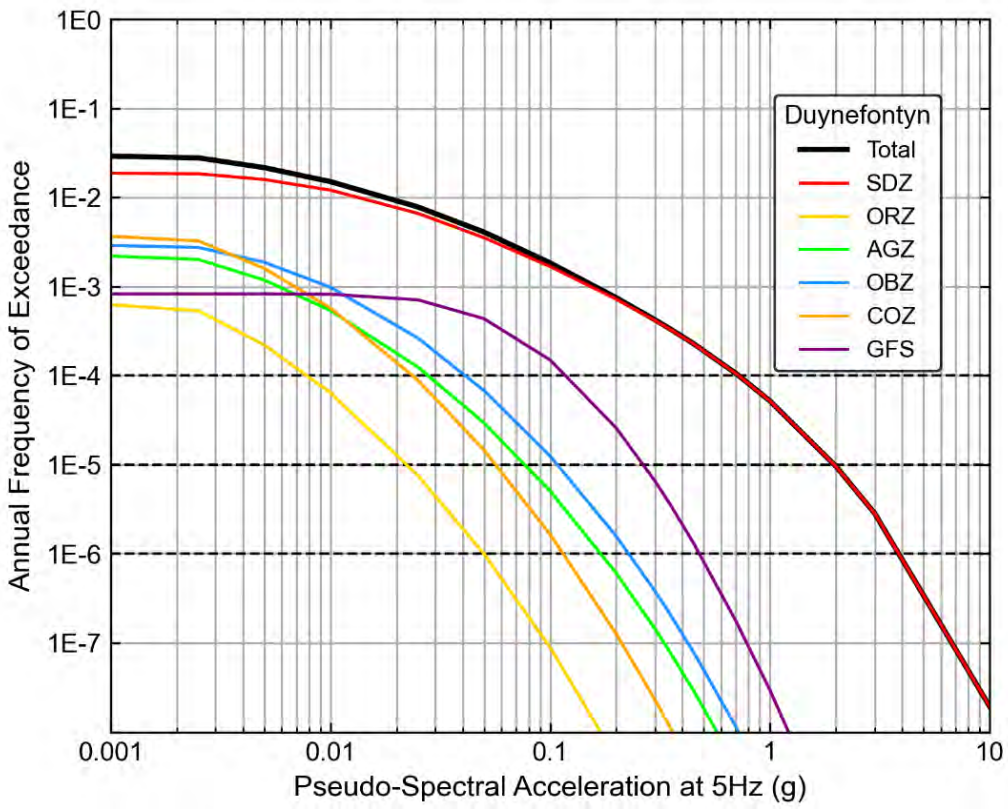

Figure 10-14. Source contribution hazard curves for 5 Hz at the new build site at Duynefontyn.

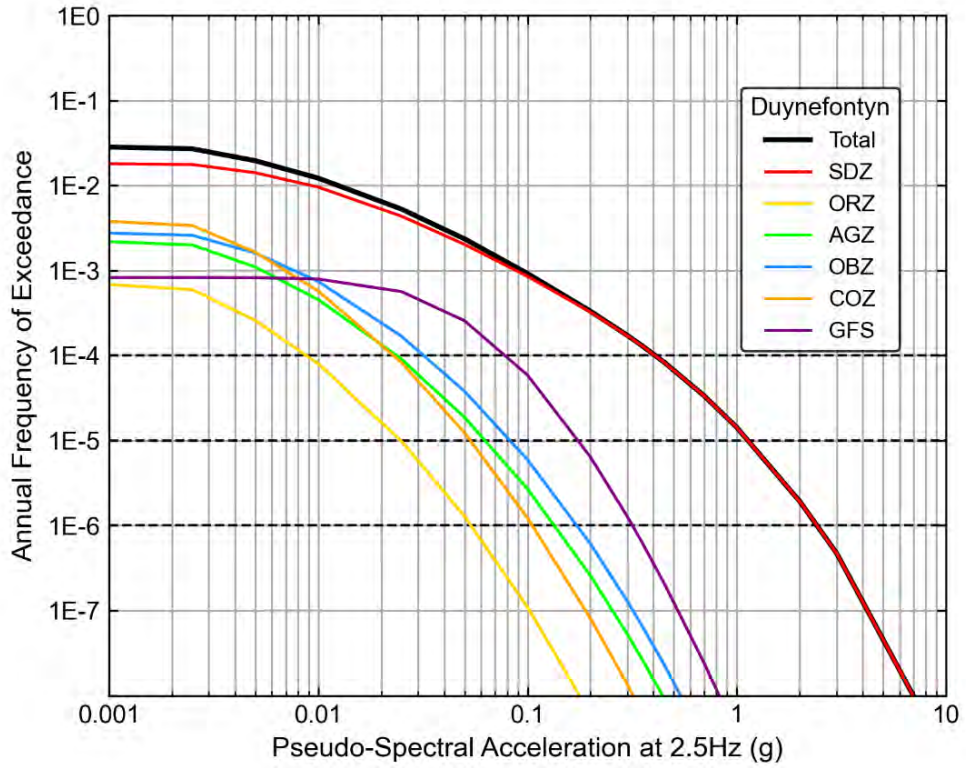

Figure 10-15. Source contribution hazard curves for 2.5 Hz at the new build site at Duynefontyn.

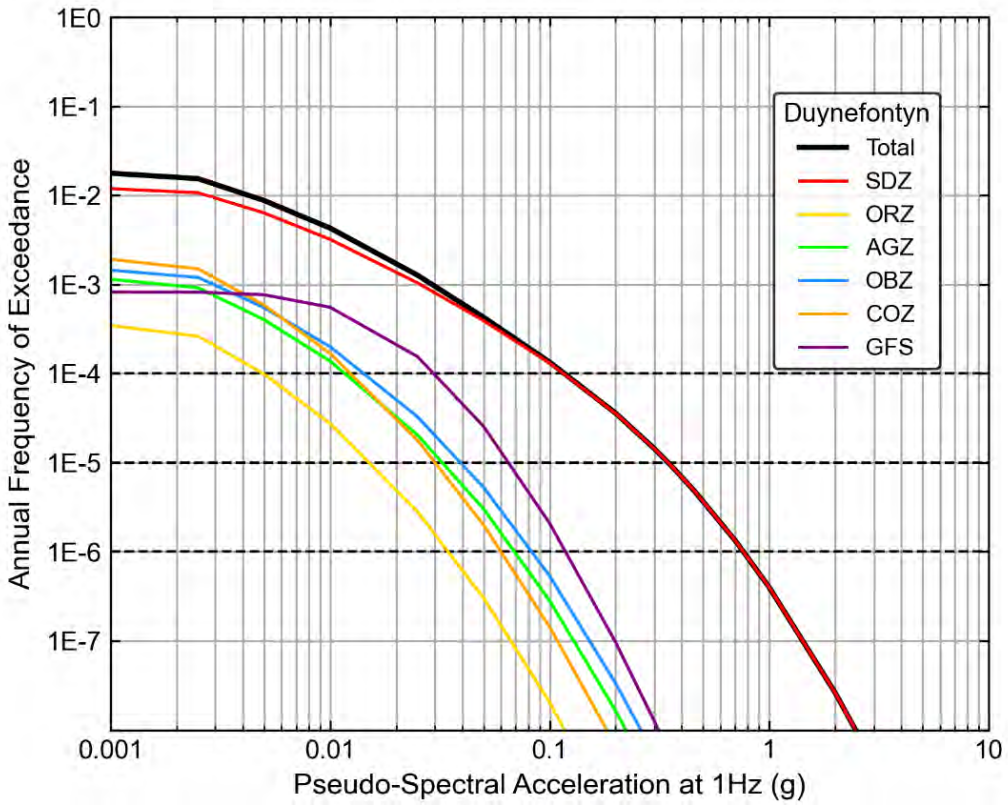

Figure 10-16. Source contribution hazard curves for 1 Hz at the new build site at Duynefontyn.

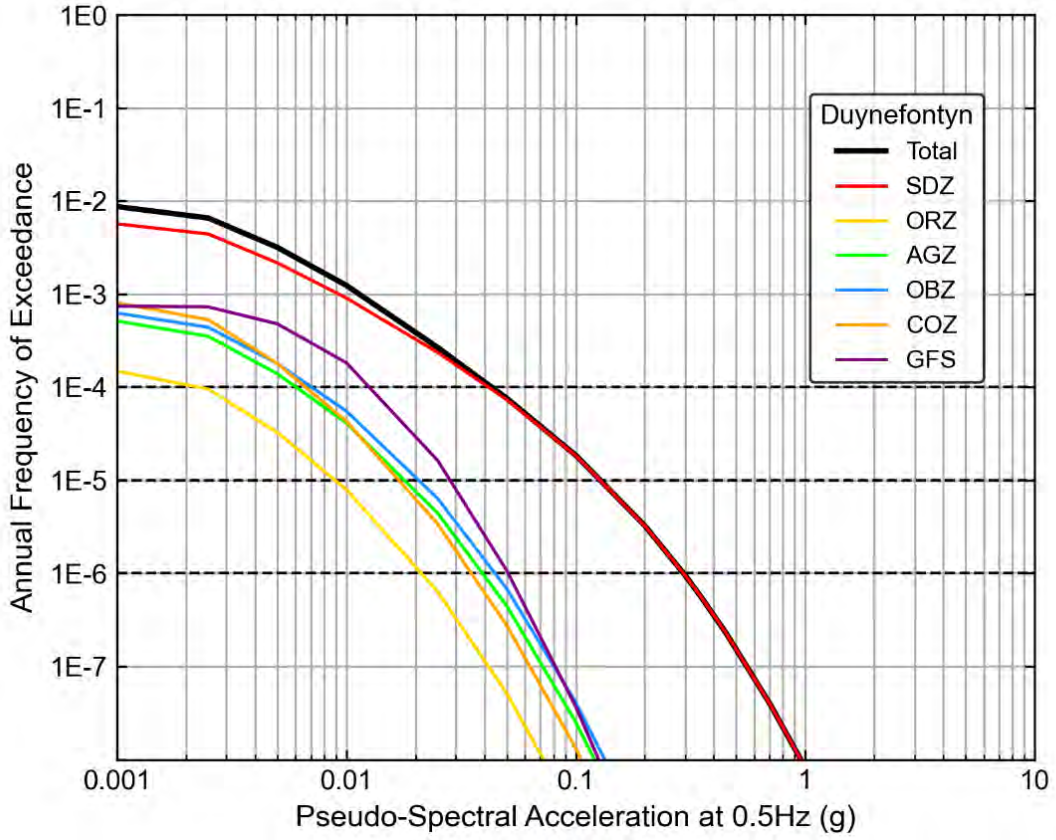

Figure 10-17. Source contribution hazard curves for 0.5 Hz at the new build site at Duynefontyn.

10.3.1.3 Contributions by magnitude, distance and epsilon scenarios

The following section presents the disaggregation of the total mean hazard by magnitude and distance at the new build site at Duynefontyn for the ten oscillator frequencies. The disaggregation was performed for AFEs of 10^{-4}, 10^{-5}, and 10^{-6}. Figure 10-18 to Figure 10-27 show the hazard disaggregation results at each of the three AFEs for various magnitude and distance pairs for all ten oscillator frequencies.

As demonstrated in the figures and Table 10-4, earthquakes with approximately **M** 6.0 located close to the site are the dominant contributors to the hazard. For oscillator frequencies of 10 to 100 Hz the modal magnitude and distance is **M** 5.1 to 5.3 at 15 km. It should be noted that the modal magnitude and distance are taken as the centre of the disaggregation bins. For oscillator frequencies of 0.5 and 5 Hz the modal magnitude and distance ranges from **M** 5.5 to 6.1 at 15 km. The mean magnitudes are slightly higher than the mode, ranging from **M** 5.8 to 6.3 for 10^{-4}. For smaller oscillator frequencies, larger more distant earthquakes contribute slightly more to hazard, but this contribution is still minimal compared to the nearby earthquakes in the SDZ. The epsilon values for all oscillator frequencies at 10^{-4} range widely from less than negative two to above positive two. At lower AFEs, this changes to epsilons primarily greater than one for all oscillator frequencies.

Table 10-4. Modal and Mean magnitude and distance pairings for the new build site at Duynefontyn.

Frequency (Hz)	10^{-4}				10^{-5}				10^{-6}			
	Mode		Mean		Mode		Mean		Mode		Mean	
	M	Dist. (km)	M	Dist. (km)	M	Dist. (km)	M	Dist. (km)	M	Dist (km)	M	Dist. (km)
100	5.3	15	5.9	13.7	5.5	7.5	5.9	9.1	5.5	7.5	5.9	7.4
50	5.1	15	5.9	14.3	5.5	7.5	5.9	9.6	5.5	7.5	5.9	7.6
33	5.1	15	5.8	14.7	5.5	7.5	5.9	9.9	5.5	7.5	5.9	7.7
25	5.1	15	5.8	14.5	5.5	7.5	5.9	9.7	5.5	7.5	5.9	8.2
20	5.1	15	5.9	14.3	5.5	7.5	5.9	9.4	5.5	7.5	5.9	8.1
10	5.1	15	5.9	14.3	5.5	7.5	5.9	9.6	5.5	7.5	5.9	8.4
5	5.5	15	5.9	13.3	5.5	7.5	6.0	8.9	5.5	7.5	6.0	7.5
2.5	5.5	15	6.0	13.6	5.9	7.5	6.1	8.5	5.9	7.5	6.3	6.3
1	6.1	15	6.2	17.5	6.3	7.5	6.4	8.6	6.5	7.5	6.6	6.1
0.5	6.1	15	6.3	26.0	6.5	7.5	6.6	10.5	6.5	7.5	6.7	6.1

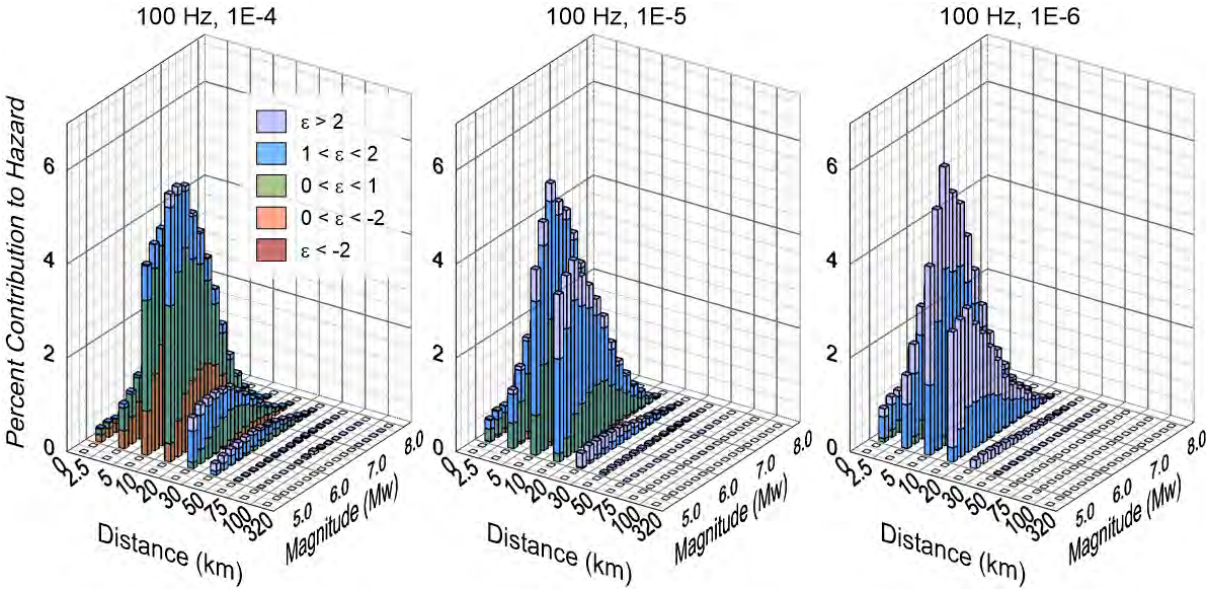

Figure 10-18. Disaggregation for AFEs of 10^{-4}, 10^{-5}, and 10^{-6} at 100 Hz at the new build site at Duynefontyn.

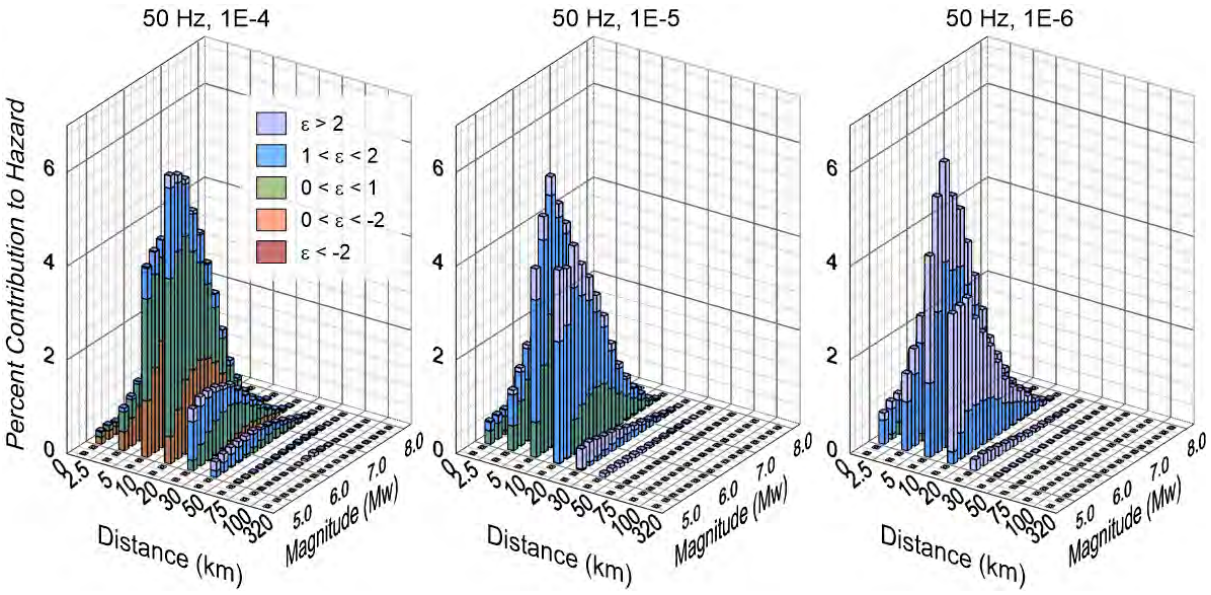

Figure 10-19. Disaggregation for AFEs of 10^{-4}, 10^{-5}, and 10^{-6} at 50 Hz at the new build site at Duynefontyn.

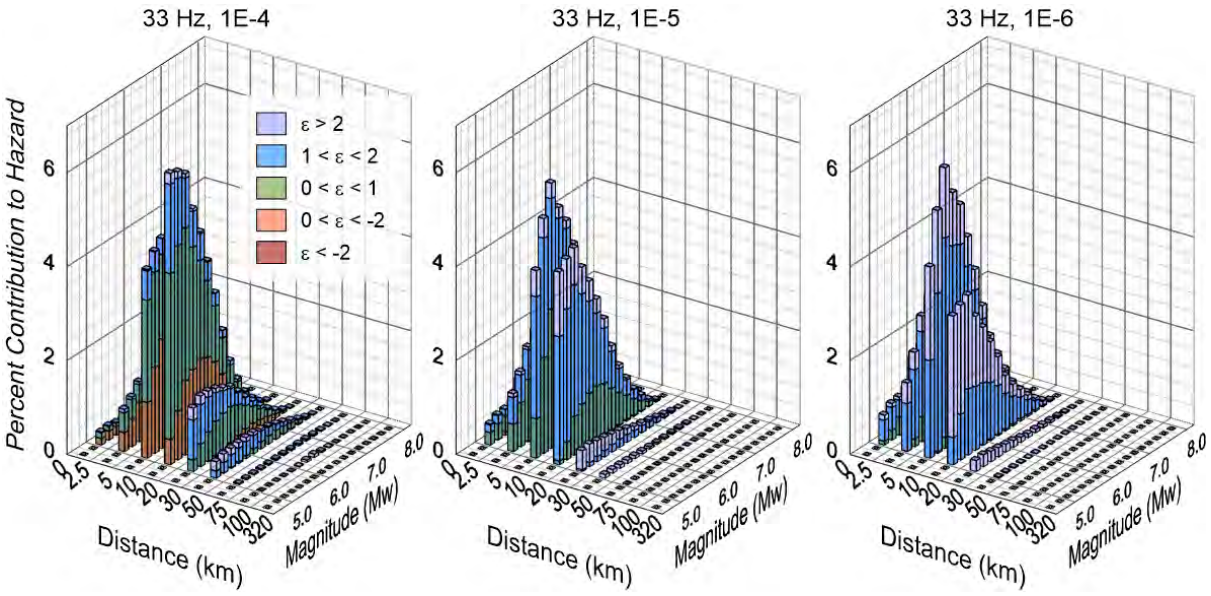

Figure 10-20. Disaggregation for AFEs of 10^{-4}, 10^{-5}, and 10^{-6} at 33 Hz at the new build site at Duynefontyn.

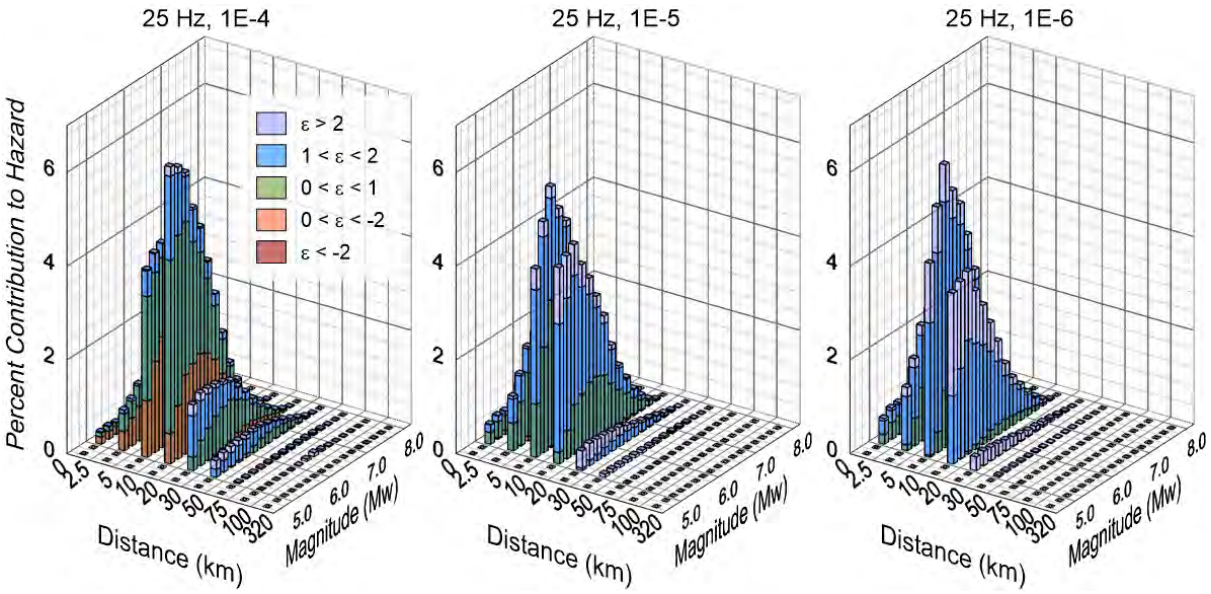

Figure 10-21. Disaggregation for AFEs of 10^{-4}, 10^{-5}, and 10^{-6} at 25 Hz at the new build site at Duynefontyn.

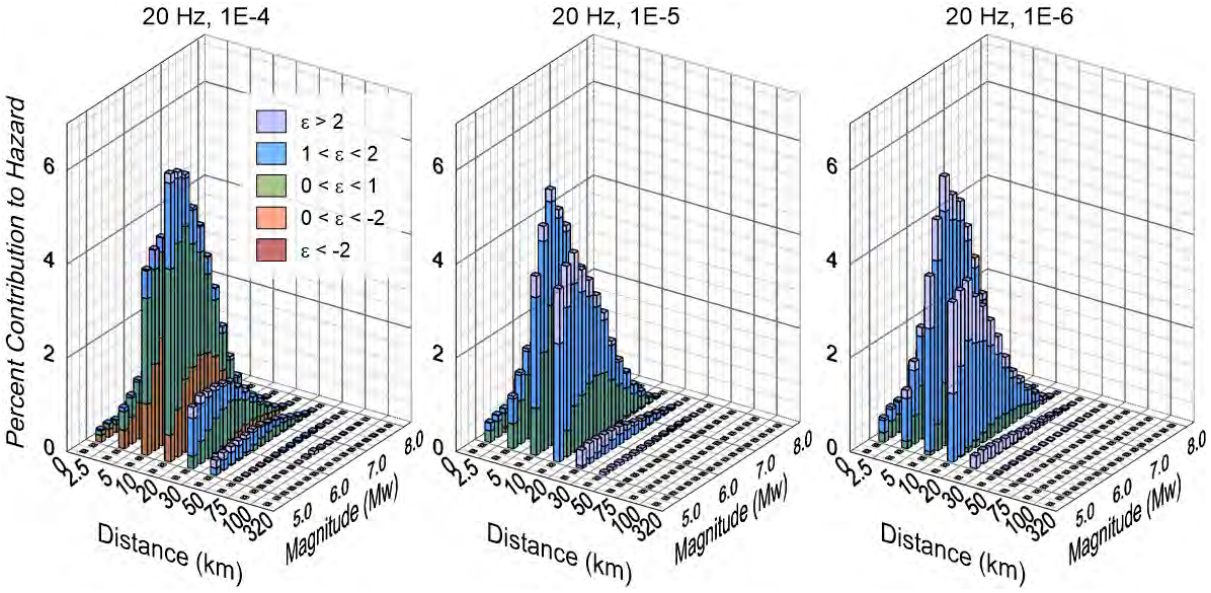

Figure 10-22. Disaggregation for AFEs of 10^{-4}, 10^{-5}, and 10^{-6} at 20 Hz at the new build site at Duynefontyn.

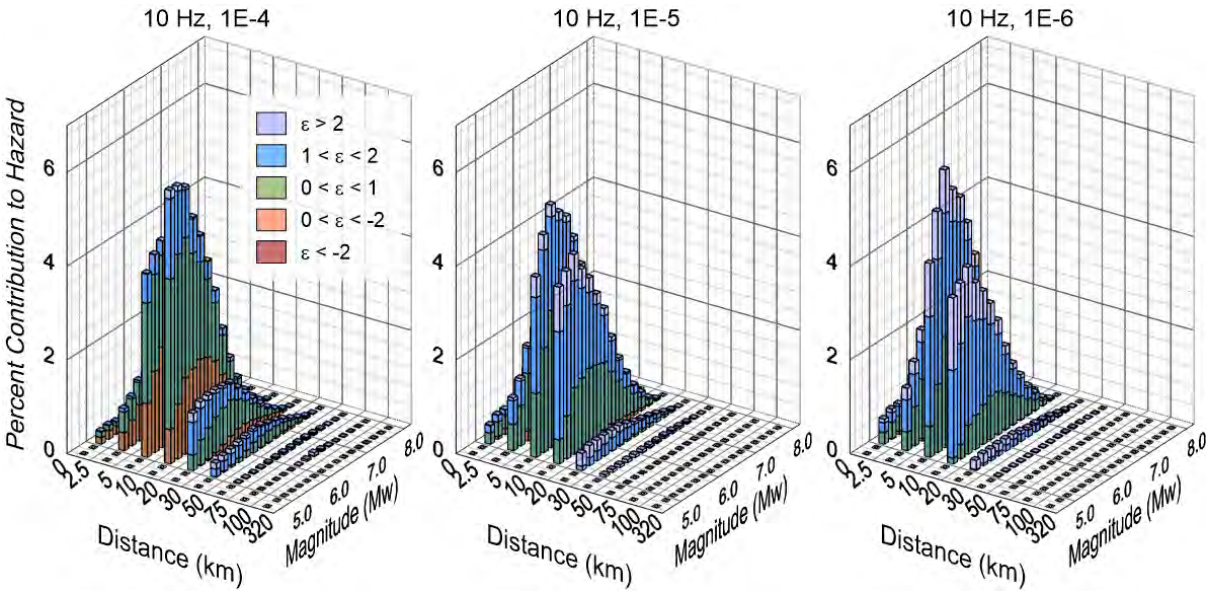

Figure 10-23. Disaggregation for AFEs of 10^{-4}, 10^{-5}, and 10^{-6} at 10 Hz at the new build site at Duynefontyn.

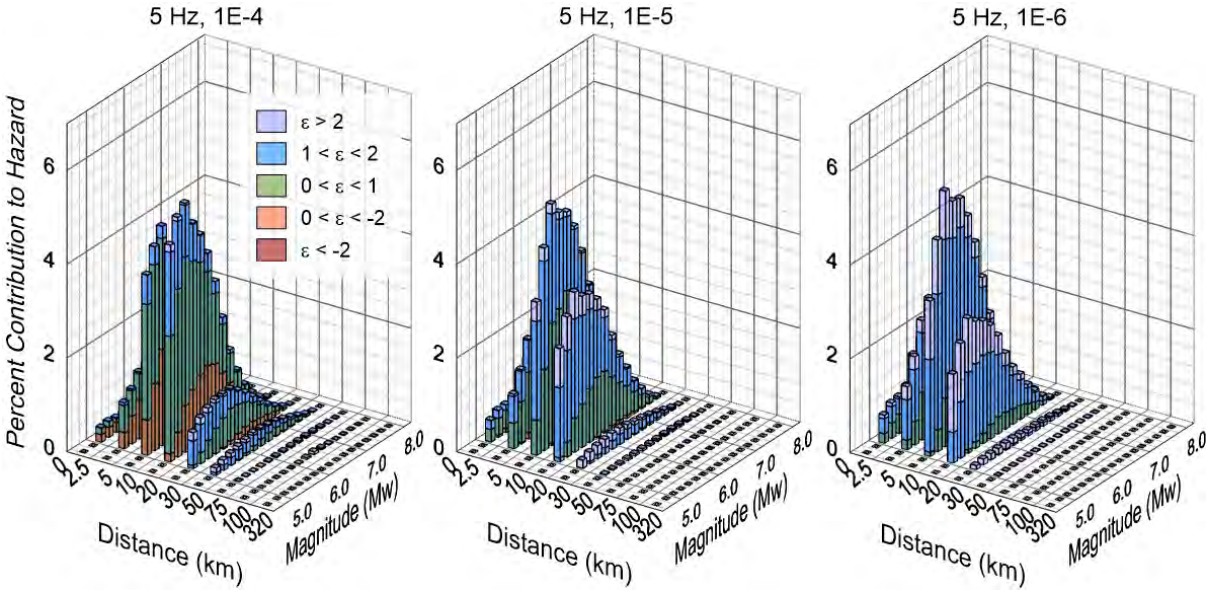

Figure 10-24. Disaggregation for AFEs of 10^{-4}, 10^{-5}, and 10^{-6} at 5 Hz at the new build site at Duynefontyn.

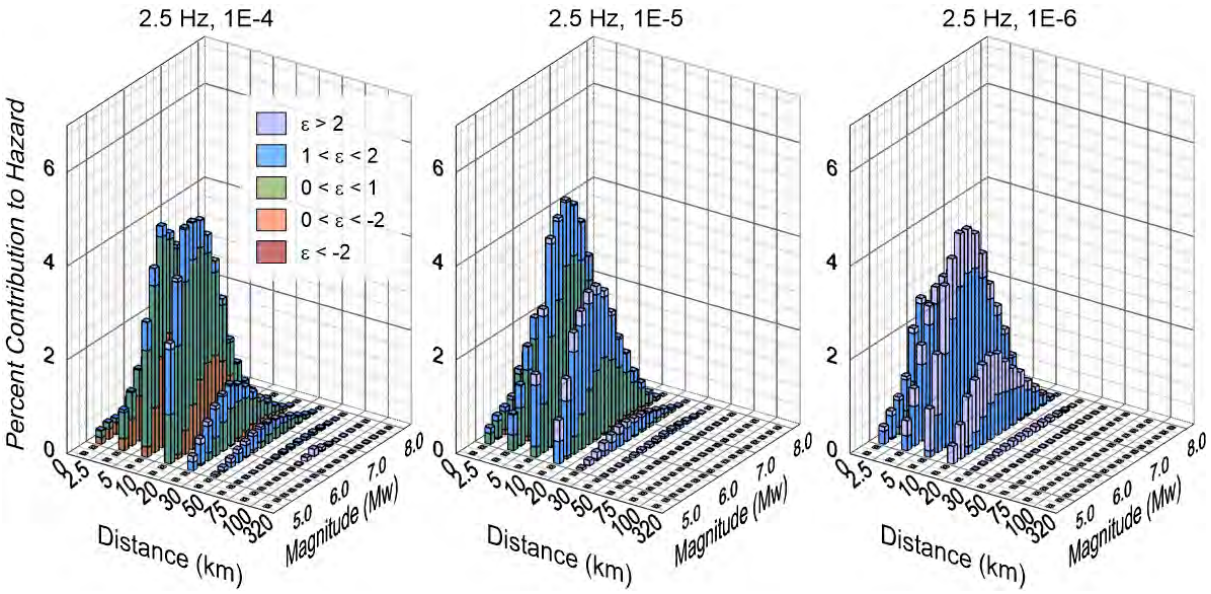

Figure 10-25. Disaggregation for AFEs of 10^{-4}, 10^{-5}, and 10^{-6} at 2.5 Hz at the new build site at Duynefontyn.

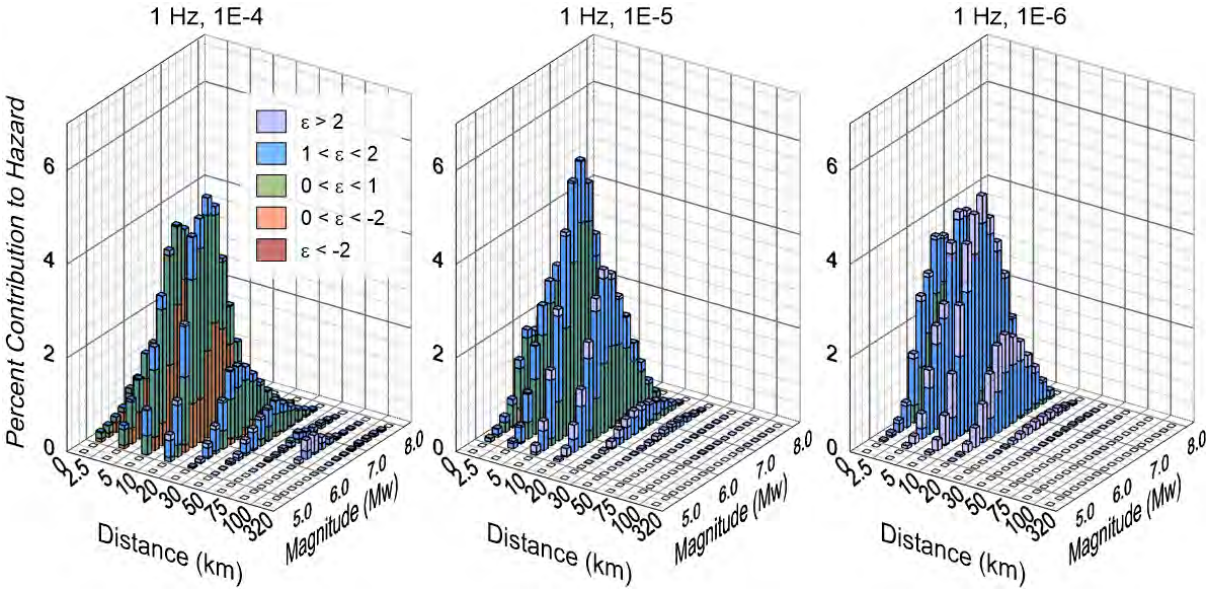

Figure 10-26. Disaggregation for AFEs of 10^{-4}, 10^{-5}, and 10^{-6} at 1 Hz at the New Build at Duynefontyn.

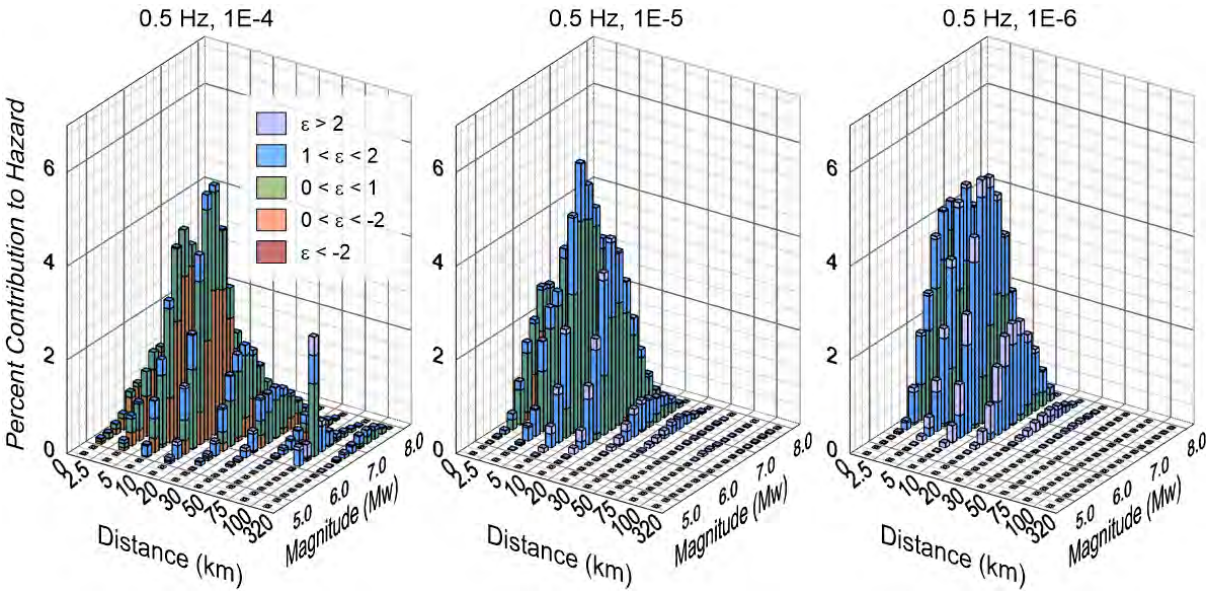

Figure 10-27. Disaggregation for AFEs of 10^{-4}, 10^{-5}, and 10^{-6} at 0.5 Hz at the new build site at Duynefontyn.

10.3.1.4 Uniform hazard response spectra

The UHRS represent the ground-motion at a specific AFE through the ten oscillator frequencies. The UHRS are calculated by interpolating the total mean hazard curves in log-space, at each period, at AFEs of 10^{-3}, 10^{-4}, 10^{-5}, 10^{-6}, 10^{-7}, and 10^{-8}. The six UHRS are depicted in Figure 10-28 and summarised in Table 10-5.

As shown in Figure 10-28, the shapes of the UHRS are relatively broad with the largest accelerations between 5 and 20 Hz. There are several contributing factors related to the complexity of the site geology that lead to the broad spectral shape. The large variability in the V_S profiles at the site contributes large epistemic uncertainty to the spectral accelerations between 5 and 20 Hz. The large variability in V_S is reflective of the complexity of the site as described in Sections 4.4 and 4.5. The broad shape captures the variability of more narrowly peaked spectra occurring at different frequencies. For example, in Figure 9-104 the highly variable contributions from eight borehole V_S profiles demonstrates this result. The largest variability is at 10 Hz, thus the UHRS peaks at this value for lower AFEs.

Additionally, the large spread in κ_0 contributes to the epistemic uncertainty in the high frequency ground motions above 10 Hz reflecting the limited earthquake data available to constrain κ_0. For example, Figure 9-105 shows a broad range of amplification at 25 Hz due to the epistemic uncertainty in κ_0.

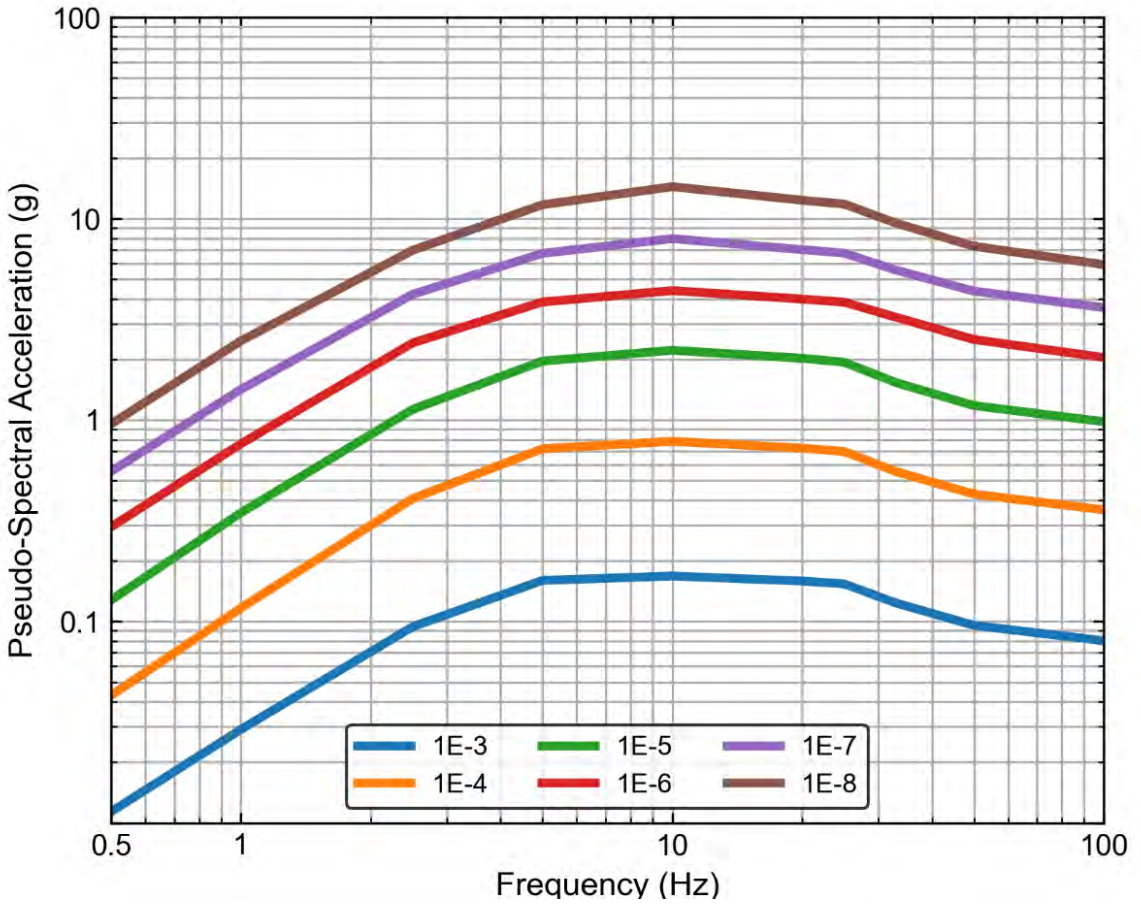

Figure 10-28. Uniform hazard spectra for the new build site at Duynefontyn.

Table 10-5. Uniform hazard spectra and design spectrum results for the new build site at Duynefontyn.

Frequency (Hz)	10^{-3}	10^{-4}	10^{-5}	10^{-6}	10^{-7}	10^{-8}
100	0.0802	0.3585	0.9821	2.0463	3.6187	5.9175
50	0.0957	0.4290	1.1800	2.5121	4.3689	7.2943
33	0.1235	0.5549	1.5354	3.2421	5.5524	9.5089
25	0.1538	0.6983	1.9386	3.8519	6.7498	11.8278
20	0.1588	0.7256	2.0278	3.9905	7.0195	12.3476
10	0.1681	0.7843	2.2209	4.3947	7.9611	14.4215
5.0	0.1599	0.7207	1.9632	3.8598	6.7282	11.7285
2.5	0.0941	0.4074	1.1301	2.4157	4.2132	6.9708
1.0	0.0291	0.1167	0.3468	0.7626	1.4206	2.4741
0.5	0.0114	0.0429	0.1278	0.2948	0.5559	0.9566

10.3.1.5 Ground-motion response spectrum

The ground-motion response spectrum (GMRS[2]) was calculated in accordance with ASCE/SEI 43-19 Section 2.2[3]. Per the requirements in ASCE/SEI 43-19, the GMRS is computed using Equation 10-3 below:

10-3

$$GMRS = SF\ x\ UHRS_{H_P}$$

where,

$UHRS_{H_P}$ = uniform hazard response spectrum for AFE of H_P

$H_P = P_F$ (selected from ASCE/SEI 43-19 Table 1-1, reproduced in Table 10-6)

SF = Scale factor computed in Equation 10-4

10-4

$$SF = Max[SF_1, SF_2, SF_3]$$

where,

10-5

$$SF_1 = A_R^{-1.0}$$

10-6

$$SF_2 = 0.6\ A_R^{-0.2}$$

10-7

$$SF_3 = 0.45$$

10-8

$$A_R = \frac{SA_{H_P}}{SA_{H_D}}$$

where,

A_R is the slope factor, defined in ASCE/SEI 43-19

SA_{H_P} is the spectral acceleration value at the AFE H_P

[2] ASCE/SEI 43-19 uses the term “design-basis earthquake” described by a design response spectrum (DRS) to specify the design basis ground motion (DBGM). The GMRS and DRS are equivalent because both are derived from the same mathematical equations. The DBGM are derived from the site GMRS with the caveat that the DBGM must meet the minimum PGA values specified in ASCE/SEI 43-19.
[3] The NRC Regulatory Guide 1.208 references ASCE/SEI 43-05 which has been superseded by ASCE/SEI 43-19.

SA_{H_D} is the spectral acceleration value at the AFE H_D

$$H_D = 10\ x\ P_F$$

Table 10-6. Summary of Earthquake Design Provisions (originally published as Table 1-1 in ASCE/SEI 43-19).

Seismic Design Category	P_f
2	4 x 10^{-4}
3	10^{-4}
4	4x10^{-5}
5	10^{-5}

H_P was set equal to P_F for SDC 5 as 10^{-5} and, therefore, H_D for the new build site at Duynefontyn is equal to 10^{-4}. The UHRS associated with each of these AFE values are presented in Figure 10-29. Using the spectral acceleration values associated with these two AFEs, the slope factor (A_R) was calculated at each of the ten oscillator frequencies. The scale factor (SF) was then calculated using Equations 10-5 through 10-7 and applied to the $UHRS_{H_P}$ at each frequency.

A comparison of the GMRS with the UHRS for AFE of 10^{-4} through 10^{-5} is presented in Figure 10-29 below and the development of the GMRS is demonstrated in Table 10-7.

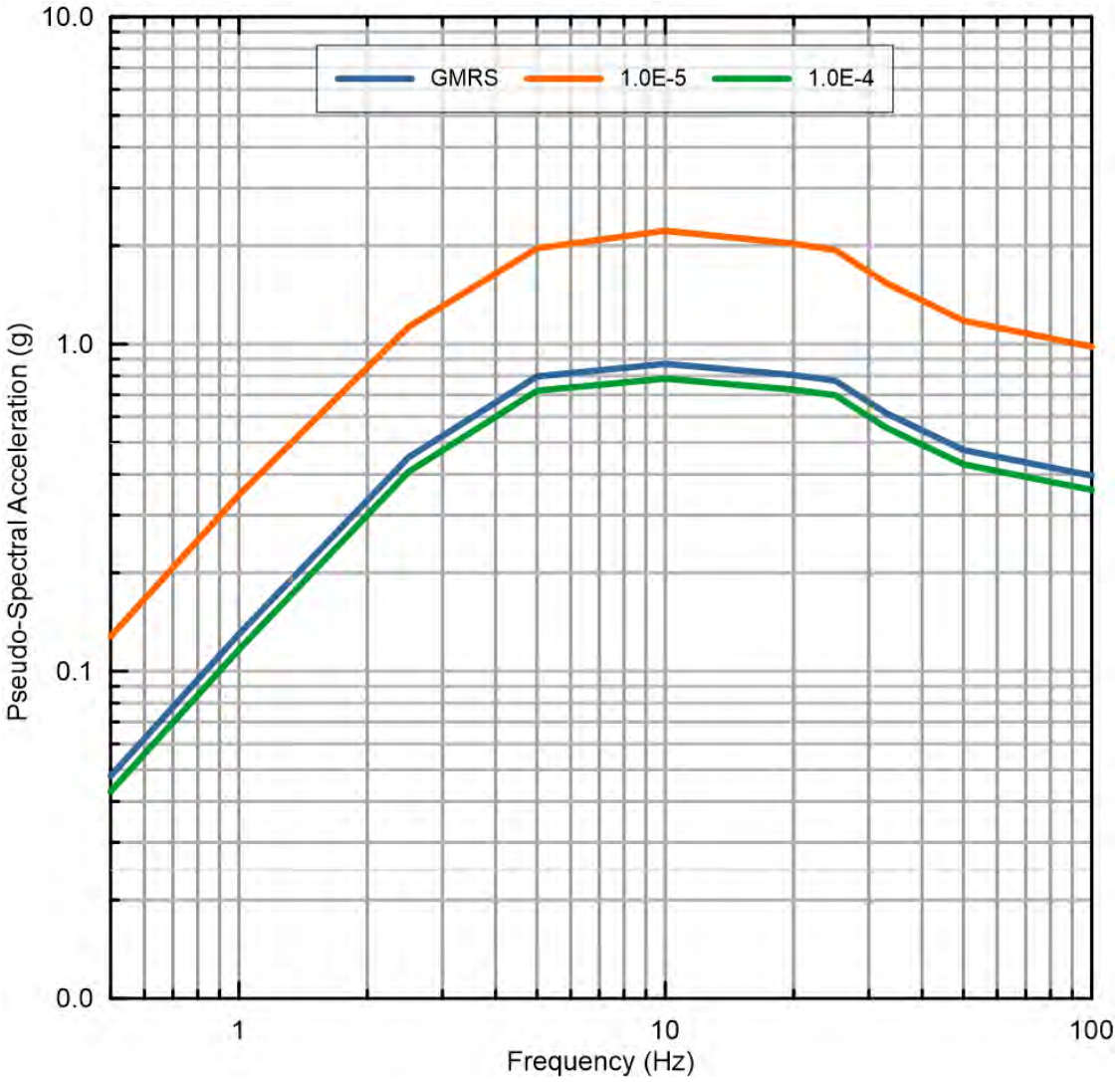

Figure 10-29. Ground-motion response spectrum for the new build site at Duynefontyn.

Table 10-7. Ground-motion response spectrum results for the new build site at Duynefontyn per ASCE/SEI 43-19.

Frequency (Hz)	$\frac{Sa10^{-4}}{Sa10^{-5}}$	SF_1 $Ratio^{-0.1}$	SF_2 $0.6 * Ratio^{0.2}$	SF_3	GMRS
100	0.365	1.106	0.734	0.45	0.397
50	0.364	1.106	0.735	0.45	0.475
33	0.361	1.107	0.735	0.45	0.614
25	0.360	1.107	0.736	0.45	0.773
20	0.358	1.108	0.737	0.45	0.804
10	0.353	1.110	0.739	0.45	0.870
5.0	0.367	1.105	0.733	0.45	0.797
2.5	0.361	1.107	0.736	0.45	0.451
1.0	0.336	1.115	0.746	0.45	0.130
.5	0.336	1.115	0.746	0.45	0.048

In order to provide some contextual comparisons for the horizontal GMRS at the new build site at Duynefontyn and the KNPS (presented here and further outlined in Section 10.4), the design basis response spectrum is compared with the GMRS from three nuclear power plant (NPP) sites in the Eastern United States, whose locations are shown in Figure 10-30. The GMRS are compared in Figure 10-31, which also shows the USNRC RG 1.60 (USNRC, 2014) design response spectra anchored at 0.30g. These GMRS were developed by the USNRC staff as part of the review of all updated seismic hazard curves for all US commercial nuclear power plants (USNRC, 2021). The updated hazards were required following the accident at the Fukushima Dai-ichi NPP, and in response to Commission direction.

Pilgrim and Vogtle are considered to have moderate hazards compared to low hazard sites like Hope Creek. Several observations can be made with regards to Figure 10-31 starting with the fact that the GMRS for Pilgrim, Vogtle, the new build site at Duynefontyn and the KNPS exceed the USNRC RG 1.60 design spectrum at low oscillator frequencies. This reflects a common outcome of the post-Fukushima seismic hazard analysis, that the standard design spectra at almost all hard rock and stiff soil sites in the Central Eastern United States (CEUS) were shown to underrepresent the high-frequency ground motions above about 10 Hz. This is also evident in the updated GMRS for the new build site at Duynefontyn and the KNPS. Within this context, the updated hazard developed in this study shows that the results for the new build site at Duynefontyn and the KNPS are not unusual and can be viewed as being consistent with the U.S. experience. To support the seismic evaluations, EPRI conducted high-frequency seismic testing of a diverse set of typical plant control components. The results of this test program were documented in EPRI (2015).

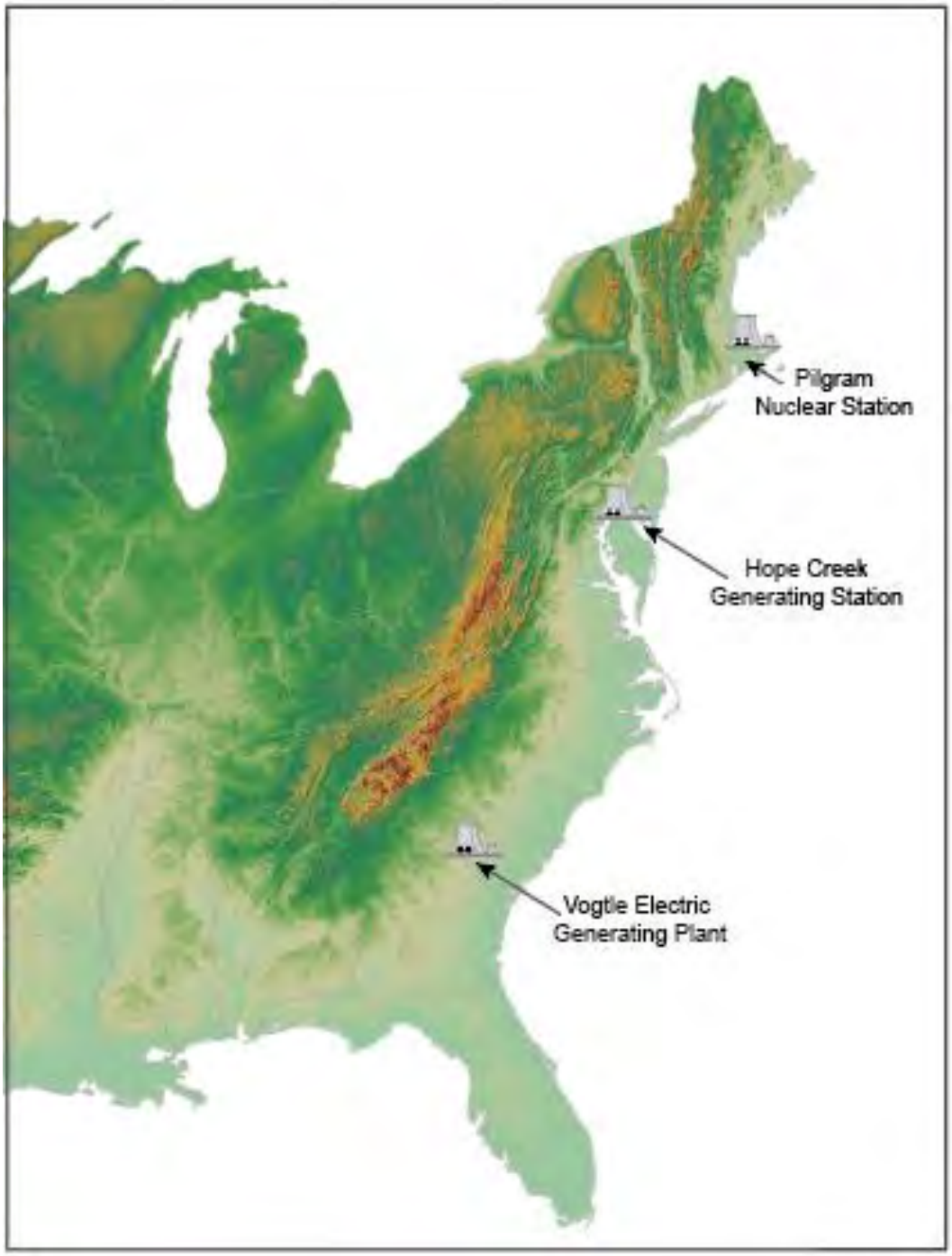

Figure 10-30. Digital Elevation Map of the eastern U.S. showing the location of the three commercial NPPs sites provided in the GMRS comparisons.